

AD-A070305

NAVY TACTICAL APPLICATIONS GUIDE
VOLUME 2
ENVIRONMENTAL
PHENOMENA
AND EFFECTS

DEFENSE METEOROLOGICAL
SATELLITE PROGRAM (DMSP)

Prepared under the direction of
Robert W. Fett

TACTICAL APPLICATIONS DEPARTMENT

Naval Environmental Prediction
Research Facility
Monterey, California 93940

1979



ORIGINAL CONTAINS COLOR PLATES: ALL DOCS.
REPRODUCTIONS WILL BE IN BLACK AND WHITE

THE WALTER A. BOHAN COMPANY

2026 OAKTON STREET, PARK RIDGE, ILLINOIS 60068
APPLIED RESEARCH IN SATELLITE METEOROLOGY AND OCEANOGRAPHY

UNCLASSIFIED

F52551

ZF52551/001

READ INSTRUCTIONS
BEFORE COMPLETING FORM

REPORT DOCUMENTATION PAGE		READ INSTRUCTIONS BEFORE COMPLETING FORM
1. REPORT NUMBER NAVENVPREDRSCHFAC Technical Report 77-04	2. GOVT ACCESSION NO.	3. RECIPIENT'S CATALOG NUMBER
4. TITLE (and Subtitle) Navy Tactical Applications Guide. Volume II Environmental Phenomena and Effects.	5. TYPE OF REPORT & PERIOD COVERED	
7. AUTHOR(s) Robert W. Fett, Paul E. La Violette, Martin Nestor, Jerry W. Nickerson, and Kevin Rabe	6. PERFORMING ORG. REPORT NUMBER The Walter A. Bohan Company N00228-76-C-3025	
8. PERFORMING ORGANIZATION NAME AND ADDRESS The Walter A. Bohan Company 2026 Oakton Street Park Ridge, Illinois 60068	10. PROGRAM ELEMENT, PROJECT, TASK AREA & WORK UNIT NUMBERS 62759N. ZF52-551-001. NEPRF WU: 6.2-9	
11. CONTROLLING OFFICE NAME AND ADDRESS Naval Air Systems Command Department of the Navy Washington, D.C. 20361	12. REPORT DATE January 1979	
14. MONITORING AGENCY NAME & ADDRESS (if different from Controlling Office) Naval Environmental Prediction Research Facility Monterey, California 93940	15. NUMBER OF PAGES 161	
16. DISTRIBUTION STATEMENT (of this Report) Approved for Public Release Distribution Unlimited	16. SECURITY CLASS. (of this report) Unclassified	
17. DISTRIBUTION STATEMENT (of the material enclosed in Block 06, if different from Report) NEPRF TR-77-049702-2	18a. DECLASSIFICATION/DOWNGRADING SCHEDULE	
18. SUPPLEMENTARY NOTES Original manuscript for case studies was submitted during calendar year 1977.	19. KEY WORDS (Continue on reverse side if necessary and identify by block number) Defense Meteorological Satellite Program (DMSP) Cloud Lines Fog Air-Sea Interaction Technical rept., Oceanic Fronts Oceanic Eddies Upwelling Internal Waves	
20. ABSTRACT (Continue on reverse side if necessary and identify by block number) Large- and local-scale atmospheric phenomena and effects, detected in DMSP visible and infrared imagery, are illustrated and correlated with conventional surface and upper-air data. Oceanographic phenomena are similarly described and documented. Examples of large-scale atmospheric phenomena are; jet streams, cellular cloud patterns, anomalous cloud lines, cloud lines in general, and vortical cloud patterns. Local-scale atmospheric effects include; land and sea breezes; valley-ridge circulation patterns; fog, haze, and atmospheric pollution; severe weather; and air-sea interaction.		

DD FORM 1 JAN 73 1473 EDITION OF 1 NOV 68 IS OBSOLETE
S/N 0102-014-6601 |

UNCLASSIFIED

SECURITY CLASSIFICATION OF THIS PAGE (When Data Entered)

059 910

79 116

UNCLASSIFIED

SECURITY CLASSIFICATION OF THIS PAGE (When Data Entered)

19. Key Words (continued)

Jet Streams
Cellular Cloud Patterns
Anomalous Cloud Lines
Vertical Cloud Patterns

Land and Sea Breeze
Valley-Ridge Cloud Patterns
Severe Weather

20. Abstract (continued)

The oceanographic section contains examples of oceanic fronts and eddies, upwelling, internal waves, coastal sediment, and sea ice.

The examples shown are presented as case studies, following detailed introductions which provide background concerning the phenomena and their usefulness in determining related parameters for environmental analysis and prediction.

Accession Log	
NTIS GRANT	
DDC TAB	
Unannounced	
Justification	
By _____	
Distribution _____	
Availability Codes _____	
Dist	Available or special
A	

UNCLASSIFIED

SECURITY CLASSIFICATION OF THIS PAGE (When Data Entered)

NAVY TACTICAL APPLICATIONS GUIDE
VOLUME 2
ENVIRONMENTAL
PHENOMENA
AND EFFECTS

DEFENSE METEOROLOGICAL
SATELLITE PROGRAM (DMSP)

Prepared under the direction of
Robert W. Fett

TACTICAL APPLICATIONS DEPARTMENT
Naval Environmental Prediction
Research Facility
Monterey, California 93940

1979



ORIGINAL CONTAINS COLOR PLATES: ALL DCP.
REPRODUCTIONS WILL BE IN BLACK AND WHITE

THE WALTER A. BOHAN COMPANY

2026 OAKTON STREET, PARK RIDGE, ILLINOIS 60068
APPLIED RESEARCH IN SATELLITE METEOROLOGY AND OCEANOGRAPHY

Foreword

Volume 1 of the Navy Tactical Applications Guide was devoted to an analysis of many of the ambiguities inherent in data from the Defense Meteorological Satellite Program (DMSP). Sunglint and anomalous gray shade interpretations were particularly stressed in association with the effects of continental and island barriers. Volume 2 shifts the emphasis from basic image analysis to a study of those phenomena and effects of particular concern to Navy operating forces. These are abundantly illustrated and described in operationally relevant terms.

A dominant theme appearing throughout this second volume is the importance of air-sea interaction. The case studies included illustrate in detail the effects of the atmosphere upon the ocean, not only in wind wave development but also in thermal structure changes. Similarly, ocean influences upon the overlying atmosphere are documented, on both the local and synoptic scales.

Volume 2 is based largely on the research of Mr. Robert W. Fett, Head, Tactical Applications Department, Naval Environmental Prediction Research Facility (NEPRF); but significant contributions were made by Dr. Paul E. LaViolette, Naval Ocean Research and Development Activity (NORDA), by LCDR Martin Nestor, former Royal Navy Exchange Officer to NEPRF, and by Mr. Jerry W. Nickerson and Mr. Kevin Rabe, both of NEPRF.

Though the unique quality and characteristics of the DMSP sensor system are stressed, it is expected that the user of other image sources will also find much practical use for this guide. To this end, comments are solicited for consideration in the development of improvements and/or supplements to this and future similar publications.



P.A. PETIT
Captain, U.S. Navy
Commanding Officer, NEPRF

Acknowledgements

The assistance of Russell Chambers, Bruce Bigler, and AG2 Jerry Tomlinson in developing the documentation for many of the case studies in this volume is gratefully acknowledged. Photographer Dennis Daigle of NEPRF processed many of the original photographs used in this publication. The correlative meteorological and oceanographic data used in the case studies were provided by the Fleet Numerical Weather Center, Monterey, Calif., and the Naval Weather Service Detachment, Asheville, N.C. Appreciation is also extended to the personnel of the DMSP sites at Rota, Spain, and San Diego, Calif.; and aboard the aircraft carriers USS Constellation, USS Kitty Hawk, and USS John F. Kennedy. The assistance of Warrant Officer Ronald Shemanski, Navy Satellite Van, San Diego, is especially acknowledged for providing many of the special enhancements of DMSP data used in this guide.

The assistance of the staff of The Walter A. Bohan Company is acknowledged; in particular, the special efforts of Walter A. Bohan and John J. Bates for their critical review of the case studies, suggestions for improvement, and arrangement of the materials presented. In addition, Lido A. Andreoni is responsible for the design of the format of the publication and the presentation of layouts. Gregory E. Terhune assisted in the preparation of the case study materials, and also participated in the review and editing of the text. The high quality of the reproduction of the satellite imagery used in the case studies, and the excellent printing job of the publication, is due to the combined efforts of Peter M. Samorez and Michael E. Brock.

Contents

<i>Foreword</i>	iii
<i>Introduction</i>	vii

Section 1

Large-Scale Atmospheric Phenomena and Effects

1A Jet Stream	1A-1
1B Cellular Cloud Patterns	1B-1
1C Anomalous Cloud Lines	1C-1
1D Cloud Lines	1D-1
1E Vortical Cloud Patterns	1E-1

Section 2

Local-Scale Atmospheric Phenomena and Effects

2A Land and Sea Breezes	2A-1
2B Valley-Ridge Circulations	2B-1
2C Fog, Haze, and Air Pollution	2C-1
2D Severe Weather	2D-1
2E Air-Sea Interaction	2E-1

Section 3

Oceanographic Phenomena and Effects

3A Oceanic Frontal Systems	3A-1
3B Oceanic Eddies	3B-1
3C Upwelling	3C-1
3D Internal Waves	3D-1
3E Other Phenomena	3E-1

Appendix

Sea Surface Temperature Gradient Analysis Using Enhanced Infrared Imagery	A-1
--	-----

Introduction

During the past few years, there has been an increasing awareness of the need to bridge the gap between large-scale weather system forecasts and the determination of the associated local-scale weather phenomena—often the dominant concern of the Navy forecaster—within the large-scale systems. High quality, high resolution DMSP imagery provides information, on a timely basis, on local-scale weather phenomena within the large-scale systems; and this information, when used in conjunction with conventional meteorological products, can help to bridge that gap. In addition, DMSP imagery provides details on oceanographic phenomena and on air-sea interactions which are also of great importance to the Navy forecaster in enhancing his ability to provide environmental support to surface and subsurface operations.

The purpose of this volume of the Navy Tactical Applications Guide is to illustrate the types of environmental information provided in DMSP imagery, and in this presentation, to stress the potential for an improved analysis and prediction capability. The number of topics covered in each section is limited; however, they have been selected to emphasize operational applications and to extend, where possible, existing concepts of data interpretation, focusing on the unique characteristics of the DMSP sensor and display system.

Section 1

Large-Scale Atmospheric Phenomena and Effects

1A Jet Streams

 Jet Stream Cloud Patterns 1A-1

Case Studies

- 1 Strong subtropical jet stream
 Mexico—Southwest U.S. 1A-2
- 2 Subtropical jet stream
 Tropical Mid-Pacific—Winter 1A-4
- 3 Weak subtropical jet stream
 Tropical Mid-Pacific—Summer 1A-6
- 4 Topographic effects: lee clearing vs lee convection 1A-8

1B Cellular Cloud Patterns

 Cellular Cloud Pattern Areas 1B-1
 Formation and Development of Cellular Cloud Patterns 1B-2

Case Studies

- 1 Open and closed cellular cloud patterns
 behind a cold front 1B-4
- 2 Appearance of jet streams, positive vorticity centers,
 surge lines, and cloud lines in cellular cloud fields 1B-6
- 3 Evolution of positive vorticity centers
 within cellular cloud fields 1B-10
- 4 Identification of surface ridge lines in oceanic
 anticyclones and ahead of cold fronts 1B-12
- 5 Appearance of open cellular cloud patterns
 in areas of strong surface winds 1B-16
- 6 Clear areas produced by low-level horizontal divergence
 in cellular cloud fields—eastern North Pacific 1B-18

1C Anomalous Cloud Lines

 Formation and Evolution of Anomalous Cloud Lines 1C-1

Case Studies

- 1 Oceanic anticyclone—eastern North Pacific 1C-4
- 2 Anomalous cloud line formation
 in areas of vertical wind shear 1C-6
- 3 Oceanic anticyclone—in advance of a cold front 1C-8

1D Cloud Lines

Cloud Lines and Low-Level Wind Flow Patterns 1D-1

Case Studies

- 1 Estimating wind direction from cloud lines
in tropical oceanic areas 1D-2
- 2 Cloud lines over land 1D-4
- 3 Cloud line formation over water
in areas of cold air advection 1D-6
- 4 Use of cloud lines in locating central areas
of oceanic anticyclones 1D-8
- 5 Inhibiting effect of wet ground
on convective cloud line formation 1D-10

1E Vortical Cloud Patterns

Vortical Cloud Pattern Systems 1E-1

Case Studies

- 1 Mature mid-latitude frontal vortex—
eastern North Atlantic 1E-2
- 2 Vortical cloud patterns within a cold polar trough—
eastern North Atlantic 1E-4
- 3 Structure of a cutoff low—North Pacific 1E-6
- 4 Weak tropical wave or "screaming eagle"—
eastern North Pacific 1E-8

1A Jet Streams

Jet Stream Cloud Patterns

The term "jet stream" is applied in meteorology to the high-level, narrow, quasi-horizontal band of winds of speeds 26 m s^{-1} (50 kt) or greater. Two main jet stream systems are usually distinguished: the polar-front jet stream, associated with extratropical frontal systems; and the subtropical jet stream, overlying the poleward boundary of the subtropical high pressure areas. The subtropical jet is usually found near the 12 km (200-mb) level, while the polar jet is best developed near the 9 km (300-mb) level.

Jet streams are frequently revealed by the presence and configuration of cirrus cloudiness in meteorological satellite data. Such cloudiness appears to be the result of vertical and horizontal motions induced by the jet stream. For example, as wind speeds increase, approaching the jet stream core, upper-level speed divergence is developed in the right rear quadrant. Anticyclonic shear, associated with this speed divergence, is also developed. The strong upper-level divergence requires, through continuity, strong lower-level convergence and upward vertical motion, resulting in the production of cirrus cloudiness under favorable atmospheric conditions.

Empirically, it has been found that the jet stream core tends to parallel the northern edge of associated cirrus cloudiness. The cirrus cloudiness often ends abruptly, casting a shadow on lower-level cloudiness.

In the polar jet, lower-level cloudiness is widespread and frontal or cellular in nature. In the subtropical jet, subsidence and reduced lower-level baroclinicity restrict the development of underlying cloudiness, except that produced by terrain or interaction effects over areas with marked low-level instability.

Case 1 Jet Streams

Strong subtropical jet stream Mexico—Southwest U.S.

A strong subtropical jet stream, extending northeast from the Baja Peninsula area into the southwest portion of the United States, is indicated by the cirrus cloud pattern seen in Fig. 1A-2a. The axis of the jet stream is roughly parallel to the cloud band, with the core of the jet to the north of the band. The northern edge of the cirrus cloudiness is normally sharper than the southern edge.



1A-2a. FTV-31. Enlarged View. DMSP VHR Low Enhancement. Strong Subtropical Jet Stream.
1804 GMT 19 May 1974.

This j
transver
axis. Ar
Fig. 1A
vertical
verse clo
the nortl
the soul
supportc
over All
El Paso
transver
turbulen

Importa
1. Subt

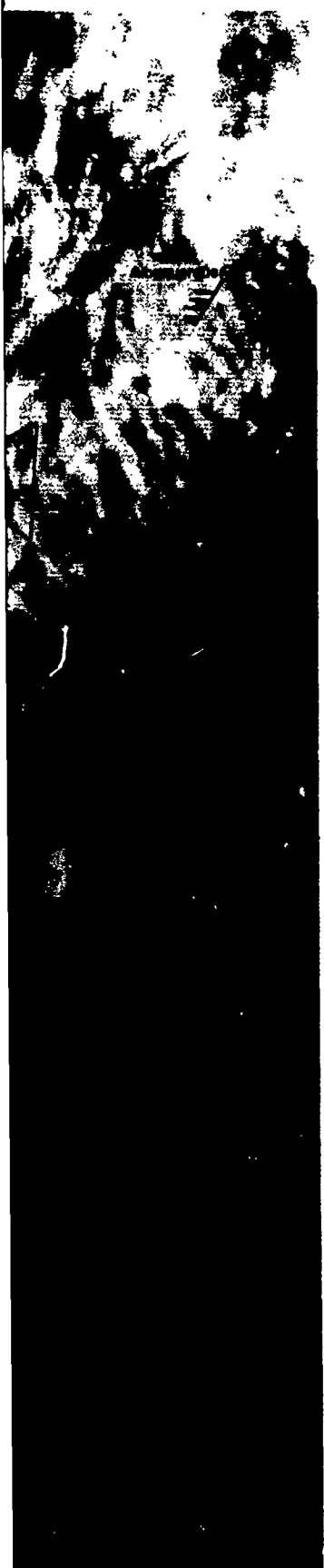
2. Billio
effec

3. An t
stron



IA-3a. FTV-31. Enlarged View. DMSP VHR Low Enhancement. Transverse Line Formation. 1804 GMT 19 May 1974.

Reference
Anderson,
and for
and Su
NOAA



This jet stream cloud pattern also shows cirrus billow clouds in a transverse line formation with the lines sloping at an angle to the jet axis. An enlarged section of the cirrus billow cloud area is shown in Fig. 1A-3a. The transverse cloud lines are produced by effects of vertical wind shear. When horizontal wind shear is present the transverse cloud lines will be distorted, as in this case. Stronger winds along the northern edge of the cirrus have advected the lines faster than along the southern edge where the lines lag behind. This observation is supported by the 300-mb wind data which show 41 m s^{-1} (80 kt) winds over Albuquerque, near the jet core, and 30 m s^{-1} (58 kt) winds over El Paso, to the south of the core. This characteristic banding of the transverse cloud lines is usually an indication of severe to extreme turbulence at levels near the jet core (Anderson *et al.*, 1974).

Important Conclusions

1. Subtropical jet streams can be identified by cirrus cloud bands.
2. Billow cloud patterns in a subtropical jet stream are produced by effects of vertical wind shear.
3. An upwind sloping of the transverse cloud lines is associated with strong horizontal shear.

Reference

- Anderson, R.K., et al., 1974: Applications of meteorological satellite data in analysis and forecasting. ESSA Tech. Report. NESC 51 (*including supplement, Nov. 1971, and Supplement No. 2, March 1973*). National Environmental Satellite Service, NOAA, Washington, D.C., 350 pp.

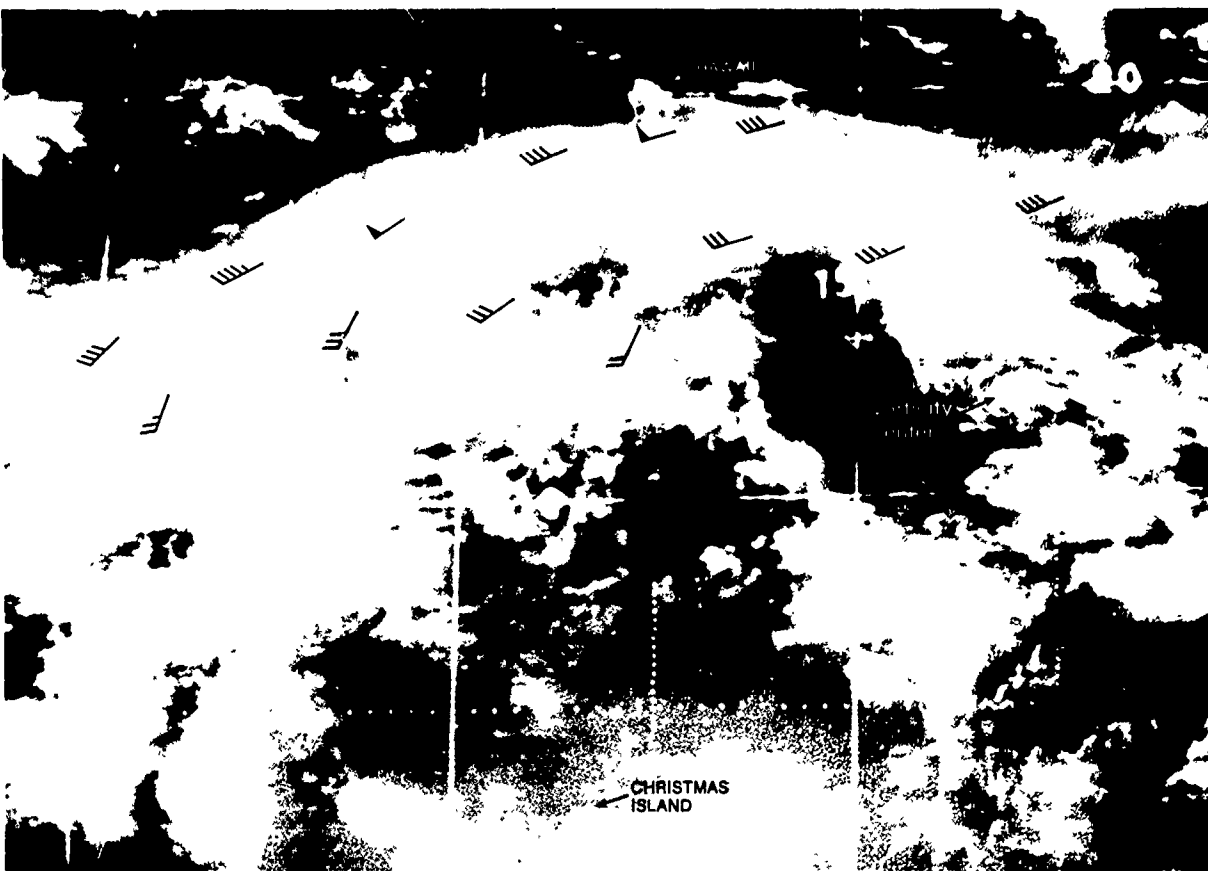
Case 2 Jet Streams

Subtropical jet stream Tropical Mid-Pacific—Winter

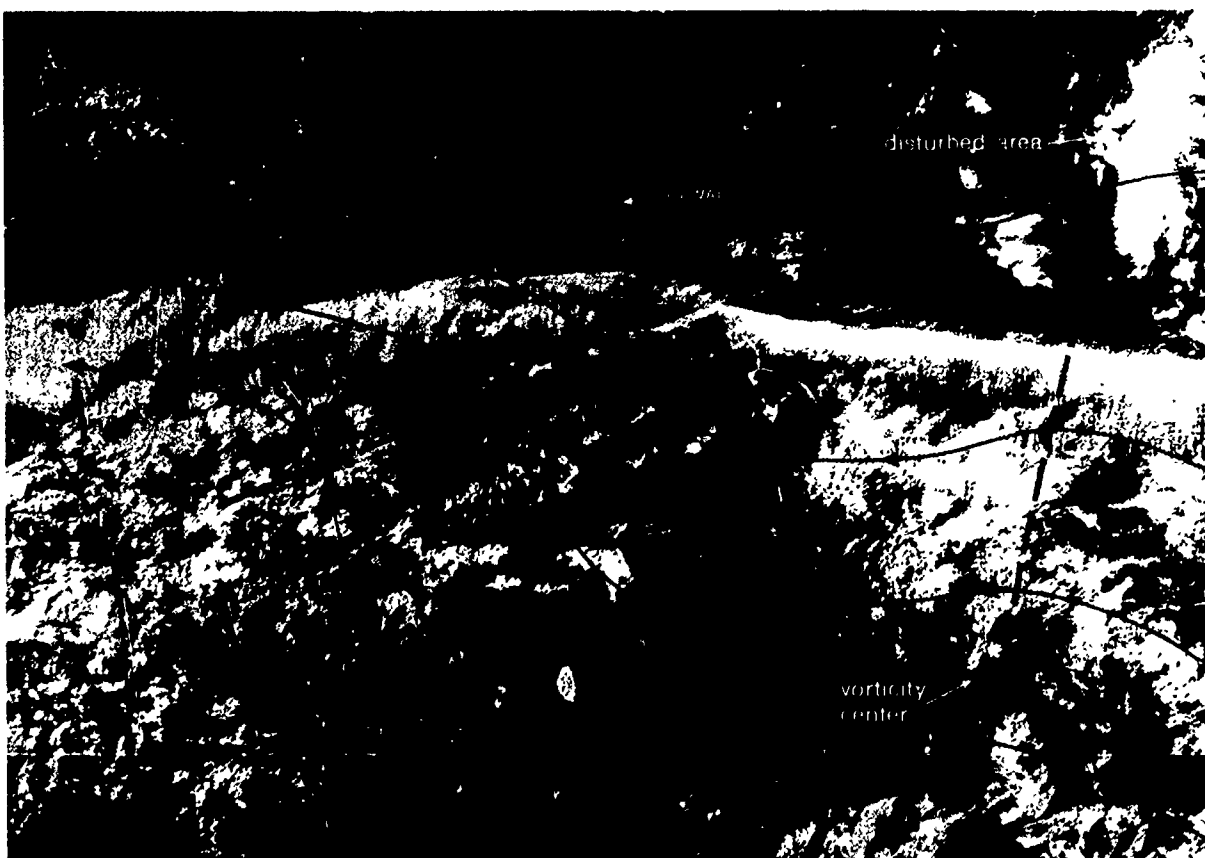
A DMSP VHR view of the central Pacific, in the vicinity of the Hawaiian Islands, is shown in Fig. 1A-4a. Just south of Hawaii, a long band of cirrus with closely spaced transverse filaments indicates the presence of a subtropical jet stream. Using an animated sequence of ATS-1 imagery, individual cirrus cloud elements were tracked and cloud motion vectors were obtained from which wind velocities at the cirrus level were estimated. An enlarged ATS-1 picture, approximately 4 hours after the time of the DMSP pass, with some of the upper-level cloud motion vectors superimposed, is shown in Fig. 1A-5a. These data confirm the presence of a jet stream with maximum speed of about 26 m s^{-1} (50 kt) along the northern edge of the cirrus band.



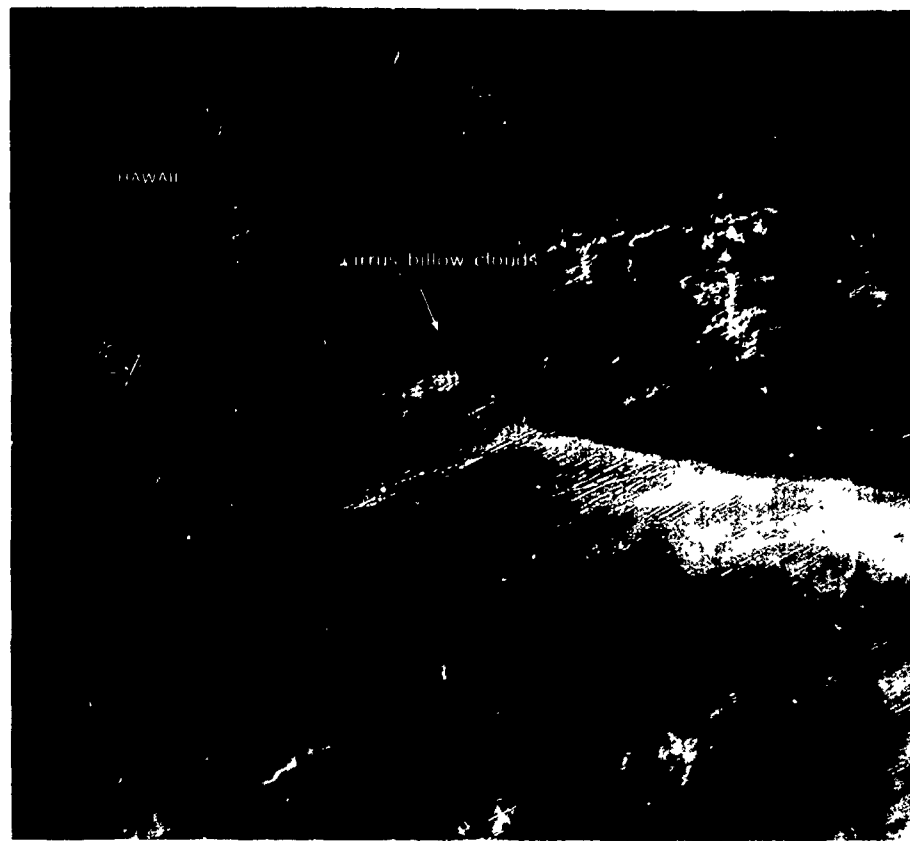
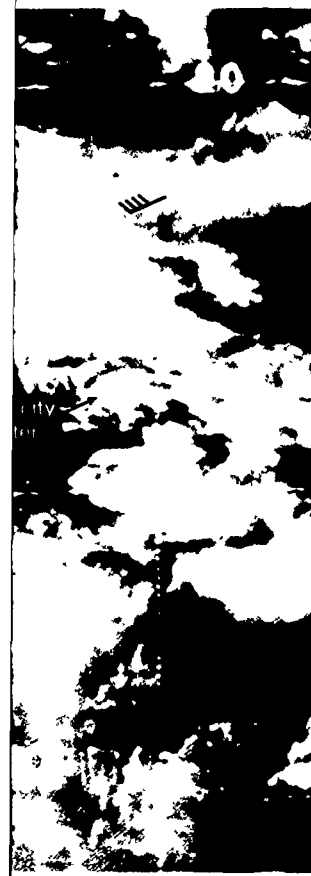
1A-4a. FTV-26. DMSP VHR Low Enhancement. Subtropical Jet Stream. 1755 GMT 10 October 1971.



1A-5a. ATS-1. Visible Picture. Subtropical Jet Stream. 2226 GMT 10 October 1971.
Upper-Level Cloud Motion Vectors.



1A-5b. FTV-26. DMSP VHR Low Enhancement. Lower-Level Cloudiness. 1755 GMT 10 October 1971.
Low-Level Streamlines (see text).



IA-5c. FTV-26. Enlarged View. DMSP VHR Low Enhancement. Cirrus Billow Clouds.
1755 GMT 10 October 1971.

Upper-air data from Hilo, Hawaii, near the northern edge of the cirrus band, provide excellent verification of the jet stream aloft and the accuracy of the ATS-1 derived cloud motion vectors. The winds reported from Hilo about 6 hours after the DMSP data were as follows: 300-mbs, 360/04 kt; 250-mbs, 260/45 kt; and 200-mbs, 270/41 kt. These data suggest that the jet stream core was near the 250-mb level. Moderate to severe turbulence between 300- and 250-mbs was a distinct possibility due to the strong vertical wind shear between these levels.

Of additional interest are areas of lower-level cloudiness south of the jet and a disturbed area to the north. The low-level wind flow in these areas can be estimated from ATS-1 data. Fig. 1A-5b shows the low-level streamlines, based on ATS-1 winds, superimposed on the DMSP picture. The wind field has been subjected to a time-space extrapolation to adjust it to the time of the DMSP picture. The streamline analysis shows that the areas of lower-level cloudiness, and the clear area between, are associated with a trough-ridge-trough pattern. Also, note that a vorticity center is apparent along the eastern trough axis, in both the DMSP and ATS data.

In the enlarged view (Fig. 1A-5c) note the small area of close, regularly spaced cirrus billow clouds just southeast of Hawaii. According to the upper-air data at Hilo, winds at this level are about 23 m s^{-1} (45 kt). Such regularly spaced billow clouds are produced by strong vertical shear in a thin layer.

Important Conclusions

1. Upper-level cloud motion vectors closely approximate conventional upper-air data and can be used to estimate jet stream velocities.
2. Streamline analyses, derived from low-level cloud motion vectors, are useful for interpreting weather patterns observed in satellite imagery.
3. Close, regularly spaced cirrus billow clouds associated with a subtropical jet stream indicate the presence of strong vertical shear in the area.

Case 3 Jet Streams

*Weak subtropical jet stream
Tropical Mid-Pacific—Summer*



IA-6a. FTV-29. DMSP VHR Low Enhancement. Weak Subtropical Jet Stream. 1848 GMT 27 June 1974.



IA-7a. FTV-29, DMSP VHR Low Enhancement. Weak Subtropical Jct Stream, 1848 GMT 27 June 1974
Upper-Level Aircraft Wind Observations (Heights) and Streamline Analysis, 2100 GMT 27 June 1974.

In the su
streams, an
27 June 19
transverse i

The pro
provides an
stream. R/
3,700 m (12,
260° at 10,8
wind speed.
When these
within a few
cirrus band
mid-Pacific
shear to the
nearly perp

Between
the spiral t
tropical dis
associated w
sification a
the disturb
mental con

Important

1. A weak
irregular
2. Transv
indicati
3. In the F
for loca

Reference
Sadler, Jame
trough. N
Prediction



In the summer, horizontal temperature differences, and hence jet streams, are usually weaker than in winter. The DMSP imagery on 27 June 1974 (Fig. 1A-6a) shows an irregular band of cirrus, with transverse filaments, just southeast of Hawaii.

The proximity of this cirrus band to upper-air observing stations provides an opportunity to verify that the cirrus is associated with a jet stream. RAOB data at Kauai reveal light westerly flow starting at 3,700 m (12,000 ft) and reaching a maximum speed of 23 m s^{-1} (45 kt) from 260° at 10,860 m (34,000 ft). The upper-air data at Hilo was similar, with wind speeds reaching 26 m s^{-1} (50 kt) from 270° at 10,800 m (34,000 ft). When these reports are combined with the available pilot reports, gathered within a few hours of the time of the DMSP data, it is apparent that the cirrus band is associated with a jet stream along the southern edge of the mid-Pacific trough (Fig. 1A-7a). In the absence of pronounced horizontal shear to the south of the jet, note that the transverse cloud lines appear nearly perpendicular to the jet stream core.

Between Hawaii and Christmas Islands, the convective cloudiness and the spiral band organization indicate the presence of a weak low-level tropical disturbance. Sadler (1976) noted that the subtropical jet stream, associated with the summer mid-Pacific trough, can influence the intensification and development of tropical disturbances. However, in this case, the disturbance is not in a location with respect to favorable environmental conditions for further intensification.

Important Conclusions

1. A weak subtropical jet stream can be recognized by the presence of an irregular, cirrus band and associated transverse filaments.
2. Transverse filaments aligned nearly perpendicular to the jet are an indication of weak, horizontal shear.
3. In the Pacific, in summer, subtropical jet stream cirrus are often useful for locating the southern edge of the mid-Pacific trough.

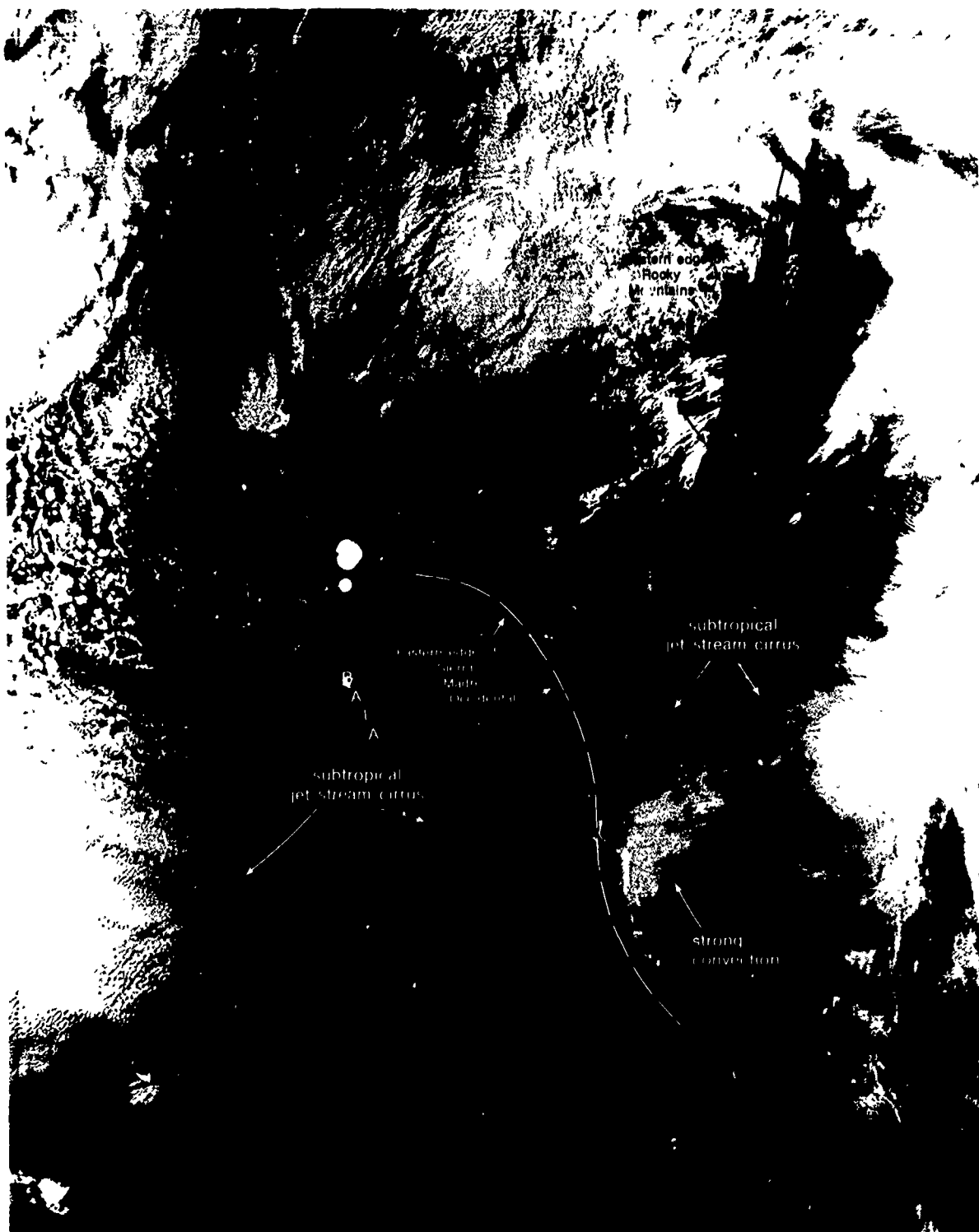
Reference

- Sadler, James C., 1976: Tropical cyclone initiation by the tropical upper-tropospheric trough. NAVFNPREDRSCHFAC Tech. Paper No. 7-76, Naval Environmental Prediction Research Facility, Monterey, Calif. 103 pp.

Case 4 Jet Streams

Topographic effects: lee clearing vs lee convection

Sometimes the cirrus associated with a jet stream appears as a band of faint cloud streaks. This is the case in Fig. 1A-8a which is a DMSP picture of the western portion of North America.



1A-8a. FTV-29. DMSP VHR Low Enhancement. Lee Clearing vs Lee Convection. 1527 GMT 10 April 1974.

The convective cloudiness just east of the Sierra Madre Occidentals and the filmy cirrus streaks over Baja help to indicate the presence of a jet. Notice that cloud tops at the southern end of the convection, east of the Occidentals, are not being advected eastward as rapidly as those to the north. This suggests that the jet core is to the north of the convective area.

The 200-mb wind reports and isotach analysis for 1200 GMT are superimposed on the DMSP imagery (Fig. 1A-9a). In the data sparse region off Baja, the isotach analysis does not show the subtropical jet stream suggested by the cirrus streaks in the imagery. To the north, a polar jet is indicated by the isotach analysis, but is not apparent in the DMSP imagery due to lack of cloudiness at the jet level.

It is of interest that a clear slot is associated with the westerly flow east of the Rockies, in contrast to intense convective activity associated with a similar westerly flow in the lee of the Occidentals.

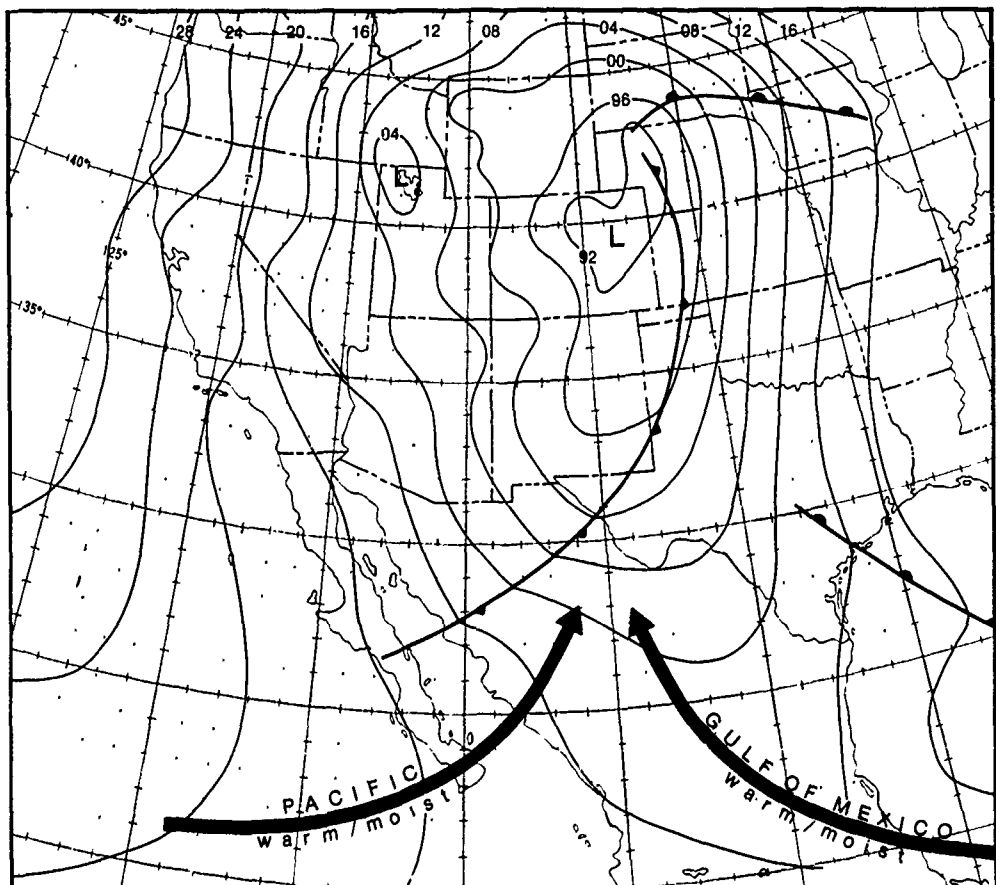


1A-9a. FTV-29, DMSP VHR Low Enhancement Lee Clearing vs Lee Convection. 1527 GMT 10 April 1974.
200-mb Wind Observations and Isotachs. 1200 GMT 10 April 1974.

The synoptic situation at the surface is illustrated below (Fig. 1A-9b). This analysis shows that a cold front extends southwestward from Nebraska and dissipates over northern Mexico. The clear slot in the lee of the Rockies is just west of the cold front. It is also in the region of cyclonic shear north of the polar jet, an area of reduced upper-level divergence. This effect, in addition to the downslope motion in the subsiding air behind the front produces the prominent clear slot. The convective cloudiness to the east of the Occidentals is in the warm air mass ahead of the cold front, and warm moist air from both the Pacific and the Gulf of Mexico is converging in this area. This lower-level convergence combined with the strong upper-level divergence south of the jet stream core acts as an efficient mechanism to create strong upward vertical motion, and the convection observed. The two opposite lee effects observed provide a good example of the importance of relating all available information in order to correctly interpret meteorological satellite data.

Important Conclusions

1. Thin, filmy, cirrus streaks can be used to deduce the presence of a jet stream.
2. Cirrus cloudiness produced by thunderstorm activity may help to reveal a jet stream location.
3. Jet stream flow perpendicular to mountain ranges may be associated with lee clear areas due to downslope motion. However, they may also be associated with lee convective cloudy areas. The key to understanding which pattern to expect lies in a thorough examination of the flow at all levels.



1A-9b. NMC Surface Analysis, 1800 GMT 10 April 1974.

1B Cellular Cloud Patterns

Cellular Cloud Pattern Areas

Cellular cloud pattern areas are observed over the oceans during all seasons. Such areas develop at low levels in the cold air behind polar fronts over the ocean and in subtropical oceanic high pressure systems. They are easy to recognize in satellite imagery because of their distinctive cloud forms. Cellular cloud patterns are useful in identifying regions of cold air advection, cyclonic and anticyclonic flow, areas of positive vorticity advection, positive vorticity centers, locations of polar jet streams, and surface ridge lines.

Formation and Development of Cellular Cloud Patterns

In general, cellular cloud patterns form in large, shallow regions of cool, moist, maritime air moving over a warmer sea surface. The air is heated from below by the warm sea surface, and cooled from above by radiational cooling from the top of a strong temperature inversion which caps the marine layer. In cellular cloud patterns behind cold fronts, the temperature inversion is intensified by large-scale sinking motion. Skies are usually cloud-free in the dry, subsiding air above cellular cloud pattern areas.

Two basic types of cellular cloud patterns, open cells and closed cells, are observed in satellite imagery (Hubert, 1966). According to Krishnamurti (1975), observations indicate that there is good agreement between regions of large-scale descending motion in the cloud layer and the occurrence of open cellular cloud patterns, and between regions of large-scale descending motion in the cloud layer and the occurrence of closed cellular cloud patterns. Recently, Shew and Agee (1977) have shown that open (closed) convection cells occur only in those layers where eddy viscosity (the turbulent transfer of momentum by eddies, giving rise to an internal fluid friction) predominately decreases (increases) with height, providing such layers are convectively unstable. In addition, Richl (1954) and Augstein, Schmidt, and Ostapoff (1974) show that for convective development in undisturbed trade wind areas, the maximum horizontal divergence and the strongest winds occur just below the cloud base in the sub-cloud layer and there is very little horizontal divergence in the cloud layer. This condition is favorable for the formation of hexagonal-shaped cellular cloud patterns, as demonstrated in simulated laboratory experiments. Because of the uneven development of cellular cloud patterns in the atmosphere, the patterns appear as rings or semicircles of cumulus clouds in the open-cell areas, and as nearly circular-shaped areas of stratocumulus clouds in closed-cell areas.

Open cells (Fig. 1B-3a) have descending motion in the central area of the cells and upward motion in the outer edges of the cells, with cumulus clouds forming in the areas of upward motion and the central area remaining cloud-free. Closed cells (Fig. 1B-3b) have upward motion in most of the area covered by the cells and descending motion in just the outer edges of the cells. Stratocumulus clouds are formed in the area of upward motion, and the outer edges (area between cells) may be cloud-free but are generally covered by thinner layers of stratocumulus or stratus clouds. The vertical wind shear in the cloud layer must be small or non-existent in order that cellular cloud patterns form and be maintained. The horizontal wind speed is indicated by the broken shaft arrows in the illustration. The longer the arrow the higher the wind speed. When strong vertical wind shear occurs within the cloud layer, the cellular cloud pattern is disrupted and the clouds form into bands or lines oriented along the shear vector.

As the cool, maritime polar air in which cellular cloud patterns form moves equatorward around the eastern portion of subtropical highs, the height of the base of the inversion rises in response to warmer sea surface temperatures. The convective layer depth, defined as the distance from the lifting condensation level (LCL) to the inversion base, increases correspondingly. Cellular cloud depth is found to be roughly proportional to the convective layer depth.

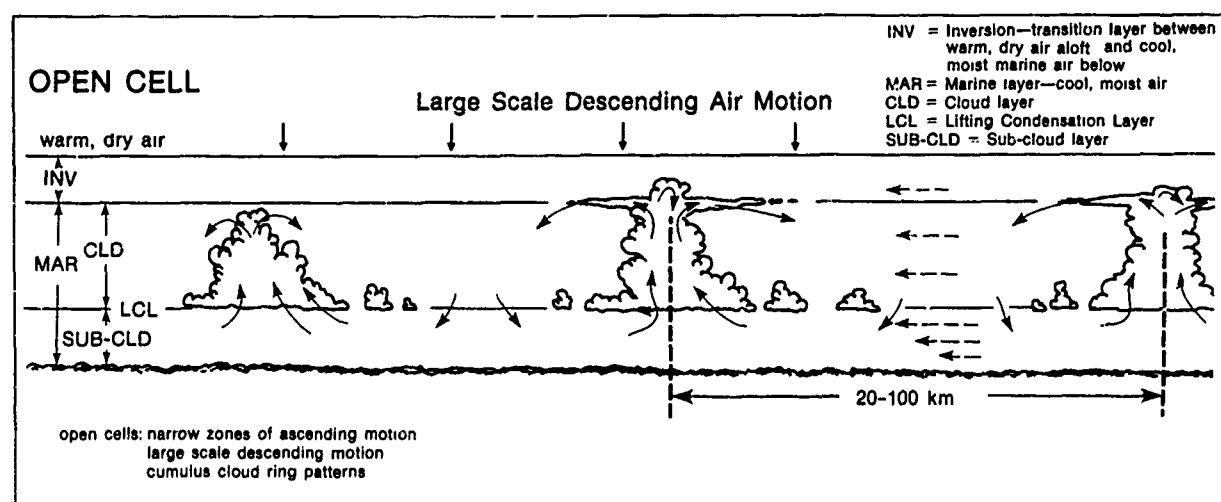
Cellular clouds under stable conditions do not always reach the inversion level. In particular, under such conditions in the open cell cases, vertical development is suppressed through entrainment of dry air

by large-scale descending motion. As the effect of subsidence becomes less, cumulus clouds in the cellular pattern extend to the base of the inversion and then spread laterally under the inversion. Individual cloud tops sometimes penetrate the stratus or stratocumulus cloud deck into the region above the inversion.

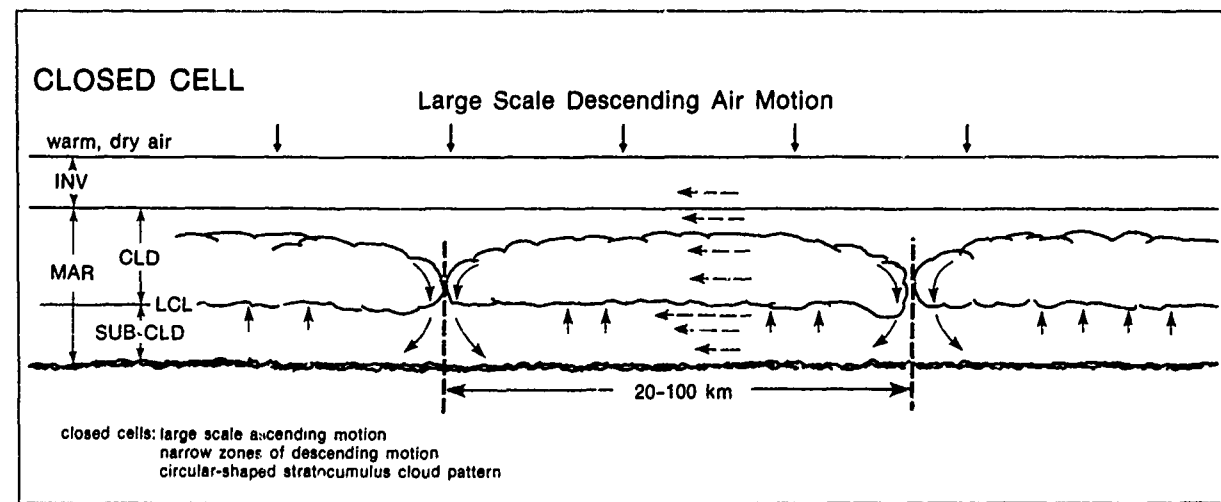
Under unstable conditions, the large-scale descent of air above the marine inversion may penetrate downward, reinforcing the sinking motion in the central region of the open cells. This action weakens or destroys the marine inversion and, in a cyclonic flow regime, cumulus rapidly develop into cumulonimbus. Such development is particularly favored to the rear of cold fronts in areas of maximum positive vorticity advection at mid-levels.

References

- Augstein, E., H. Schmidt, and F. Ostapoff, 1974: The vertical structure of the atmospheric planetary boundary layer in undisturbed trade winds over the Atlantic Ocean. *Bound. Layer Meteor.*, 6, 129-150.
 Hubert, L.F., 1966: Mesoscale Cellular Convection. Rep. No. 37, Meteor. Satellite Lab., National Environmental Satellite Service, Washington, D.C.
 Krishnamurti, R., 1975: On cellular cloud patterns. Part 3. Applicability of the mathematical and laboratory models. *J. Atmos. Sci.*, 32, 1373-1383.
 Richl, H., 1954: *Tropical Meteorology*. McGraw-Hill, New York, Chaps. 1-2.
 Shew, P., and E.M. Agee, 1977: Kinematic analysis and air-sea heat flux associated with mesoscale cellular convection during AMTEX 75. *J. Atmos. Sci.*, 34, 793-801.



1B-3a. Typical Open Cellular Cloud Pattern.



1B-3b. Typical Closed Cellular Cloud Pattern.

Case 1 Cellular Cloud Patterns

Open and closed cellular cloud patterns behind a cold front

A large area of open and closed cellular cloud patterns is observed over the North Atlantic Ocean in the DMSP picture at 0835 GMT 30 November 1975 (Fig. 1B-4a). The cellular cloud patterns have formed in the cold air behind a frontal cloud band which extends from North Africa into Southern Europe. Note that the cellular cloud field is confined offshore of Spain, except along the northern border of Spain where some of the clouds have moved onshore and changed form or dissipated. North of Spain, in the Bay of Biscay, the globular-shaped cloud pattern indicates an area of intense convective activity.

The open cells located off the coast of Spain are in a region of straight or cyclonically curved flow (see surface analysis Fig. 1B-5a). The smaller open-cell diameters indicate regions where the height of the inversion is quite low. Larger open-cell diameters indicate areas with a higher inversion base. A closed cellular cloud pattern predominates in the anticyclonic flow towards the center of the high.

A transitional area "T" occurs where the surface flow changes from straight or cyclonic to anticyclonic. In this area, increased subsidence can result in a local intensification of the marine inversion. Cumulus convection in the open cells in such an area is suppressed and the tops of active cumulus tend to spread out into a stratocumulus deck, with the root cumulus gradually dissipating. An aircraft reconnaissance photo (below) clearly illustrates this process. The top of the cumulus has flattened out under the inversion, and only a remnant of the root cumulus remains.

The transition area helps locate the region where the flow begins turning anticyclonically and where surface wind speeds, and thus sea state, normally begin to decrease.

Considerable cumulonimbus activity is evident over the Bay of Biscay, to the west of France. The surface pressure analysis (Fig. 1B-5a) indicates the presence of a weak trough over the area. The 500-mb height and isotherm analysis (Fig. 1B-5b) reveals a cold trough over the thunderstorm activity. Note that the cumulonimbus activity is located below the coldest temperatures at 500-mb ($<-30^{\circ}\text{C}$). This arrangement of globular-shaped cumulonimbus clouds over an oceanic region appears often in association with upper cold lows or cold troughs and is therefore very helpful in locating the presence of such features (see Sec. 1E).



Aircraft Reconnaissance Photo. Cellular Cloud Pattern Transitional Stage.



1B-4a. FTV-29. DMSP VHR Low Enhance 0835 GMT 30 November 1975.

Important Conclusions

1. Open cellular cloudiness is t cyclonic flow.
2. Closed cellular cloudiness is t anticyclonic flow.
3. Areas of transition from o delineating where anticyclonic decrease in surface wind spe

front

observed
35 GMT
rns have
nds from
d field is
of Spain
form or
r-shaped
y.

f straight
5a). The
nt of the
as with a
inates in

ges from
bsidence
Cumulus
e tops of
with the
ce photo
ulus has
the root

w begins
thus sea

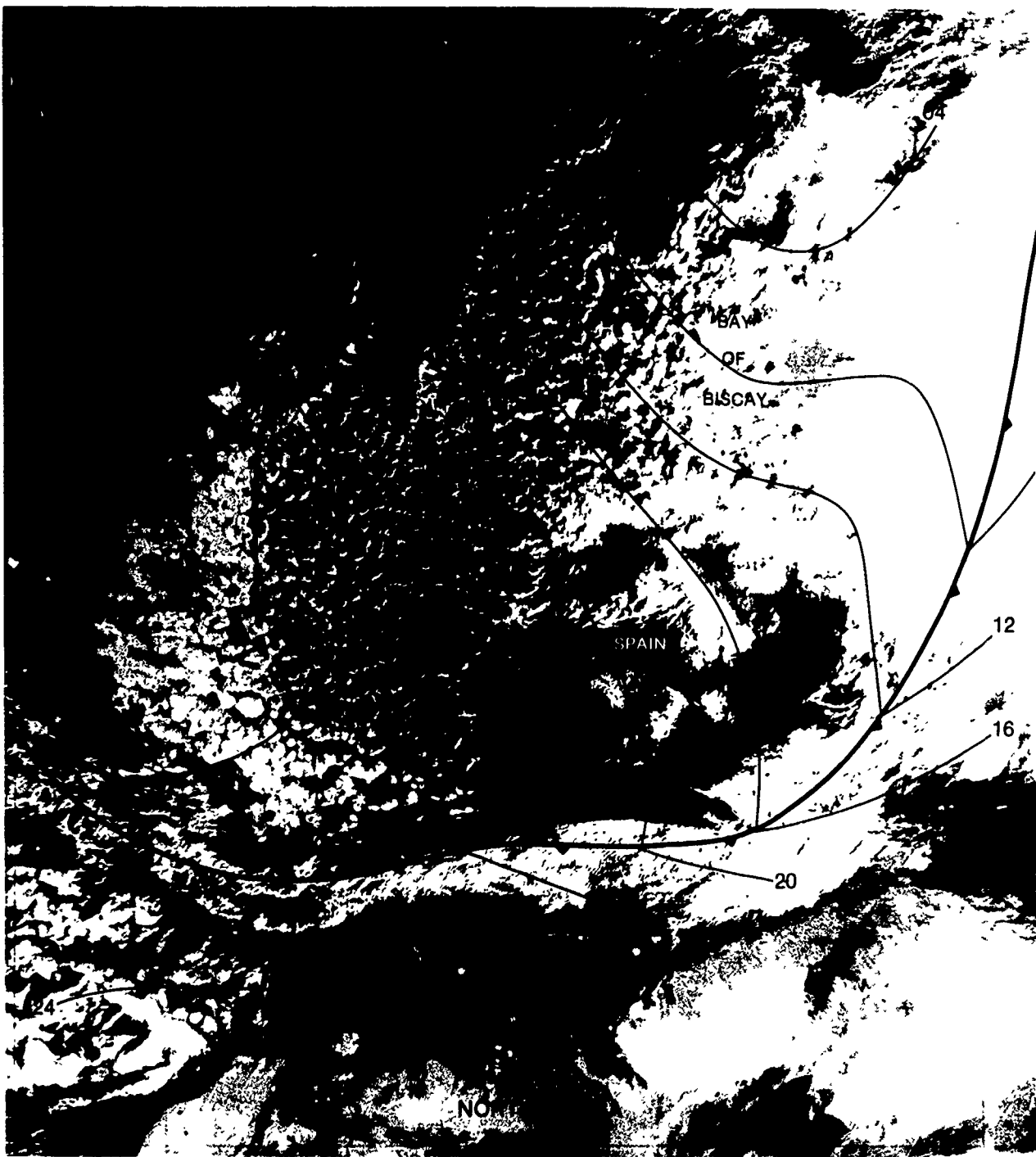
f Biscay,
1B-5a)
500-mb
over the
located
engagement
c region
hs and is
eatures



1B-4a. FTV-29. DMSP VHR Low Enhancement. Open and Closed Cellular Cloud Patterns Behind a Cold Front.
0835 GMT 30 November 1975.

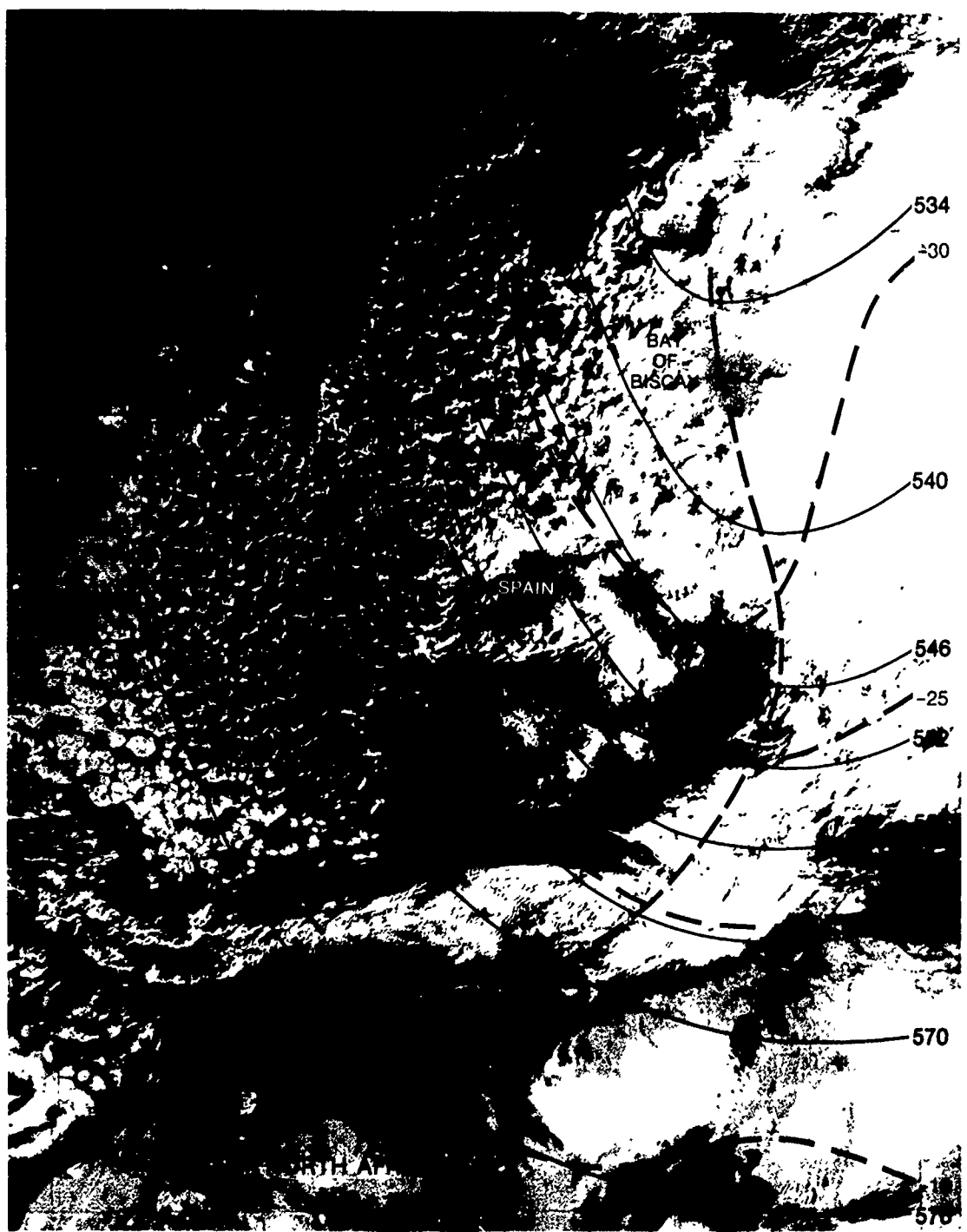
Important Conclusions

1. Open cellular cloudiness is typically found in a region of straight or cyclonic flow.
2. Closed cellular cloudiness is typically found in a region of divergent or anticyclonic flow.
3. Areas of transition from open to closed cell types are useful for delineating where anticyclonic flow begins to dominate, and a marked decrease in surface wind speed and hence sea state can be anticipated.



IB-5a. FTV-29. DMSP VHR Low Enhancement. Open and Closed Cellular Cloud Patterns Behind a Cold Front.
0835 GMT 30 November 1975.
Surface Analysis. 1200 GMT 30 November 1975.

IB-5b. FTV-29.
0835 GMT 30
500-mb Height



Behind a Cold Front.

IB-5b. FTV-29. DMSP VHR Low Enhancement. Open and Closed Cellular Cloud Patterns Behind a Cold Front.
0835 GMT 30 November 1975.
500-mb Height Contours and Isotherms. 1200 GMT 30 November 1975.

Case 2 Cellular Cloud Patterns

Appearance of jet streams, positive vorticity centers, surge lines, and cloud lines in cellular cloud fields

There are a number of atmospheric features that can be identified in cellular cloud fields. They can be recognized by abrupt changes in the cloud forms over the area, from the usual open or closed cell cloud patterns. The features include jet streams, positive vorticity centers (PVC's), surge lines, and cloud lines.

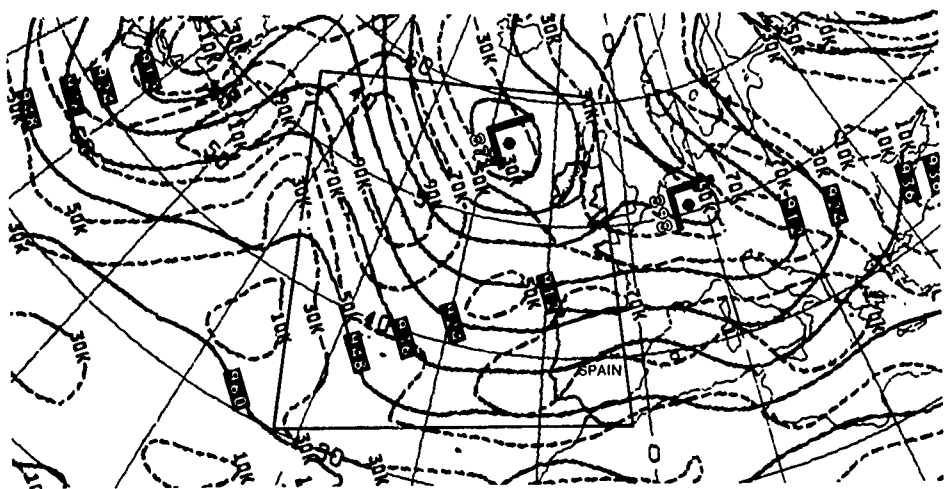


IB-6a. FTV-29. DMSP VHR Low Enhancement. Cellular Cloud Patterns. 0926 GMT 14 October 1975.

An extensive cellular cloud field is observed over the eastern North Atlantic in the DMSP picture shown in Fig. 1B-6a. The NMC surface analysis (Fig. 1B-7a) indicates that the open cellular cloud pattern is located in the cyclonic flow behind a cold front which has passed the Azores and is advancing across Spain. Over the mid-North Atlantic, the closed cellular cloud pattern is located in the divergent flow along the eastern portion of the high pressure area. Sea surface isotherms are oriented almost normal to the cold air flow in which the cellular cloud patterns are observed, indicating a heating of the cold air mass from below—a necessary condition for the formation of cellular cloud fields.



1B-7a. FTV-29. DMSP VHR Low Enhancement. Cellular Cloud Patterns. 0926 GMT 14 October 1975.
NMC Surface Analysis and Sea Surface Isotherms. 1200 GMT 14 October 1975.



300-mb Analysis.
Heights/Isotachs.
1200 GMT
14 October 1975.

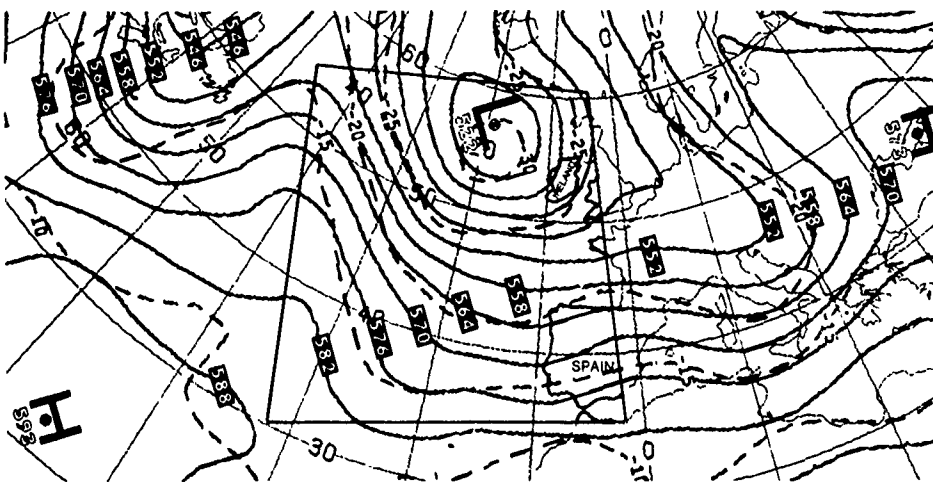


1B-8a. FTV-29. DMSP VHR Low Enhancement. Cellular Cloud Patterns. 0926 GMT 14 October 1975.
300-mb Isotachs. 1200 GMT 14 October 1975.

Atmosphere

Polar jet stream

Cellular
separating
the position
page 1B-8.
stream loca-
superimpo-
separating
stream cro-
anticycloni-
another br



500-mb Analysis.
Heights/Temperatures.
1200 GMT
14 October 1975.

Positive vorticity

A large cumulonimbo-
(Fig. 1B-9a).
(Fig. 1B-7)
(chart, top)

In addition to the view. To the circulation indicates the pattern "B" in the center, indicating weather, the development

Surge line

In general, air flow becomes apparently in areas the cross line labeled discontinuous upstream from determine is an abrupt change in inversion layer. Available wind of 10 reported in

Cloud line

When viewed or longitude shear front point C is Note that stronger winds case, the directional change in segments its effects appear

Reference
Huschke, R.
638 pp.



1B-9a. FTV-29. Enlarged View. DMSP VHR Low Enhancement. Small Scale Features. 0926 GMT 14 October 1975.

500-mb Analysis.
Heights/Temperatures.
1200 GMT
14 October 1975.

Atmospheric features revealed in cellular cloud fields

Polar jet stream

Cellular cloud patterns typically form in the air behind cold fronts. The zone separating open from closed cellular cloud patterns in these cases normally defines the position of the upper-level polar jet. The NMC 300-mb analysis (chart, top of page 1B-8) shows an isotach maximum, indicating the presence of a polar jet stream located over the mid-Atlantic. Note that the axis of the isotach pattern, superimposed on the DMSP picture (Fig. 1B-8a), is located above the zone separating open from closed cellular cloud patterns. This is typical for a polar jet stream crossing a cellular cloud field from north to south. To the south, the anticyclonically curved cirrus cloudiness, with a sharp poleward edge, indicates another branch of the polar jet in the large-scale flow over this region.

Positive vorticity centers

A large area of convection, showing cumulus, cumulus congestus, and small cumulonimbus, is observed within the open cellular cloud field over the Atlantic (Fig. 1B-9a). This convection is not associated with the surface lows to the east (Fig. 1B-7a), but occurs in the cyclonic flow under a 500-mb cold low aloft (chart, top of page 1B-9).

In addition, two organized convection patterns can be identified in this enlarged view. To the north, the cloud pattern "A" shows curved bands around an apparent circulation center at low levels with a squall line along the eastern sector. This indicates the presence of a developing positive vorticity center. The convection pattern "B", to the south, shows less development and no apparent circulation center, indicating only the presence of an area of positive vorticity advection. Identification of such areas is important not only for locating areas of severe weather, but because of the future potential of such areas for rapid storm development. (See Case 3 for the further development of these vorticity centers.)

Surge lines

In general, the diameter of open cells increases from north to south in the cold air flow behind polar fronts over the ocean. In most areas this change is gradual, apparently as a result of a slow lifting of the marine inversion. However, in other areas the change is quite abrupt, as it is in the area north and south of the dashed line labeled "surge line" in Fig. 1B-9a. A surge line is defined as a line along which a discontinuity in the wind speed occurs, with the wind speed normally strongest upstream from the surge line (Huschke, 1959). Data in this case are inadequate to determine whether or not the line represents such a discontinuity. However, there is an abrupt change from small to large open cell diameters across the line. Such a change implies a lifting of the inversion south of the line, and with the higher inversion lower wind speeds would be expected in the open cells south of the line. Available wind reports at 1200 GMT, about 2½ hours after the DMSP pass, show a wind of 23 m s^{-1} (45 kt) to the north of the surge line. A wind of 8 m s^{-1} (15 kt) is reported in the larger open cell area immediately south of the surge line.

Cloud lines produced in cellular cloud fields by vertical wind shear

When vertical shear exists, the cellular patterns are reoriented into cloud lines or longitudinal roll-type clouds. The roll cloud is aligned parallel to the vertical shear from the base to the top of the cloud. The longitudinal roll-type cloud at point C is indicative of the presence of low-level vertical wind shear in that area. Note that the roll cloud is parallel to the jet core, and may be a reflection of the stronger winds extending down from the jet to lower-levels over the area. In this case, the effect is due to an increase of wind speed with height with little, if any, directional change involved. Where directional shear effects are present, an abrupt change in the open cellular cloud pattern can also be expected. The short line segments in Fig. 1B-9a are aligned with cloud lines where vertical directional shear effects appear to be present.

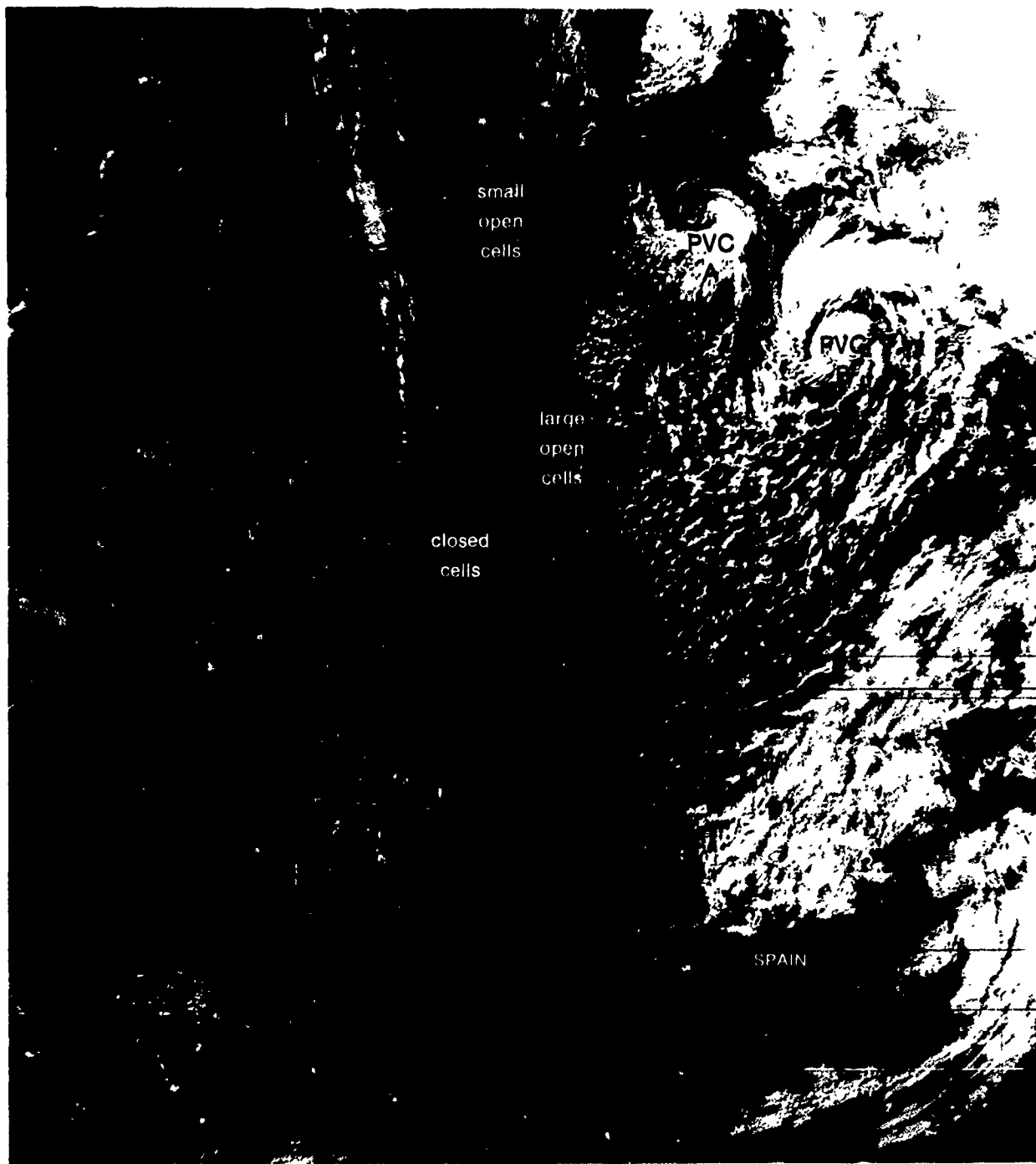
Reference

Huschke, R.E. (Ed.), 1959: *Glossary of Meteorology*. American Meteorological Society, Boston, 638 pp.

Case 3 Cellular Cloud Patterns

Evolution of positive vorticity centers within cellular cloud fields

A DMSP picture of the North Atlantic (Fig. 1B-10a) shows the continued evolution of the positive vorticity center within the cellular cloud field discussed in Case 2. The positive vorticity center "A" at the edge of the open cellular pattern is now characterized by spiraling cloud bands, with a distinct clear slot penetrating to the center. The tight spiral cloud bands indicate that this PVC is in a well developed stage characterized by cumulonimbus, squalls, and heavy seas.



1B-10a. FTV-29. DMSP VHR Low Enhancement. Evolution of PVC's Within Cellular Cloud Fields. 0908 GMT 15 October 1975.



1B-11a FIV-29 DMSP VHR Low Enhancement. Evolution of PVC's Within Cellular Cloud Fields. 0908 GMT 15 October 1975.
NMC Surface Analysis. 1200 GMT 15 October 1975.

The enhanced cumulus area "B" on the previous day has developed into a positive vorticity center and shows broad, spiraling cloud bands which wrap around the center. The surface analysis (Fig. 1B-11a) locates a single, closed low-pressure center near the southern PVC, but no closed center near the PVC to the north. For operational purposes, the necessity for using satellite data in addition to conventional data in synoptic analysis is evident, since the two PVC's were not identified in the conventional analysis but were clearly revealed in the DMSP picture.



ds 0908 GMT 15 October 1975.



1B-11b. FTV-29. Enlarged View DMSP VHR Low Enhancement. Cellular Cloud Field. 0908 GM T 15 October 1975 Surface Observations. 1200 GM T 15 October 1975.

A closed cellular pattern (Fig. 1B-11a) is observed over the region of divergent flow east of the high pressure ridge. The total area of closed cells is small and merges with a general area of stratocumulus to the west. At the northern edge of the closed cellular pattern, a bright cloud band oriented north-south reveals the continued presence of an upper-level jet stream over the area.

In an enlarged view of the open cellular region (Fig. 1B-11b), the abrupt change from large open cells to small open cells locates a possible surge line. The single wind report of 5 m s^{-1} (10 kt) just south of this line suggests the type of wind reduction anticipated as open cells suddenly increase in diameter and in vertical extent. However, reports in other areas show winds just as strong south of the line as north of the line. More studies will be required to document wind effects associated with surge lines and these principally may be derived from geostationary satellite data. Meanwhile, the DMSP user should be aware of the phenomena and alert to potential effects when operating in the areas of possible surge lines.

Important Conclusions

1. Spiral cloud bands within a broader open cellular cloud field reveal the presence of well-developed positive vorticity centers.
2. Because positive vorticity centers can develop rapidly, it is important to detect them early and carefully monitor their further development.

Case 4 Cellular Cloud Patterns

Identification of surface ridge lines in oceanic anticyclones and ahead of cold fronts



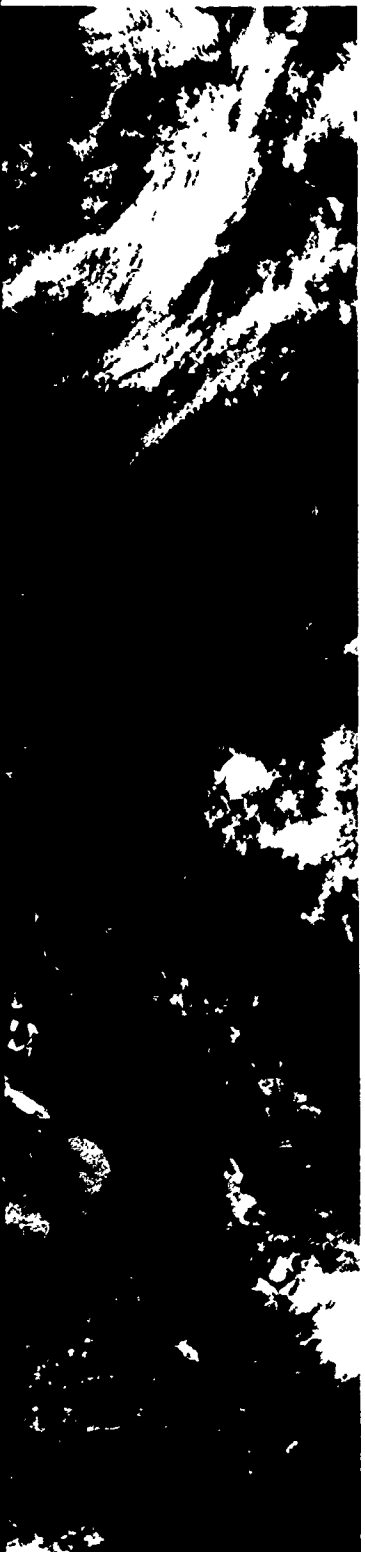
IB-12a. FTV-29. DMSP VHR Low Enhancement. Surface Ridge Line in an Oceanic Anticyclone. 1622 GMT 17 July 1975.

Surface
Larg
contain
cellular
straight
flow fiel
to close
surface
flow).

The d
Californ
ridge lin
line ana
north c
patterns
(see Sec
lines is
Thus, t
surface
orienta
separati
Case 3)



IB-13a. FTV-29. DMSP VHR Low Enhancement. Surface Ridge Line in an Oceanic Anticyclone. 1622 GMT 17 July 1975.
Surface Observations and Streamline Analysis 1200 GMT 17 July 1975.



Surface ridge line in an oceanic anticyclone

Large oceanic anticyclones may show cellular cloud fields that contain an abrupt transition from open cellular cloud patterns to closed cellular cloud patterns (Fig. 1B-12a). The open cells are associated with straight or cyclonic flow, the closed cells with anticyclonic flow. If the flow field is oriented normal to the edge of the area of abrupt transition to closed cells, then this edge may be used to locate the position of the surface ridge line (area of maximum antclonic curvature of the wind flow).

The distinct northern edge of the closed cellular cloud pattern off the California coast (Fig. 1B-12a) suggests the location of a possible surface ridge line. Anticyclonic flow in this region is confirmed by the streamline analysis based on ship reports (Fig. 1B-13a). Straight flow occurs north of this region where an area of broken, open cellular cloud patterns is observed. Anomalous cloud lines have formed in this area (see Sec. 1D, Case 1). A marked anticyclonic curvature of the streamlines is observed along the edge of the closed cellular cloud pattern. Thus, the edge of this band of closed cells marks the extension of a surface ridge line into this area. Note that the flow here is normal to the orientation of the ridge line. This is in contrast to parallel flow separating areas of open and closed cells behind cold fronts (see Sec. 1C, Case 3).

In another example (Fig. 1B-14a), the distinct northern edge of a closed cellular cloud pattern in the eastern Pacific again suggests the location of a surface ridge line. Climatologically, this area is known to be dominated by anticyclonic flow. Ship observations show nearly straight flow in the open cellular cloud area in the center of the picture. Anticyclonic flow occurs over the remainder of the area, with a maximum curvature in the flow observed along the northern edge of the closed cellular pattern. This distinct edge, then, marks the extension of a surface ridge line into the area.

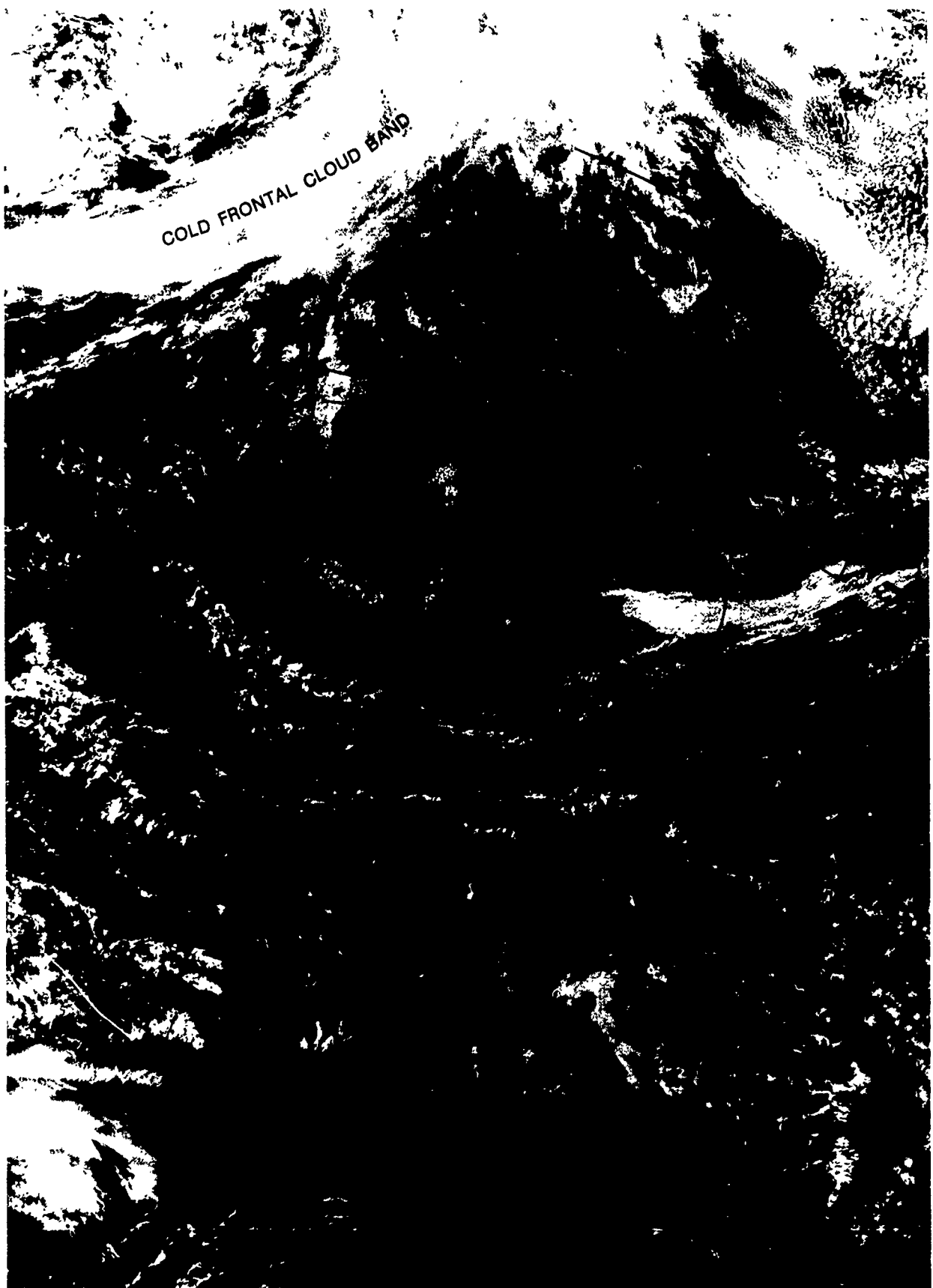


1B-14a. FTV-29, DMSP VHR Low Enhancement. Surface Ridge Line in an Oceanic Anticyclone. 1739 GMT 28 November 1975.
Surface Observations and Streamline Analysis. 1800 GMT 28 Nov. mb - 1975.

Surface
A d
sugges
anoma
cellula
cold fi
observ
anticyc
northe

Impor

1. A
ce
co
lin
2. Th
the
str



1B-15a. FTV-31. DMSP VHR Low Enhancement. Surface Ridge Line Ahead of a Cold Front. 2132 GMT 26 June 1974.
Surface Observations and Streamline Analysis. 0000 GMT 27 June 1974.



Surface ridge line ahead of a cold front

A distinct, narrow cloud band ahead of an advancing cold front suggests the position of a surface ridge line (Fig. 1B-15a). A number of anomalous cloud lines (see Sec. 1C) and a small area of broken open cellular cloudiness are observed north of this band and ahead of the cold front. A surface streamline analysis, based on ship observations, reveals anticyclonic flow over the area. The marked anticyclonic curvature of the streamlines, that occurs along the northern edge of the cloud band, identifies the ridge line.

Important Conclusions

1. An abrupt change from open cellular cloud patterns to closed cellular cloud patterns in large oceanic anticyclones, or ahead of cold fronts, is a useful indicator of the location of a surface ridge line.
2. This is in contrast to conditions observed behind cold fronts, where the transition from open cells to closed cells indicates a change from straight or cyclonic to anticyclonic flow.

Case 5 Cellular Cloud Patterns

Appearance of open cellular cloud patterns in areas of strong surface winds



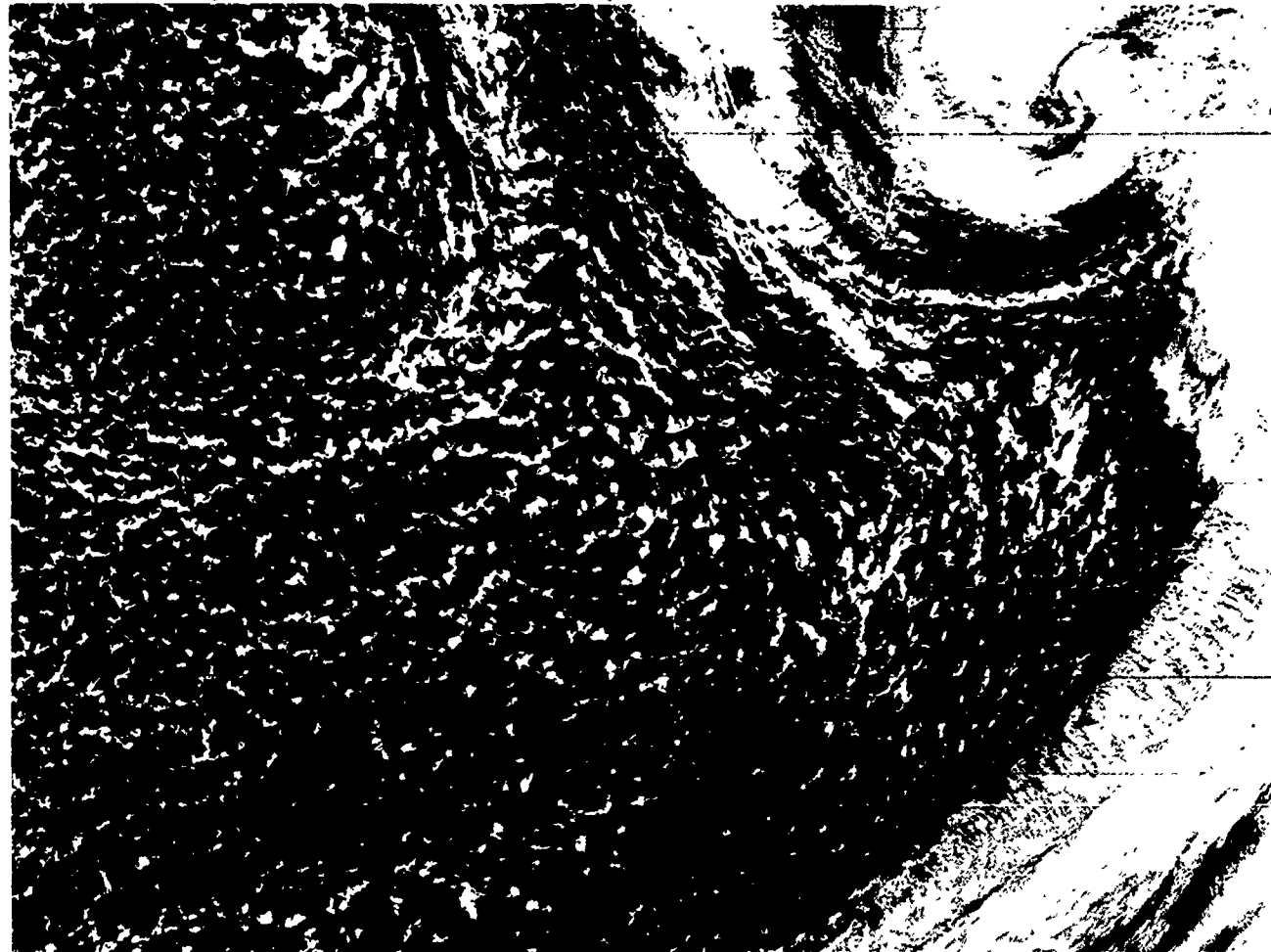
1B-16a. FTV-35, DMSP LF Low Enhancement. Open Cellular Cloud Patterns. 1921 GMT 1 November 1977.
Surface Wind Reports and Streamline Analysis. 1800 GMT 1 November 1977.

Open cellular cloud patterns appear distinctly different in areas of strong surface winds as compared to areas where the winds are weaker. Fig. 1B-16a shows a DMSP LF picture with surface winds and streamline analysis covering the eastern Pacific and western U.S. coast. The open cellular cloud pattern in area "A", behind the front, where winds up to 26 m s^{-1} (50 kt) are reported, is very different in appearance from the open cellular cloud pattern in area "B", which is near the center of a subtropical anticyclone. Wind speeds in this area are generally less than 10 m s^{-1} (20 kt). The cells in area "A" are larger in diameter and are made up of cumulus congestus and cumulonimbus cloud elements.

An enlargement of area "A" (Fig. 1B-17a) reveals more clearly some of the small-scale details in the open cellular cloud pattern. Note especially the progressively longer cloud lines in the cellular clouds from the left-hand portion of the picture toward the frontal vortex center. These cloud lines indicate that strong vertical wind shear is present. When such lines are located in areas of intense convective instability, strong surface winds are observed. This is due to the eddy momentum transfer of the stronger winds aloft down to the surface. Large-scale descent of air behind the cold front reinforces the sinking motion in the central region of the open cells, contributing to this effect.

The NMC surface isobaric analysis with wind reports (Fig. 1B-17b) shows that considerable variability in wind speeds occurs, despite the strong, relatively uniform pressure gradient about the low. Winds of 8 m s^{-1} (15 kt) are found interspersed with reports of up to 26 m s^{-1}

1B-17a. FTV-35. Enlarged View. DMSP LF Low Enhancement. Open Cellular Cloud Patterns. 1921 GMT 1 November 1977.



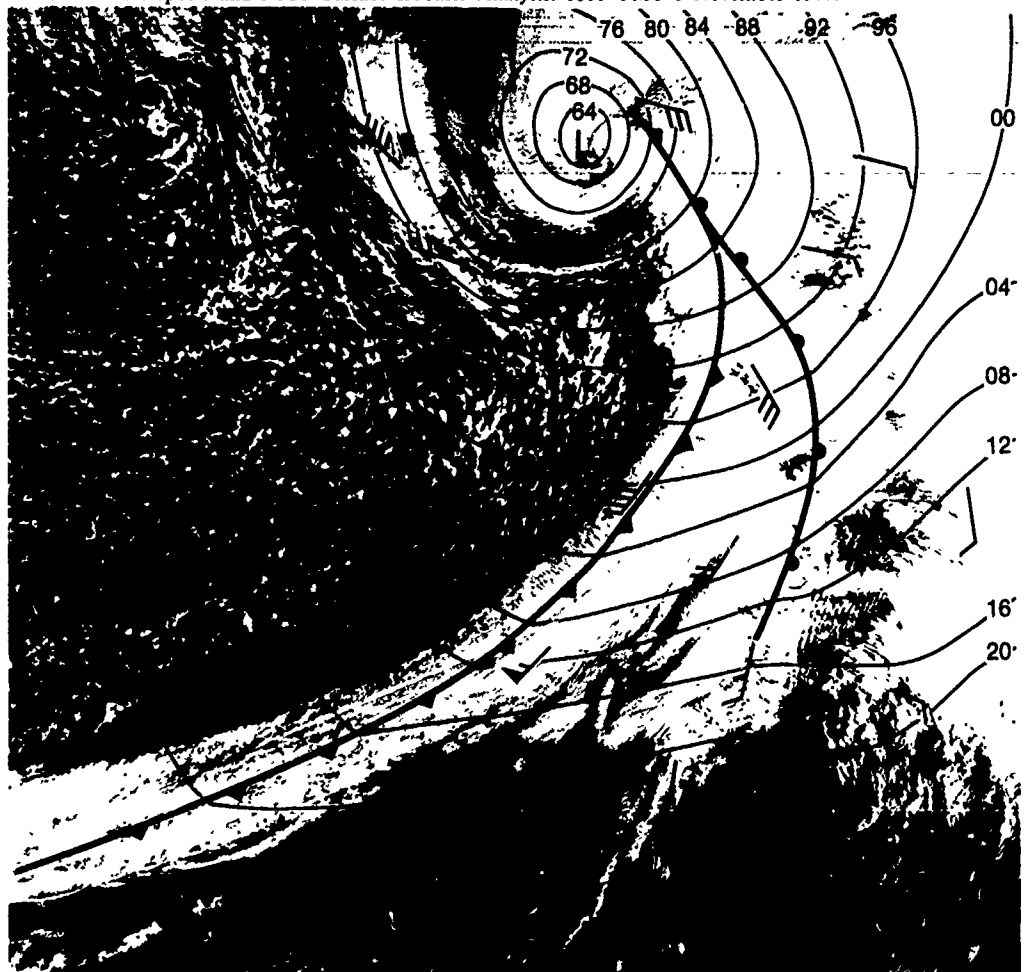
(50 kt), without any large changes in the pressure gradient. Such variability can be anticipated in a region with such strong convection, where updrafts and downdrafts increase or alternately decrease surface wind speeds appreciably through vertical transport of eddy momentum.

In contrast to the wind speed variability in the open cells behind the front (area "A"), sustained strong winds occur along the frontal boundary. This is where the flow accelerates as it crosses the isobars, approaching the low pressure center. Hurricane force winds were generated by this storm causing a grounding of ships and capsizing of smaller vessels in the Seattle, Washington, area shortly after the time of this analysis.

Important Conclusions

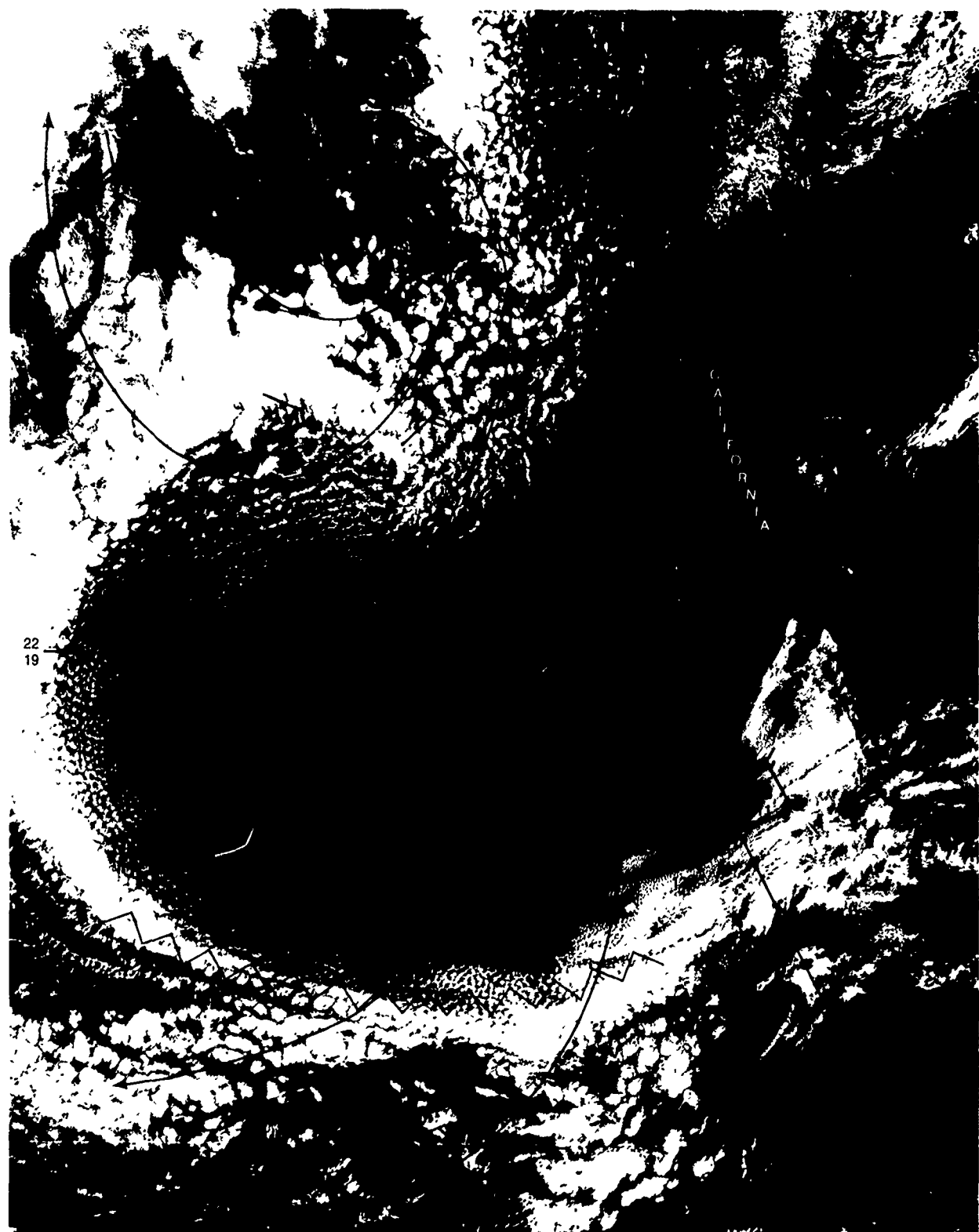
1. Large diameter, open cellular cloudiness, with convective elements of cumulus congestus and cumulonimbus forming portions of the cells and interspersed in a field of short cloud lines, are typically observed in strong, low-level wind areas, behind oceanic polar fronts. Considerable variability of surface wind speeds ranging from light to strong, over short distances, is characteristic of this type of open cellular cloud pattern.
2. Small diameter, open cellular cloudiness in subtropical high pressure areas is indicative of a low-level inversion. Surface wind speeds in such areas are generally less than 10 m s^{-1} (20 kt).

1B-17b. FTV-35. DMSP LF Low Enhancement. Open Cellular Cloud Patterns. 1921 GMT 1 November 1977. Surface Wind Reports and NMC Surface Isobaric Analysis. 1800 GMT 1 November 1977.



Case 6 Cellular Cloud Patterns

Clear areas produced by low-level horizontal divergence in cellular cloud fields—eastern North Pacific



IB-18a. FTV-35. DMSP LF Special Enhancement. Clear Zones in Cellular Cloud Fields. 1734 GMT 18 April 1977.
Surface Reports and Streamline Analysis. 1800 GMT 18 April 1977.



1B-19a. FTV-35. DMSP LF Normal Enhancement. Clear Zones in Cellular Cloud Fields. 1907 GMT 30 May 1977.
Surface Reports and Streamline Analysis. 1800 GMT 30 May 1977.



A DMSP view (Fig. 1B-18a) of the eastern North Pacific off the U.S. West Coast shows an extensive cellular cloud field with a large clear area southwest of California. The northeast-southwest orientation of this area suggests that the clearing may be due to dry, continental air flowing southwestward from the land to the ocean. The surface streamline analysis, however, reveals that this is not true. Winds are generally northerly, flowing parallel, rather than perpendicular, to the coast. The clear area is seen to be an area of strong surface wind diffluence, which suggests the presence of strong low-level divergence. Under such conditions cloudiness, which would be normally present over the area, is dissipated by compensating subsidence.

Fig. 1B-19a shows another example of the phenomenon off the U.S. West Coast. The clear area is again found in the region of pronounced surface streamline diffluence, with probable low-level divergence and subsidence. The appearance of such patterns southeast of high pressure centers is a frequent occurrence off the U.S. West Coast. Climatology favors such formations, due to the presence of semi-permanent high pressure areas to the west and semi-permanent troughs over the region of the Gulf of California.

Important Conclusion

1. Pronounced clear areas in oceanic cellular cloud patterns are often associated with low-level streamline diffluence with accompanying low-level divergence.

1C Anomalous Cloud Lines

Formation and Evolution of Anomalous Cloud Lines

Anomalous cloud lines are bright, persistent low-level plume-like clouds (narrow at the source and wide at the trailing end) that occur over the ocean. They are produced by the interaction of effluents, from the stack exhausts of ships, with air near the top of shallow, moist, marine layers. Anomalous cloud lines appear in oceanic anticyclones during all seasons, but most frequently in the summer months, within a regime which is favorable for cellular cloud formation.

The formation of anomalous cloud lines has been identified as a ship induced phenomena (Conover, 1969). Observation of a ship producing an anomalous cloud line was reported by a United Airlines pilot (Parmenter, 1972), and additional sightings have been noted since that time. Heat, moisture, and condensation nuclei are carried upward by the buoyancy of hot gases in the stack exhaust from fuel-oil powered ships. In areas where the marine layer is shallow and capped by an inversion, water droplets form on nuclei in the effluent as it rises into the air that is saturated or slightly supersaturated. Fog or heavy haze is almost always reported in these areas. As the ship moves through the area, a cloud trail remains behind that develops into a distinct, bright cloud line. It has the appearance of a cloud plume—narrow at the source, spreading laterally with time and with little vertical development, since the cloud line forms near the top of a marine layer capped by an inversion.

References

- Conover, J. H., 1969: New Observations of Anomalous Cloud Lines. *J. Atmos. Sci.*, **24**, 1153-1154.
Parmenter, F. C., 1972: Ship Trails or Anomalous Cloud Lines. *Mon. Wea. Rev.*, **100**, 646-647.

Anomalous cloud lines are found in areas of oceanic anticyclones where the marine layer is depressed by an inversion, with heights generally between 0.5 km and 1.0 km (1,650-3,300 ft). In the region of formation (Fig. 1C-2a), there is low, scattered stratus to broken stratocumulus cloudiness that appears as a small diameter, open cellular cloud pattern in visible satellite imagery. The open cellular cloud pattern usually occurs within a generally larger area of closed cellular clouds that have bases ranging from 1.0-1.8 km (3,000-6,000 ft).

Under favorable atmospheric conditions, anomalous cloud lines can persist for long time periods. After 24 hours, gradual change and erosion makes it difficult to identify a given cloud line in satellite imagery. When available, the more frequent geostationary satellite imagery may provide continuity over the area, useful for tracking such lines.

Ships are not always observed in an area showing persistent anomalous cloud lines. This can be attributed to the time lag between the formation and development of a visible cloud line, and/or the departure of the ship from the area. Cloud lines hundreds of kilometers in length, being swept along in the prevailing flow, have been observed many hours after ships have crossed and left an area favorable for anomalous cloud line formation.

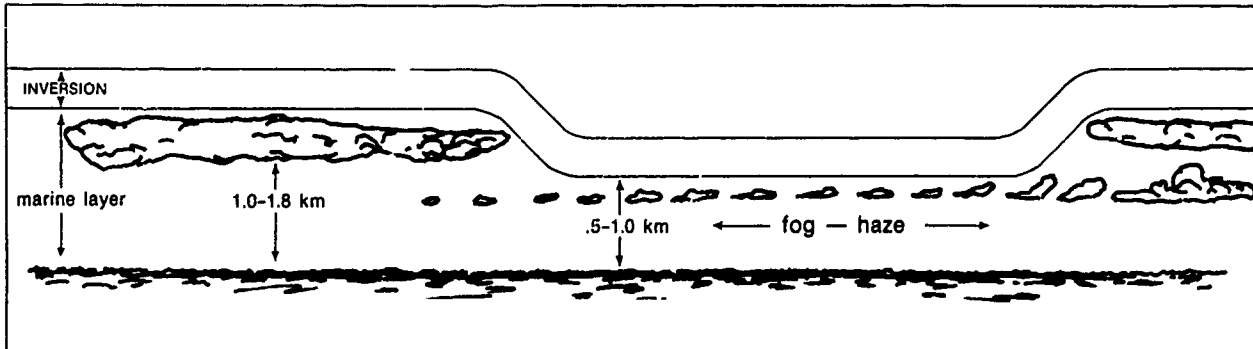
In general, anomalous cloud lines are not aligned with the prevailing synoptic flow. When several ships transverse the same area, it is not uncommon that cloud lines are observed to cross one another in an apparently random manner. Not all ships generate cloud lines—this may be related, in part, to differences in propulsion systems.

Atmospheric conditions favorable for the formation of anomalous cloud lines include:

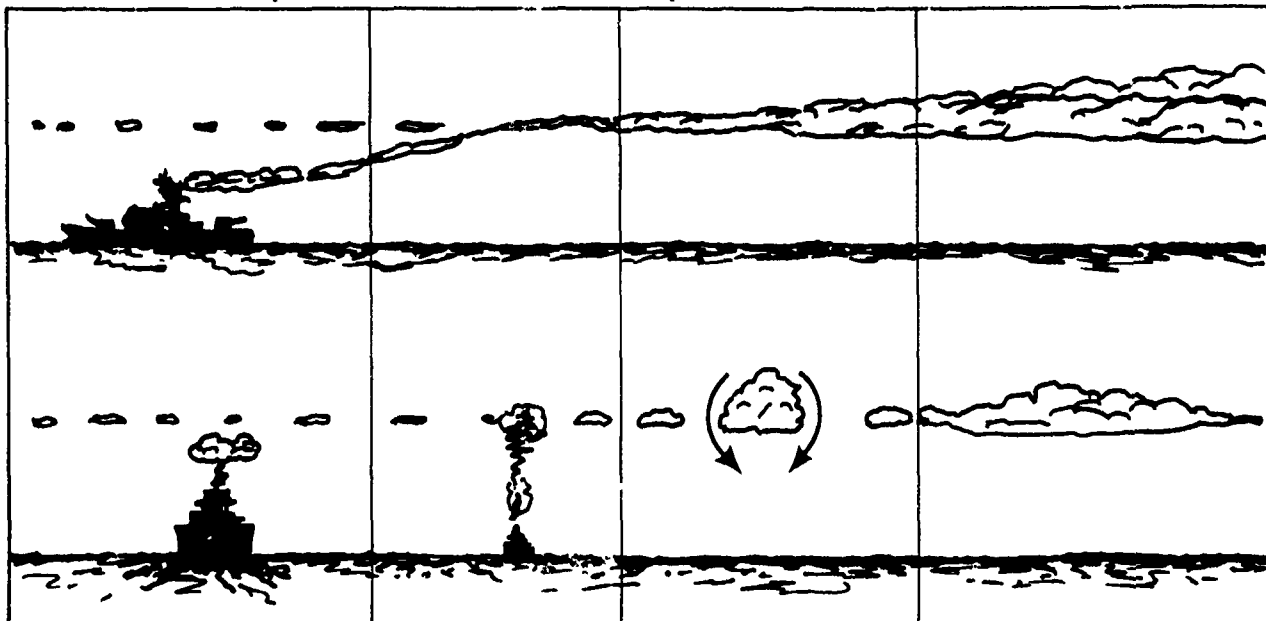
- 1) A shallow marine layer that is cool, moist, and convectively unstable, capped by a strong inversion with dry air aloft. At the top of the sub-cloud layer there should be saturated or slightly supersaturated conditions and a deficiency of hygroscopic cloud particles or condensation nuclei.
- 2) Air temperature colder than the sea surface temperature. Because the marine layer is shallow and moist, air temperatures lower than sea surface temperatures are conducive to haze and fog formation. Observations indicate that restrictions to visibility are almost always present in anomalous cloud line areas.
- 3) Light to moderate wind speed in the sub-cloud layer, and the absence of vertical wind shear in the cloud layer.

The sequence of events in the development of an anomalous cloud line with reference to a ship underway, is illustrated schematically in Fig. 1C-3a.

1C-2a. Schematic of an area of closed cellular clouds showing a depressed marine layer and an open cellular cloud pattern region.



IC-3a. Formation and development of an anomalous cloud line as a ship transits the area.



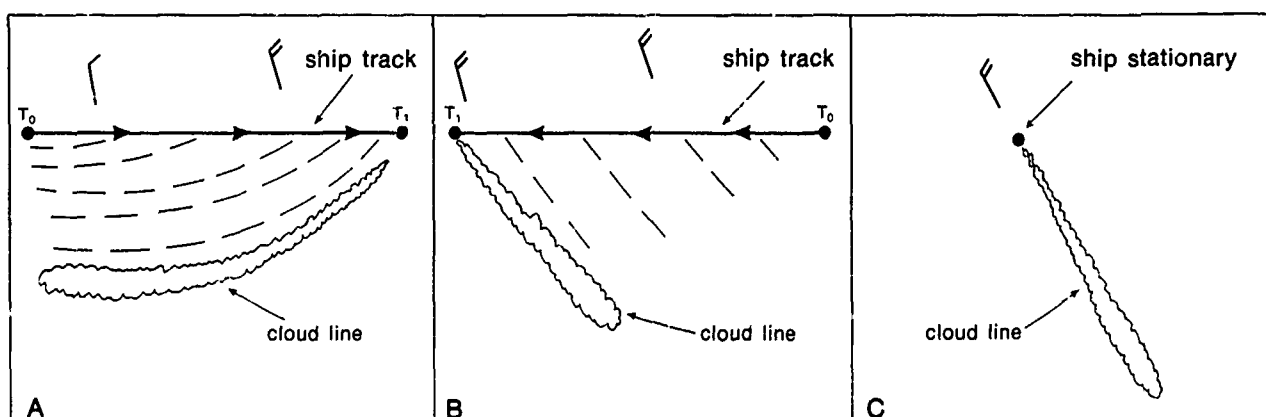
5 minutes
Bouyancy of the hot stack gases carries effluent (heat, moisture, nuclei, etc.) to the vicinity of the base of the inversion (top of the marine layer).

1 hour
The lifting condensation level is near the base of the inversion. Some scattered stratocumulus clouds are observed forming through natural convection processes. The air in this region is saturated or slightly supersaturated. Nuclei in the effluent increases droplet formation; this releases latent heat of condensation which increases convective activity in the region where the anomalous cloud line begins to form and develop.

2 hours
Continued addition of condensation nuclei by rising effluent increases the release of latent heat, which results in the development of the cloud line. As the cloud line expands into the dry air above the inversion, evaporation and radiational cooling along the top and sides of the clouds causes a downdraft to develop. The downdraft entrains surrounding air as it sinks down through the inversion. The combination of removing moist air from below the inversion into the developing clouds and bringing drier air down from above the inversion, results in the dissipation of the scattered stratocumulus clouds that may be present along either side of the developing anomalous cloud line.

4 to 16 hours
After the cloud line formation process has been going on for some time, less effluent reaches the area, due to the ship moving away, and the addition of latent heat is reduced and the convective activity decreases. The strong stability above the inversion suppresses the cloud line, and it begins to spread laterally.

As an anomalous cloud line is formed, the prevailing flow and direction of ship movement affect the appearance and configuration of the cloud line as shown below.



A
The ship course and speed remain constant and the wind field changes with time, resulting in a curved cloud line.

B
The ship course and speed remain constant, the ship course being at an angle with a wind field that does not change with time. The cloud line is straight, but at an angle with the ship track.

C
The ship is stationary in a uniform wind field. A similar result would be obtained if the ship was underway upwind or downwind, parallel to a wind greater than the speed of the ship.

Case 1 Anomalous Cloud Lines

Oceanic anticyclone—eastern North Pacific

An excellent example of anomalous cloud line formation can be seen in the DMSP picture (Fig. 1C-4a) northwest of Guadalupe Island. These lines appear as distinct, bright cloud plumes emanating from a point source. They appear to be located within a relatively clear area. However, a careful examination of an enlarged view of this area (Fig. 1C-5a) reveals many gray shades (NTAG, Vol. 1, Sec. 2B) on the edge of a sunglint area, indicating an abundance of moisture at low levels. Also, some discrete clouds are visible suggesting the possible presence of many small cloud elements beyond satellite resolution. DMSP data must be carefully examined to obtain an accurate estimate of total cloud cover.

The continued development of the anomalous cloud lines is observed in an enlarged SMS-2 visible picture of the same area about 5½ hours later (Fig. 1C-5b). During this time, the cloud lines have grown significantly in length and some new lines have apparently been generated. Also, considerably more cloudiness appears in the area where the cloud lines have formed.

The convective nature of anomalous cloud line formation is indicated by a suggestion of clear channels on either side of the lines in the area outlined on the SMS-2 picture. The clear channels appear more dramatically on a photograph taken from the manned Apollo-Soyus spacecraft (Fig. 1C-5c) at approximately the same time as the SMS-2 picture. The pictures suggest a suppression of cloudiness on either side of the lines due to sinking motion and entrainment of dry air from aloft, with rising motion in the center of the cloud lines. Note also that the clear channels become less evident near the anomalous cloud line source.

The higher resolution Apollo-Soyus photograph also reveals an extensive open cellular cloud field in which the anomalous cloud lines are embedded. SMS-2 infrared data and RAOB data from Guadalupe (Fig. 1C-5d) confirm that the cloud lines are a low-level phenomena. Warm temperatures (dark gray shades) are observed over the area in the infrared picture. The 1200 GMT RAOB for Guadalupe shows a strong low-level inversion, indicating that cloud tops in the anomalous cloud line area did not exceed 500 m (1,600 ft).

Important Conclusions

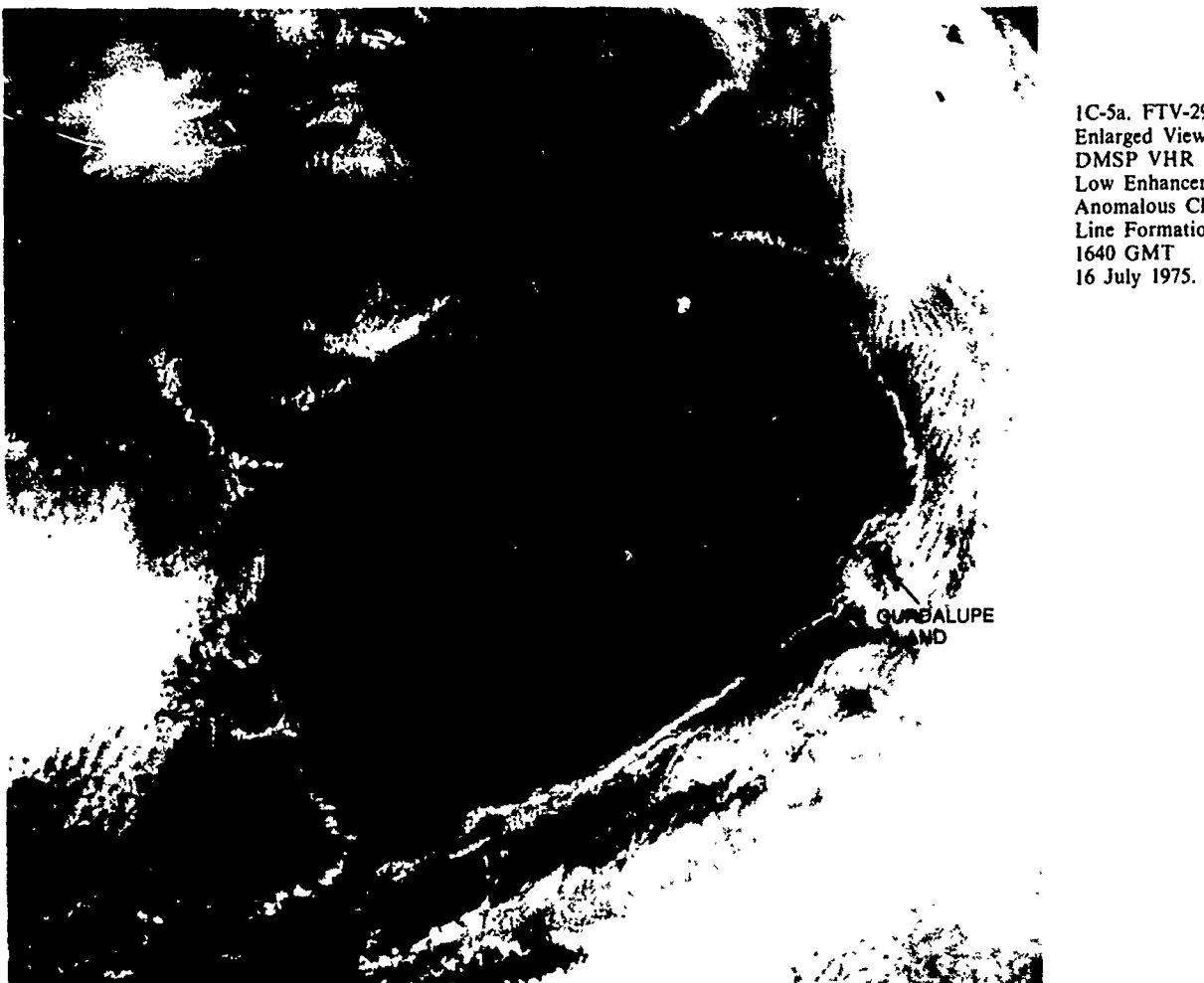
1. The presence of anomalous cloud lines is indicative of ship movement within a shallow, moist, marine layer capped by a strong inversion.
2. Anomalous cloud lines are enhanced lines of convective cloudiness. Clear channels often appear on either side due to sinking motion and entrainment of dry air from aloft.



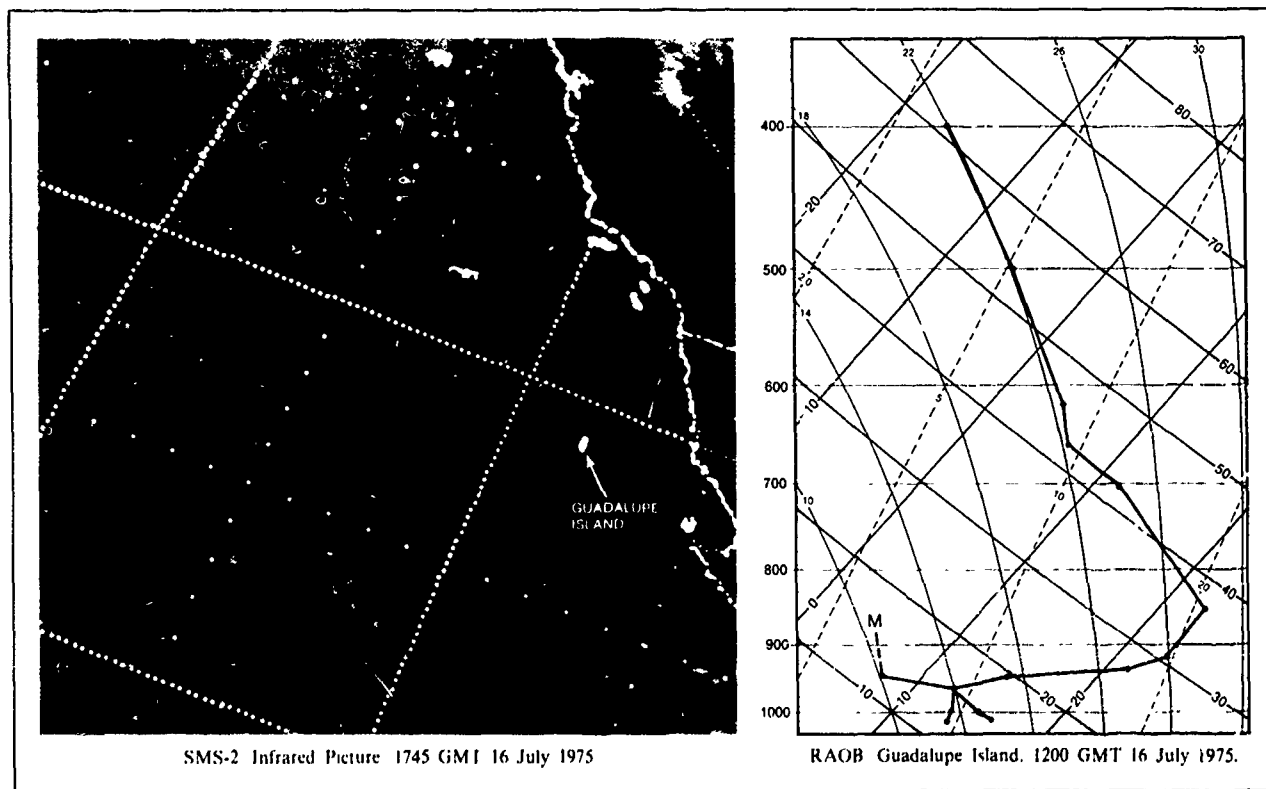
IC-4a. FTV-29. DMSP VHR Low Enhanc



IC-4a. FTV-2^c DMSP VHR Low Enhancement. Anomalous Cloud Line Formation. 1640 GMT 16 July 1975



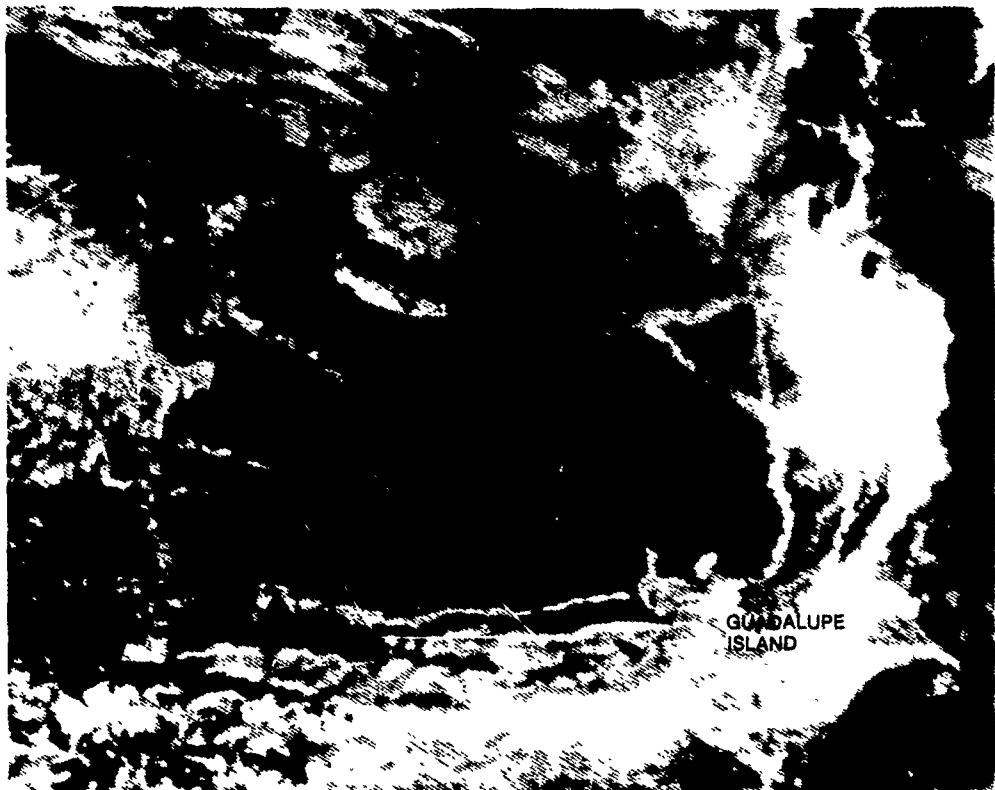
IC-5b. SMS
2215 GMT



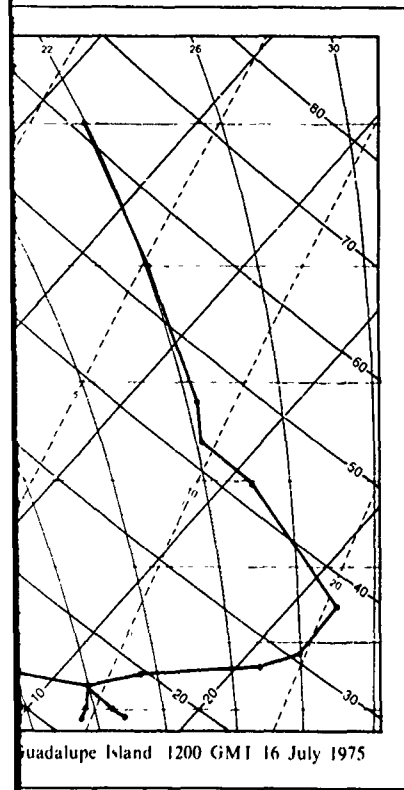
IC-5d. Low-level Data.

IC-5c. Apoll

IC-5a. FTV-29.
Enlarged View.
DMSP VHR
Low Enhancement
Anomalous Cloud
Line Formation.
1640 GMT
16 July 1975.



IC-5b. SMS-2. Enlarged View. Visible Picture. Development of Anomalous Cloud Lines.
2215 GMT 16 July 1975. (Area Outline of Fig. IC-5c.)



IC-5c. Apollo-Soyus Photograph. Development of Anomalous Cloud Lines. 2220 GMT 16 July 1975.

Case 2 Anomalous Cloud Lines

Anomalous cloud line formation in areas of vertical wind shear



IC-6a. FTV-29. DMSP VHR Low Enhancement. Anomalous Cloud Line Formation in Areas of Vertical Wind Shear.
1623 GMT, 28 July 1975.
Surface Observations, 1800 GMT 28 July 1975.

Anomalous cloud lines develop a striated appearance when sufficient vertical wind shear is present within the cloud layer. Short cloud lines develop parallel to the vertical shear vector in the cloud layer and form an angle with the axis of the line. An example of this formation, ahead of a cold front, is observed in a DMSP picture of the eastern North Pacific just off the coast of California (Fig. 1C-6a). A number of anomalous cloud lines, many with transverse bands, are observed within a broken open cellular cloud pattern. Note, in the enlarged view (Fig. 1C-7a), that many of the open cells have been disrupted and form cloud lines indicating the presence of vertical shear in the area. Additional verification of the presence of vertical shear is that the cloud lines are not aligned with the surface flow as indicated by ship reports (see Sec. 1D).



IC-7a FTV-29. Enlarged View DMSP VHR Low Enhancement. Striated Anomalous Cloud Lines. 1623 GMT 28 July 1975.

Case 3 Anomalous Cloud Lines

Oceanic anticyclone—in advance of a cold front

Areas with atmospheric conditions suitable for the formation of anomalous cloud lines often exist for a number of days. New lines form as ship activity continues in the area, while the older lines dissipate as they expand horizontally and evaporate or blend into the cloud cover which surrounds them. Such an area is observed off the California coast in the DMSP picture on 6 May 1974 (Fig. 1C-8a).

Note the difference between the anomalous cloud lines and the cloud lines that have formed due to vertical wind shear within the cloud layer. The anomalous cloud lines appear in a random fashion, often crossing one another, as distinct, bright lines. The cloud lines resulting from vertical shear appear in an orderly fashion and are not distinctively brighter than the surrounding cloud field. Ship observations within the anomalous cloud line area show widespread fog.

A large area of stratus and closed cellular cloudiness is observed south of the cloud line region. Also, a cold front advancing into the region is indicated by the cloud band in the northwest corner of the picture and the surface analysis for this date.

On the following day (Fig. 1C-9a), the area of anomalous cloud line formation has moved to the southeast in advance of the cold frontal cloud band. A clear, dark area indicating the presence of drier air (NTAG, Vol. 1, Sec. 2B) now appears between the two regimes. A thin strip of a lighter gray shade begins at the southern edge of the clear area, indicating the presence of more moist air in the area. Most of the previous day's lines have dissipated and number of new lines have formed.

No anomalous cloud lines appear in the DMSP picture for the next day (Fig. 1C-9b). The cold front has advanced into the area causing an extensive field of stratus due to lifting of the inversion throughout the area. The cold front has essentially dissipated, as evidenced by the absence of the frontal cloud band observed in the pictures on the two previous days.

Important Conclusion

1. Anomalous cloud line formation areas, with atmospheric conditions of haze and fog, are strongly persistent and can be tracked from day to day.



1C-8a. FTV-29. Enlarged View. DMSP
1601 GMT 6 May 1974.
Ship Observations (1800 GMT) and Su



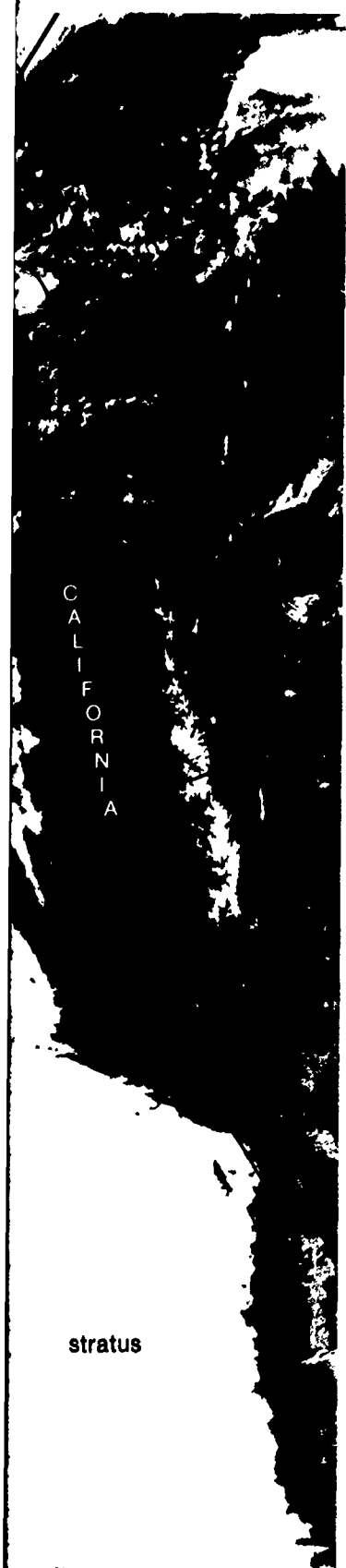
IC-8a. FTV-29. Enlarged View. DMSP VHR Low Enhancement. Anomalous Cloud Line Area in Advance of a Cold Front.
1601 GMT 6 May 1974.
Ship Observations (1800 GMT) and Surface Analysis (1500 GMT). 6 May 1974.



IC-9a. FTV-31. Enlarged View. DMSP VHR Low Enhancement.
Movement of an Anomalous Cloud Line Area in Advance of a Cold Front. 1543 GMT 7 May 1974.
Surface Analysis 1500 GMT 7 May 1974.



IC-9b. FTV-29. E
Dissipation of an
Surface Analysis.



C-9b. FTV-29. Enlarged View. DMSP VHR Low Enhancement.
Dissipation of an Anomalous Cloud Line Area. 1524 GMT 8 May 1974.
Surface Analysis. 1500 GMT 8 May 1974.

7 May 1974.

1D Cloud Lines

Cloud Lines and Low-Level Wind Flow Patterns

Cloud lines are rows of cumulus clouds formed when air is heated from below as it is advected over ocean or land surfaces (Kuettner, 1959). The cloud elements may be connected to form individual cloud lines of varying length and spacing; or the cloud elements may appear as long, narrow rows of closely spaced cloud lines (sometimes referred to as cloud streets). The width of a cloud line is small in comparison to its length. Characteristically, cloud lines appear in meteorological satellite data as a series of parallel or nearly parallel cumulus rows.

The orientation of cloud lines relative to the wind direction depends on the vertical wind structure. Under conditions where there is no change of wind direction with height, but an increase of wind speed with height through the cloud layer, the cloud lines are parallel to the surface wind direction. When there is a change of wind direction with height through the cloud layer, the cloud lines will cross the low-level flow at an angle. In this case, the cloud lines are aligned parallel to the thermal wind vector through the cloud layer, i.e., parallel to the directional shear between the base and top of the cloud layer.

Cloud lines are useful not only in determining low-level wind direction, but also as indicators of atmospheric moisture content, air-sea temperature differences, and low-level stability. The curvature of the flow suggested by cloud lines can often be used to estimate the location of the central areas of high and low pressure systems.

Reference

Kuettner, J., 1959: The band structure of the atmosphere. *Tellus*, 11, 267-294.

Case 1 Cloud Lines

Estimating wind direction from cloud lines in tropical oceanic areas

The tendency for cumulus clouds to form long rows, often up to 185 km (100 n mi) in length, can be observed in all latitudes, but it appears as the predominate form of cloud organization over the tropical oceans. In an examination of cloud lines between 10°N and 10°S, over the Atlantic and eastern Pacific, using satellite data, Gaby (1967) showed that equatorial cloud lines have a consistent orientation approximately parallel to the surface wind direction. In a further investigation of cloud lines over the equatorial mid-Pacific, using high resolution DMSP data, Brandli (1974) found the alignment and surface wind direction to be within 20° on all occasions, and coincident 20% of the time. These observations indicate that, in tropical oceanic areas, cloud lines may be useful in estimating the low-level wind direction.

The long, narrow, straight, and widely spaced cloud lines observed over the South China Sea (Fig. 1D-3a) suggest a nearly constant wind direction over the entire area paralleling the cloud line formations. The cloud alignment suggests basic wind flow components from the south or possibly from the north. The ambiguity may be resolved by noting that convective cloudiness is observed forming along the southern coast of Hainan Island and not over the northern coast. This cloudiness is produced by the forced ascent of southerly flow over the mountainous terrain of southern Hainan. This inference is confirmed by a ship reporting an 8 m s^{-1} (15 kt) southerly wind in the cloud line area to the southeast of Hainan. An earlier report (1800 GMT 20 May), due south of the island, also showed southerly flow at speeds of about 10 m s^{-1} (20 kt).

The narrowness of the lines and their wide spacing are an indication that air-sea temperature differences over the area are small. This condition is confirmed by several ships in the area reporting air temperatures very close to that of the underlying sea.

Important Conclusions

1. Cloud line orientation over tropical oceanic regions is a useful indicator of surface wind direction.
2. Lines remaining parallel over long distances indicate near constant wind direction at low-levels.
3. Narrow, widely spaced cloud lines are indicative of small air-sea temperature differences.

References

- Brandli, H. W., 1974: Cumulus cloud lines or streets near the Equator. *Bull. Amer. Meteor. Soc.*, 55, 315-317.
Gaby, D.C., 1967: Cumulus cloud lines vs surface wind in equatorial latitudes. *Mon. Wea. Rev.*, 95, 203-208.



ID-3a. FTV-28. DMSP VHR Low Enhancement Cloud Lines Over the South China Sea. 2312 GMT 20 May 1973.
Surface Wind Observations. 0000 GMT 21 May 1973.

Case 2 Cloud Lines

Cloud lines over land

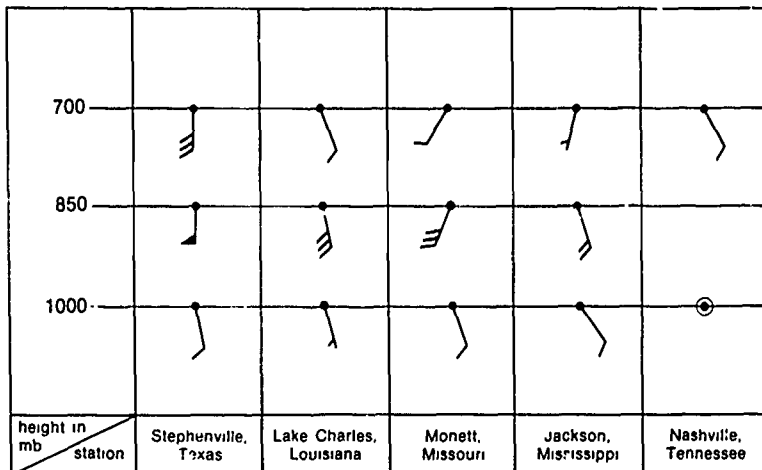
The long, curved, north-south oriented cloud lines over the western Gulf States (Fig. 1D-4a) suggest a broad, southerly flow from the Gulf of Mexico advancing inland. Southerly flow over this area is confirmed by surface observations (enlarged view, Fig. 1D-5a) which show south to southeast winds with speeds of $5-10 \text{ m s}^{-1}$ (10-19 kt). Note that the cloud lines are generally parallel to the low-level wind flow. This indicates there is little directional shear with height through the cloud layer. At the same time, wind speeds should increase with height through the cloud layer, a necessary condition for cloud line formation.



ID-4a. FIV-29. DMSP VHR Low Enhancement. Convective Cloud Lines Over Land. 1446 GMT 19 June 1975.



ID-5a. FTV-29. Enlarged View. DMSP VHR Low Enhancement. Convective Cloud Lines Over Land. 1446 GMT 19 June 1975.
Surface Analysis. 1800 GMT 19 June 1975



ID-5b. Upper-Level Wind Observations 1200 GMT 19 June 1975.

These conditions are verified by upper-level wind data (Fig. 1D-5b) from stations within the cloud line area. For example, wind reports from Lake Charles and Stephenville show light southeasterly surface winds, remaining southeasterly at upper levels, with speeds increasing to 16 m s^{-1} (1 and 51 kt) respectively, at the 850-mb level.

The cloud lines curve anticyclonically around the high pressure area, as shown by the surface observations and pressure analysis (Fig. 1D-5a). Inversion heights should lower from the cloud line area in the direction of the center of high pressure. RAOB data show this to be the case. Oklahoma City, just north of Stephenville, has an inversion height of 1,520 m (5,000 ft) which lowers to 460 m (1,500 ft) at Nashville.

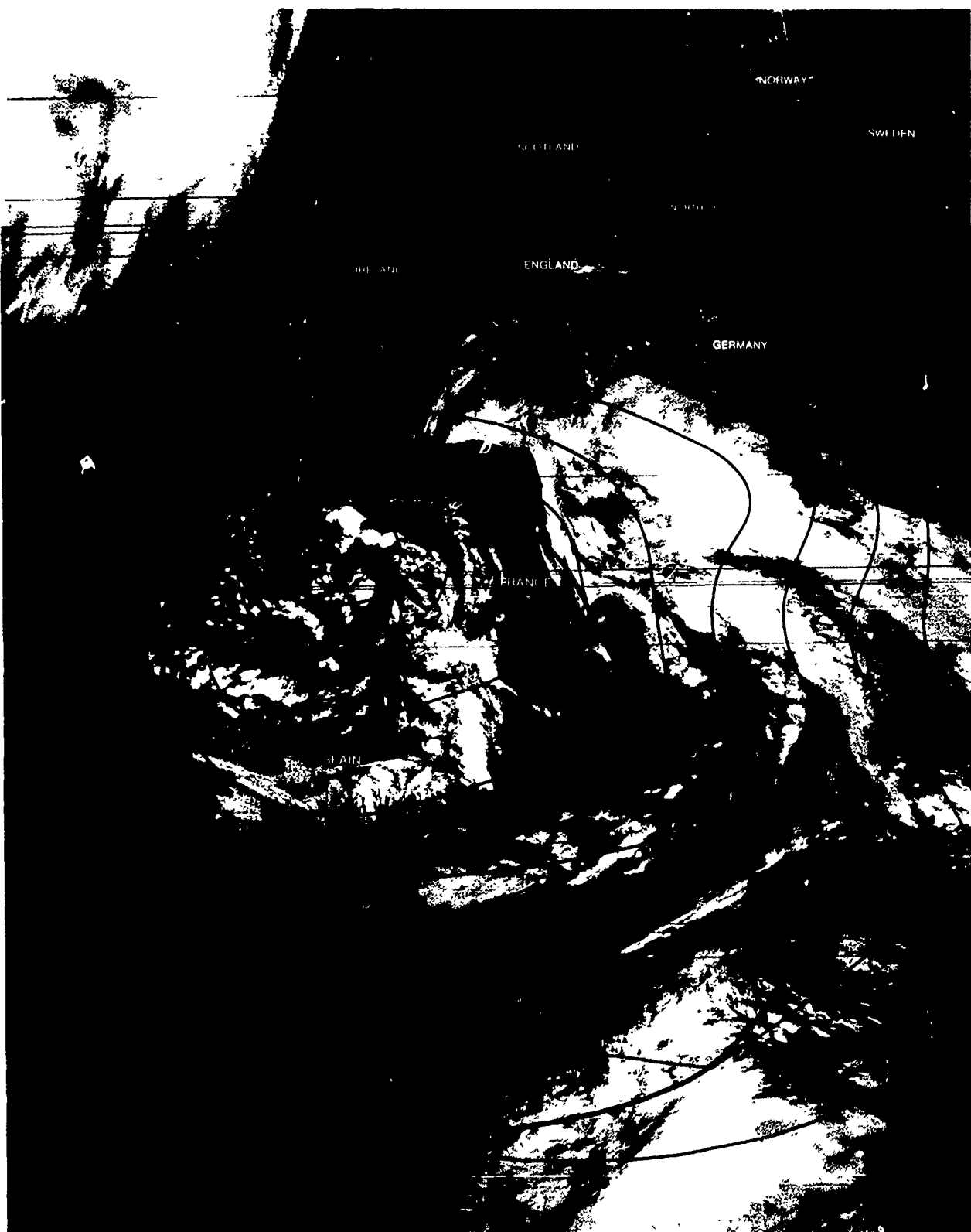
The fact that the cloud lines do not appear until some distance inland emphasizes the need for heating from below to produce the convection necessary for the cloud line formation. This observation is also useful for resolving the problem in determining the direction of the basic low-level flow.

Important Conclusions

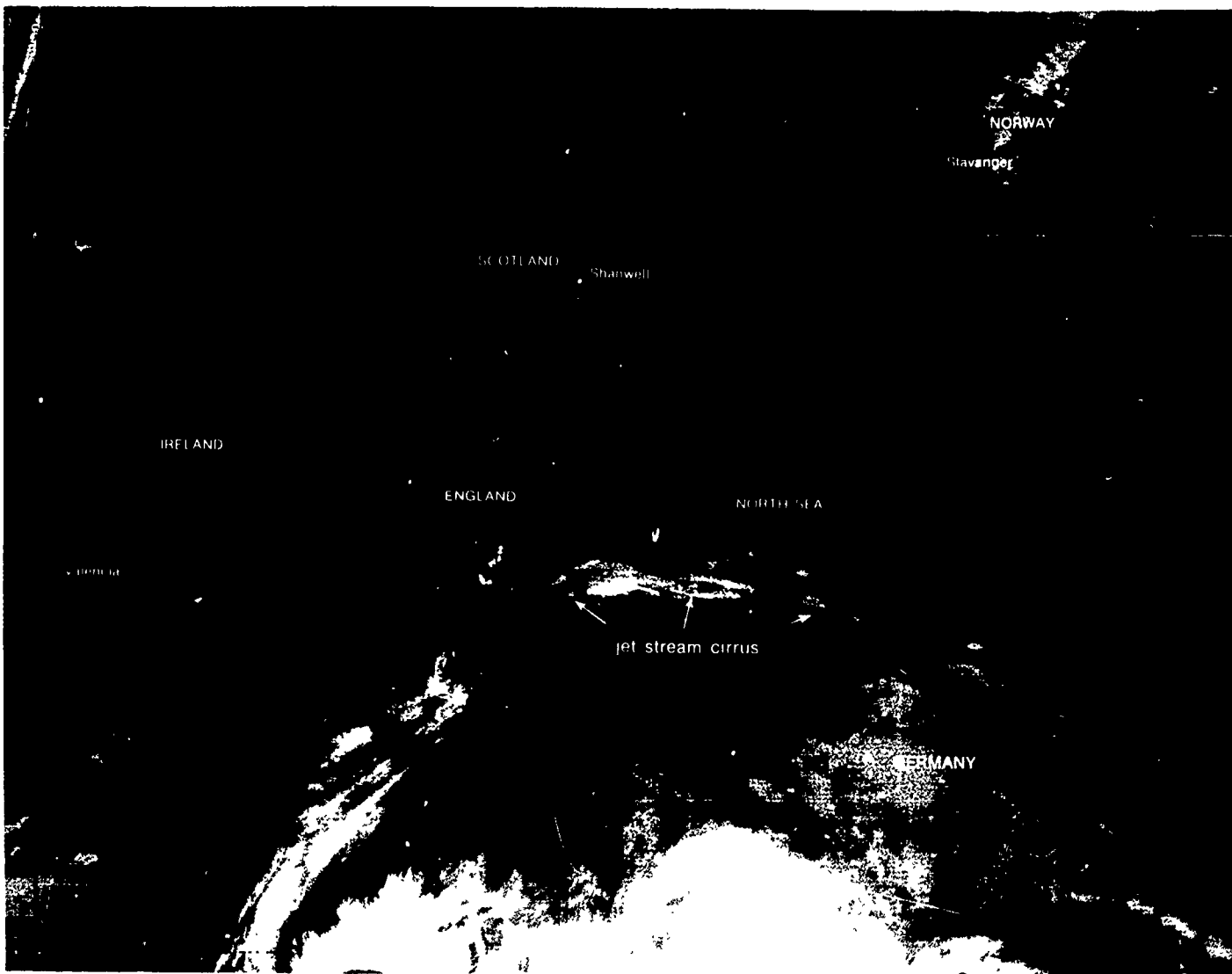
1. Cloud lines oriented parallel to the surface wind indicate there is little or no directional shear of the wind with height through the cloud layer. Wind speeds, however, increase with height through the cloud layer.
2. The direction of the low-level flow can be inferred by taking into consideration the effects of onshore or offshore flow on the beginning of convective cloud formation.

Case 3 Cloud Lines

Cloud line formation in areas of cold air advection over water



1D-6a. FTV-33. DMSP WHR Normal Enhancement. Cloud Line Formation Over Water. 0622 GMT 31 January 1976.
Surface Analysis. 0600 GMT 31 January 1976.



ID-7a. FTV-33 Enlarged View. DMSP WHR Normal Enhancement. Cloud Line Formation Over Water. 0622 GMT 31 January 1976.

A DMSP WHR (High Resolution, IR) picture of western Europe with superimposed surface analysis, is shown in Fig. 1D-6a. The surface analysis indicates that the cloud lines observed in the North Sea have formed in strong southeasterly flow which ultimately turns anticyclonically around a high pressure area centered over Norway, and cyclonically around a low pressure system west of France. An enlarged view of this cloud line area is shown in Fig. 1D-7a. The cloud lines have formed in cold air which has been heated from below as it moved from continental areas over the warmer sea surface. The thickness of the lines and the narrow spacing indicates a large air-sea temperature difference. The fact that the lines are parallel to the low-level wind direction suggests that there is little directional shear through the cloud layer. RAOB reports from the area (Fig. 1D-7b) confirm this condition and also reveal the presence of strong speed shear, a necessary condition for cloud line formation.

To the north of these lines, increased subsidence and lighter winds, combined with anticyclonic flow, are related to an extensive area of stratus or fog. The RAOB data show an inversion base near ground level at Stavanger, Norway, which rises to the south, reaching the 850 mb level at Shanwell, Scotland and Valencia, Ireland.

Ov
the s
inver
cloud
cyclo

Impo

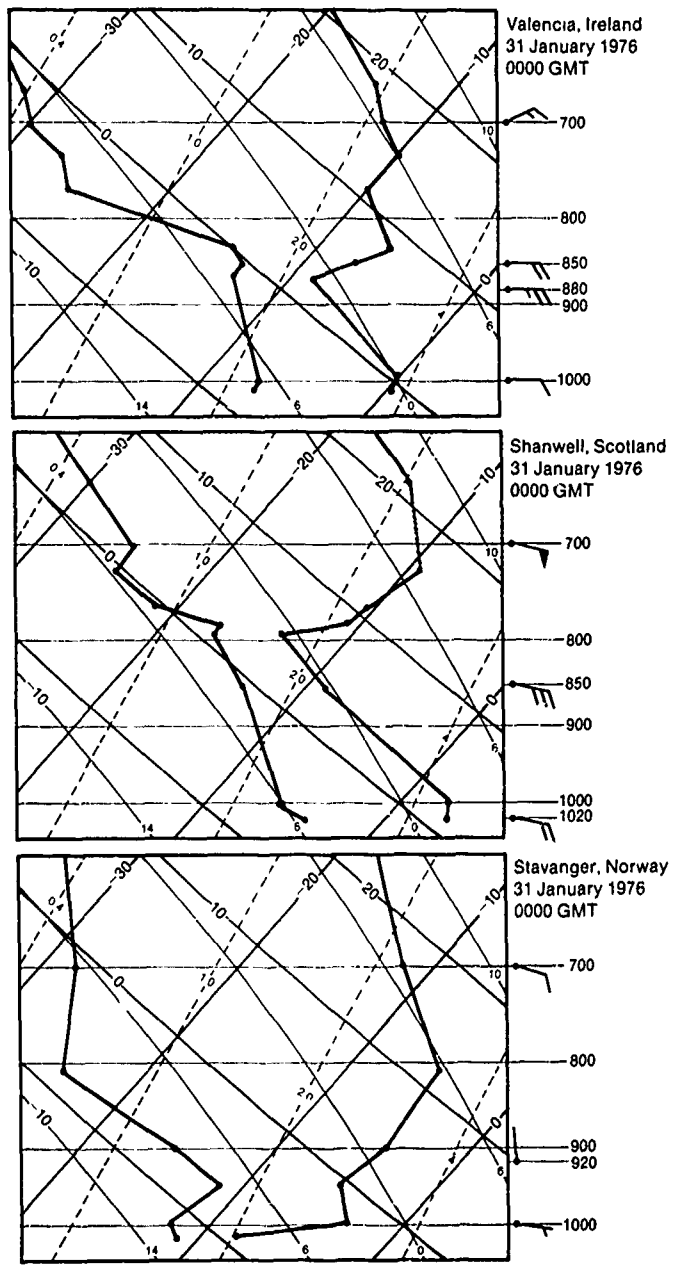
1. B
2. L
3. T

so

NORWAY
Stavanger

GERMANY

water 0622 GMT 31 January 1976.



ID-7b. RAOB Data.

Over Scotland, and further to the west, terrain induced wave clouds have formed in the strong, moist low-level flow. Formation of such clouds is dependent on the strong inversion over this area (NTAG, Vol. 1, Sec. 2C, Case 3). Cloud lines and some wave clouds are also observed west of Ireland. Line formation near Valencia begins turning cyclonically as a result of the strong low pressure system to the south.

Important Conclusions

1. Broad patterns of cloud lines are frequently found in the low-level flow around high and low pressure areas.
2. Looking downwind, decreased inversion heights may be anticipated to the right of cloud line patterns generated in flow around anticyclones.
3. Thick, narrowly spaced cloud lines, over oceanic areas, are indicative of large air-sea temperature differences; the air being much colder than the water.

Case 4 Cloud Lines

Use of cloud lines in locating central areas of oceanic anticyclones

High pressure areas are regions of subsidence and low-level horizontal divergence and are generally, therefore, cloud-free. Occasionally, rows of low-level cumulus cloud lines will clearly define the location and areal extent of the central portion of an anticyclone.

In Fig. 1D-8a, sharply curved rows of cumulus cloud lines, approximately 1700 km northeast of Hawaii, define an oval-shaped open area within a large, closed cellular cloud field typical of anticyclones in the eastern North Pacific.

Surface wind reports and a surface streamline analysis (Fig. 1D-9a) reveal how closely the cloud lines define the central area of the oceanic



ID-8a. FTV-35. DMSP LF Low Enhancement. Cloud Lines Locating the Central Area of an Oceanic Anticyclone. 2031 GMT 9 April 1977.

anticyclone. Note that swell heights to the east and southeast of the central area, where the fetch extends for a considerable distance from the north, are rough and range from 7 to 13 ft. In addition, swells to the north of the central area are moderate. To the west of the central area, in an area of changing wind direction and short fetch, the seas and swells are slight (3 ft). Thus, the central area of the anticyclone, and the area to the west, are zones of reduced sea heights within the expansive region covered by the anticyclone. Such information is extremely useful for ship routing, where avoidance of rough seas can reduce transit time and damage to ship and cargo.

Important Conclusion

1. The central area of oceanic anticyclones can often be located by rows of sharply curved cumulus cloud lines.

Legend

Wave Period (sec)/Wave Height (ft)
Swell Direction/Swell Period (sec)/Swell Height (ft)

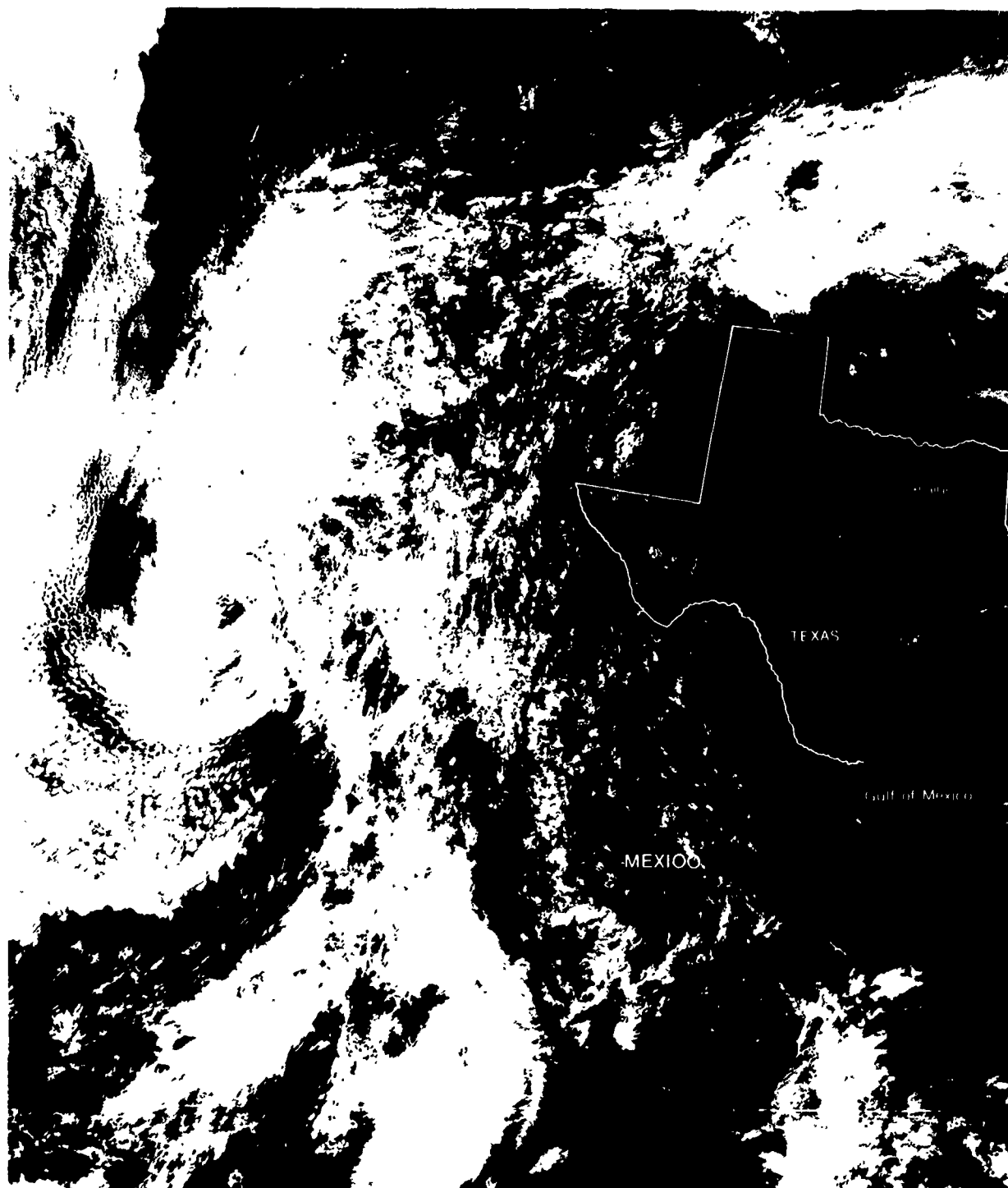


ID-9a. FTV-35. DMSP LF Low Enhancement Cloud Lines Locating the Central Area of an Oceanic Anticyclone. 2031 GMT 9 April 1977.
Surface Wind Reports, Sea State Reports, and Streamline Analysis. 1800 GMT 9 April 1977.

Case 5 Cloud Lines

Inhibiting effect of wet ground on convective cloud line formation

Where land has been soaked with rain, an inhibiting effect on early morning convective cloud formation is often observed. Such an area will appear slightly darker in DMSP visible imagery than the surrounding dry land areas. This is due to the lower reflectivity of the wet land area in comparison to the dry land.



ID-10a. FTV-35. DMSP LF Low Enhancement. Inhibiting Effect of Wet Ground on Convective Cloud Formation. 1815 GMT 16 August 1977

In Fig. 1D-10a, the oval-shaped, cloud-free area over central Texas is an excellent example of the inhibiting effect of wet ground on convective cloud line formation. During the previous night and preceding 48 hours numerous thunderstorms were reported in this area. In the morning, the surface air temperature rises rapidly in the clear areas over dry land, but more slowly in clear areas over wet land. Thus, convective activity is observed over the dry land areas, while a cloud-free region is observed over the rain-soaked area.



1D-11a. FTV-35. Enlarged View. DMSP LF Low Enhancement. Inhibiting Effect of Wet Ground on Convective Cloud Formation. 1815 GMT 16 August 1977. Surface Wind Reports. 1800 GMT 16 August 1977.

In the enlarged view (Fig. 1D-11a) surface wind reports reveal that there is weak southerly anticyclonic flow over Texas. Note that the cloud lines reflect the curvature of this flow. A weak sea breeze front has developed along the Gulf Coast, and the inhibiting effect of the bays and rivers on convective cloud formation is also evident in this area.

Important Conclusion

1. Early morning convective activity is inhibited over rain-soaked areas in comparison to surrounding dry land areas due to slower rising surface air temperatures over the wet ground.

1E Vortical Cloud Patterns

Vortical Cloud Pattern Systems

Spiral cloud lines and cloud bands which converge toward a common center are called vortical cloud patterns and are associated with areas of cyclonic flow and cyclonic vortices in the atmosphere. Vortical cloud patterns are observed in satellite imagery at mid and high latitudes in long wave troughs, along frontal cloud bands, in the cold air behind frontal cloud bands, and in cut-off lows. In tropical latitudes, vortical cloud patterns occur with the formative, mature, and dissipative stages of tropical cyclones and in upper-level troughs and cold lows.

In the weaker stages of development, a vortical cloud pattern does not necessarily indicate a closed circulation in the cloud layer. However, mature vortical cloud patterns are usually accompanied by a closed circulation.

The characteristic appearance (size, shape, and structure) of a vortical cloud pattern is an indication of the stage of development and type of cyclonic disturbance that is occurring. Similarities in cloud patterns may be observed when a disturbance is in a given stage of development. Thus, by properly identifying these patterns, it is possible to classify the type of disturbance with respect to development and to estimate its intensity (Anderson *et al.*, 1974).

Reference

Anderson, R.K., *et al.*, 1974: Applications of meteorological satellite data in analysis and forecasting. ESSA Tech. Report NESCR 51 (including supplement, Nov. 1971, and Supplement No. 2, March 1973). National Environmental Satellite Service, NOAA, Washington, D.C., 350 pp.

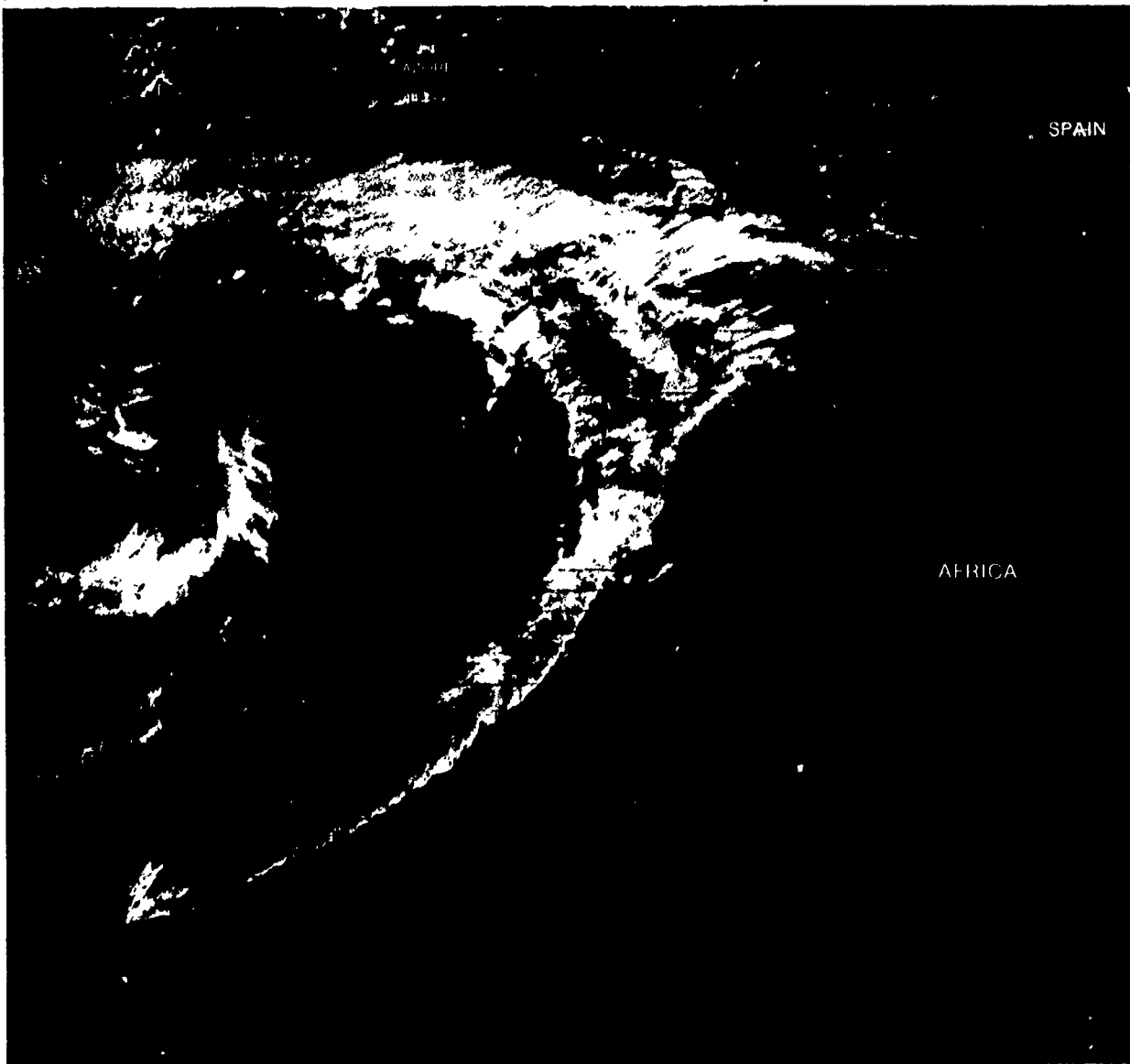
Case 1 Vortical Cloud Patterns

Mature mid-latitude frontal vortex—eastern North Atlantic

Fig. 1E-2a is a DMSP LF picture of a vortical cloud pattern typical of a mature frontal vortex development. The NMC surface analysis for 1200 GMT 8 April indicated that this frontal vortex was associated with a mature occluded frontal system. Note that the vortical cloud pattern consists of an intense spiral cloud band near the center of the vortex, a well-defined, large, east-west oriented cloud band to the north, and a fragmented, narrow cloud band extending to the southwest.

Within the spiral cloud bands near the vortex center, numerous cumulonimbus cloud clusters can be observed. Intense convective activity is also associated with a large cloud band to the north. The TS infrared picture (Fig. 1E-3a) more clearly reveals the areas of intense convective activity, and the areal extent of high clouds (bright tones) in the large cloud band. This picture also shows that there is a rapid decrease in the brightness level along the frontal cloud band extending

1E-2a. FTV-35. DMSP LF Low Enhancement. A Mature Frontal Vortex. 1221 GMT 8 April 1977.

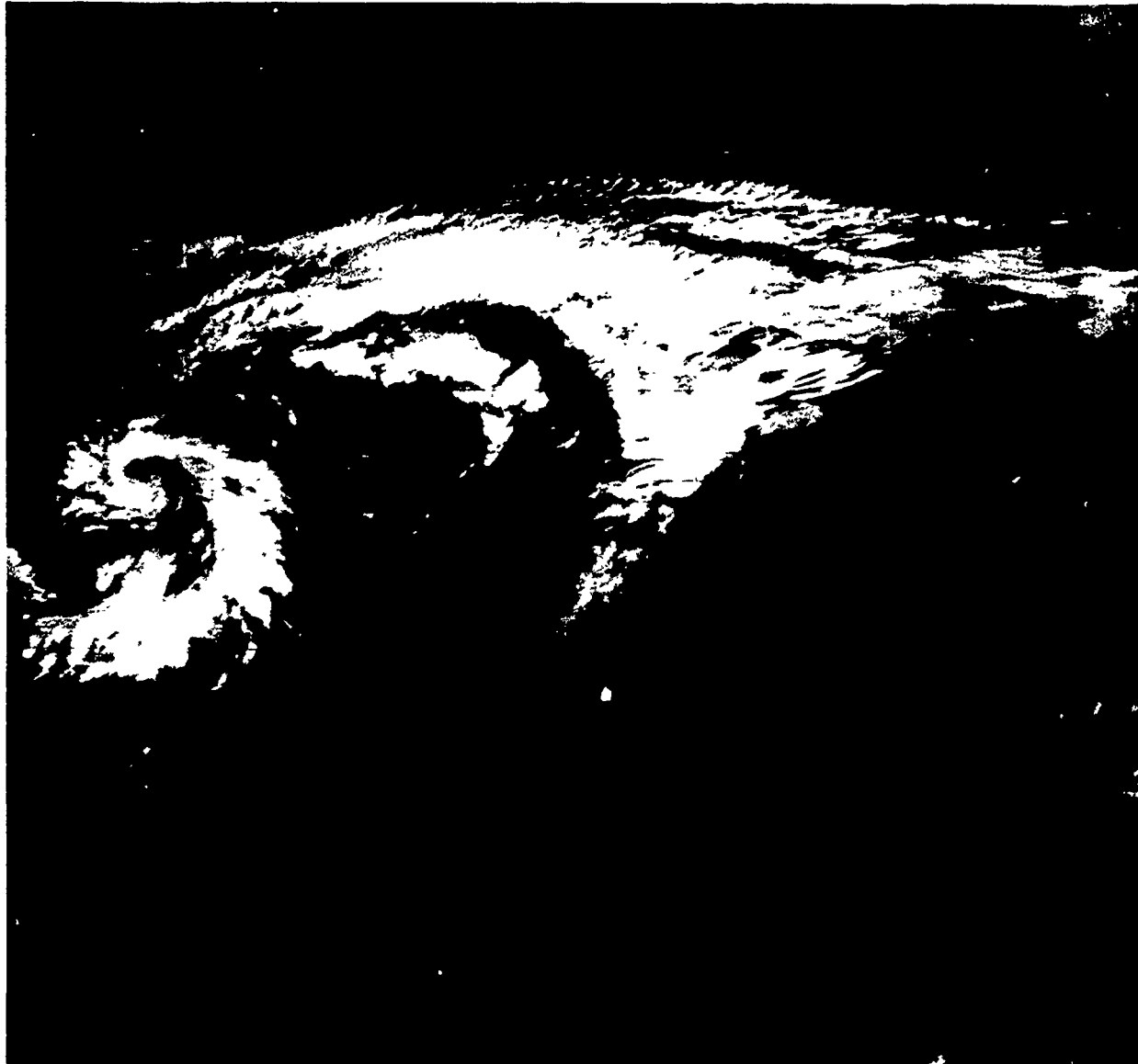


to the southwest. This indicates lower-level cloudiness and less convective activity, suggesting that the front is weak in that area.

The streamline analysis (Fig. 1E-3b) shows an asymptote of convergence extending the length of the frontal cloud band to the north of the storm center. This is also an area of strong surface pressure gradient and winds (30-40 kt). As a result of the high winds and long fetch, the seas are very rough (up to 10 ft seas and 26 ft swells). The cloud band extending to the southwest is associated with much weaker lower-level convergence, and weaker surface winds, with resultant lower seas and swells.

Classical Kelvin ship wave cloud patterns (see NTAG, Vol. 1, Sec. 2C, Case 3), to the lee of the Azores, indicates the presence of a pronounced low-level inversion and strong low-level winds. A RAOB for Lajes, Azores (not shown) near the time of the DMSP data, verified a strong inversion starting at the 800 mb level, with extremely dry air above. Winds over Lajes ranged 30 to 50 kts from the surface to the 200 mb level, giving some indication of the immense energy driving the system.

1E-3a. FTV-35. DMSP TS Normal Enhancement. A Mature Frontal Vortex. 1221 GMT 8 April 1977.



Important Conclusions

1. Cloud bands in vertical cloud patterns showing intense convective activity are associated with low-level streamline convergence asymptotes.
2. When such intense convective cloud bands extend in the same direction over long distances, a long fetch develops and progressively higher seas may be anticipated.
3. Infrared data are useful in determining the active weather producing areas of vertical cloud patterns, and distinguishing these areas from other areas where banding of clouds may be evident but convergence and resultant weather activity are weak.

1E-3b. FTV-35. DMSP LF Low Enhancement. A Mature Frontal Vortex. 1221 GMT 8 April 1977.
Surface Wind Reports and Streamline Analysis. 1200 GMT 8 April 1977.

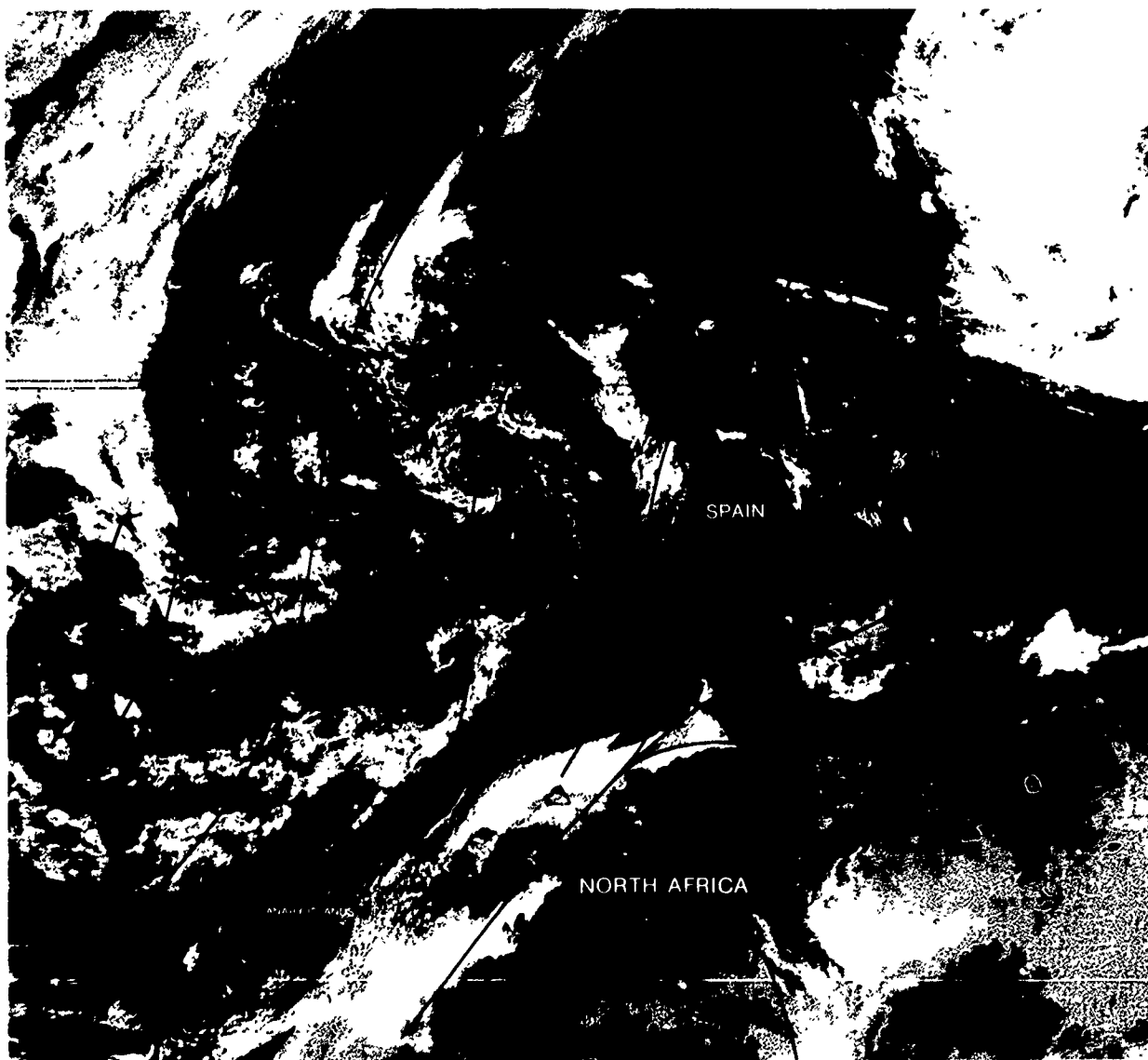


Case 2 Vortical Cloud Patterns

Vortical cloud patterns within a cold polar trough—eastern North Atlantic

In a visible picture of the eastern North Atlantic (Fig. 1E-4a), several weak vortical cloud patterns are observed extending southwestward from the west coast of Spain toward the Canary Islands. The clouds forming the vortical patterns are at middle and lower levels, with some cirrus aloft. Surface wind reports and a surface streamline analysis show weak northerly flow over the area and provide little clue as to the cause of the vortices.

The upper-level wind reports and streamline analysis (Fig. 1E-5a), however, indicate a fairly intense closed circulation within a polar trough which extends southwestward over the vortical cloud patterns. The fact that the vortex and trough decrease in intensity downward indicates that this system is an upper cold low and, therefore, is conditionally unstable. Surface reports of towering cumulus and

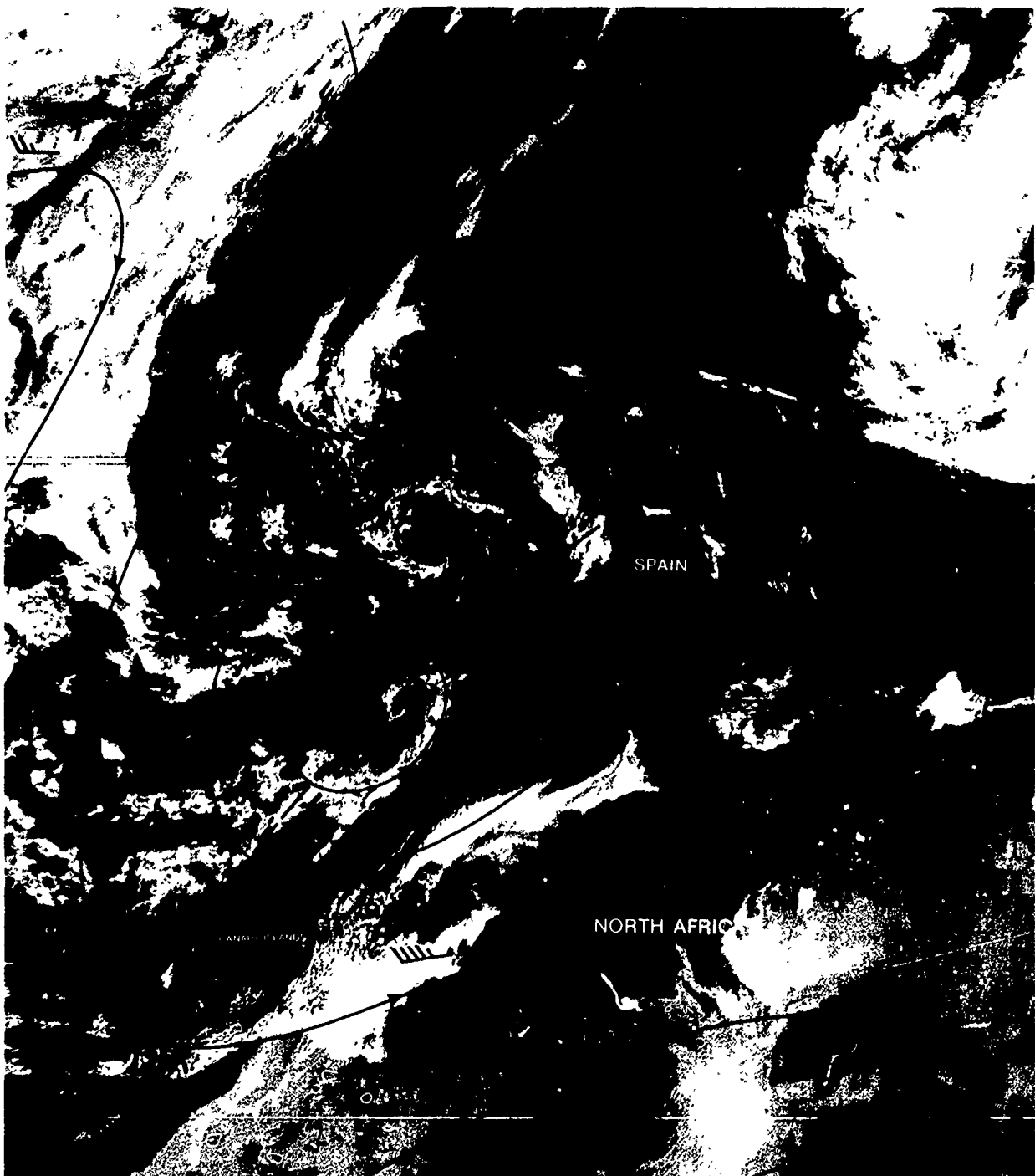


1E-4a. FTV-29. DMSP VHR Low Enhancement. Vortical Cloud Patterns Within a Cold Polar Trough. 0847 GMT 22 June 1975.
Surface Wind Reports, Low Cloud Type, and Streamline Analysis. 1200 GMT 22 June 1975.

cumulonimbus confirm the suggested thermodynamic structure over this area. In addition, the existence of the vortical cloud patterns at middle and lower levels indicates that there has been a transfer of cyclonic vorticity and momentum downward.

Important Conclusion

1. Upper cold lows and polar troughs influence the production of middle and lower level vortical cloud patterns through conditional instability and the transfer of cyclonic vorticity and momentum from upper to lower levels.



IE-5a. FTV-29. DMSP VHR Low Enhancement. Vortical Cloud Patterns Within a Cold Polar Trough. 0847 GMT 22 June 1975.
Upper-Level AIREPS and Streamline Analysis. 0600 GMT 22 June 1975.

Case 3 Vortical Cloud Patterns

Structure of a cutoff low—North Pacific¹

IE-6a. FTV-34. DMSP VHR 1

On 15 October 1971, a DMSP visible picture (Fig. 1E-6a) revealed an intense squall line and spiral bands of cirrus cloudiness in the eastern semicircle of a cutoff low over the mid-North Pacific. The cutoff low is separated from a cold frontal cloud band to the north, and the squall line and spiral cloud bands cover an extensive area. The NMC 300 mb and 500 mb analyses below reveal that this system is cutoff, equatorward of the basic westerly flow. The few available reports from the surface analysis in the area of the cutoff low show that winds are not particularly intense and that there is little indication of any organized severe weather. The numerous cumulonimbus observed in the DMSP picture, however, suggest that within the intense squall line area high winds, high seas, and heavy rains could be anticipated. The streamline analysis (Fig. 1E-7a) reveals the low-level flow pattern associated with the cutoff system. Note the strong confluence of winds and speed convergence, indicating strong low-level convergence, into the squall line area.

Upper-level wind reports and streamline analysis, superimposed on the corresponding infrared picture (Fig. 1E-7b), reveal that winds aloft turn anticyclonically over the squall line area and exhibit anticyclonic speed shear, producing upper-level divergence. Upper-level divergence combined with strong, low-level convergence are common aspects of most severe squall line developments.

The infrared picture also reveals the brilliant white tone of the squall line area, indicating the vertical extension of this feature to upper-levels. To the southwest, the squall line tapers to a point—a typical characteristic of intense squall lines. The tapered end is where new thunderstorms develop rapidly. Over land, such development is frequently accompanied by tornado activity occurring in many of the individual thunderstorm cells (Anderson *et al.*, 1974).

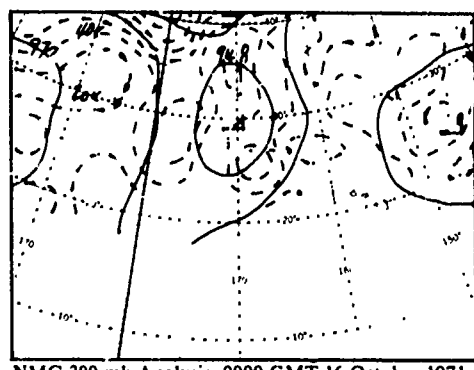
Important Conclusion

1. Cutoff lows are deep cyclonic circulations that may aid the development of squall lines along the asymptote of confluence in advance of the storm center.

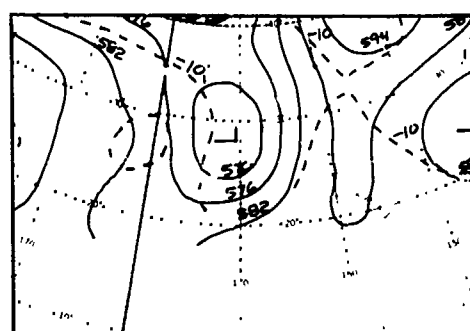
Reference

Anderson, R.K., *et al.*, 1974: Applications of meteorological satellite data in analysis and forecasting. ESSA Tech. Report NESR 51 (*including supplement, Nov. 1971, and Supplement No. 2, March 1973*), National Environmental Satellite Service, NOAA, Washington, D.C., 350 pp.

1. This particular storm system was the subject of a research film report by R.W. Fett, 1974: Upper Cold Lows and Cutoff Lows, North Pacific Ocean, WAB-371, under contract N66314-74-C-1208, *The Walter A. Bohan Company*, Park Ridge, Illinois.

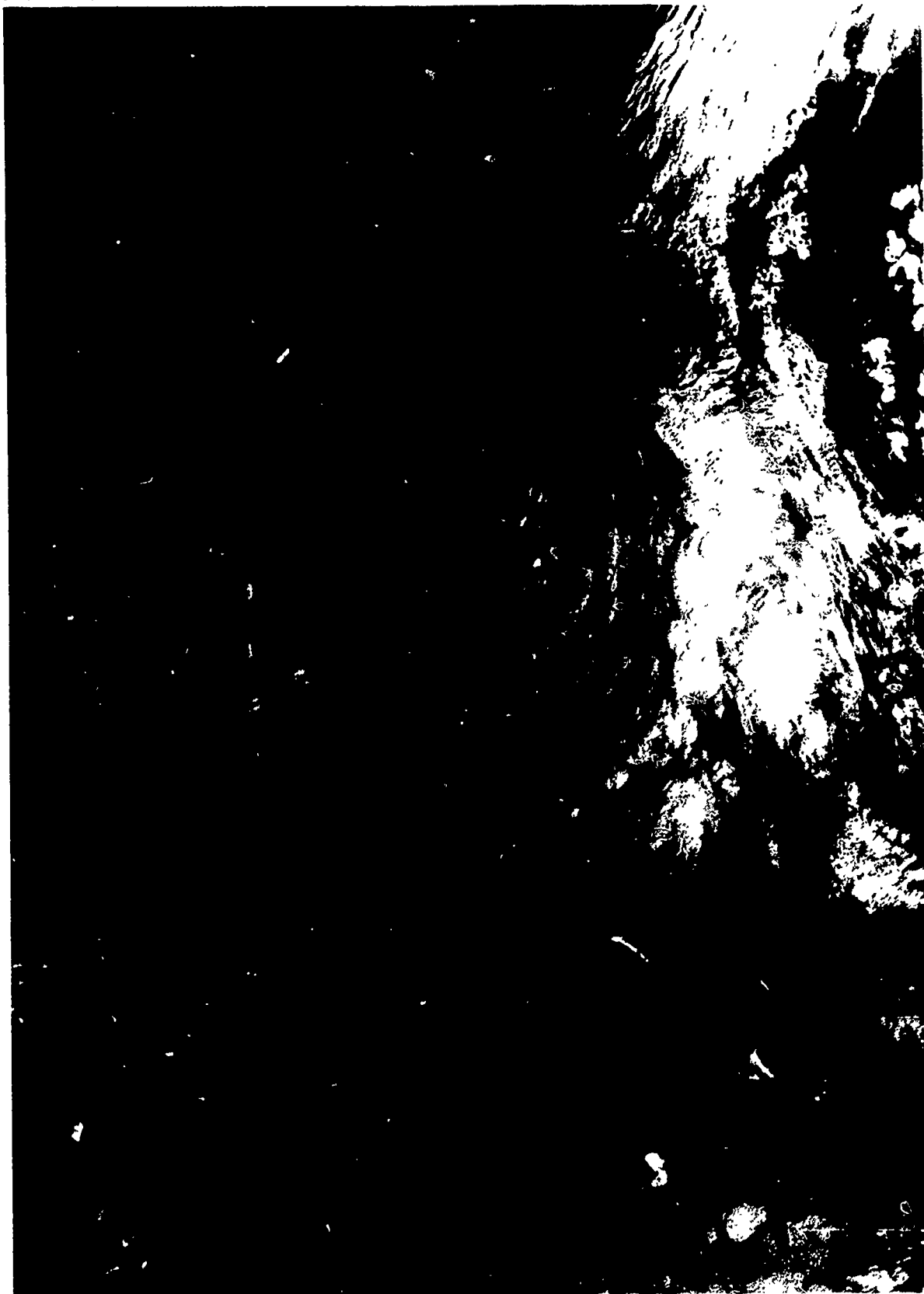


NMC 300 mb Analysis. 0000 GMT 16 October 1971.



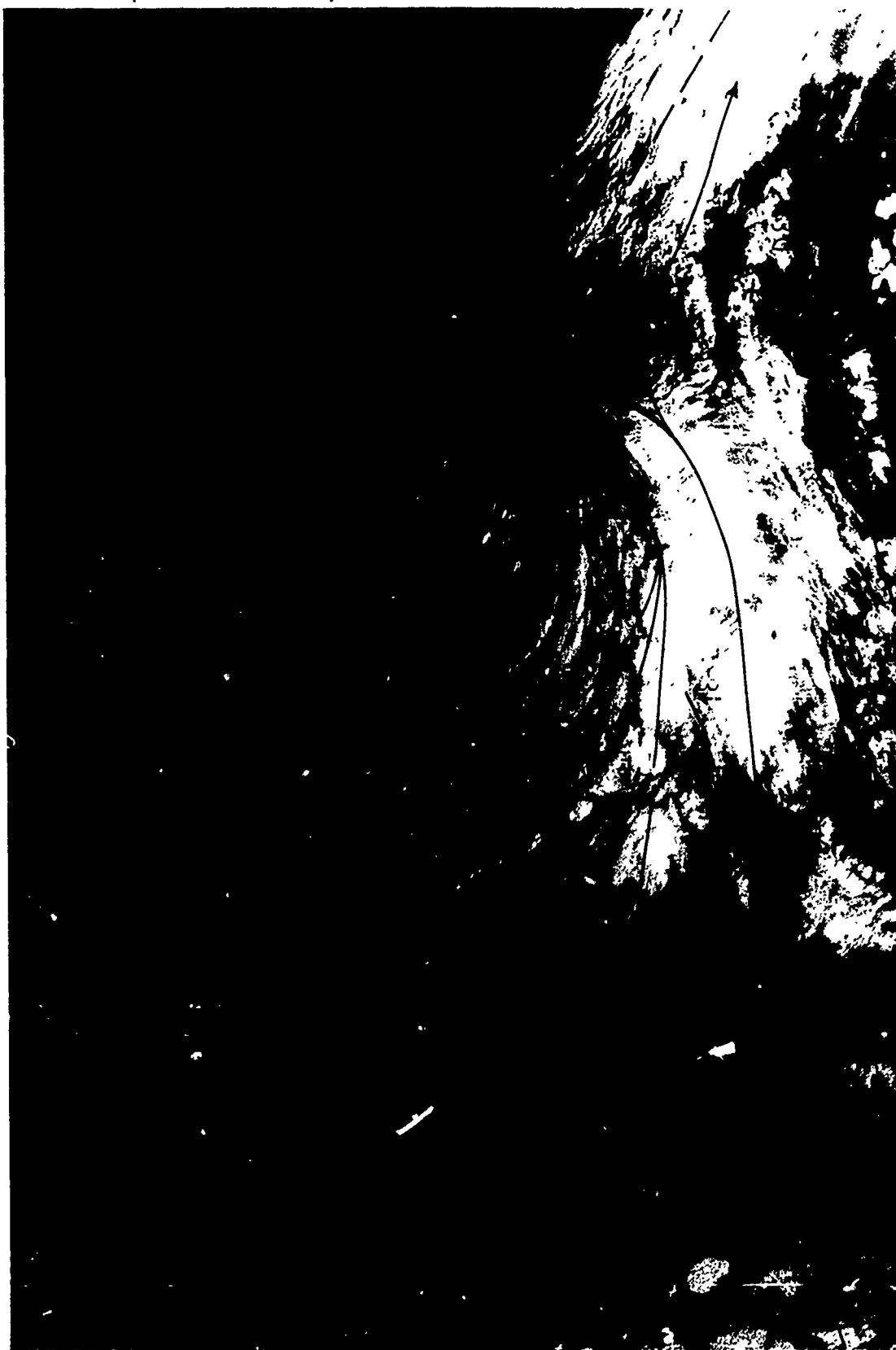
NMC 500 mb Analysis. 1200 GMT 16 October 1971.

1E-6a. FTV-34. DMSP VHR Low Enhancement. A Cutoff Low. 1901 GMT 15 October 1971.



1E-6

IE-7a FTV-34. DMSP VHR Low Enhancement. A Cutoff Low. 1901 GMT 15 October 1971
Surface Wind Reports and Streamline Analysis. 1800 GMT 15 October 1971.



IE-7b FTV-34
Upper-Level Win

IE-7b, FTV-34 DMSP IR Normal Enhancement A Cutoff Low 1901 GMT 15 October 1971
Upper-Level Wind Reports and Streamline Analysis 1800 GMT 15 October 1971

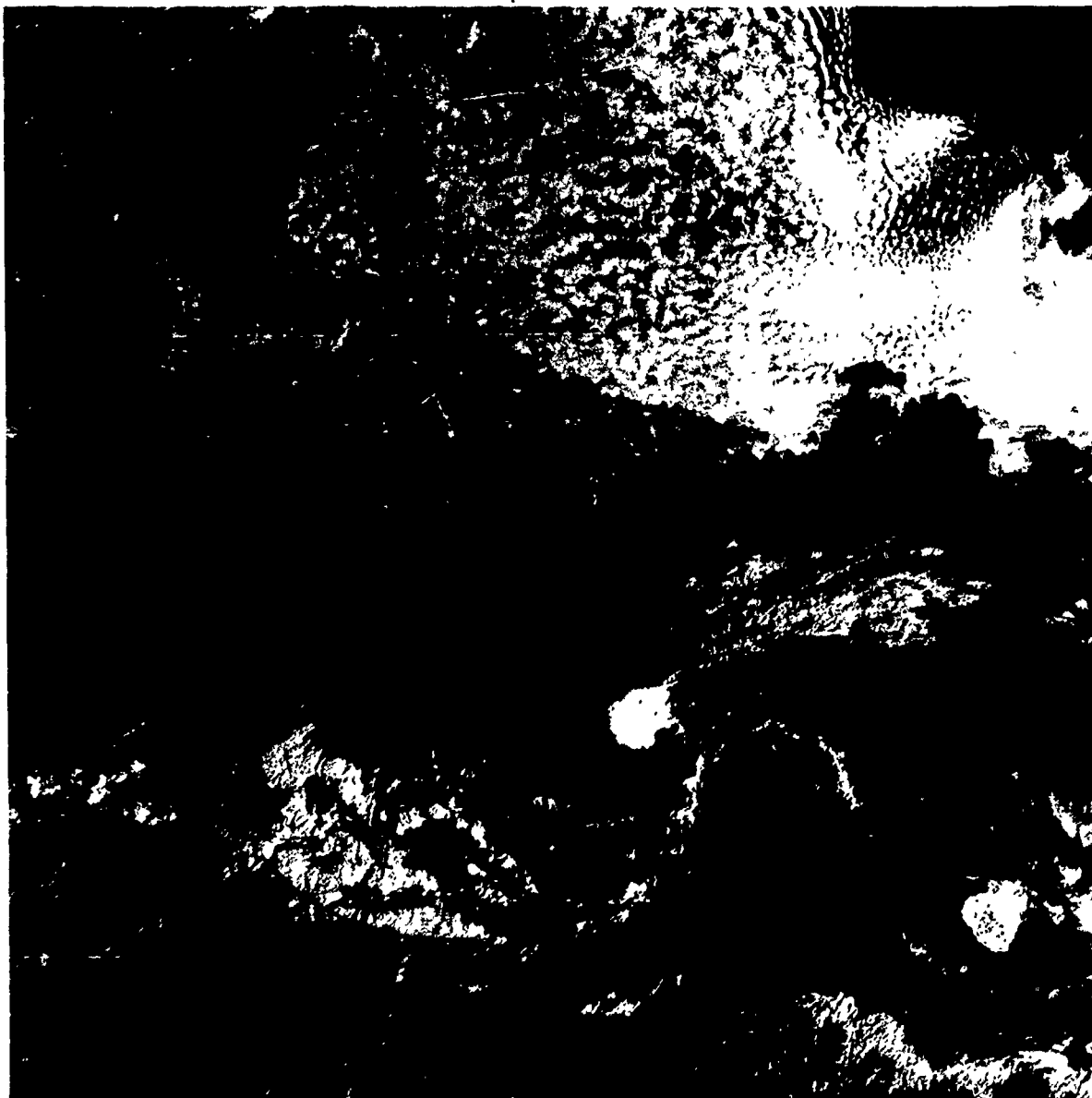


Case 4 Vortical Cloud Patterns

Weak tropical wave or "screaming eagle"—eastern North Pacific

In an early morning (0803 LST) DMSP pass over the eastern North Pacific (Fig. 1E-8a), two weak tropical waves can be observed. The wave furthest west (#1) has no well-defined center of circulation, but does have the characteristic inverted-V cloud pattern associated with such phenomena (Frank, 1969). Convective cloudiness and cumulonimbus activity is wide spread throughout this system. The following wave (#2, immediately to the east) does have a fairly well-defined circulation center suggested by the curved cloud lines and spiral cloud bands. The major weather associated with this system is limited to a small area of intense convection near the suggested center of circulation. Although the position of these two waves over the colder water west of 120°W makes it unlikely that they will develop further, such development cannot be ruled out since storms that occasionally strike the Hawaiian Islands originate in this area.

1E-8a FTV-26. DMSP VHR Low Enhancement. Weak Tropical Waves. 1603 GMT 3 October 1971.





IE-9a FTV-26, DMSP VHR Low Enhancement
Detail of Screaming Eagle Cloud Pattern
1603 GMT 3 October 1971

IE-9b. FTV-26 DMSP VHR Low Enhancement. Weak Tropical Waves. 1603 GMT 3 October 1971.
Low-Level Streamlines. 1800 GMT 3 October 1971.



The
circula
many
"screa
Fig. 11
pattern

An a
south
appear
and ca
which
anticyc
with e
inverte

A lo
reports
have fo
the tro
easterl
zonal c
istic of
classica

Import
1. We
pat
cha
the

Referenc
Fett, R.
Trop
No 1
Frank, N
Revie
Sadler, J
TIRC
Hawa

Low Enhancement.
Cloud Pattern.

71.



The broad "wing-like" cloudy pattern extending northeast from the circulation center of wave #2 is a distinctive and characteristic feature of many weak, non-developing tropical waves. This has prompted the term "screaming eagle" to be used in the designation of such phenomena. Fig. 1E-9a is a detail of wave #2 with the superimposed screaming eagle pattern.

An area of weak sunglint is also visible in Fig. 1E-8a, extending north-south along 115°W. Notice the dark gray shade within the sunglint that appears south of the apex of wave #2. This pattern indicates calm winds and calm seas. This observation is in agreement with empirical studies which indicate that this area is often an area of high pressure and/or anticyclonically turning flow. The vortex center and trough associated with each of these systems is located immediately to the west of the inverted-V apex (Fett, Nagle, Mitchell, 1973).

A low-level streamline analysis (Fig. 1E-9b), derived from ship reports and ATS-3 cloud motion vectors, reveals that these two systems have formed in a monsoon-like trough with southwesterly flow south of the trough, and easterly flow to the north. This is in contrast to classical easterly wave disturbances which form from perturbations in a basic zonal easterly flow. Monsoonal trough-type development is characteristic of easterly North Pacific disturbances (Sadler, 1963), although classical easterly wave developments have also been observed.

Important Conclusion

1. Weak tropical waves are often associated with vertical cloud patterns of curved cloud lines and spiral cloud bands and/or with a characteristic inverted-V cloud pattern which forms to the east of the disturbance center.

References

- Fett, R.W., R.E. Nagle, W.F. Mitchell, 1973: The Low Level Structure of Weak Tropical Waves, Environmental Prediction Research Facility, Technical Paper No. 3-73, Monterey, CA., 26 pp.
- Frank, N.L., 1969: The inverted-V cloud pattern--an easterly wave, *Monthly Weather Review*, 97, No. 2, 130-140.
- Sadler, J.C., 1963: Tropical Cyclones of the Eastern North Pacific as Revealed by TIROS Observations, Hawaii Institute of Geophysics Report No. 33, University of Hawaii, 39 pp.

Section 2

Local-Scale Atmospheric Phenomena and Effects

2A Land and Sea Breezes

Land and Sea Breeze Circulations	2A-1
Formation and Characteristics of Land and Sea Breeze Fronts.....	2A-2
Land and Sea Breeze Fronts as Observed in DMSP Imagery.....	2A-2

Case Studies

- 1 Intense land breeze front in a mountainous coastal region—Taiwan 2A-3
- 2 Land breeze fronts in a flat topography coastal region—Florida and Yucatan Peninsula 2A-6
- 3 Thunderstorms along sea breeze fronts and a line of thunderstorms produced by converging land breeze fronts—Malay Peninsula and Sumatra 2A-8

2B Valley-Ridge Circulations

Valley-Ridge Circulations and Cloud Formation	2B-1
Valley-Ridge Circulation Systems	2B-2

Case Studies

- 1 Convective cloudiness patterns in organized valley-ridge circulation systems—North Vietnam 2B-4
- 2 Fog patterns in mountainous terrain—Southeast Asia 2B-6

2C Fog, Haze, and Air Pollution

Detection of Fog, Haze, and Air Pollution in DMSP Imagery	2C-1
--	------

Case Studies

- 1 Faint anomalous gray shades associated with haze and fog over water—U.S. West Coast 2C-2
- 2 Band of fog and haze over land—U.S. Central Plains 2C-4
- 3 Appearance of fog, haze, and air pollution over land in moonlight areas—Central U.S. 2C-6
- 4 Smoke plumes over water—Gulf of Mexico 2C-8
- 5 Advection-radiation fog in nighttime infrared imagery—U.S. Gulf Coast Region 2C-10

2D Severe Weather

Severe Weather Detection and Tracking 2D-1

Case Studies

- 1 Severe thunderstorms ahead of a short-wave trough over open water—Central Mediterranean Sea 2D-2
- 2 Isolated severe thunderstorm—U.S. Central Plains 2D-4

2E Air-Sea Interaction

Effects of Air-Sea Interactions on Local-Scale Phenomena 2E-1

Case Studies

- 1 Marine haze formation over cold coastal upwelled water..... 2E-2
- 2 Identification of local sea state in sunglint areas where upwelling, cold eddies, or warm eddies are present 2E-4
- 3 Anomalous gray shade patterns produced offshore in cold, continental air outbreaks—Sea of Japan adjacent to the Asiatic Continent 2E-6
- 4 Anomalous gray shade patterns produced offshore by strong, cold winds funneling through gaps in mountainous coastal terrain—Gulf of Tehuantepec 2E-8
- 5 Formation of convective cloud lines along oceanic fronts—The Gulf Stream..... 2E-12
- 6 Detection of shallow water cooling areas—Bahama Banks..... 2E-14

2A Land and Sea Breezes

Land and Sea Breeze Circulations

In coastal areas, land and sea breeze circulations develop as a result of the differential heating and cooling of the land and water surfaces. Once the land or sea breeze circulation has formed, factors such as the land-sea temperature difference, the prevailing gradient wind flow, and local topography influence the strength and evolution of the circulation.

Formation and Characteristics of Land and Sea Breeze Fronts

At nighttime, under clear skies and calm winds, the land cools more rapidly than the adjacent sea. Over the land, the pressure aloft falls in response to the contraction of the air columns at lower levels. This produces a pressure gradient aloft from sea to land, and a landward movement of the air aloft begins. The pressure at lower levels over the land then rises, and a seaward movement of the surface air results. In this way, the land breeze circulation cell is established.

The contrast between the cool air that moves seaward and the warmer maritime air offshore, creates a mesoscale frontal boundary at the leading edge of the land breeze, which is referred to as the land breeze front. Convective cloud lines and thunderstorms may develop along this frontal boundary. Fig. 2A-2a is a schematic illustrating the major features of the land breeze circulation cell.

As daytime heating begins, a reversal of the flow pattern described above occurs and the sea breeze circulation cell is established. In the sea breeze circulation, warmer air over the land rises and is replaced by cooler, denser air from over the water (Fig. 2A-2b). Features of this flow regime include the development of convective cloud lines and thunderstorms in areas of convergence along the sea breeze frontal boundary inshore, and the absence of convective cloudiness along and off the coastline in the area of the subsiding return flow aloft.

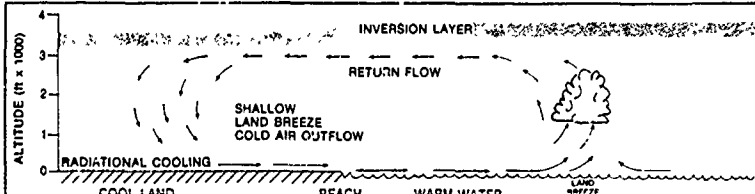
Land and Sea Breezes as Observed in DMSP Imagery

DMSP satellite imagery provides a unique set of observations for detecting and assessing the effects of land and sea breeze circulations — effects which are more difficult to ascertain in conventional data. For example, the location, extent, and intensity of the land and sea breeze fronts can be determined from observations of cloud forms and, in particular, convective cloud lines that form along these fronts. Sea state may be inferred when these areas are illuminated by sunglint. In the case of the sea breeze circulation, air in the subsiding branch of the return flow offshore warms adiabatically, and in doing so, stabilizes the low-level lapse rate. The warming process dissipates haze droplets and improves low-level visibility, and these changes in haze droplet concentration may appear as a gray shade difference in the imagery. In addition, the stable lapse rate over the water, with warm, dry air aloft and cool, moist air near the surface, is a condition favorable for anomalous propagation of radio and radar signals (Meyer, 1971).

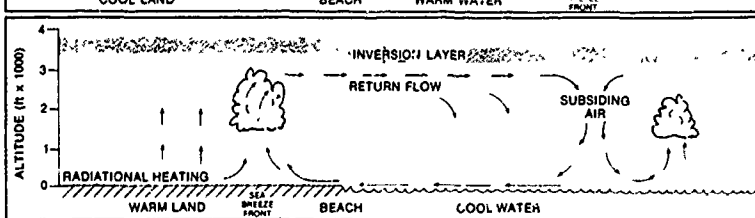
Reference

Meyer, J.H., 1971: Radar observations of land breeze fronts. *J. of Appl. Meteor.*, **10**, 1224-1232.

2A-2a. Major Features of the Land Breeze Circulation Cell.



2A-2b. Major Features of the Sea Breeze Circulation Cell.



Case 1 Land and Sea Breezes

Intense land breeze front in a mountainous coastal region— Taiwan

Some of the most intense land breeze fronts are observed in mountainous coastal regions. After sunset, under clear sky conditions, the air at higher elevations cools and drains to lower levels. Along the way, the normal land breeze is intensified by the downslope winds caused by this radiational cooling effect. If the slopes are steep, the wind gains a "fall" velocity which not only strengthens the land breeze but also produces gusty, surface wind conditions. When the prevailing gradient flow is onshore, intense convective activity may form out to sea in the convergent area along the land breeze frontal position.

A Landsat montage of Taiwan (Fig. 2A-3a) clearly reveals the mountainous terrain extending from north to south along the eastern half of the island. Mountain elevations exceed 3000 m (10,000 ft) in this area. Although clouds obscure the eastern shoreline, the mountains slope sharply down to the sea in that area.

2A-3a. Landsat
Montage of Taiwan.
MSS-6.
1555 GMT
30 January 1973.



By
iness a
terran
slopes
nimbu
ished
almost

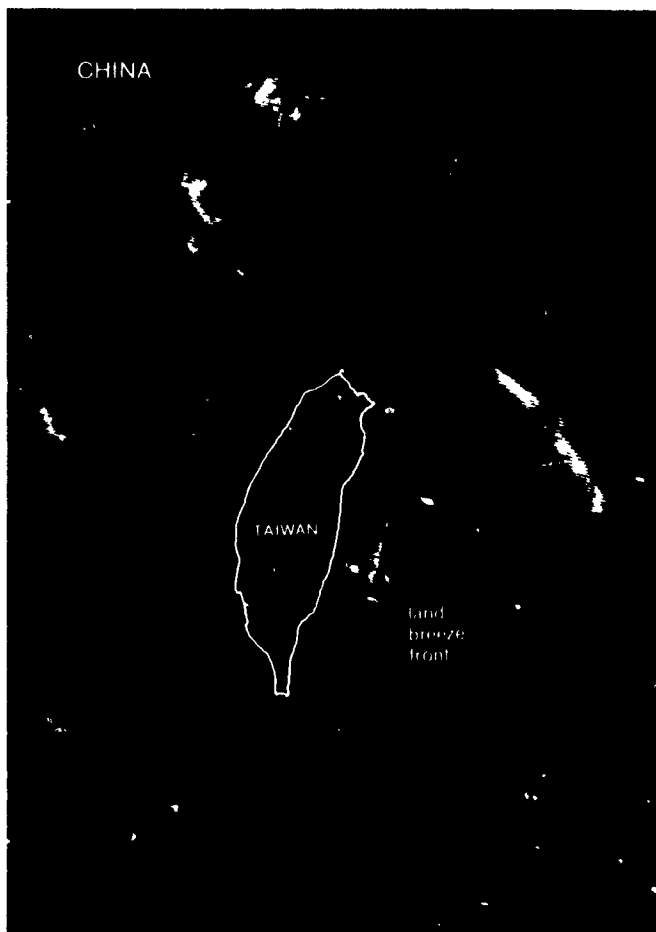
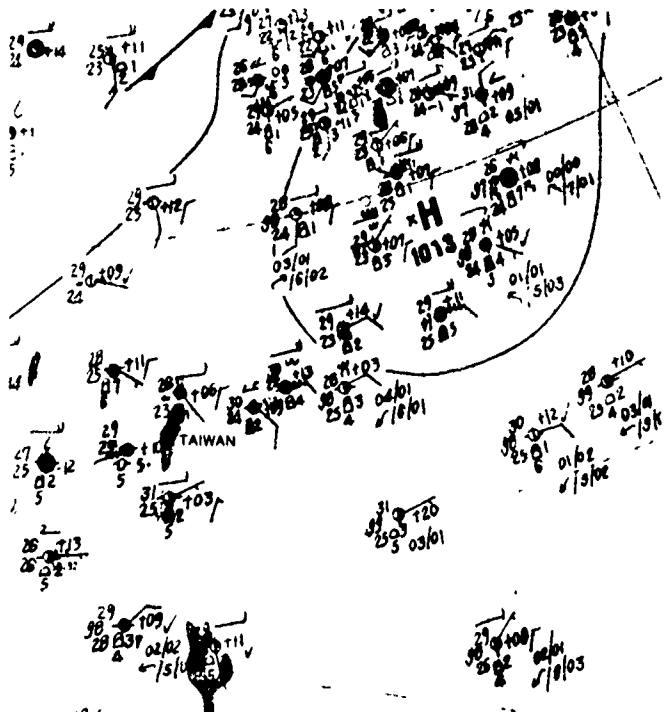
Tow
activi
region
island
guished
Over n
storm
bright

By
has al
Some l
west co
iness ju
to dete
formed
a conv
breeze.

An excellent example of the land breeze front, showing intense convective activity, is illustrated in the following series of enlarged DMSP views over Taiwan. The picture sequence covers a 32-hour period, for the full life cycle of a land breeze event.

The first view of a developing land breeze front is shown in a DMSP HR nighttime visible picture (Fig. 2A-4a). At this time, 0001 LST 3 August (1601 GMT 2 August), the land breeze front location is identified by a weak convective cloud line which begins at the southern tip of Taiwan, extends offshore (approximately 50 km) parallel to the eastern shore, and disappears in the cloudiness at the north tip of the island.

In the early morning view of this area about nine hours later (Fig. 2A-4b), the land breeze front has intensified considerably and is located further offshore. A surface analysis near this time (page 2A-4) shows light easterly flow and a weak high pressure area dominating the region. The picture reveals that numerous cumulonimbus have developed along the front, with some anvil cirrus plumes extending far out to sea as a result of northwesterly flow aloft. Isolated cumulonimbus also appear northeast of the island in an extension to the land breeze front. These cells may have originally formed offshore and then drifted north during the course of the morning, advected by the prevailing flow.



2A-4a. FTV-31. Enlarged View. DMSP HR Low Enhancement.
Land Breeze Front, Formative Stage
1601 GMT 2 August 1974.



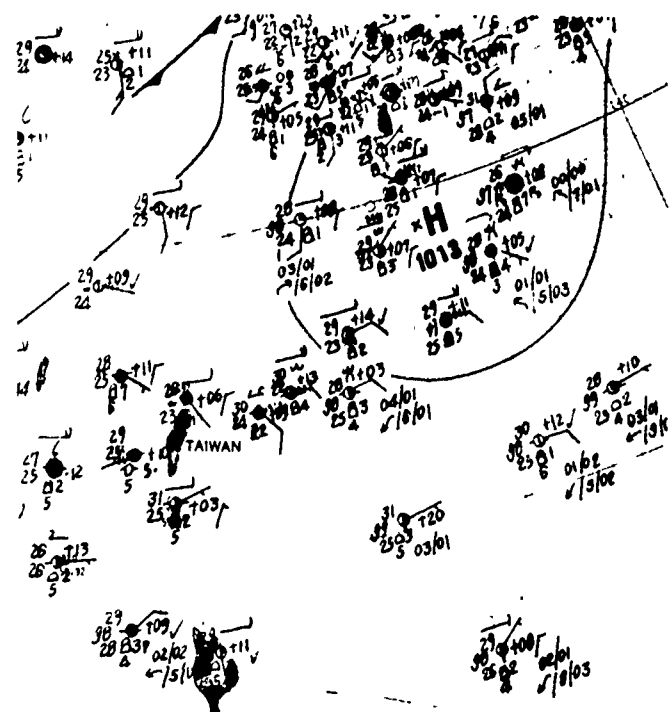
2A-4b. FTV-29. Enlarged View. DMSP VHR Low Enhancement.
Land Breeze Front, Intense Convective Activity.
0045 GMT 3 August 1974.

2A-4c. F
Land Br
0300 GM

front, showing
following series
picture sequence
of a land breeze

front is shown in
2A-4a). At this
gust), the land
convective cloud
Taiwan, extends
the eastern shore,
tip of the island.

out nine hours
has intensified
more. A surface
light easterly flow
the region. The
have developed
extending far
aloft. Isolated
the island in an
cells may have
forth during the
prevailing flow.



Surface Analysis. 0000 GMT 3 August 1974.

By mid-morning (Fig. 2A-4c), diurnal convective cloudiness appears along the highest elevations of the mountainous terrain. This indicates a reversal of flow on the mountain slopes, and signals the end of the land breeze regime. Cumulonimbus development along the land breeze front has diminished considerably, and the cells north of the island have almost completely dissipated.

Toward early evening (Fig. 2A-5a), the diurnal convective activity has reached its maximum over the mountainous region of the island. Some individual cumulonimbus clusters can be distinguished along the western edge of the convective cloud area. Over mainland China a lightning flash from a large thunderstorm can be observed. Taipei can be readily identified from a bright spot produced by the city lights.

By midnight (Fig. 2A-5b), the diurnal convective activity has almost ceased over the mountainous region of the island. Some local convective cloudiness, however, remains along the west coastline. The absence of organized convective cloudiness just offshore, to the east of the island, makes it difficult to determine whether or not a land breeze circulation has formed at this time, in contrast to the previous morning, when a convective cloud line indicated the presence of a land breeze. Extensive cloudiness covering the island during much



2A-4b. FTV-29. Enlarged View. DMSP VHR Low Enhancement.
Land Breeze Front, Intense Convective Activity.
0045 GMT 3 August 1974.



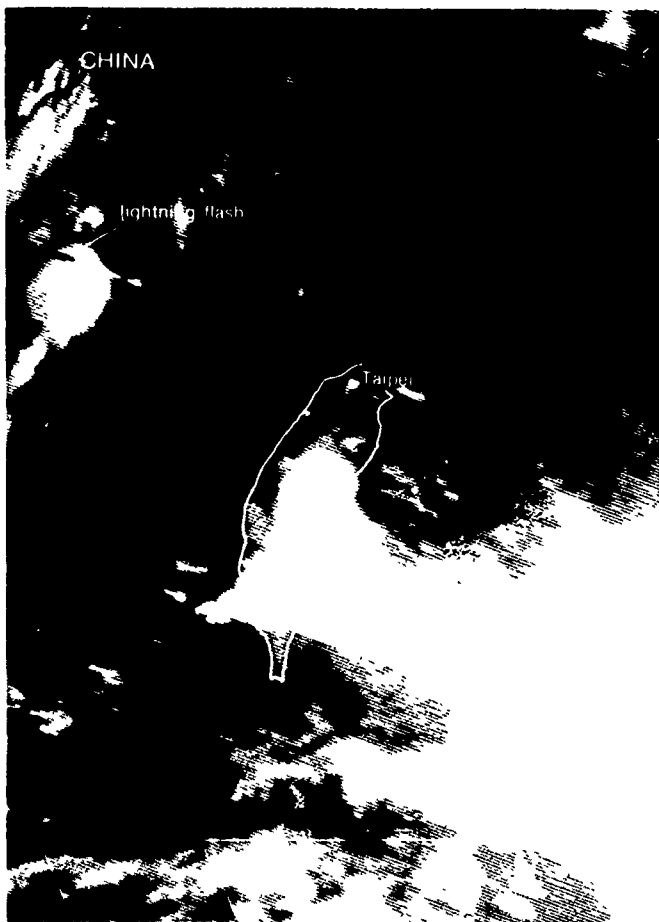
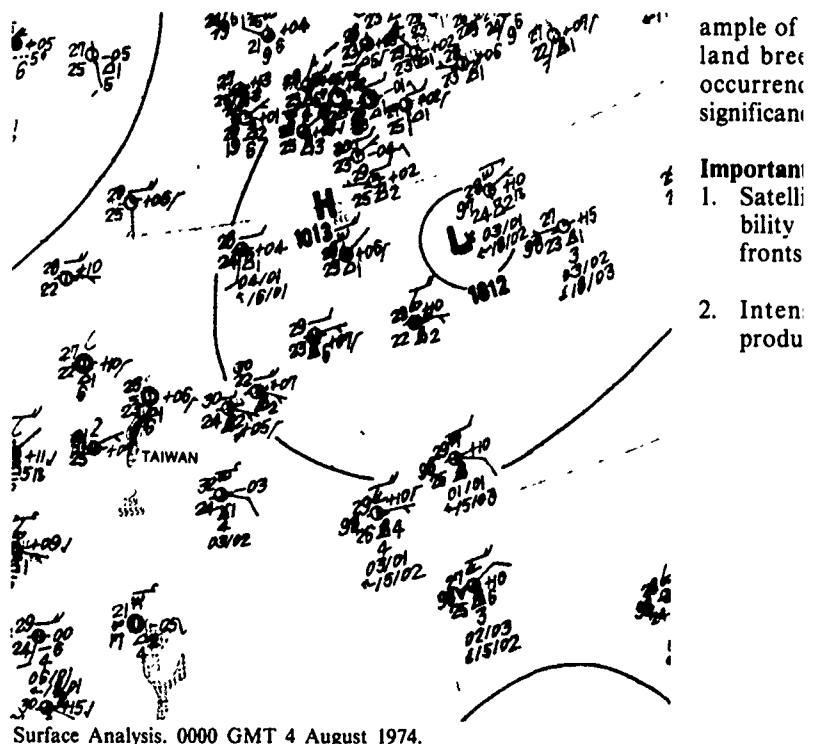
2A-4c. FTV-31. Enlarged View. DMSP VHR Low Enhancement.
Land Breeze Front, Dissipating Stage.
0300 GMT 3 August 1974.

of the nighttime hours, would be expected to reduce the radiational cooling effect normal under clear sky conditions, so that an intense land breeze front would not be anticipated.

The early morning DMSP pass on 4 August (Fig. 2A-5c) shows a clear view of the island and the mountainous terrain along the east coast. Another land breeze front, showing convective activity, has formed off the northeast coastline. However, it is weak compared to the intense land breeze front that formed off the east coast on the previous day. The surface analysis (page 2A-5) shows that light easterly winds and high pressure continue to dominate the area. To the southwest, the convection along the front disappears. However, a thin convective cloud line, off the southern tip of the island, suggests the presence of weak land breeze frontal convergence.

A weak land breeze front can also be detected off the western coastline on this date. The presence of such a feature indicates very weak flow over the area. This observation is verified by the surface analysis, valid very close to the time of the DMSP image. Note that the position of the land breeze front to the north of the cloud line can be inferred from changes in the gray shade pattern.

In summary, this DMSP sequence has provided an ex-



2A-5a. FTV-29. Enlarged View. DMSP HR Low Enhancement. Convective Activity Over Mountainous Terrain. 1327 GMT 3 August 1974.



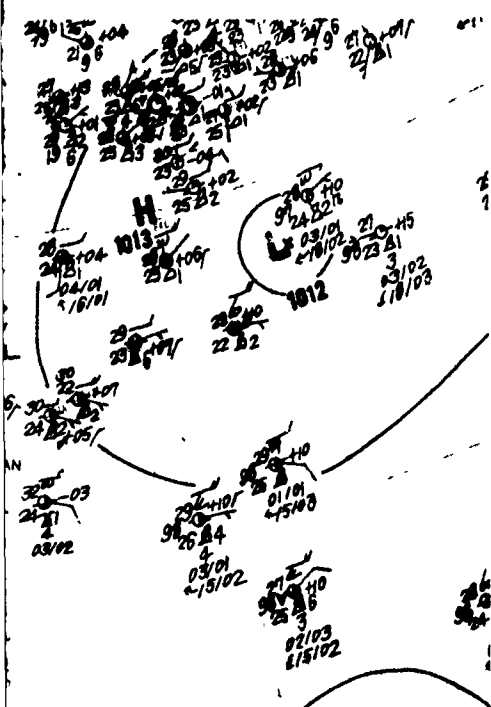
2A-5b. FTV-31. Enlarged View. DMSP HR Low Enhancement. Dissipating Convective Activity Over Mountainous Terrain. 1542 GMT 3 August 1974.

ample of
land breez
occurrence
significan

- Important
1. Satelli
bility
fronts
2. Inten
produ



2A-5c. FTV
Land Breez
0027 GMT

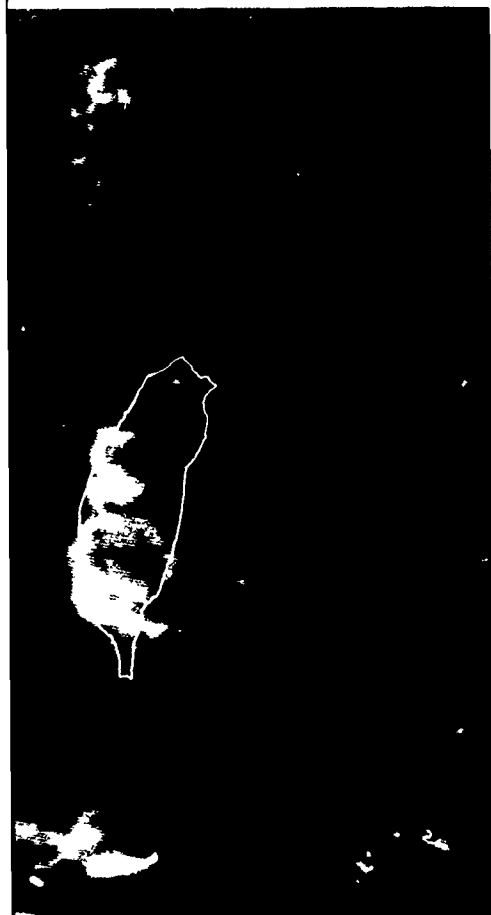


0000 GMT 4 August 1974.

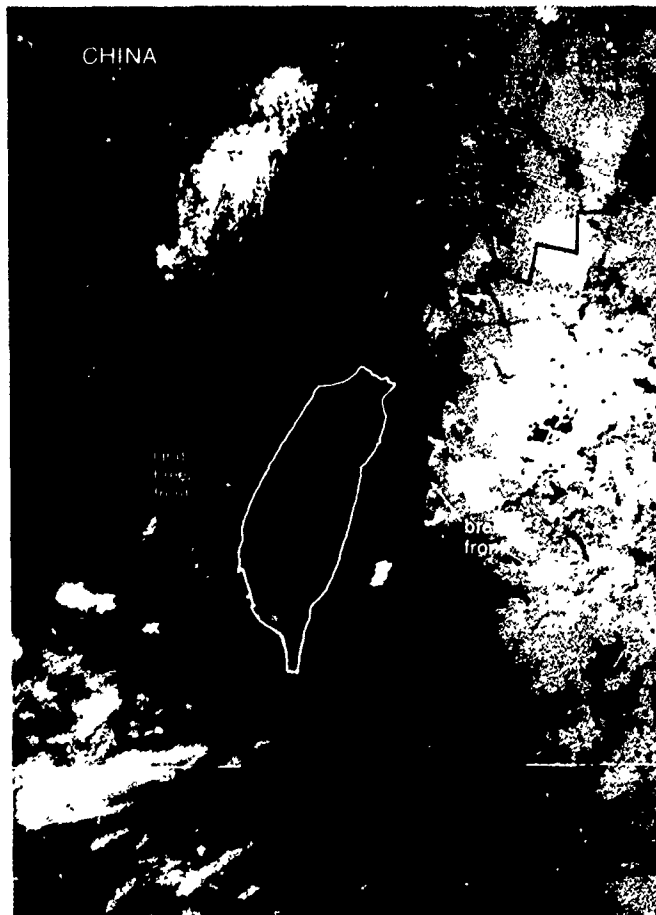
ample of the formation, development, and dissipation of a land breeze front, with intense convective activity. The occurrence of such local-scale phenomena can be of major significance to offshore and land terminal operations.

Important Conclusions

1. Satellite data are of unique importance in terms of capability to detect and monitor the evolution of land breeze fronts.
2. Intense land breeze fronts can be significant weather producers over relatively large areas.



2A-5a. FTV-29. Enlarged View. DMSP HR Low Enhancement.
Convective Activity Over Mountainous Terrain.
0027 GMT 4 August 1974.



2A-5c. FTV-29. Enlarged View. DMSP VHR Low Enhancement.
Land Breeze Front, Formative Stage.
0027 GMT 4 August 1974.

Case 2 Land and Sea Breezes

Land breeze fronts in a flat topography coastal region— Florida and Yucatan Peninsula

Land breeze frontal convective cloud lines are observed, in many instances, paralleling coastlines. The presence of such convective cloud lines indicates that low-level convergence is occurring between the land breeze and the prevailing flow over the water surface. The intensity of the convective activity depends on the strength of the low-level convergence along the land breeze front.

Fig. 2A-7a is a DMSP LS nighttime visible picture of the Gulf of Mexico and surrounding land areas. Numerous bright spots, produced by city lights, appear over the land areas. Some of the larger metropolitan areas can be readily identified. A distinct land breeze frontal cloud line is observed off the west coast of Florida, extending from near Key West to Apalachicola. The location of the cloud line ranges from 80 to 160 km off the coast. Isolated cumulonimbus, with cirrus anvils, can be discerned in the convective cloud line. This implies strong, low-level convergence along the frontal boundary.

A less distinct land breeze front is observed north of Yucatan. The absence of cumulus congestus and cumulonimbus activity along the frontal boundary indicates weak low-level convergence, resulting in a lesser developed land breeze cloud line.

During the winter months, the shallow coastal waters off the west coast of Florida, and many other continental areas, become much colder than the deeper waters offshore, producing a thermal boundary offshore. Convective cloud lines may form along the warm side of this boundary, due to low-level flow convergence effects (see Sec. 2E, Case 2). Since convective cloud lines may form along oceanic thermal boundaries in areas where land breeze frontal cloud lines may also be expected, it is necessary to take into account air-sea interaction effects so as not to misinterpret the satellite data and the actual cause for the observed phenomenon.

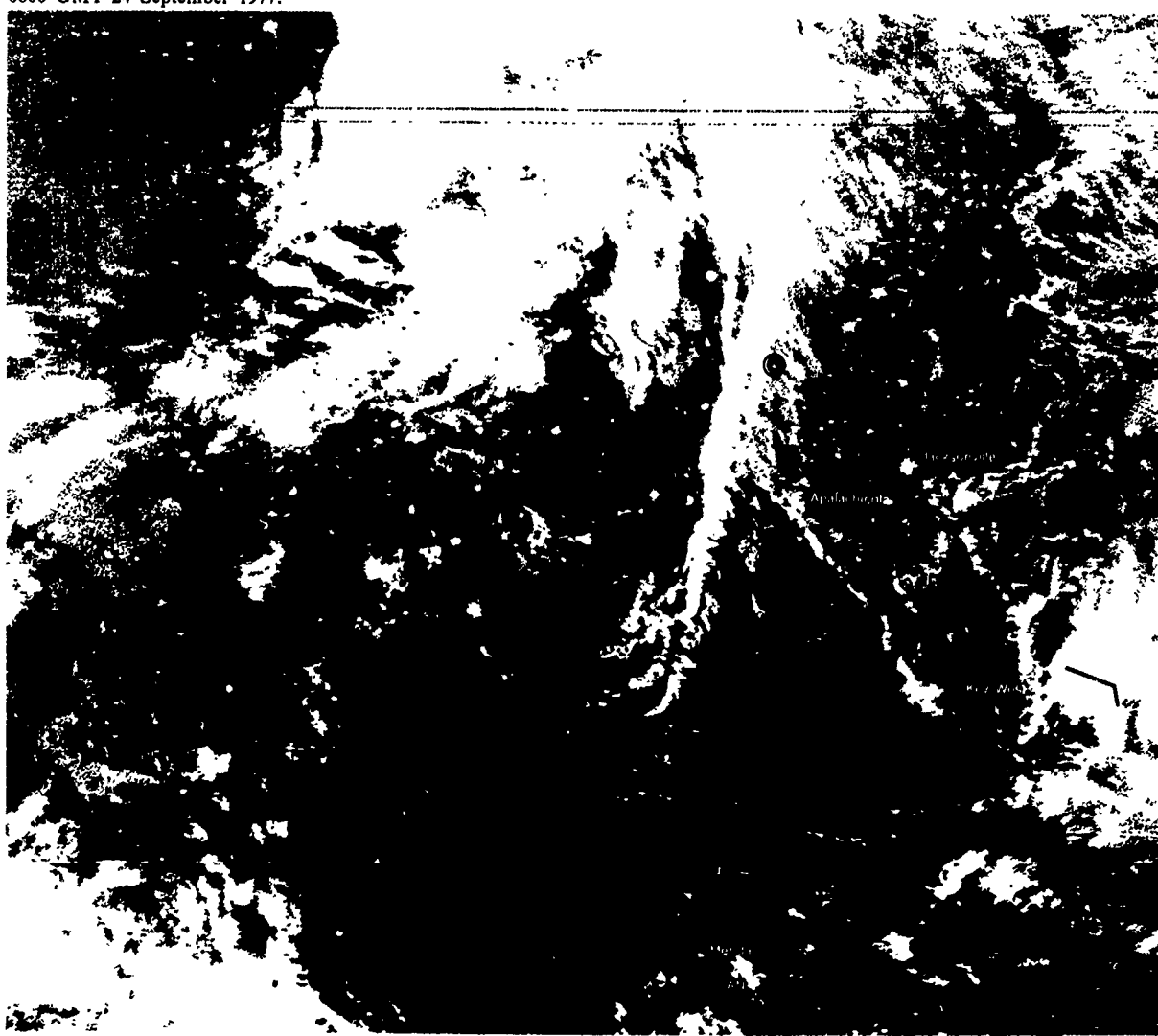
2A-7a. FTV-35. DMSP LS Low Enhancement.

Land Breeze Frontal Cloud Lines.

0558 GMT 24 September 1977.

Surface Wind Reports and Streamline Analysis.

0600 GMT 24 September 1977.



Case 3 Land and Sea Breezes

Thunderstorms along sea breeze fronts and a line of thunderstorms produced by converging land breeze fronts—Malay Peninsula and Sumatra

Fig. 2A-8a is a DMSP VHR view, shortly after local noon, of the Malay Peninsula, showing the intrusion of sea breeze fronts on both sides of the peninsula. The sea breeze fronts are identified by discontinuous lines of cumulus clouds, a short distance inland, extending north from Singapore along both coastlines.

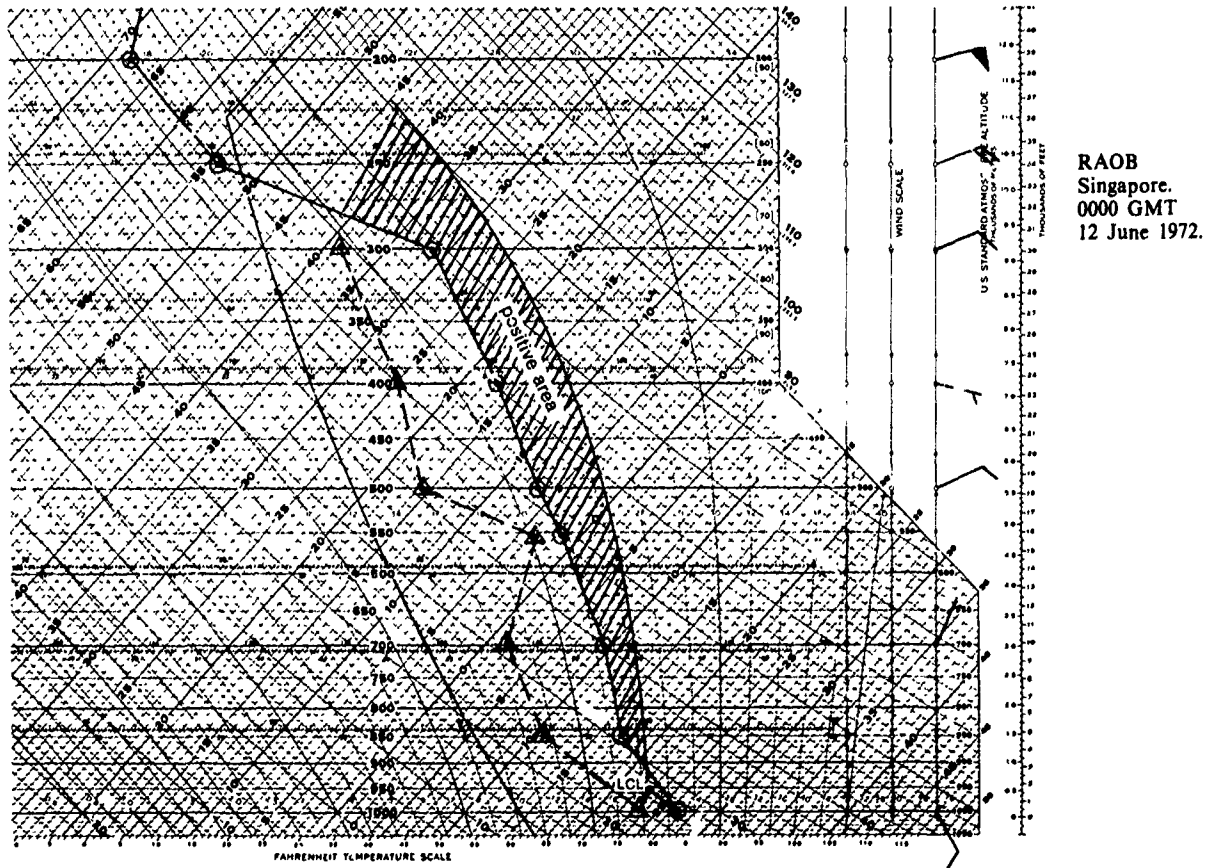


2A-8a. FTV-28. DMSP VHR Low Enhancement. Thunderstorms along Sea Breeze Fronts and Converging Land Breeze Fronts. 0551 GMT 12 June 1972.

In the vicinity of Singapore, some of the cumulus along the sea breeze fronts have developed into cumulonimbus with cirrus anvil tops streaming to the west. The early morning Singapore RAOB (below) shows a low, lifting condensation level (LCL) at about 960 mb, and a large positive energy area—conditions favorable for convective storm development. The sounding also shows strong vertical shear near the 200 mb level in the easterly winds aloft, which accounts for the anvil cirrus streaming to the west from the cumulonimbus.

A line of thunderstorms is also observed over the Strait of Malacca, between the Malay Peninsula and Sumatra, and the cloud line appears to parallel the coastline of the Malay Peninsula. Surface charts (not shown) at 0700 LST (5 hrs before picture time) and 1900 LST (7 hrs after picture time) report calm winds under a ridge of high pressure over the Strait of Malacca and the Malay Peninsula, and light southerly flow towards the strait from Sumatra. Short, narrow, cumulus cloud lines over central and eastern Sumatra confirm the light, low-level southerly flow.

The line of thunderstorms in the Strait of Malacca appears to have been produced by convergence in the low-level flow of land breeze circulations from the Malay Peninsula and Sumatra meeting over the Strait of Malacca. Elevations along the northeast coast of Sumatra range from 7100 to 9300 ft, rising abruptly from the sea. Although there is a flat coastal region along the western shore of the Malay Peninsula, the terrain rises rapidly to over 7000 ft about 80 n mi inland. Local land breeze circulations during the previous night from both shores would be strengthened by downslope winds from the high coastal terrain and since the terrain over Sumatra is much higher and nearer the coastline, the land breeze would be stronger and the line of thunderstorms formed closer to the Malay Peninsula coastline.



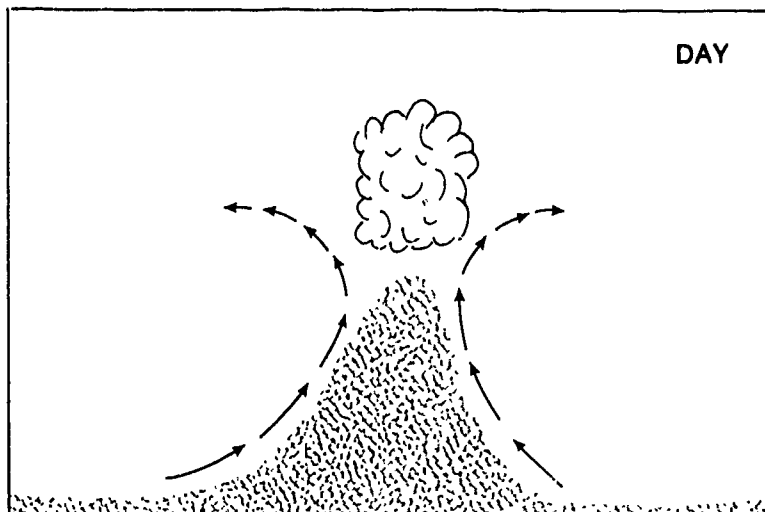
2B Valley-Ridge Circulations

Valley-Ridge Circulations and Cloud Formation

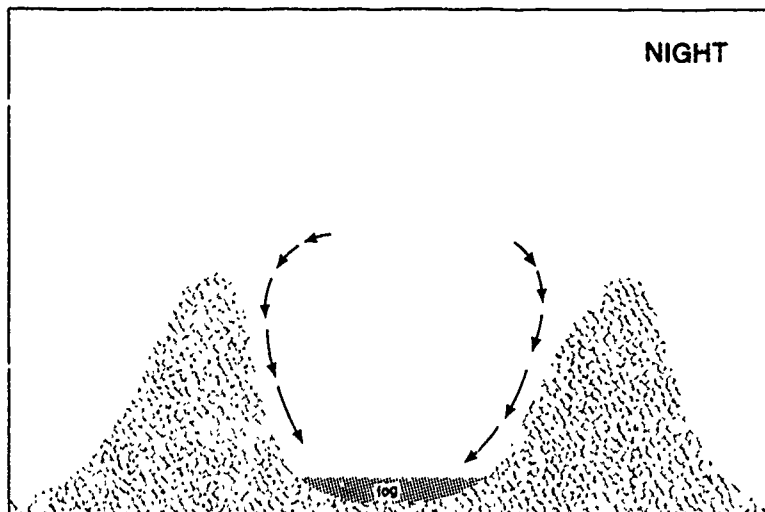
Differential heating and cooling of air over mountainous terrain results in local wind circulations. During the day, winds generally flow upslope and convective cloudiness tends to form along the peaks and ridge lines. At night, the winds flow downslope, the ridge lines become clear, and colder air accumulates in the valleys where fog may form. The convective cloudiness or fog patterns that form under these circulation systems can be observed in satellite imagery and related, in detailed topographical charts, to specific locations. As a result, the data can be used for accurate "pin-point" assessment and prediction of weather over target and terminal areas.

Valley-Ridge Circulation Systems

At sunrise, the tops of mountains and upper slopes are heated first. This differential heating at the top of the mountain causes air to rise and a circulation to develop such that air begins to move upslope. As the lower slopes are also heated a general upslope wind develops. A compensating current forms near the mountain tops and descends over the valley (Fig. 2B-2a). The upslope motion of air favors convective cloud development above the ridges, while subsiding motion suppresses cloud development over the valleys.



2B-2a. Upslope Circulation and Convective Cloud Formation.



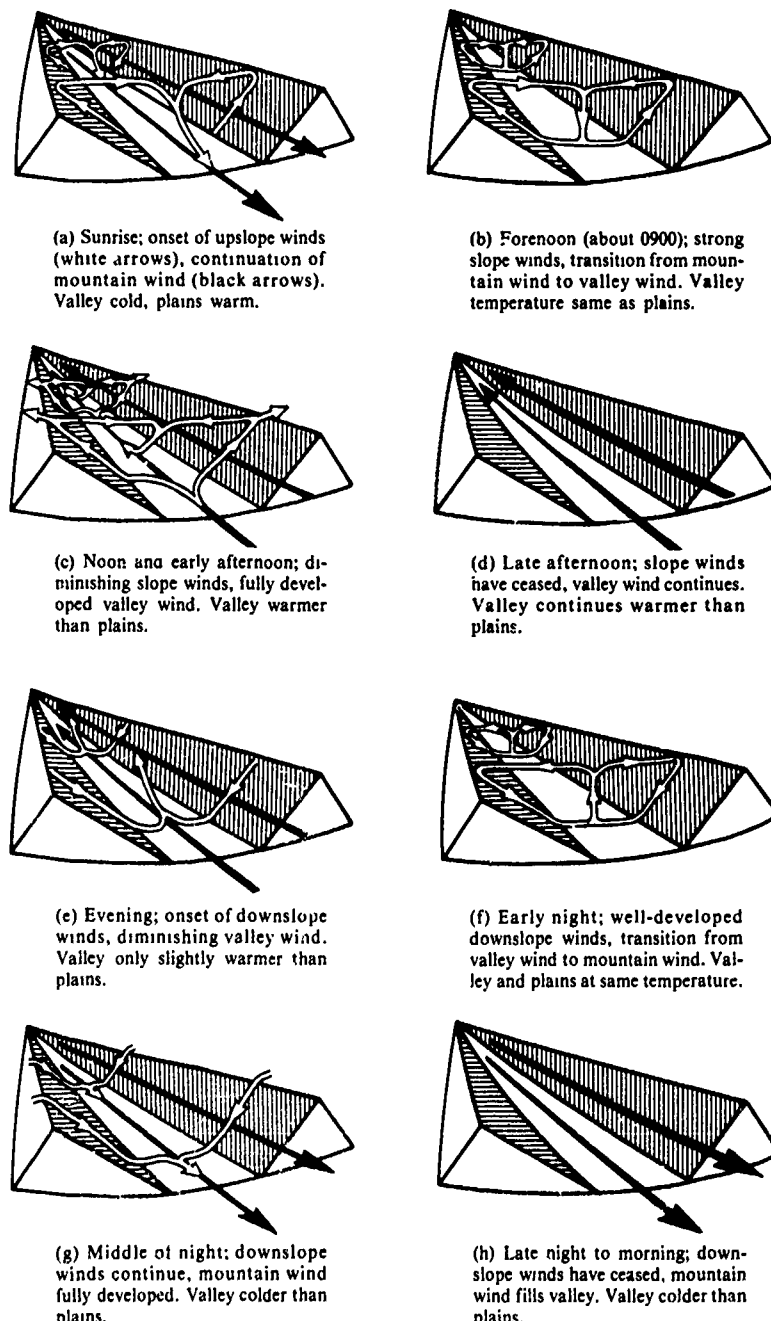
2B-2b. Downslope Circulation and Fog Formation.

After sunset, the air along the slopes is cooled by radiation, becomes more dense than the air over the valley, and begins to drain down the mountain sides. As the radiational cooling continues, a general downslope wind develops (Fig. 2B-2b). Later, fog may form in the cool air which has accumulated in the valley.

A typical valley has slopes on two sides and, in addition, may also slope from higher to lower elevations. Slope winds are also produced by differential heating and cooling effects along the axis of the valley. A strong up-valley, or mountain wind (toward higher elevations), may develop during the late afternoon, while a strong down-valley, or valley wind (toward lower elevations), may develop during the late night (Defant, 1951). The interaction of the mountain and valley wind systems with the upslope and downslope wind fields discussed above is illustrated below.

Reference

Defant, F., 1951: Local Winds. *Compendium of Meteorology*, Amer. Meteor. Soc., Boston, pp. 655-672.



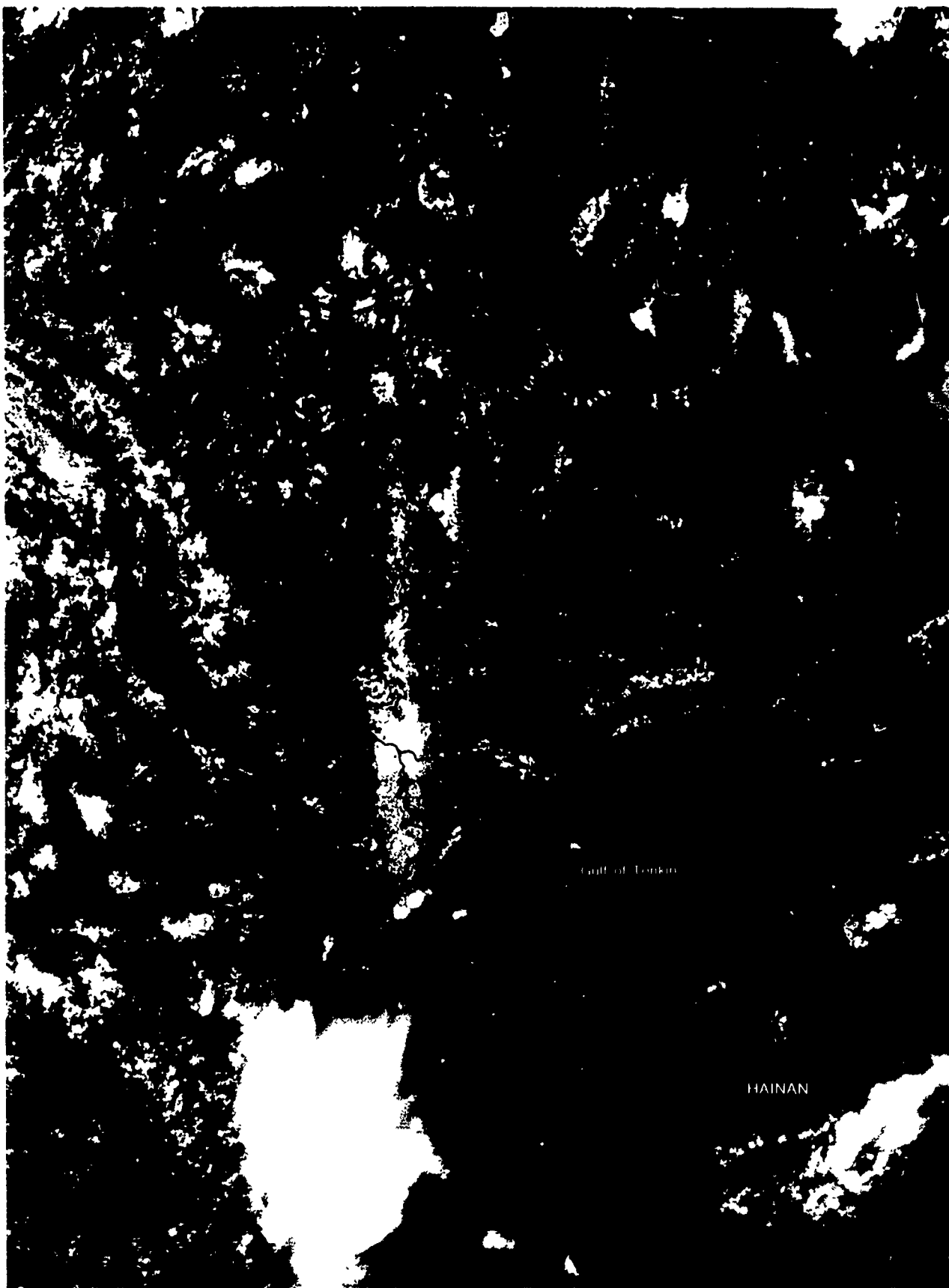
Case 1 Valley-Ridge Circulations

Convective cloudiness patterns in organized valley-ridge circulation systems—North Vietnam

Organized valley-ridge circulation systems are best developed under conditions of weak, undisturbed synoptic-scale flow. Such a condition existed over North Vietnam on 7 June 1973. The DMSP visible picture for 1200 LST (Fig. 2B-4a), shows convective cloud areas which, at first glance, may seem to be randomly distributed. However, when an enlarged view of this region (Fig. 2B-5a) is compared with a good topographic map, it is apparent that the cloud covered areas appear over ridges or areas of higher elevation, and that clear areas appear over valleys or areas of low elevation.



2B-4a. FTV-28, DMSP VHR Low Enhancement. Convective Cloudiness in Organized Mountain Valley-Ridge Circulation Systems.
0500 GMT 7 June 1973.



2B-5a. FTV-28. Enlarged View. DMSP VHR Low Enhancement. Convective Cloudiness Conforming to High Terrain Contours.
0500 GMT 7 June 1973.

2B 5

2B-5
High

A
revo
elev
from
but
Thu
pred
mac

Imp
1.



ng to High Terrain Contours.



2B-5b. FTV-28. Enlarged View. DMSP VHR Low Enhancement. Convective Cloudiness conforming to High Terrain Contours. 0522 GMT 2 June 1972.

A DMSP picture over the same area about a year earlier (Fig. 2B-5b) reveals an almost identical cloud distribution pattern over the higher elevations between the Red River and Black River. It may be concluded from these examples that the cloudiness is not randomly distributed, but strongly reflects the valley-ridge circulation system in the area. Thus, under these meteorological conditions, the weather becomes very predictable, which permits individual target and terminal forecasts to be made with great precision.

Important Conclusion

1. Under conditions of weak synoptic-scale flow, convective cloudiness over mountainous regions conforms to high terrain contours, and reflects the valley-ridge circulation system in the area.

Case 2 Valley-Ridge Circulations

Fog patterns in mountainous terrain—Southeast Asia

At night, in mountainous regions, under weak gradient flow, cool air drains down the mountain slopes into the valleys and lower elevations. The cool air accumulates in the valleys and, under clear skies, radiational cooling creates favorable conditions for the formation of radiation fog. In deep valleys with river systems, the fog will conform to the meanders of the river system.



2B-6a. FTV-26. DMSP VHR Low Enhancement. Fog Patterns in Mountainous Terrain. 0059 GMT 22 January 1972.

A DMSP VHR view over Southeast Asia (Fig. 2B-6a) on 22 January 1972, shows fog in the valleys and over river systems in the mountainous regions of northern Vietnam, northern Laos, and southern China. An enlarged view (Fig. 2B-7a) shows intricate details of the valley fog pattern. Such patterns have been used to precisely locate prominent geographical features for satellite imagery gridding purposes (Fett, 1964).

Reference

Fett, R.W., 1964: New geographic gridding technique. Air Weather Service, Scott AFB, Illinois. Unpublished manuscript.



2B-7a. FTV-26. Enlarged View. DMSP VHR Low Enhancement. Fog Patterns in Mountainous Terrain. 0059 GMT 22 January 1972.

2C Fog, Haze, and Air Pollution

Detection of Fog, Haze, and Air Pollution in DMSP Imagery

Small aerosol particles in the atmosphere deflect incident solar radiation by a process called scattering. The type of scattering that occurs is governed by the diameter (d) of the particle in relation to the wavelength (λ) of the incident radiation. The DMSP visible sensor is responsive to wavelengths extending from 0.4 to 1.1 μm . For d/λ ratios much less than 1 (dry haze and smoke particles), Rayleigh scattering occurs (Johnson, 1954). The DMSP visible sensor, however, has only a limited response to Rayleigh scattering effects. For d/λ ratios between 1 and 10 (light fog, haze, and air pollution), Mie scattering occurs. These phenomena appear as anomalous gray shades in DMSP visible imagery. For d/λ ratios greater than 10 (clouds and dense fog), solar ray reflection and geometric optical effects occur. In DMSP visible imagery, such areas tend to appear white against the generally darker earth background.

The DMSP visible sensors are especially effective in revealing light fog, haze, and air pollution because the spectral interval of the sensors extends into the near infrared wavelengths and provides a major portion of the total response at such wavelengths. In the near infrared wavelengths ($>0.7 \mu\text{m}$), the contrast between clear and hazy or foggy areas is accentuated, in contrast to other satellite systems which yield a peak sensor response at shorter wavelengths. Thus, the DMSP system is uniquely designed to distinguish more readily between clear areas and areas of light fog, haze, or air pollution (Tomasi and Guzzi, 1977). The contrast between clear areas and hazy or polluted areas is most distinct over oceans and lakes, because liquid water absorbs strongly in the visible through the near infrared wavelengths. Therefore, dry atmospheric areas over the ocean, in regions remote from sunglint, appear very dark in comparison to adjacent hazy areas, which appear as lighter-toned gray shades due to scattering and reflective effects.

Since Mie scattering is a highly directional type of scattering, the detection of light fog, haze, and air pollution depends on: (1) the solar illumination angle, (2) the sensor viewing angle, and (3) the angle between the two. Mie scattering has a maximum in the forward direction, a minimum near 100° (as measured from the direction of the incident ray), and a secondary peak in the backward direction. Thus, light fog, haze, and air pollution are best revealed in DMSP visible pictures in areas to the east of the satellite subpoint track for spacecraft with an early morning ascending node, and to the west of the satellite subpoint track for spacecraft with a late afternoon ascending node. The area directly below the spacecraft shows a minimal scattering effect and a reduced capability to produce the anomalous gray shade pattern.

Log enhancement tables are recommended for processing DMSP VHR or LF imagery to reveal areas of light fog, haze, and air pollution. In the log enhancement mode, the contrast between gray shade steps in areas of lower reflectivity is increased so that such phenomena are more readily distinguished from other features.

References

- Tomasi, C., and R. Guzzi, 1977: Experimental comparison between visible and near infrared attenuation of solar radiation in hazes and fogs. *Quart. J. Roy. Meteor. Soc.*, 103, 191-197.
Johnson, J.C., 1954: *Physical Meteorology*. Technology Press of the Mass. Inst. of Tech., John Wiley & Sons, New York, and Chapman & Hall, Ltd., London, pp. 43-81.

Case 1 Fog, Haze, and Air Pollution

Faint anomalous gray shades associated with haze and fog over water—U.S. West Coast

An early morning (0727 LST) view of the U.S. West Coast (Fig. 2C-2a) shows the Monterey Bay area covered by a uniform, light-tone anomalous gray shade pattern which extends out along the Pacific Coast. This gray shade pattern is identified as dense haze or fog, and suggests reduced surface visibilities. The reduced surface visibilities are confirmed by surface observations at Monterey Airport, located near the bay. At 0749 LST, an indefinite, obscured ceiling of 300 ft and 2 mi visibility, in fog, were reported at the airport. Note, to the east of Monterey Bay, the large area of dense stratus/fog in the Sacramento-San Joaquin Valley.

2C-2a. FTV-36.
DMSP LF
High Enhancement.
Anomalous Gray Shade
Patterns of Fog
and Haze. 1527 GMT
8 December 1977.



Another DMSP view of this area (Fig. 2C-3a) was acquired about 3 hours later, at 1038 LST. By this time, diurnal heating effects have dissipated most of the haze and fog over the Monterey Bay area. Observations at Monterey Airport, near this time, show improving surface conditions. A special observation, at 1025 LST, reported scattered cloud cover at 500 ft and at 20,000 ft, with surface visibility of 3 mi in haze and fog. Surface conditions continued to improve rapidly at the airport, with scattered cloud cover at 20,000 ft and visibility of 7 mi reported at 1045 LST, seven minutes after the DMSP picture over the area. A close examination of Monterey Bay (Fig. 2C-3b), however,

2C-3a. FTV-35. DMSP LF Log Enhancement.
Faint Anomalous Gray Shade Patterns of Fog
and Haze. 1838 GMT 8 December 1977.
(Area Outline of Fig. 2C-3b.)



2C-3b. FTV-35. Enlarged View.
DMSP LF Log Enhancement.
Faint Anomalous Gray Shade
Patterns of Fog and Haze.
1838 GMT 8 December 1977.



continues to show faint traces of the anomalous gray shade pattern—
suggesting the persistence of hazy conditions and poor visibilities over
the water. A similar faint, anomalous gray shade pattern, at the edge of
a narrow stratus/fog band, suggests another area of reduced surface
visibility over water in the area to the west of San Francisco.

Important Conclusion

1. Faint anomalous gray shade patterns over water near coastal regions are indicative of poor low-level visibilities.

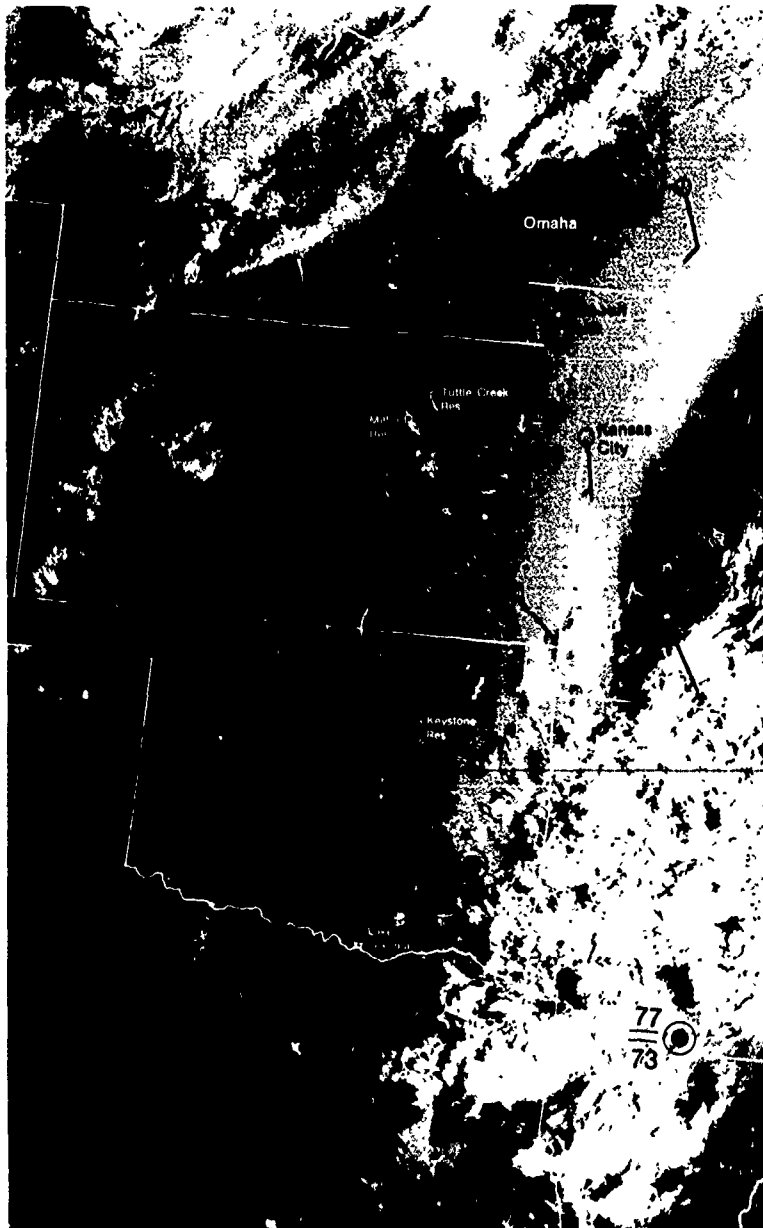
Case 2 Fog, Haze, and Air Pollution

Band of fog and haze over land—U.S. Central Plains

In an early morning view of the U.S. Central Plains (Fig. 2C-4a), a distinct, light-toned band is observed covering eastern Oklahoma and western Arkansas, and extending to the north through Kansas to the edge of the picture. The eastern boundary of the band ends abruptly, forming a sharp contrast with the adjacent cloudless land area, while the western boundary of the band gradually fades in brightness. Contours of surface visibility reveal that the lowest visibilities occur along the eastern sector of the band where it appears to be most dense in the pictures.



2C-4a. FTV-36. DMSP LF Normal Enhancement. Fog and Haze over Land. 1317 GMT 20 July 1977.
Surface Visibility Reports (in miles). 1200 GMT 20 July 1977.



2C-5a. FTV-36. Enlarged View.
DMSP LF
Normal Enhancement.
Fog and Haze over Land.
1317 GMT 20 July 1977.
NMC Surface Reports.
1200 GMT 20 July 1977.

In an enlarged view of the area (Fig. 2C-5a), the 1200 GMT surface reports show that the band coincides with a widespread area of fog and haze. These reports also indicate that southerly flow from the Gulf of Mexico is the source of the moist air which, cooled to saturation during the clear sky nighttime conditions, forms the area of reduced surface visibilities. Note that the Missouri River and several lakes are visible through the light-toned band, indicating that only a thin veil of fog and haze covers this area. Hourly observations (below) from Kansas City, Mo., and Omaha, Nebr., show the gradual restriction of the surface visibilities that occurred during the early morning hours in this area.

Omaha			Kansas City		
Time (LST)	Sky and Ceiling (hundreds of feet)	Visibility (miles)	Time (LST)	Sky and Ceiling (hundreds of feet)	Visibility (miles)
0050	CLR	7	0047	CLR	10
0150	CLR	7	0148	CLR	10
0250	CLR	7	0249	CLR	10
0350	CLR	7	0350	CLR	10
0450	CLR	6 H	0449	CLR	8
0550	250-SCT	4 H	0549	CLR	8
0650	250-SCT	4 H	0648	CLR	8

Case 3 Fog, Haze, and Air Pollution

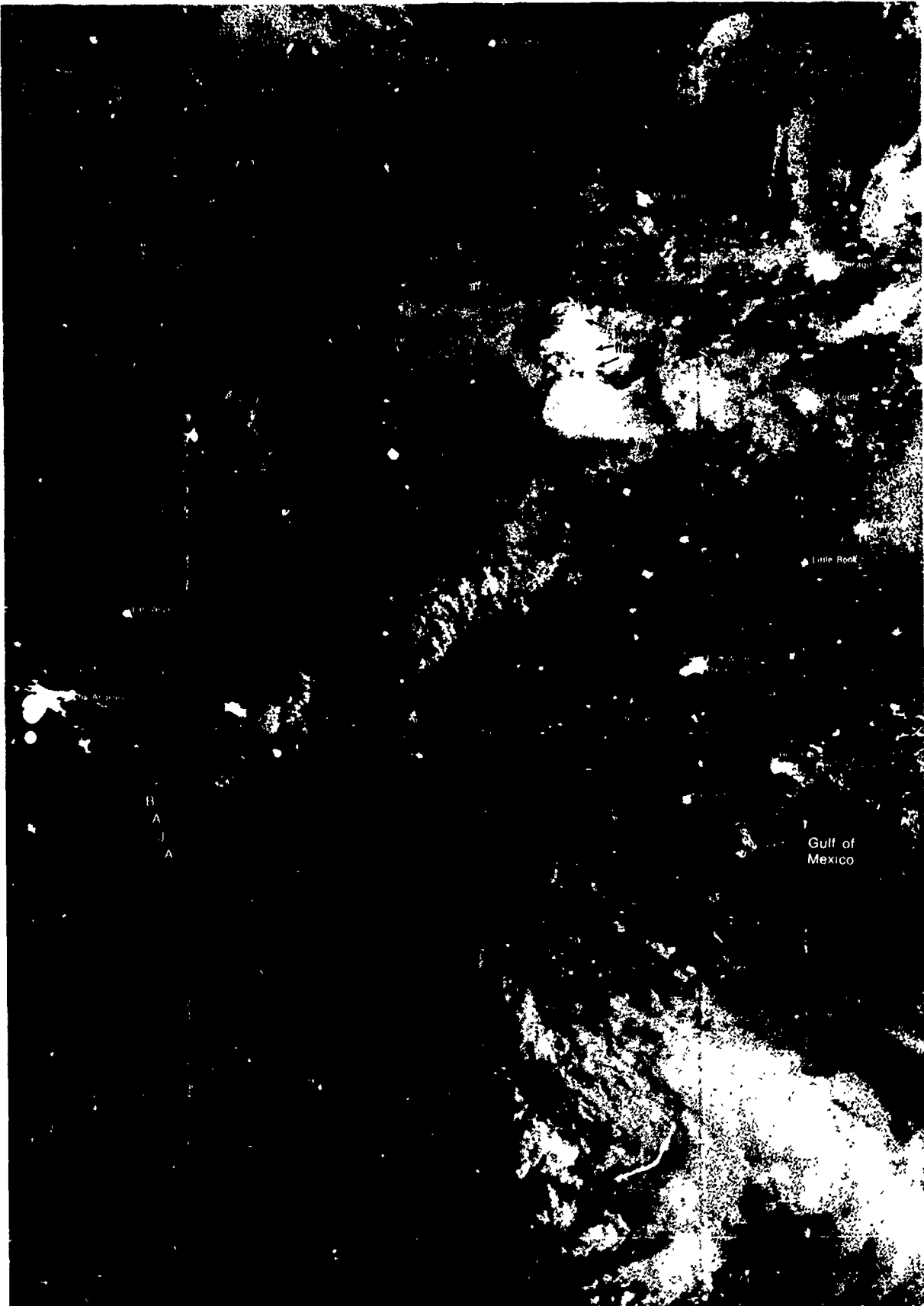
Appearance of fog, haze, and air pollution over land in moonglint areas—Central U.S.

Fig. 2C-7a is a nighttime visible image of North America taken when the moon was low on the eastern horizon. In the eastern portion of this picture, moonglint from the Gulf of Mexico and Great Lakes causes these bodies of water to appear lighter than the adjacent land areas. Further to the west, remote from the moonglint region, the waters of the Pacific and Gulf of California are darker than the land—the normally expected tonal contrast in such imagery. In addition, multiple clusters of lights from major metropolitan areas and along several of the interstate highways can be clearly identified. Note also the bright horizontal streaks caused by lightning flashes from thunderstorms over Nebraska.

Of special interest in this picture is the diffuse, light-tone area extending from Little Rock, Arkansas, to the eastern edge of the picture. This light-tone area is the result of the forward scattering of moonlight by large aerosol particles. Note that this area is almost as bright as the Gulf of Mexico and the Great Lakes. The boundary of this area, however, is indistinct in comparison to the sharp land-water contrast in the Gulf of Mexico and Great Lakes regions. Observations from stations in the moonglint area, near the time of the DMSP picture, confirm restricted visibilities in fog, haze, and smoke.

Important Conclusion

1. Areas of fog, haze, and air pollution can be detected in DMSP nighttime visible imagery in areas of moonglint, where forward scattering of the moonlight to the satellite occurs.



2C-7a. FTV-35. DMSP LS Low Enhancement. Appearance of Fog, Haze, and Air Pollution in Moonglint Areas over Land.
0703 GMT 3 September 1977.

Case 4 Fog, Haze, and Air Pollution

Smoke plumes over water—Gulf of Mexico

Since the DMSP high resolution visible sensors (VHR and LF) are capable of detecting contrails and smoke plumes from forest fires under conditions of stable flow where diffusion is minimized (see NTAG Vol. 1, Sec. 2B, Cases 18 and 19), they should also detect smoke plumes from oil well fires, electrical plants, refineries, etc., under similar atmospheric conditions. When smoke is blown out over water, or from a point over the water toward land, the rate of smoke plume diffusion is directly related to the air-sea temperature difference. If the water is colder than the air, the low-level air is stable and diffusion minimized. Conversely, if the water is warmer than the air, the low-level air is unstable and rapid diffusion of a smoke plume occurs. (Raynor *et al.*, 1975).

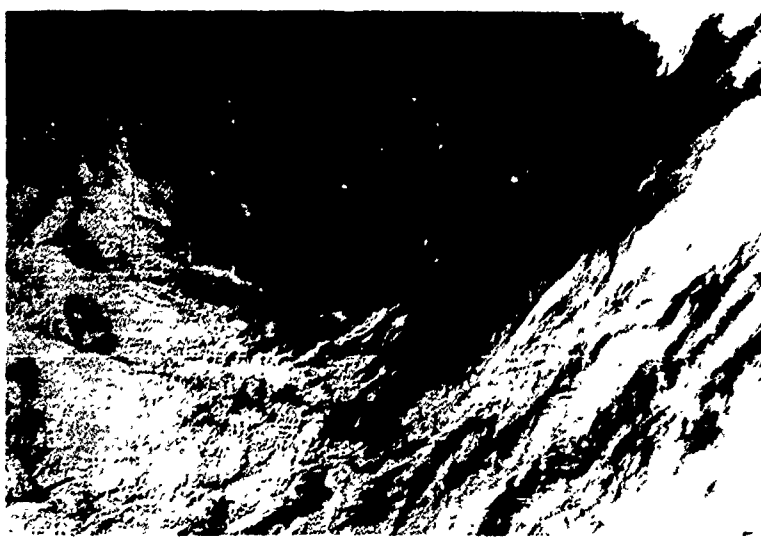
In a DMSP picture (Fig. 2C-8a) of the Vermillion Bay, Louisiana area, two middle-tone gray shade plumes ("A" and "B") are faintly evident extending offshore into the Gulf of Mexico. An enlarged view of the area (Fig. 2C-9a), reveals the plumes quite clearly. In a Landsat view (Fig. 2C-9b) of the area on the same day in Channel 5 (0.6-0.7 μm), the two plumes ("A" and "B") are also evident and can be identified as smoke plumes from oil well fires known to exist in that area. Smoke plumes from oil and gas wells in Vermillion Bay were photographed as early as November 1966 by Project Gemini astronauts (NASA, 1968). The orientation and persistence of the smoke plumes for long distances over the water suggest that the low-level flow is steady from the northeast, and that a very stable low-level lapse rate is present in the area.

Comparing the two views, notice that the hook-like turbid water pattern visible in the Landsat picture under smoke plume "A" is also visible as an anomalous gray shade hook pattern in the DMSP picture. Similarly, the turbid water at "C" and the turbid water and clouds at "D" are visible in both views.

References

- Raynor, G.W., P. Michael, R.M. Brown, and S. Sethu Ramon, 1975: Studies of atmospheric diffusion from a nearshore oceanic site, *J. of Appl. Meteor.*, 14, 1080-1094.
NASA, 1968: Earth Photographs from Gemini 6 through 12, Office of Technology Utilization, National Aeronautics and Space Administration, Wash. D.C., 327 pp.

2C-8a. FTV-29.
DMSP VHR
Low Enhancement.
Smoke Plumes over
Water. 1413 GMT
7 December 1973.

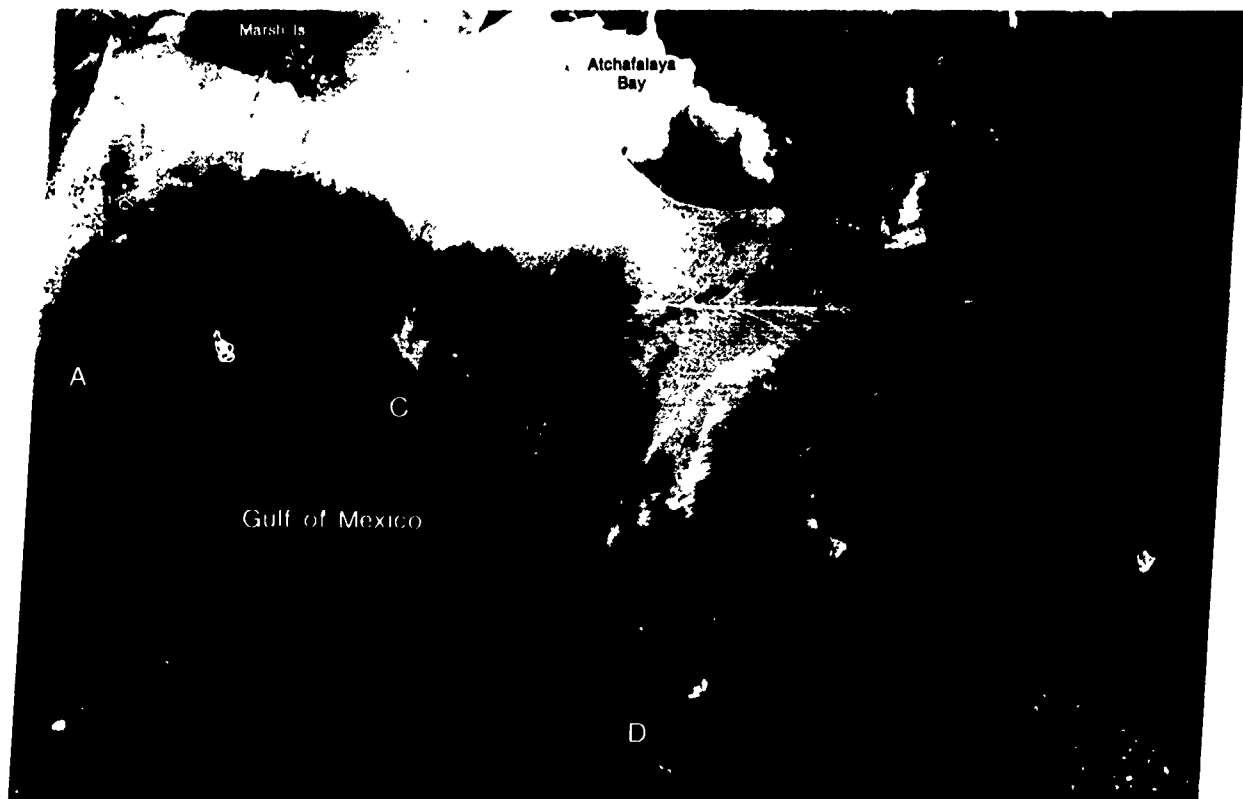


Important Conclusion

1. Smoke plumes from oil or gas well fires can be detected in DMSP high resolution visible imagery. Such smoke plumes indicate the presence of a stable lapse rate, the direction of the low-level flow, and are an indication that the water temperatures are colder than the air temperatures over the area.



2C-9a. FTV-29.
DMSP VHR
Low Enhancement.
Smoke Plumes over
Water. 1413 GMT
7 December 1973.
(Area Outline
of Fig. 2C-9b.)



2C-9b. Landsat Data. MSS-5. Smoke Plumes. 1605 GMT 7 December 1973.

Case 5 Fog, Haze, and Air Pollution

Advection-radiation fog in nighttime infrared imagery— U.S. Gulf Coast Region

Fog formation, caused by nighttime radiational cooling in warm, moist air that has come inland during the day, is a common occurrence over the Gulf Coast Region. At night, during the winter months, the moisture-laden areas will cool at a slower rate than the surrounding less moist areas. As fog is formed the radiational cooling in the moisture-laden area is further slowed, while the surrounding areas continue to cool rapidly. Many times an inversion in the moisture-laden air results such that the top of the fog is warmer than the temperature of the surrounding land area. The fog area will radiate at the warmer temperatures of the top of the fog layer, while the fog-free area radiates at the colder ground temperatures. Thus a gray shade contrast, in infrared imagery, may be observed between the fog area (dark-tone) and the surrounding clear area (light-tone).

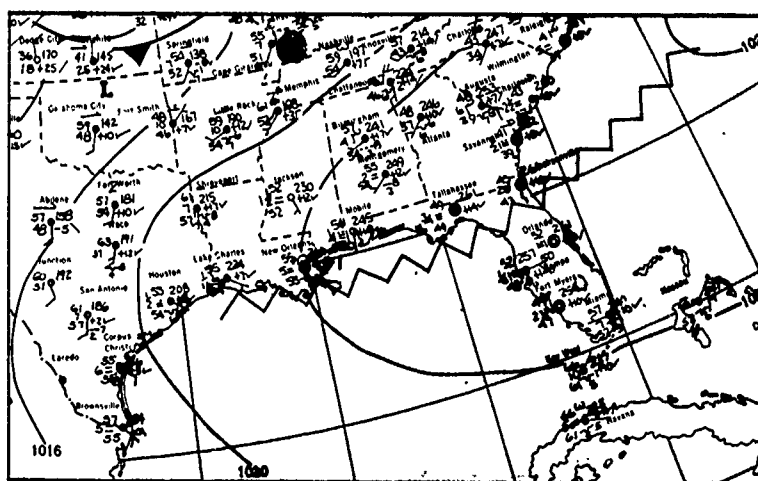


2C-10a. FTV-31. DMSP WHR Normal Enhancement. Advection-Radiation Fog. 1215 GMT 13 February 1976.

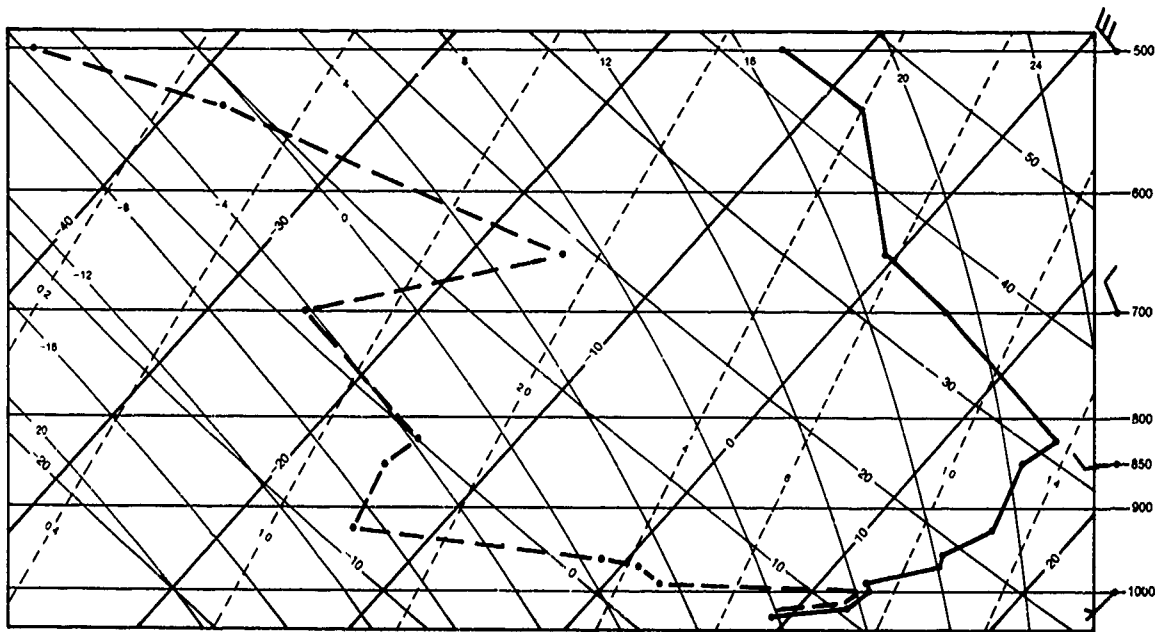
An example of such an advection-radiation fog condition is shown in Fig. 2C-10a. A darker gray shade area (warmer temperature) over the eastern Gulf Coast States stands out in marked contrast to the lighter gray shade area (colder temperature) of the surrounding fog-free terrain. The surface analysis near this time (Fig. 2C-11a) verifies the occurrence of fog at Tallahassee, Florida; Jackson, Mississippi; and Montgomery and Mobile, Alabama. The analysis also shows that the clear sky conditions, conducive for fog formation, were aided by subsidence from a strong ridge of high pressure which extended east-west along the Gulf Coast. The 1200 GMT radiosonde report from Apalachicola, Florida (Fig. 2C-11b), shows a strong inversion from the surface to 1000 mb and a very stable lapse rate to about 825 mb. The surface temperature was about 9°C, while the temperature at the top of the fog layer (1000 mb level) was 13°C—a full 4°C warmer.

Important Conclusion

1. In radiation fog, temperatures at the top of the fog layer are frequently noticeably warmer than temperatures at ground level in surrounding areas. Thus the fog may appear darker than the surrounding terrain, reversing the normal tonal contrast between fog and land.



2C-11a. NMC Surface Analysis.
1200 GMT 13 February 1976.



2C-11b. RAOB. Apalachicola, Florida. 1200 GMT 13 February 1976.

2D Severe Weather

Severe Weather Detection and Tracking

In general, the term severe weather is applied to any destructive storm, but is usually applied to severe local storms (i.e. severe thunderstorms, hail storms, and tornadoes). The Navy meteorologist must be concerned not only with the destructive winds, but also with the increased sea state that can suddenly be produced by the high winds in a rapidly developing severe storm. Satellite imagery, combined with radar, surface, and upper air reports, allows an immediate assessment of the atmospheric conditions—including moisture content at low-levels, thermodynamic stability, and vertical wind shear. Once a storm develops, the active weather areas can be identified and tracked in satellite imagery.

Case 1 Severe Weather

Severe thunderstorms ahead of a short-wave trough over open water—Central Mediterranean Sea

In autumn, when a trough extends from the Mediterranean northward between two anticyclones—one over the northeast Atlantic and the other over central Europe—cyclogenesis generally occurs over the central or western Mediterranean (Air Ministry, 1962). This is caused by the flow to the west of the trough, of northerly winds, bringing polar air to the Mediterranean, which converges with the flow along the southeast side of the trough, of continental tropical air from Africa. In addition, continental tropical air is conditionally unstable and rapidly acquires much additional moisture over the sea. When this air is lifted in advance of a developing depression or cold front, severe thunderstorms may be produced.

In an early morning DMSP WHR picture (Fig. 2D-2a) at 0551 GMT, scattered thunderstorms are observed over the central Mediterranean in advance of an upper-level trough. The position of this trough can be deduced from the alignment of anvil cirrus tops which show northwesterly flow over the western Mediterranean and southwesterly flow over the central portion of the Mediterranean. Note also, the band of subtropical jet stream cirrus that occurs to the south over Africa. The surface chart (Fig. 2D-2b), about 6 hours prior to the picture, shows a polar trough over the western Mediterranean extending to a low over the British Isles. 300 mb data (Fig. 2D-2c) verifies the existence of a short-wave trough aloft as indicated by the satellite data. Conditions favorable for thunderstorm development were revealed by the RAOB for Brindisi, Italy (foldout). This sounding shows a low lifting condensation level (LCL), a large positive energy area, and strong, mid-tropospheric wind shear.

Cyclogenesis was forecast to occur in the north central Mediterranean during the day. An unexpected occurrence, however, was the explosive development of a severe convective storm area off the northeast coast of Tunisia (Fig. 2D-3a). USS Mitscher encountered this storm on a routine cruise south of Sicily. A short time after this picture, USS Mitscher transmitted the following message (Gibbs, 1975):

UNCLAS E F T O //N03140//
TO ALL SHIPS CONCERNED
HQI 1315 WINDS IN EXCESS OF 60 MPH WITH HEAVY RAIN STORMS/N
LIGHTNING ACCOMPANIED WITH SUDDEN DROP IN BAROMETER OF .17/8
IN TWO HOURS IN AREA OF 36-38N 14-15E.
AT GENERAL QUARTERS WITH MATERIAL CONDITION ZEBRA SET.
BT
#03775

The strong winds produced a rapid increase in sea state and the higher seas persisted for some time after USS Mitscher had cleared the storm. Less than 2 hours later, the following message was relayed:

UNCLAS E F T O //N03140//
WEATHER SITREP
1. CLEARED STORM. SEAS PRESENTLY 10-12 FT, WIND 38/1 KTS.
MAX WIND EXPERIENCED 80/8 PLUS KTS. INITIAL SURVEY INDICATES
NO APPARENT DAMAGE.
2. THIS IS LAST REPORT.
BT
#03826

References

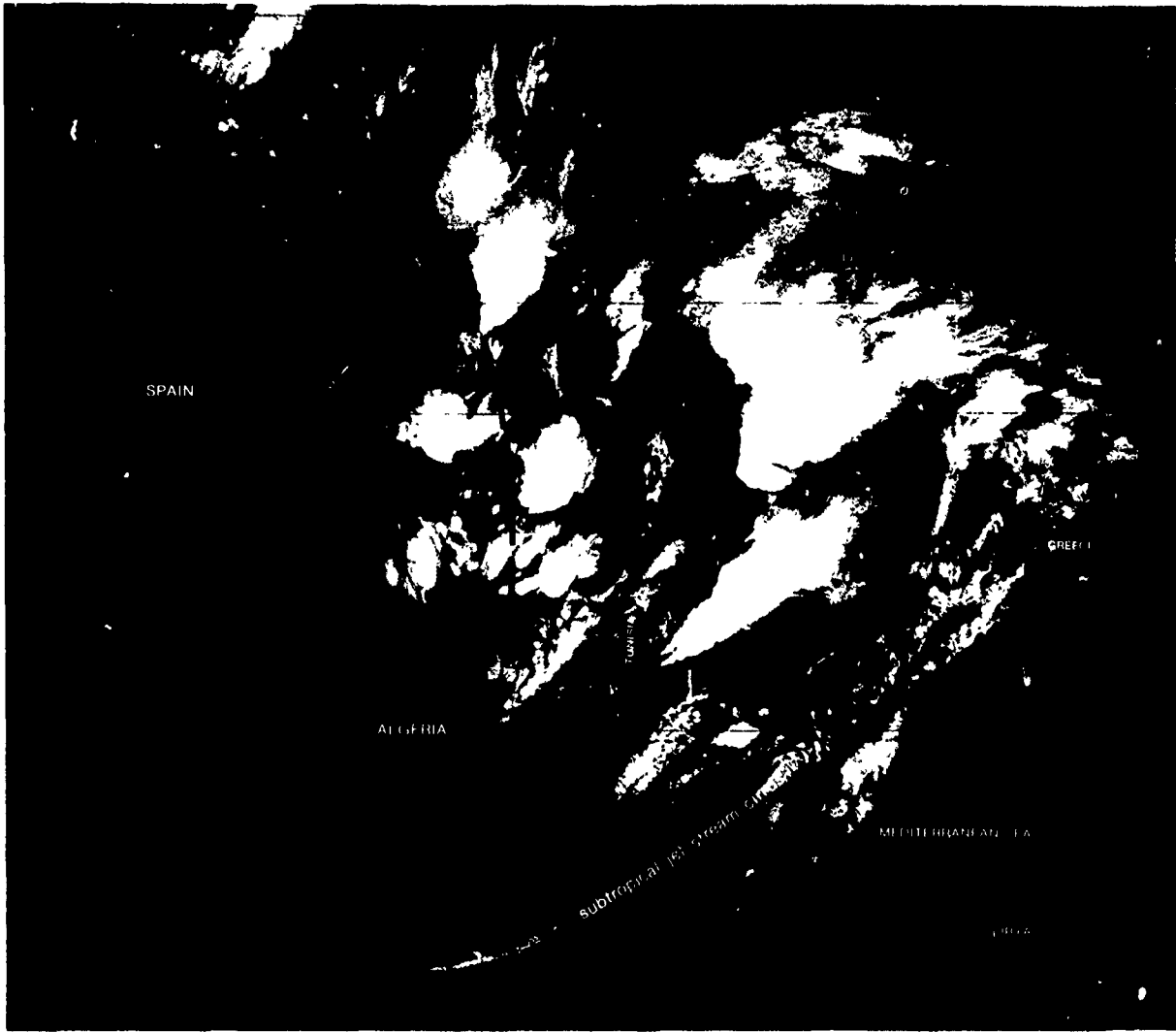
- Air Ministry, Meteorological Office, 1962: *Weather in the Mediterranean, General Meteorology*. London: Her Majesty's Stationery Office, Vol. I, 372 pp.
Gibbs LCDR M.E., 1975: Personal communication. USS J.F. Kennedy.



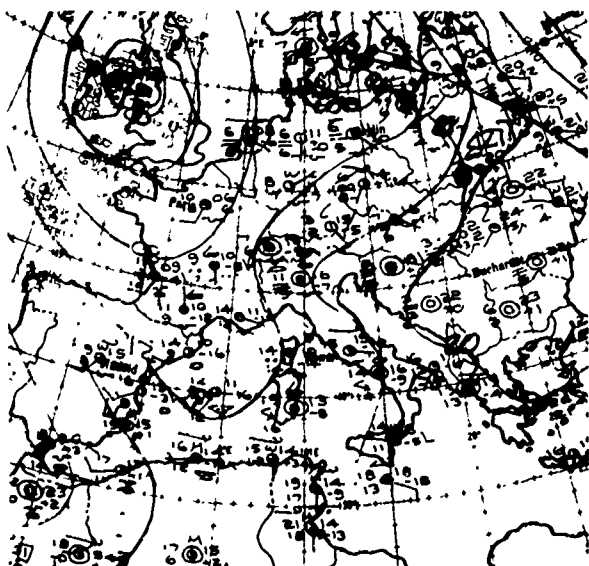
2D-2a. FTV-33. DMSP WHR T-N
0551 GMT 16 October 1975.



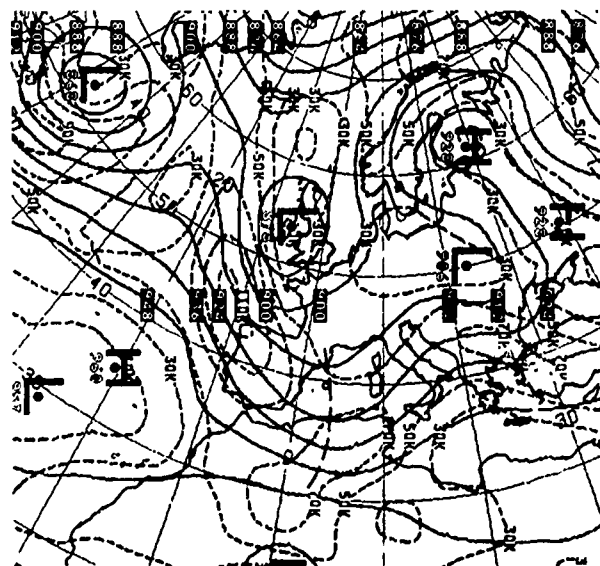
2D-2b. NMC Surface Analysis.
0000 GMT 16 October 1975.



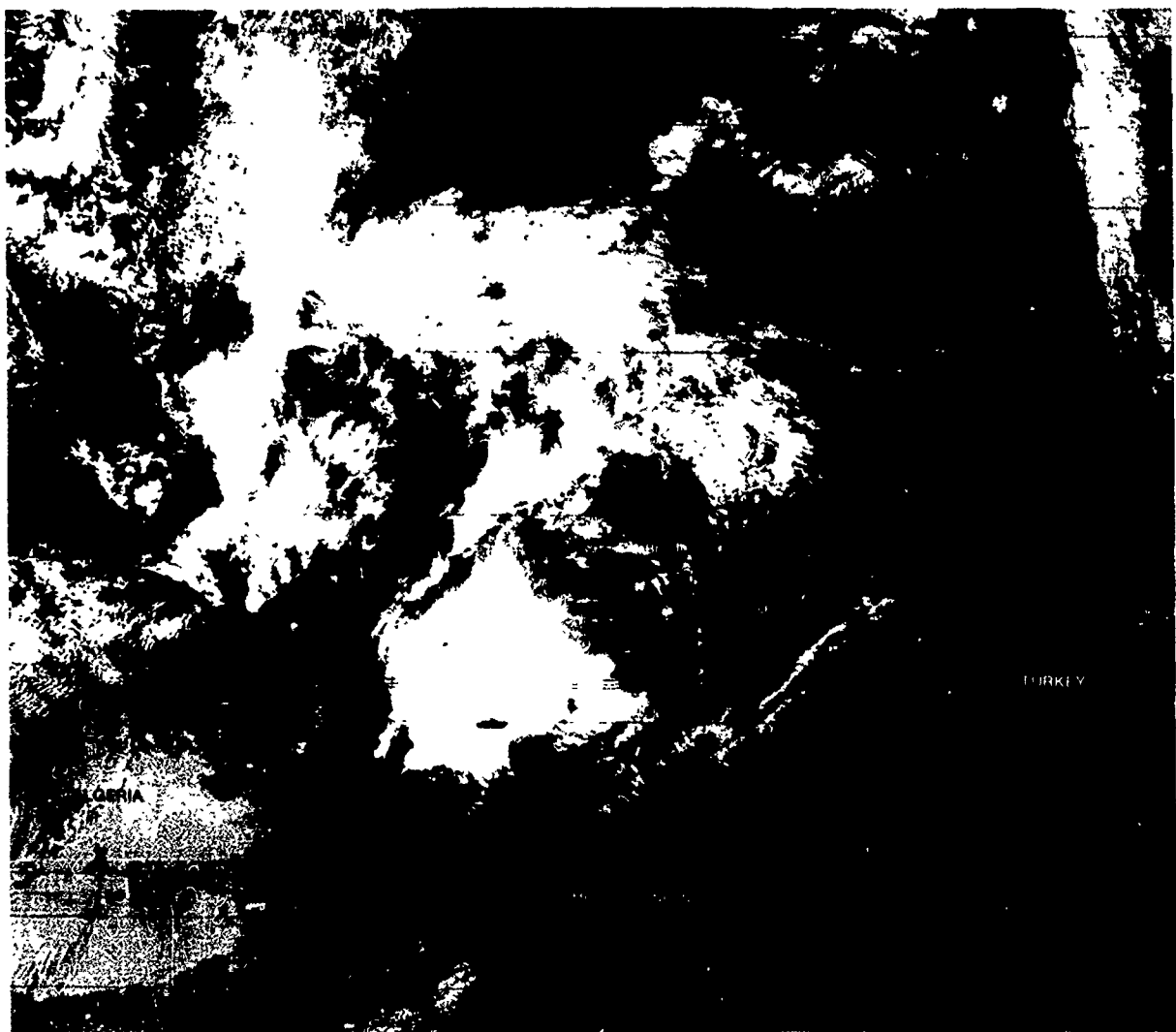
2D-2a. FTV-33, DMSP WHR T-Normal Enhancement. Scattered Thunderstorms over the Central Mediterranean.
0551 GMT 16 October 1975.



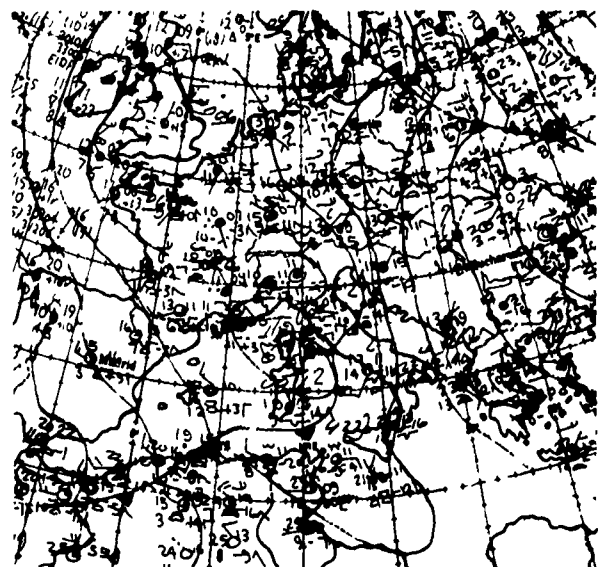
2D-2b. NMC Surface Analysis.
0000 GMT 16 October 1975.



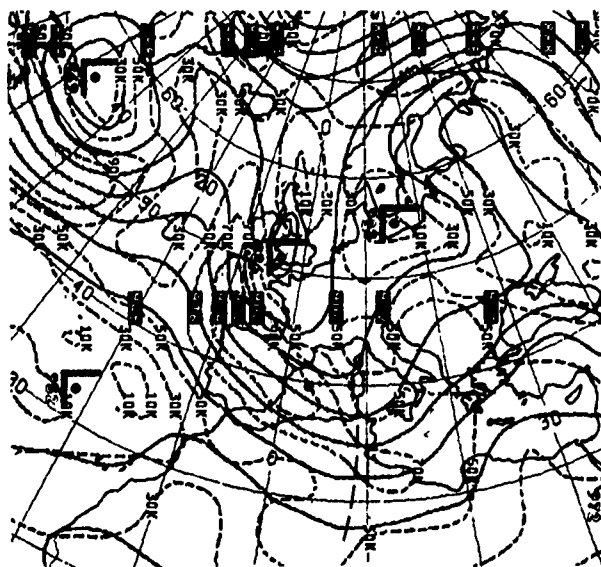
2D-2c. NMC 300 mb Contour and Isotach Analysis.
0000 GMT 16 October 1975.



2D-3a. FTV-31. DMSP VHR Low Enhancement. Intense Convective Development. 1042 GMT 16 October 1975.

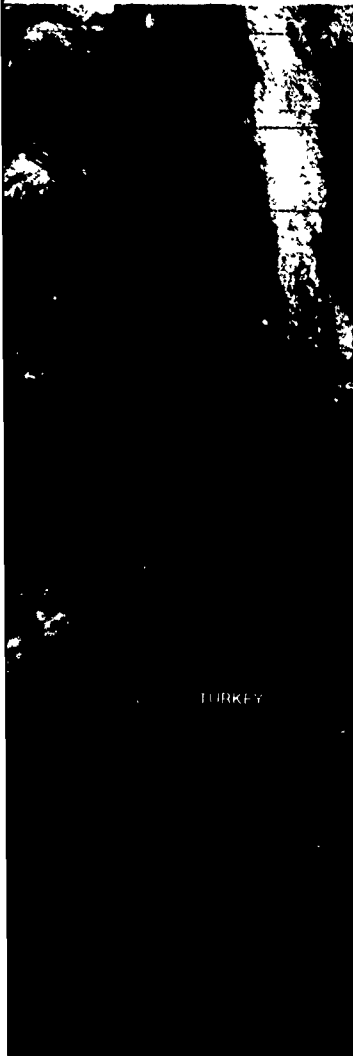


2D-3b. NMC Surface Analysis.
1200 GMT 16 October 1975.

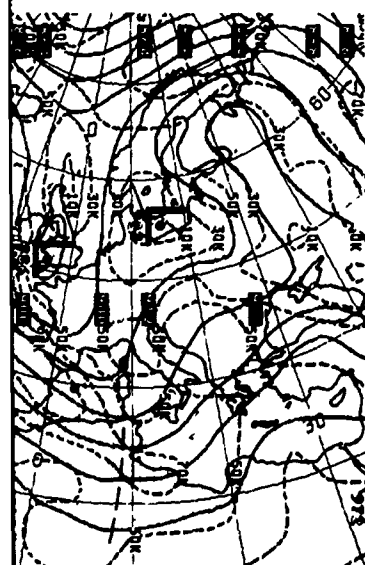


2D-3c. NMC 300 mb Contour and Isotach Analysis.
1200 GMT 16 October 1975.

The 1200 GMT weather charts show that cyclogenesis occurred near Corsica (Fig. 2D-3b), in advance of the short-wave trough at 300 mb (Fig. 2D-3c). The trough of low pressure south of Sicily in the surface analysis, however, suggests that local cyclogenesis may have also occurred in that area. This development was aided by the presence of the subtropical jet stream aloft, which provided the mechanism for upper-level divergence and rapid deepening at the surface.

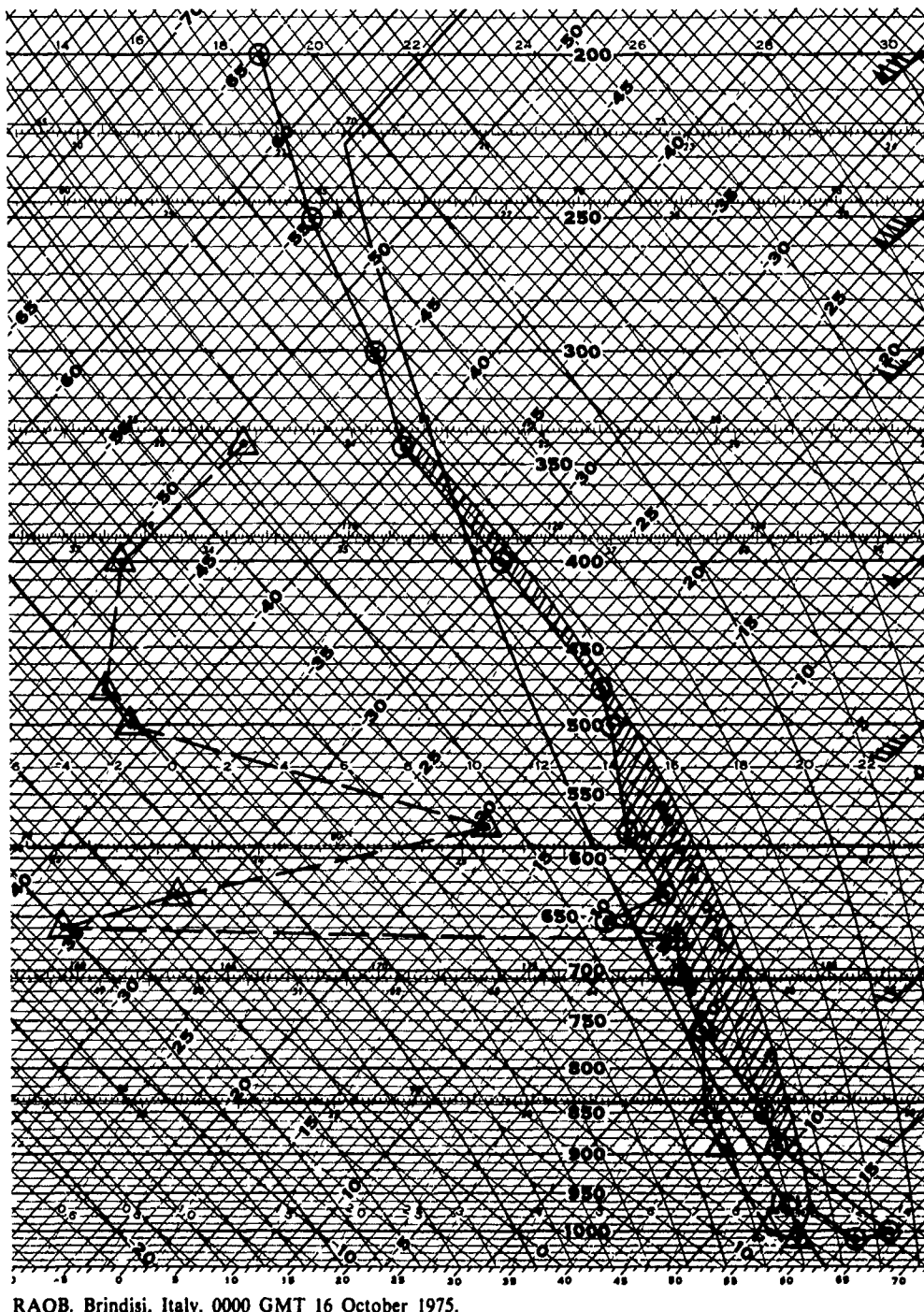


T 16 October 1975.



Mediterranean

75.



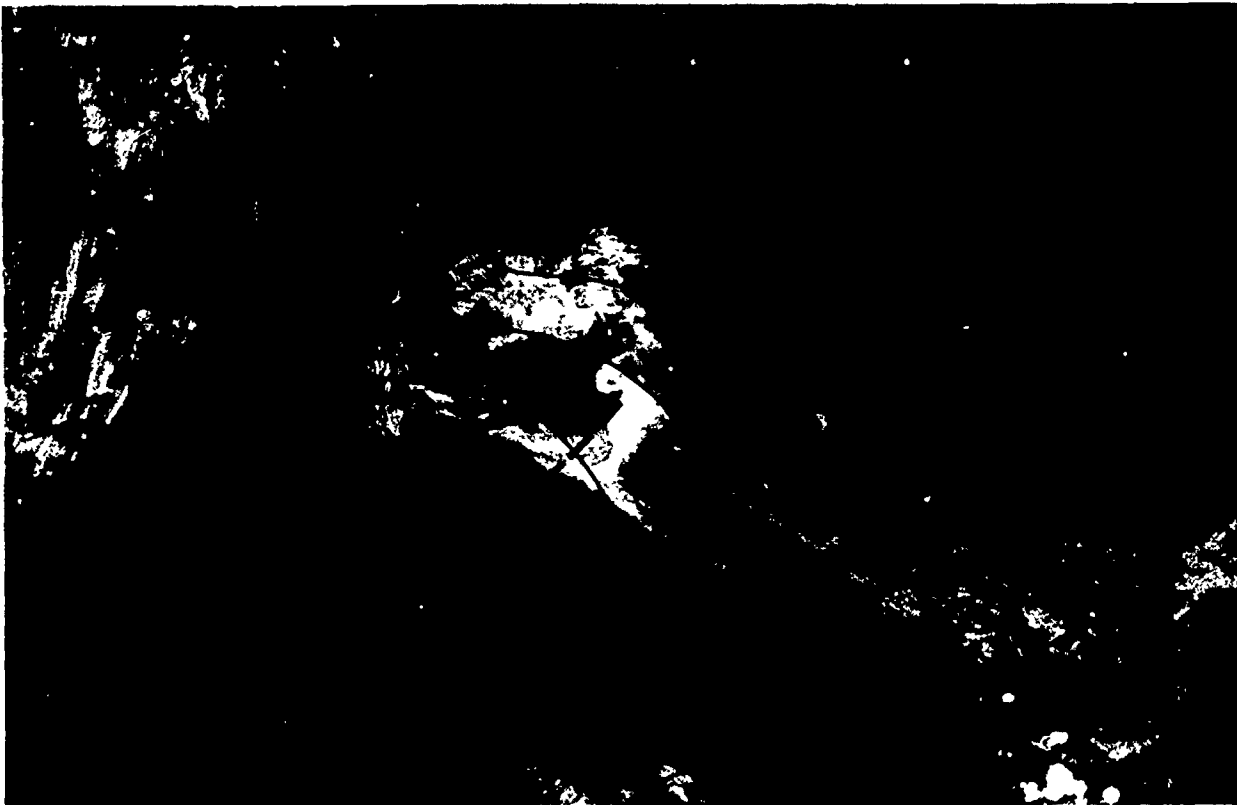
Case 2 Severe Weather

Isolated severe thunderstorm—U.S. Central Plains

Fig. 2D-4a is a DMSP LF view of a convective storm having a distinct comma configuration, which gives it the appearance of a well-developed synoptic-scale vorticity center (Johnston, 1978). The storm has developed in relative isolation and no major weather producing system appears in the area. The surface chart for 1200 GMT (not shown), five hours prior to the storm, shows a dissipating cold front separating a convective cloudy area in moist tropical air to the south from drier, more stable air to the north. A streamline analysis superimposed on the DMSP picture (Fig. 2D-5a) indicates a cyclonic turning of the winds over the area, and the presence of a short-wave trough.



2D-4a. FTV-35. DMSP LF Normal Enhancement. Isolated Severe Storm. 1724 GMT 7 May 1977.



2D-5a. FTV-35. DMSP LF Normal Enhancement. Isolated Severe Storm. 1724 GMT 7 May 1977.
Surface Reports and Streamline Analysis. 1800 GMT 7 May 1977.



2D-5b. FTV-35. DMSP TS T-Normal Enhancement. Isolated Severe Storm. 1724 GMT 7 May 1977.
200 mb Wind and Contour Analysis. 0000 GMT 8 May 1977.



The corresponding DMSP TS picture (Fig. 2D-5b) emphasizes the extreme isolation of this convective storm. The cirrus streamers in this view, and in the DMSP LF picture, as well as the 200 mb wind and contour analysis for 0000 GMT, show an anticyclonic flow at upper levels. This anticyclonic feature of the upper-level circulation is also documented by Johnston (op. cit.). The presence of anticyclonic directional and speed shear appear to be important factors in the formation process of these isolated severe storms. The distinct comma-shaped configuration in the DMSP LF picture (Fig. 2D-5c) indicates the presence of a strong, small, low-level positive vorticity center. Little or no indication of such a center can normally be detected in available surface reports.

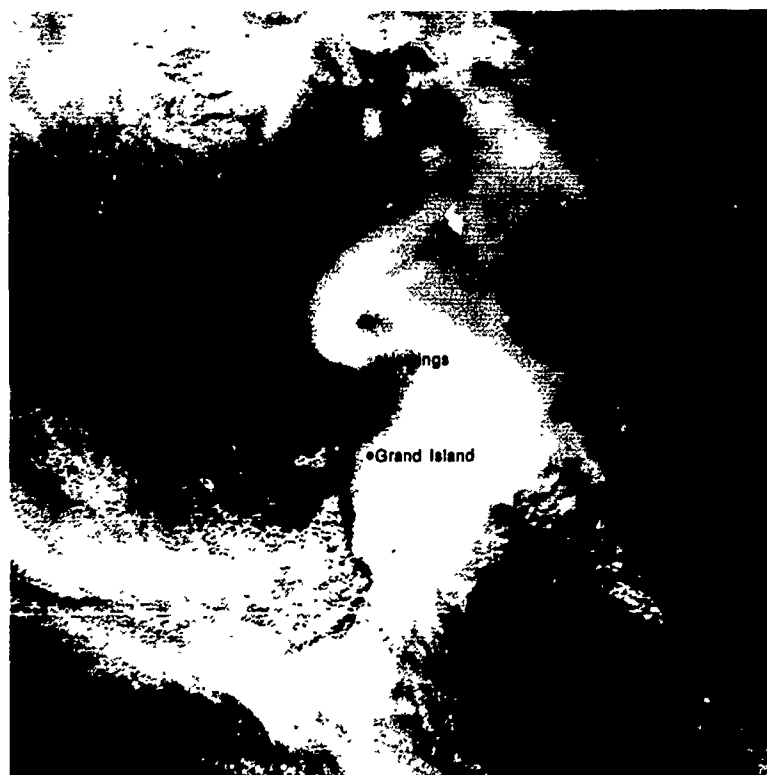
Some of the severe weather reported during this storm include: Hastings, Nebr.—funnel cloud sighted 40 mi southeast of the city at 1825 GMT; Grand Island, Nebr.—heavy thunderstorm at 1800 GMT; Emporia, Kans.—hail up to $2\frac{3}{4}$ " in diameter, earlier in the day.

Important Conclusions

1. In satellite data, isolated, tornado producing severe thunderstorms may occur in association with a comma-shaped cloud configuration, identifying a positive vorticity center. The characteristic comma-shaped cloud configuration permits early identification of the tornado producing thunderstorm complex.
2. These localized positive vorticity centers may develop along weak frontal boundaries showing some indications of cyclonic low-level flow and anticyclonic upper-level flow over the area.

Reference

Johnston, E.C., 1978: Mesoscale low-level vorticity centers associated with convection as viewed by satellite. *National Weather Digest*, 3, 12-16,



2D-5c. FTV-35. Enlarged View. DMSP LF Normal Enhancement. Characteristic Comma-Shaped Cloud Configuration of an Isolated Severe Storm. 1724 GMT 7 May 1977.

2E Air-Sea Interaction

Effects of Air-Sea Interactions on Local-Scale Phenomena

The seas supply the atmosphere with moisture by evaporation and heat—including sensible heat by radiative transfer, and latent heat of water vapor by turbulent heat transfer. The rate of heat and moisture transfer to the atmosphere is determined by the sea surface temperature, the temperature of the air and its moisture content, and the vertical gradient of temperature and humidity in the layer over the sea surface. The wind velocity is another factor controlling the transfer process (Monin, Kamenkovich, and Kort, 1974). On the larger scale, these atmosphere-ocean interactions are responsible for long-term weather anomalies and climatic changes. In this section, emphasis is on air-sea interactions that produce shorter-term, local-scale phenomena which can be observed in DMSP imagery.

The effects of air-sea interactions on the local scale may be identified in satellite imagery by noting the presence and character of cloudiness, or the absence of cloudiness. For example, areas of cold, shallow water or upwelled water, central regions of cold oceanic eddies, and cold oceanic currents will generally be free of convective cloudiness, since cold water inhibits evaporation and increases the stability of the surface atmospheric layers. Stratus decks and fog, however, will form in warm, moist air being advected over the same oceanic areas. In the case of cold air advection over a warmer sea surface, such as occurs following a cold air outbreak off the eastern coasts of continents during winter, convective clouds develop some distance offshore. Here, the underlying warmer sea surface enhances evaporation and decreases the stability of the surface atmospheric layers. Over the open oceans, diurnal convective cloudiness is similarly affected by warm or cool underlying sea surface temperatures. A warm underlying sea surface will enhance convection, while a cold underlying sea surface will inhibit convection.

Reference

Monin, A.S., V.M. Kamenkovich, and V.G. Kort, 1974: *Variability of the Oceans*. Translated by J.J. Lumley, John Wiley and Sons, New York, 1977, 241 pp.

Case 1 Air-Sea Interaction

Marine haze formation over cold coastal upwelled waters

In the DMSP LF (VHR) view of the Pacific Northwest (Fig. 2E-2a), the coastal waters from the Strait of Juan de Fuca to Cape Blanco appear to be almost cloud-free. However, a careful examination of the imagery reveals a narrow, irregular, medium-tone anomalous gray shade zone along the coast which indicates the presence of damp haze or small, unresolvable cloud elements (NTAG, Vol. 1, Sec. 2B). In particular, note that the anomalous gray shade pattern just northwest of the mouth of the Columbia River suggests the presence of an eddy formation (see enlargement).

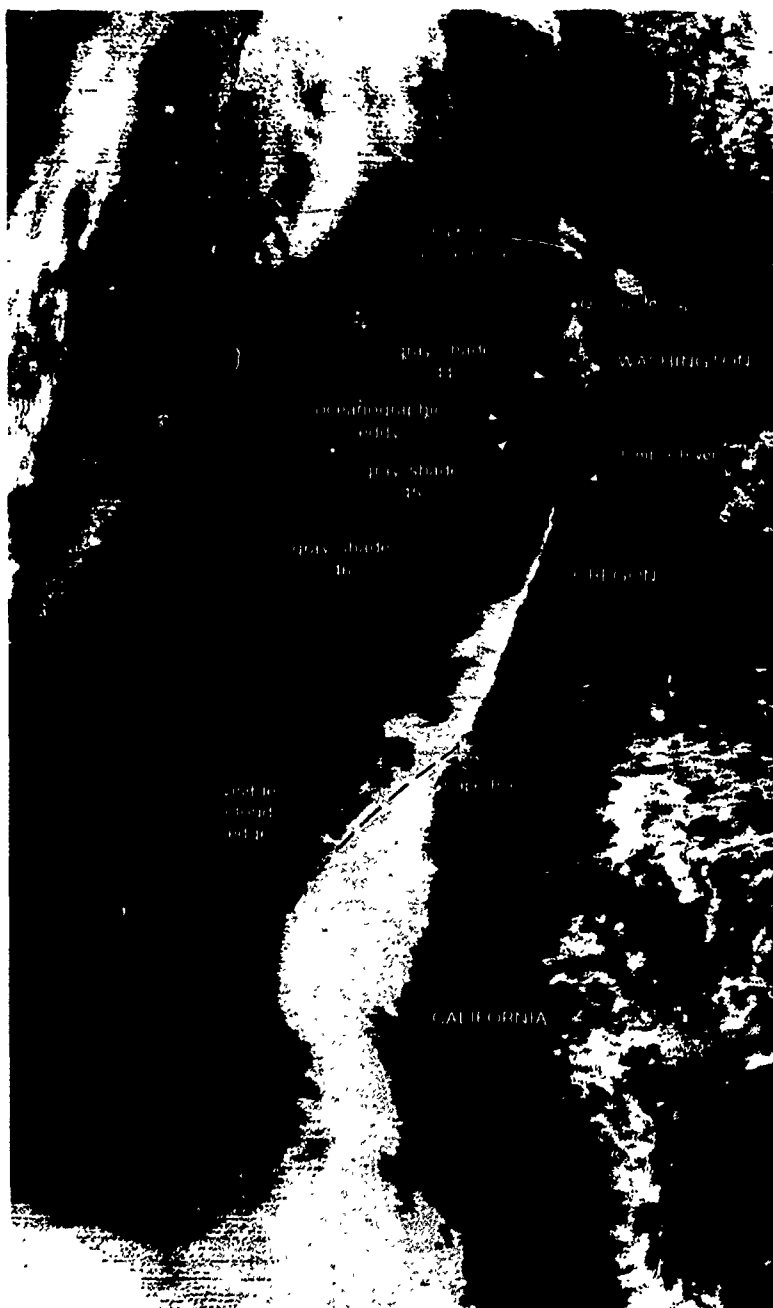


2E-2a. FTV-36, DMSP LF Low Enhancement. Marine Haze (Anomalous Gray Shade) over Cold Coastal Upwelled Waters. 2001 GMT 10 August 1977.

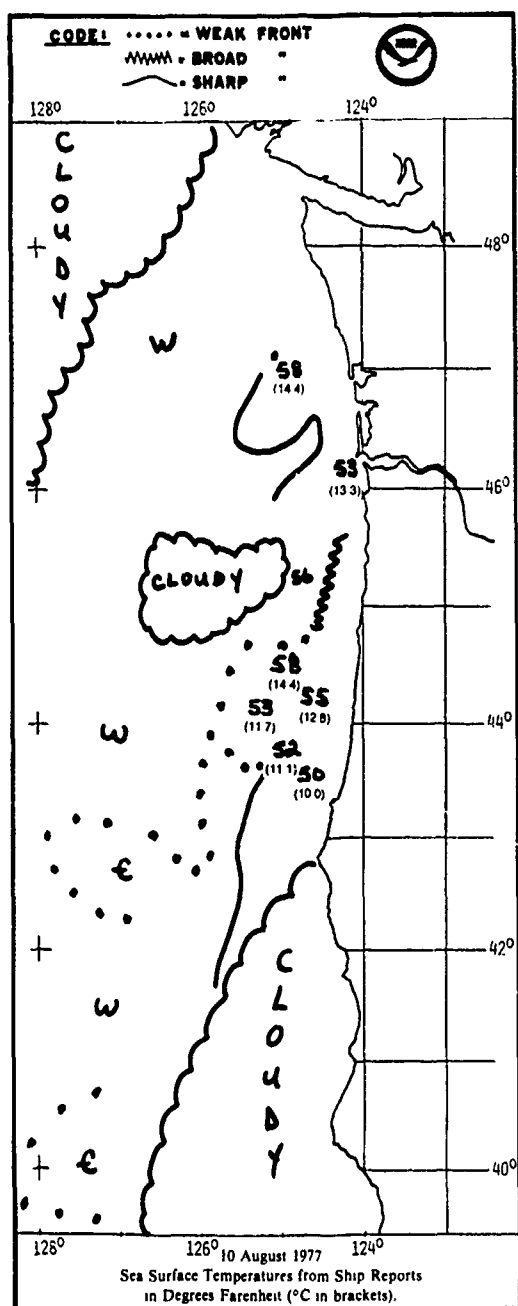
In a DMSP TS (IR) view of the same area (Fig. 2E-3a), acquired 6-hours earlier, there appears to be an oceanographic eddy in the same area as the anomalous gray shade pattern eddy in the visible imagery. The T-Normal Enhancement technique (Table 1) used to produce this infrared imagery permits a greater tonal separation of gray shades between adjacent temperature intervals (1.6°C) of these data. Gray shade 44 (light tone) corresponds to a 1.6°C temperature range, with a central value of 6.5°C (280 K). Similarly, gray shade 45 (medium tone) and 46 (dark tone) correspond to central value temperatures of 8.1°C (281 K) and 9.7°C (283 K), respectively. When these values are corrected for atmospheric attenuation (NTAG, Vol. 1, Sec. 1C, pp 1C-4 and 1C-5), adjusted central values of 13°C , 14.6°C , and 16.2°C are obtained.

Table 1

Input	Gray Shade	Output	Gray Shade
00	38	00	45
39	43	00	00
44	44	15	15
45	45	32	32
46	46	48	48
47	63	63	63



2E-3a. FTV-36. DMSP TS T-Normal Enhancement (Table Unknown). Oceanographic Eddy Formation. 1405 GMT 10 August 1977.



2E-3b. NOAA Experimental Frontal Chart.

Table 1

Input	Gray Shade	Output	Gray Shade
00	38	00	45
39	43	00	00
44	44	15	15
45	45	32	32
46	46	48	48
47	63	63	63

Ship reports show that within gray shades 44 and 45, sea surface temperatures ranged between 11.1°C and 14.4°C. These reports are consistent with the satellite data and confirm that the eddy observed in the infrared imagery is an oceanographic phenomena and is not due to an atmospheric effect. A NOAA experimental oceanic frontal analysis (Fig. 2E-3b) derived from NOAA-5 infrared imagery at about the same time as the DMSP data, clearly depicts the same eddy formation.

Radiosonde data from Quillayute, Washington (below) provides additional evidence that the eddy is not atmospheric in origin. The sounding shows a strong low-level temperature inversion from the surface to 950 mbs. Moisture forming the anomalous gray shade area would be confined below the inversion, and would radiate at a much warmer temperature than indicated by the infrared data—probably at a temperature of 20°C, or higher.

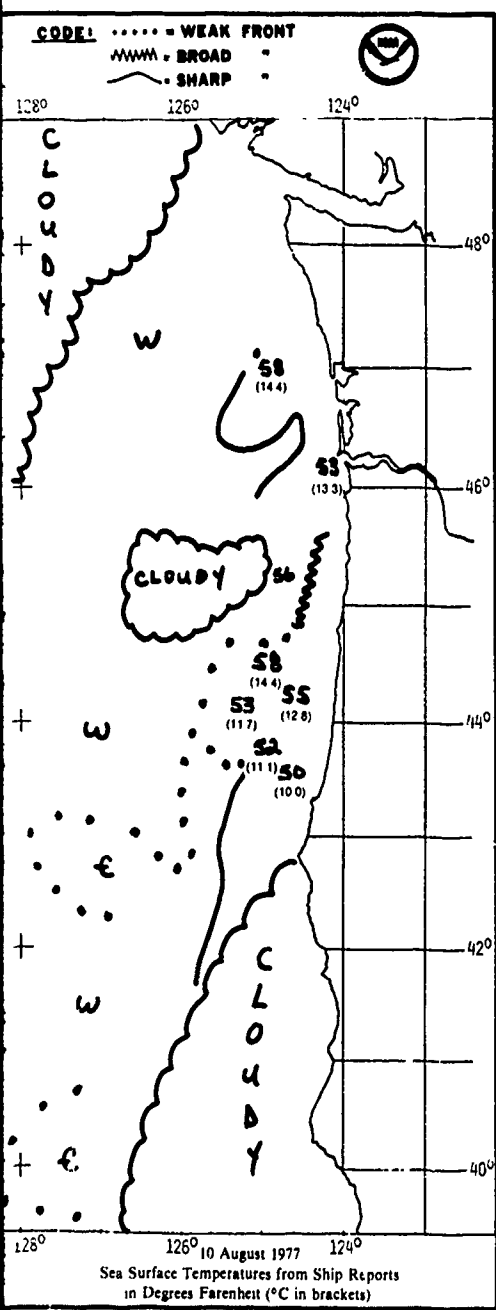
The climatology of this region provides some insight as to the relationship between the oceanographic eddy and the eddy-shaped anomalous gray shade area. In this region, the maximum coastal upwelling of cold water occurs in the California Current during the summer months and, according to Byers (1944), the maximum frequency of fog is during August—the period of this example. Fog is produced when warm, moist maritime air flows over the cold upwelled waters along the coast. The early stages of fog formation appear as anomalous gray shade patterns (NTAG, Vol. 1, Sec. 2B). The anomalous gray shade area (and the fog formation area) are restricted to the cold upwelled water zones and, consequently, often appear to conform to the pattern of the upwelled water. Note that anomalous gray shades (Fig. 2E-2a) also appear over the upwelling area along the coast to the south (corresponding to the cold water areas indicated by the infrared imagery) and along the northern boundary of the stratus cloud deck to the south of Cape Blanco.

Important Conclusions

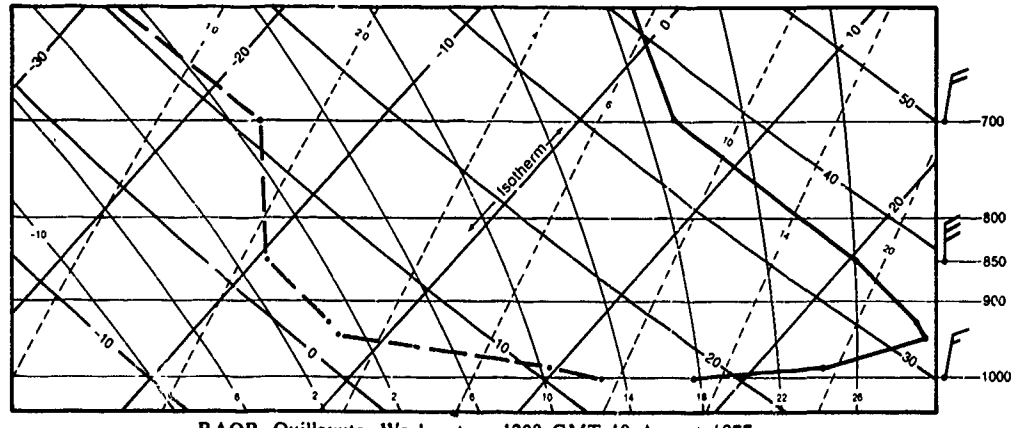
1. Anomalous gray shade patterns, indicating low-level haze or light fog, have a tendency to form over cold coastal upwelled waters.
2. The anomalous gray shade boundary often conforms to the patterns of the upwelled waters.

Reference

Byers, H.R., 1944: *General Meteorology*. McGraw-Hill Book Co., New York, 645 pp.



E-3b. NOAA Experimental Frontal Chart.



Case 2 Air-Sea Interaction

Identification of local sea state in sunglint areas where upwelling, cold eddies, or warm eddies are present

In Volume 1 (Sec. 2A, Sunglint) of this series, it was demonstrated that sunglint patterns in surface high pressure areas could be used to identify areas of calm or rough seas. It is also possible to identify local sea state in sunglint regions where oceanographic features such as upwelling, cold eddies, or warm eddies are present. Under light wind conditions and low seas, air moving over a local colder water area, such as cold coastal upwelled water or a cold oceanic eddy, will be cooled rapidly in a shallow layer near the surface. This cooling from below acts to slow vertical convection locally which, in turn, reduces wind turbulence over the area. Thus, the winds which are initially light may become calm over the local area of cold water and the wind-driven seas, correspondingly, decreased to calm conditions.

In a DMSP TS view (Fig. 2E-4a), enhanced to emphasize sea surface temperatures, cold upwelled water can be identified along the Washington-Oregon coastline. A prominent cold eddy is also located offshore just to the north of the mouth of the Columbia River, and water flowing from the Strait of Juan de Fuca has formed a large cold pool extending out to sea. In the corresponding DMSP LF view (Fig. 2E-4b), a bright sunglint pattern is observed from Vancouver Island to Oregon, where coastal stratus cloudiness begins. The presence of bright sunglint indicates that light surface winds predominate over the area. At the time of the picture, the region was under the influence of a weak high pressure gradient (not shown). Within the sunglint pattern, the more brilliant reflection reveals locally calm seas over the cold upwelled coastal waters, the cold eddy near the mouth of the Columbia River, and the cold pool of water offshore from the Strait of Juan de Fuca.



2E-4a. FTV-36, Enlarged View.
DMSP TS T-Normal Enhancement (SST-T).
Cold Water Coastal Upwelling and Cold Oceanic Eddies.
1513 GMT 12 August 1977.



2E-4b. FTV-36, Enlarged View.
DMSP LF Normal Enhancement.
Identifying Locally Calm Seas in Sunglint Patterns.
1513 GMT 12 August 1977.

Fig. 2E-5a is an enhanced DMSP WHR view of the Los Angeles Bight area which shows cold upwelled coastal waters south of San Diego and, in contrast to the above case, warm water eddies south of Santa Catalina Island and San Clemente Island. In the DMSP VHR picture acquired a short time later (Fig. 2E-5b), brilliant sunglint is observed over the upwelled coastal waters south of San Diego—indicating locally calm seas. Again this area is under the influence of high pressure, and light surface winds prevail. Note, however, that the warm eddies south of Santa Catalina and San Clemente appear as dark gray tones in the bright sunglint pattern. This indicates locally rougher seas over the warm eddies.

Since there are light winds over the area, there will be correspondingly low seas. As the air moves over the locally warmer region, it is heated rapidly from below. This increases the local vertical motions and turbulence so that the winds become stronger. The increased wind speeds produce rougher seas in comparison to the surrounding low seas.

Important Conclusions

1. Under light wind conditions and low seas, areas of cold upwelled water and cold oceanic eddies will appear as distinct bright areas in sunglint patterns, and indicate areas of locally calm seas.
2. Under light wind conditions and low seas, areas of warm oceanic eddies will appear as distinct dark gray shade areas in sunglint patterns, and indicate areas of locally rougher seas.



2E-5a. FTV-33. Enlarged View.
DMSP WHR T-Normal Enhancement (Tabl- No. 10).
Cold Water Coastal Upwelling and Warm Oceanic Eddies.
1441 GMT 23 June 1976.



2E-5b. FTV-29. Enlarged View.
DMSP VHR Low Enhancement.
Identifying Locally Calm and Rough Seas in Sunglint Patterns.
1638 GMT 23 June 1976.

Case 3 Air-Sea Interaction

Anomalous gray shade patterns produced offshore in cold, continental air outbreaks—Sea of Japan adjacent to the Asiatic Continent

Cold air flowing offshore over warmer water can be rapidly modified from below through the addition of sensible heat and water vapor. Fig. 2E-6a is a DMSP LF view of the Asiatic Continent coastal region, Japan, and the western Pacific during a winter monsoon episode. At the time of this picture, the cold polar outbreak from the Asiatic Continent has moved across Japan into the western Pacific. A cold frontal cloud band clearly defines the eastern limit of the outbreak. The area of decreased cloudiness along the Pacific coast of Honshu is due to drying out of the air as it passes downslope over the mountain range extending the length of Honshu (Tsuchiya and Fujita, 1967). Note how the cloudiness has piled-up along these same mountains on the coastal side of the Sea of Japan.

Since the polar air mass must receive a certain amount of heat and moisture from the underlying warmer sea surface in order to form convective clouds, a cloud-free area is observed between the Asiatic coast and the first convective cloud lines. The orientation of the cloud lines suggests a north to northwest low-level offshore flow, and the absence of large-scale convective buildups implies a shallow convection layer. The close spacing of the cloud lines is an indication of large air-sea temperature differences. Surface data from Vladivostok at 0000 GMT reveal a temperature of -16°C , dew point -19°C , and wind 360° at 16 kt. RAOB data from the same station and time show warmer temperatures aloft. At 850 mb, the temperature was -14.6°C , dew point -19.6°C , and wind 340° at 30 kt. Sea surface temperatures were not available offshore; however, based on climatology, they would be estimated at 0°C near the shore, and at 5°C to 10°C about 150 km offshore. The strong low-level temperature inversion would limit the development of the surface convection layer so that convective cloudiness would be restricted to low levels. Convective cloud line formation is also indicated by the presence of strong vertical wind speed shear at low levels.

An enlarged view of the Asiatic Continental coastal region (Fig. 2E-7a) reveals a broad anomalous gray shade band, in the vicinity of Vladivostok, between the shoreline and the convective cloud lines, and narrower anomalous gray shade bands offshore of the Sikhote Alin Range. The anomalous gray shades are attributed to the increased concentration of moisture introduced at low-levels due to rapid water vapor transfer from the warmer coastal waters to the cold, polar air as it moves offshore. As a result, condensation nuclei in the air grow rapidly in size and the high moisture content appears as anomalous gray shades, due to Mie scattering and/or direct solar ray reflection from the water particles. The presence of a strong stable layer over the shallow surface convection layer, as indicated by the Vladivostok RAOB, restricts the added moisture to the surface layer, and creates the conditions favorable for anomalous gray shade formation.

During a winter monsoon episode over the Sea of Japan, the high mountains in the North Korean coastal region and the Sikhote Alin Range to the northeast cause a significant blocking of low-level cold air outflow from the Asian Continent. However, river valleys and canyons provide a passage for the low-level cold air to the Sea of Japan. In Fig. 2E-7a, note that the river valleys labeled A, B, and C appear lighter in tone than the adjacent ridges. Since the rivers are frozen over and snow covered and the ridges are forested, the rivers stand out clearly against the darker background of the ridges.



2E-6a. FTV-35. DMSP LF Log Enhanc

The anomalous gray shade bands are observed to extend primarily from the river valley exits to the Sea of Japan. Note that the bands merge with the low-level cloud lines offshore and that the bands can be used to trace the direction of the low-level wind flow back to the passages in the coastal terrain. Thus, gray shade bands exiting from passages in coastal mountainous terrain indicate the direction of offshore flow. The major river valley to the north of Vladivostok (Fig. 2E-7b) accounts for the broad gray shade pattern to the south of this location. Narrower gray shade bands occur at the exits of river valleys along the Sikhote Alin Range.

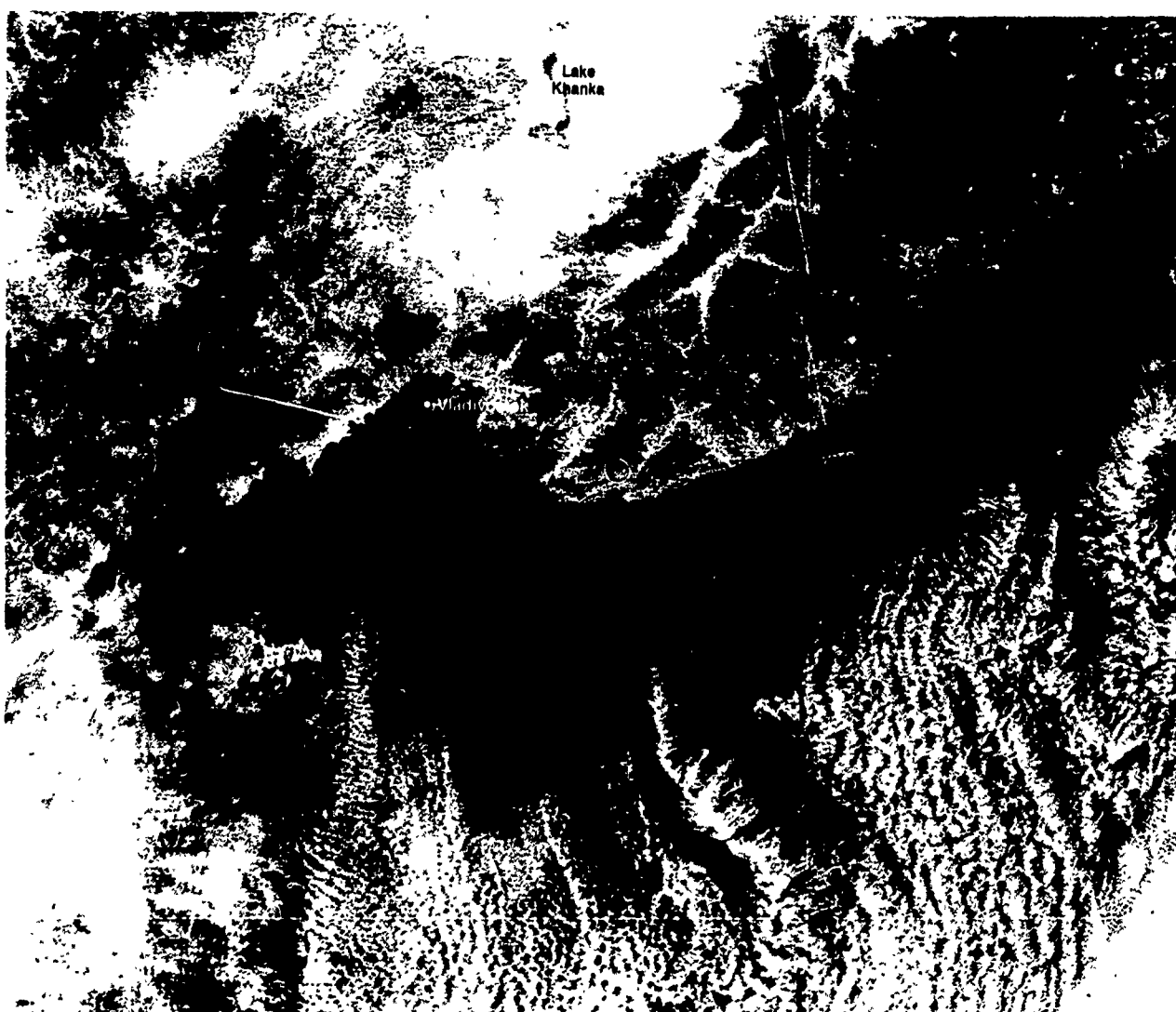


2E-6a. FTV-35. DMSP 1 F Log Enhancement. Cloud Patterns in a Winter Monsoon. 0146 GMT 2 December 1977.

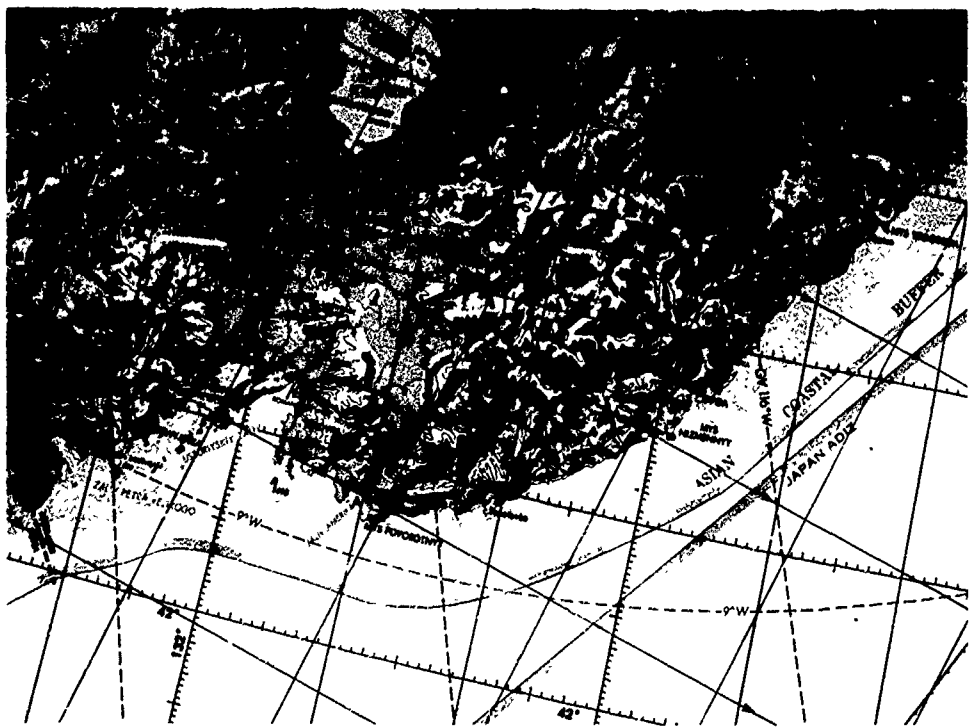
The air to the lee of the high areas in the ranges is much drier, due to downslope motion, than that reaching the sea through the passages. These areas are free of anomalous gray shades and appear as dark areas in the imagery. Since the air in these areas is dry, surface visibilities are better than in the bands, where the increased moisture content in the air produces hazy conditions. On the other hand, the cold air reaching the sea through the narrow passages is accelerated by the funneling action on the flow so that the surface winds are higher and the seas rougher than in the dark areas in the lee of the higher coastal terrain (which are sheltered areas). Thus, the anomalous gray shade bands are areas of restricted surface visibilities, stronger winds, and rougher seas as compared to adjacent dark areas which are areas of higher surface visibilities, lighter winds, and calmer seas.

Important Conclusions

1. Anomalous gray shade patterns formed in cold, continental air outbreaks over warmer coastal waters are useful indicators of low-level wind direction.
2. Wind speeds are higher, seas are rougher, and visibilities lower, in such areas, compared to adjacent darker regions.



2E-7a. FTV-35. Enlarged View. DMSP LF Log Enhancement. Anomalous Gray Shade Patterns in Mountainous Coastal Regions During a Winter Monsoon. 0146 GMT 2 December 1977.



2E-7b. Map of Asiatic Coast Adjacent to the Sea of Japan.

Reference

Tsuchiya, K., and T. Fujita, 1967: A satellite meteorological study of evaporation and cloud formation over the western Pacific under the influence of the winter monsoon. *J. Meteor. Soc. of Japan*, **45**, 232-250.

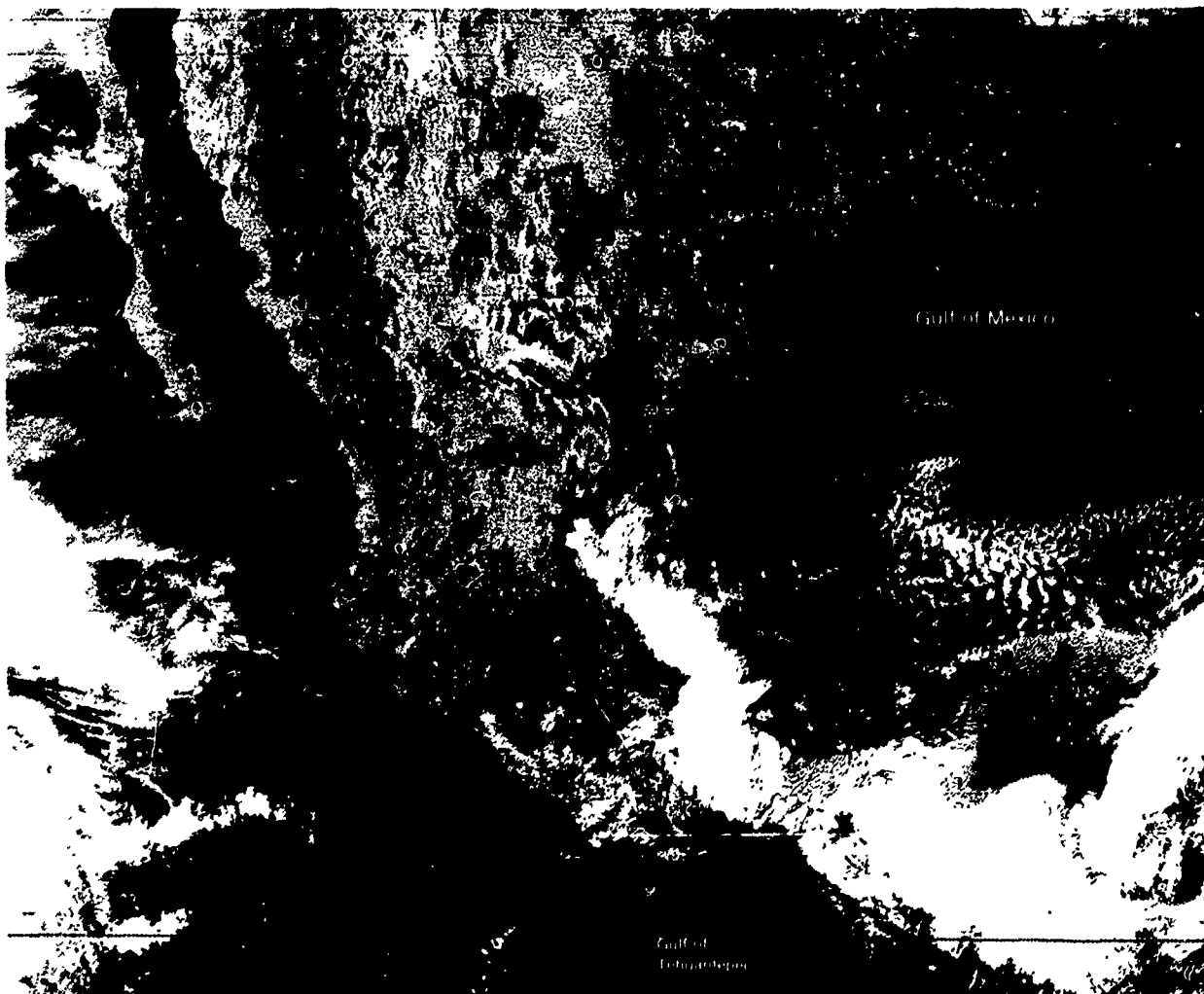
Case 4 Air-Sea Interaction

Anomalous gray shade patterns produced offshore by strong, cold winds funneling through gaps in mountainous coastal terrain—Gulf of Tehuantepec

Fig. 2E-8a is a DMSP LF view of Mexico and portions of Central America extending northward to the southern U.S. A light-toned gray shade area extends southward over the Gulf of Tehuantepec into the Pacific Ocean. An enlargement of this area is shown in Fig. 2E-9a.

The anomalous gray shade pattern is located over the region where strong, local northerly winds, called Tehuantepecers, occur during the winter months (Hurd, 1929). The Tehuantepecers sweep across the Isthmus of Tehuantepec, from the Gulf of Mexico to the Pacific Ocean, when intense polar continental anticyclones penetrate deep into the tropics.

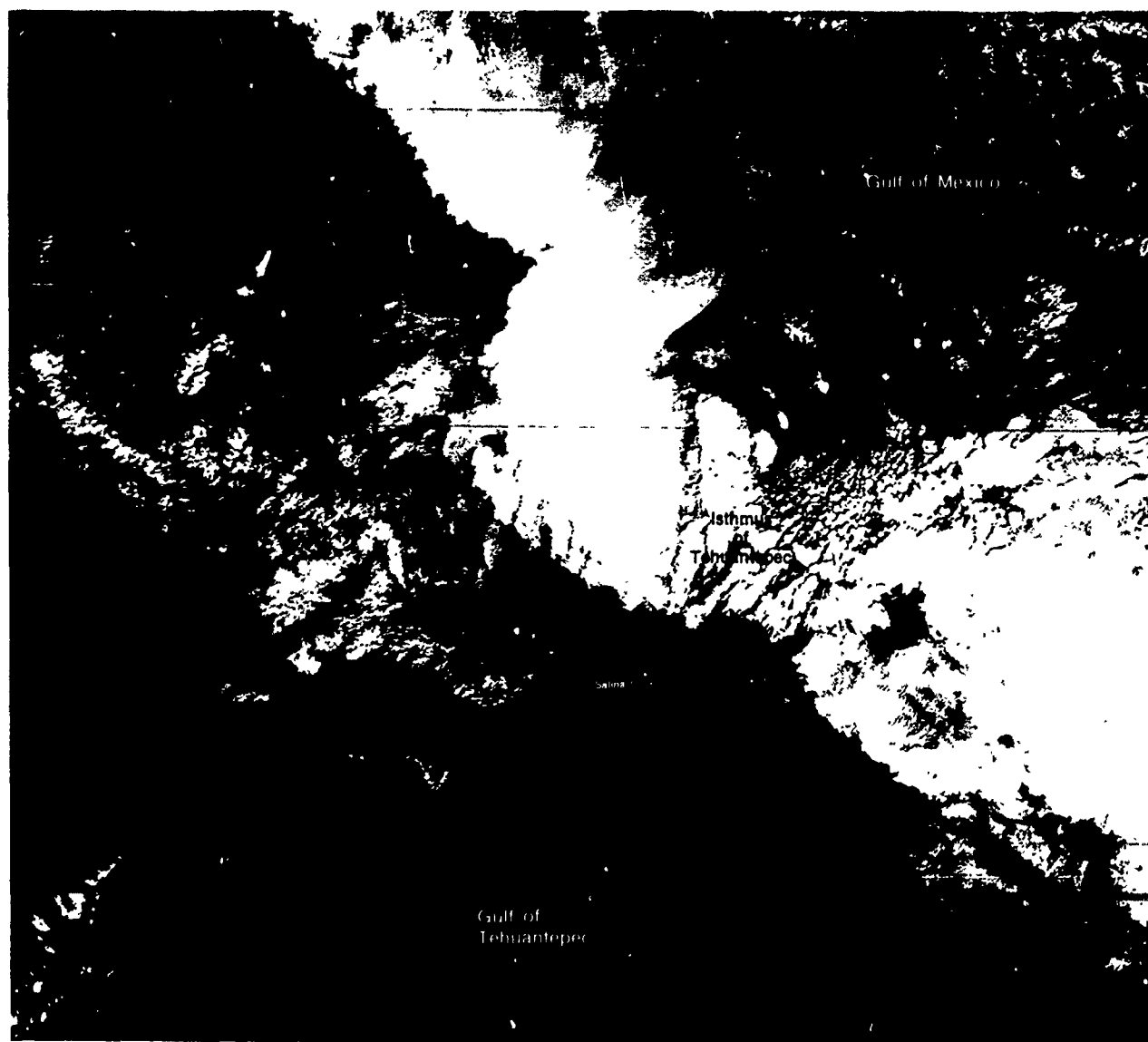
A gap in the Sierra Madre mountains (Fig. 2E-9b) provides a channel for the northerly winds. These winds accelerate to extreme velocities as a result of the pressure gradient through the area, venturi effects due to channeling, and from additional speed gained in descending from the mountain pass altitude of about 800 ft down to sea level.



2E-8a. FTV-35. DMSP LF Log Enhancement. Anomalous Gray Shade Pattern Delineating a Norther (Tehuantepecer) in the Gulf of Tehuantepec. 1746 GMT 26 January 1978.

Satellite evidence of Tehuantepecers have been described by Parmenter, 1970; Strong, De Rycke, and Stumpf, 1972; and Stumpf, 1975. These studies describe the disruption of sunglint patterns, in satellite visible imagery, due to strong winds of the Tehuantepecer roughening the sea surface; and the appearance of a distinctive cold water plume in satellite infrared data. The cold water plume is caused by the combined effect of upwelling of cold, subsurface water, due to the strong divergence of surface water away from the coast; and upwelling offshore, to the south, along the axis of the maximum wind. The upwelling widens southward and, according to Stumpf (op. cit.), this is due to the outward diffusion of colder upwelled water taking place along the wind axis. Note that the outer edges of the anomalous gray shade pattern diverge and show a similar widening to the south.

This example reveals a new aspect concerning the probable cause for the appearance of the anomalous gray shade in the DMSP visible data. The DMSP visible imagery was acquired in a region remote from sunglint so that sea state changes are not detectable as a sunglint effect. Nevertheless, a distinct light gray shade plume is evident in the region of the Tehuantepecer.



2E-9a. FTV-35. Enlarged View. DMSP LF Log Enhancement. Anomalous Gray Shade Pattern. 1746 GMT 26 January 1978.

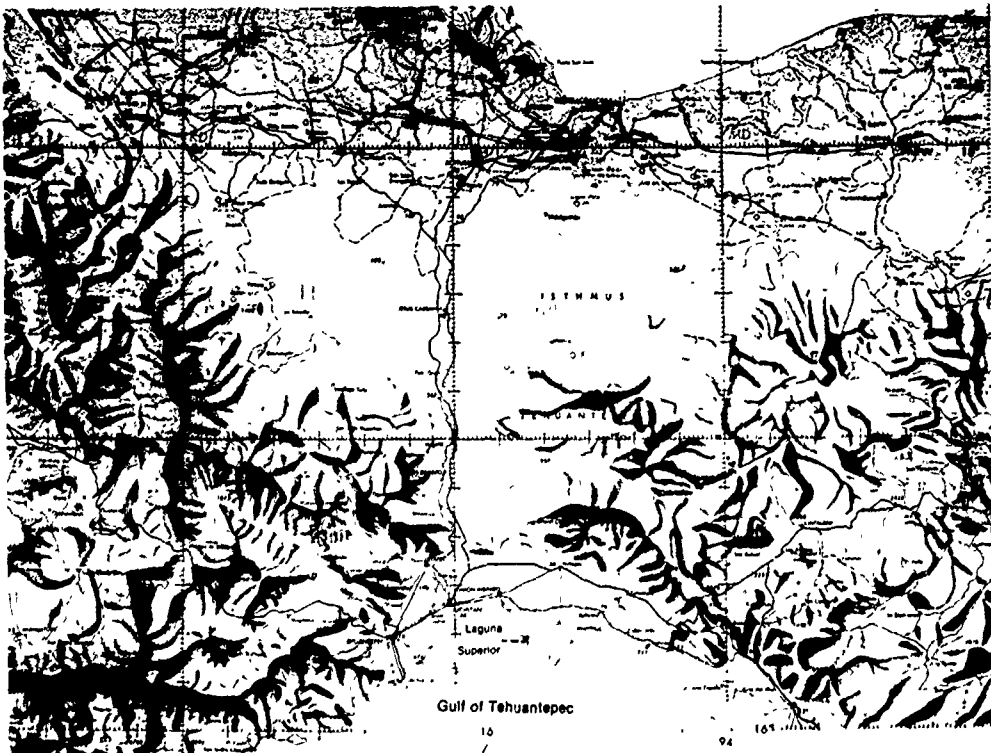
Synoptic analyses revealed that a cold front moved through the Gulf of Mexico and past the Yucatan Peninsula on 26 January 1978, just prior to the time of the DMSP data. High pressure and cold air behind this frontal zone provided ideal conditions for the onset of the Tehuantepecer. Surface observations at Salina Cruz, on the Pacific Coast, reveal its occurrence as shown below:

	Date/Time (GMT)	Temperature (°C)	Dew Point (°C)	Winds (kt)
26 Jan 78	1200	21	19	360/40
	1800	26	15	360/35
27 Jan 78	0000	25	18	360/30
	0600	22	12	360/30
	1200	21	13	360/35
	1800	23	16	030/40

These reports indicate that strong winds blew continuously on the coast at Salina Cruz for over 24 hours. This is not uncommon. A Tehuantepecer may last for several days, as long as the pressure gradient through the Isthmus of Tehuantepec is maintained. At sea, stronger winds are normally encountered. Stumpf (1975) reports that one ship in a Tehuantepecer was severely sandblasted, having encountered maximum sustained winds of 97 kt with gusts to 117 kt.

Sea-salt aerosol production has been shown to be enhanced as whitecap activity and wind speed increases (Savoie and Prospero, 1977). Heavy haze formation occurs as the cold Tehuantepecer winds flow outward across the warmer waters of the gulf, and moisture from the sea accumulates on condensation nuclei (principally sea-salt aerosols). This haze is detected in DMSP visible imagery as a result of scattering and reflection of sunlight by the particles, producing the characteristic anomalous gray shade pattern.

continued on following page



2E-9b. Topographic Map of the Isthmus of Tehuantepec.

This interpretation is additionally supported by a compilation of data concerning the frequency of occurrence of haze at sea, which reveals that, during the winter season, the Gulf of Tehuantepec is one of the world's most hazy areas (McDonald, 1938). The frequency of occurrence decreases sharply north and south of this area suggesting a strong relationship with the increased frequency of Tehuantepecer force winds during the winter season.

Because of the high wind speeds in this example, it seems plausible that whitecap formation and foam could make a significant contribution to the total sensed brightness. GOES-1 data (Fig. 2E-11a), however, acquired less than an hour prior to the time of the DMSP data (Fig. 2E-11b) show only a slight increase in brightness in the Gulf of Tehuantepec, as compared to adjacent areas. This system, although not as responsive as DMSP in sensing aerosols, is more sensitive than DMSP in revealing ocean surface features, due to the sensor's strong response at shorter wavelengths, where reflectance from a water surface is maximized (Maul, 1975). Since a brighter response is not obtained in the GOES-1 data, an aerosol effect is implied as the chief cause for the anomalous gray shade.

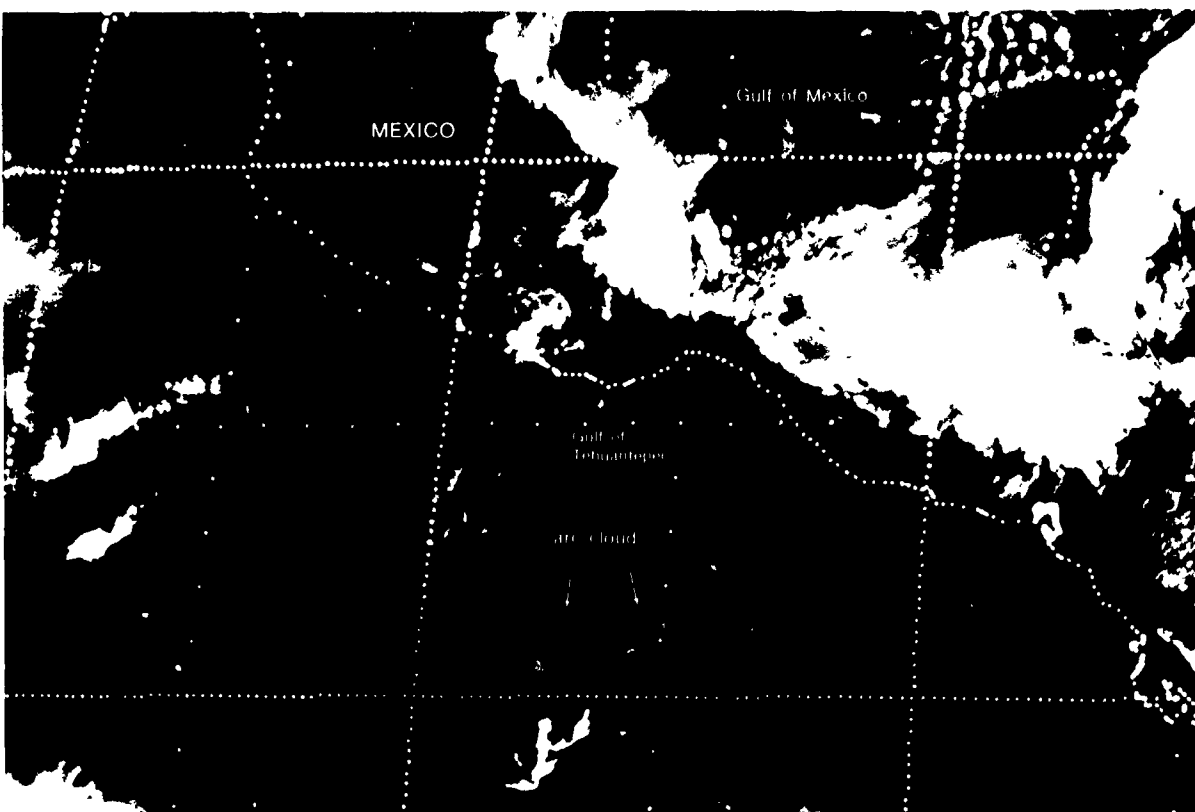
Suggestions of an arc cloud at the leading edge of the outrushing cold air can be detected in the GOES-1 data, which extends further south than the DMSP data. This cloud formation often reaches squall-line intensity accompanied by showers and heavy seas. Swells generated by the Tehuantepecer have been recorded nearly 1000 n mi to the south, at the Galapagos Islands (Hurd, op. cit.).

Note that cloud lines and cloud patches can be seen on the east and west sides of the anomalous gray shade pattern in the DMSP data (Fig. 2E-11b). These lines also can reach squall line intensity. They delineate a wind shear line and the transition zone between the strong winds and higher seas within the anomalous gray shade pattern and the lighter winds and lower seas outside the pattern.

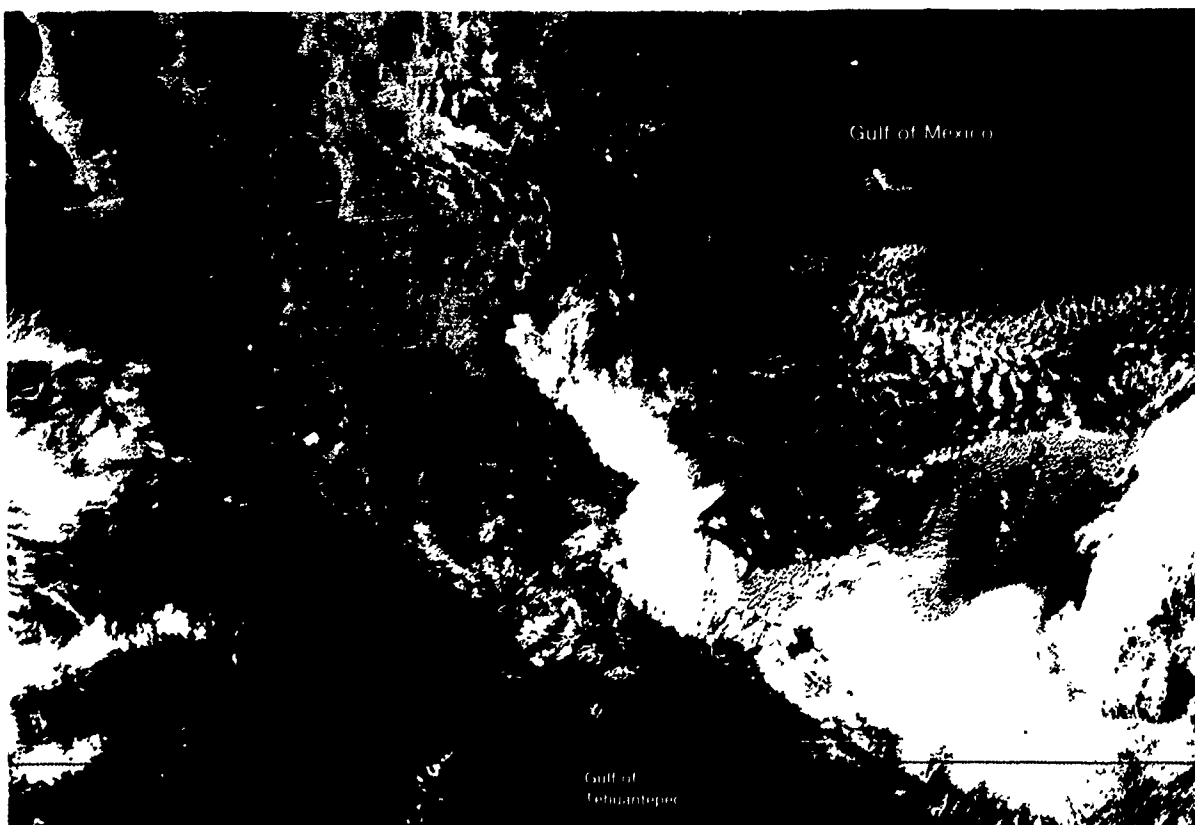
A plume similar to the anomalous gray shade pattern shown in this example has also been documented in Volume I (Sec. 2B, Case 3), in association with a mistral wind event in the Mediterranean.

References

- Hurd, W.E., 1929: Northerns of the Gulf of Tehuantepec, *Mon. Wea. Rev.*, **57**, 192-194.
Maul, G.A., 1975: On the use of the Earth Resources Satellite (LANDSAT-1) in Optical Oceanography, *Remote Sensing of Environ.*, **4**, 95-128.
McDonald, W.F., 1938: *Atlas of Climatic Charts of the Oceans*, Dept. of Agriculture, Weather Bureau, Washington, D.C.
Parmenter, F.C., 1970: A Tehuantepecer, *Mon. Wea. Rev.*, **98**, 479.
Savoie, D.L., and J.M. Prospero, 1977: Aerosol concentration statistics for the northern Tropical Atlantic, *J. Geophys. Res.*, **82**, 5954-5964.
Strong, A.E., R.J. De Rycke, and H.G. Stumpf, 1972: Satellite detection of upwelling and cold water eddies, *Proc. of Eighth Inter-Symposium on Remote Sens. of Environ.*, AMS, Boston, 1060-1081.
Stumpf, H.G., 1975: Satellite detection of upwelling in the Gulf of Tehuantepec, Mexico, *J. Phys. Oceanogr.*, **5**, 383-388.
Ibid., *Mar. Wea. Log.*, **46**, 104-105.



2E-11a. GOES-1. Enlarged View. Visible Picture. Absence of Anomalous Gray Shade in the Gulf of Tehuantepec.
1700 GMT 26 January 1978.



2E-11b. FTV-35. DMSP LF Log Enhancement. Anomalous Gray Shade Pattern Delineating a Norther (Tehuantepecer)
in the Gulf of Tehuantepec. 1746 GMT 26 January 1978.

Case 5 Air-Sea Interaction

Formation of convective cloud lines along oceanic fronts— The Gulf Stream

GOES-1 visible imagery of the Eastern U.S. shows that a cloud line formation is observed in about the same offshore location, northeast of Florida, on three successive days (Fig. 2E-12a, 12b, and 12c). The corresponding GOES-1 infrared picture (Fig. 2E-12d), on the first day, reveals a significant feature of the cloud line position—it lies along the eastern boundary of the Gulf Stream. The higher resolution of the DMSP LF picture (Fig. 2E-13a) gives a more detailed view of the cloud line, and the DMSP TS picture (Fig. 2E-13b) also substantiates the position of the cloud line along the eastern boundary of the Gulf Stream. The persistence of a cloud line and the absence of other low-level cloudiness in the area suggests that the cloud line formation is due to an air-sea interaction process.

In the DMSP LF view, a bright sunglint pattern is observed extending from the Caribbean Sea northward over Florida, with diminished intensity. Note the dark-tone patches along the eastern and western Florida coastlines—these patches indicate calm sea areas. The dark-tone indentation of the sunglint pattern to the north suggests a surface ridge line across Apalachee Bay. Surface reports and a streamline analysis (Fig. 2E-13c) confirm this interpretation. The analysis shows that the ridge continues eastward out over the area of the cloud line formation along the Gulf Stream.

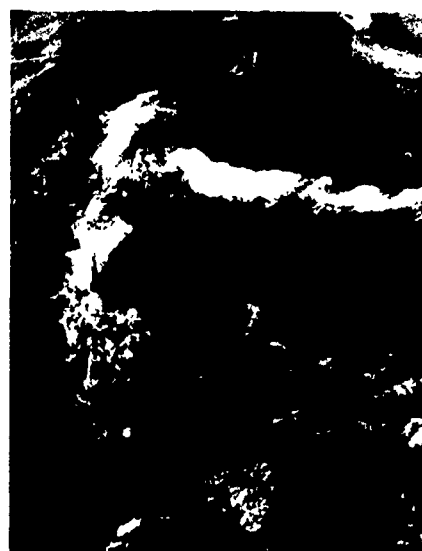
Although direct surface observations are not available in the vicinity of the cloud line, the presence of a ridge suggests very weak or calm wind conditions over the area. One might expect, therefore, that air residing over the Gulf Stream would be heated from below and, conversely, air just to the south cooled from below due to the colder Sargasso Sea temperatures and/or the presence of a large cold eddy. Thus the differential heating effect on the air on either side of the Gulf Stream would create a density discontinuity at low levels. This would induce a pressure gradient directed from the cooler air towards the warmer air over the Gulf Stream. The warm air along the boundary of the Gulf Stream would be lifted and where the condensation level was reached, convective clouds would form; this would account for the patchiness in the cloudiness along the cloud line. Cloudiness is not observed along the Gulf Stream's western edge since the continental shelf air is much drier than air further out to sea which has had a long history in a maritime environment.

Important Conclusion

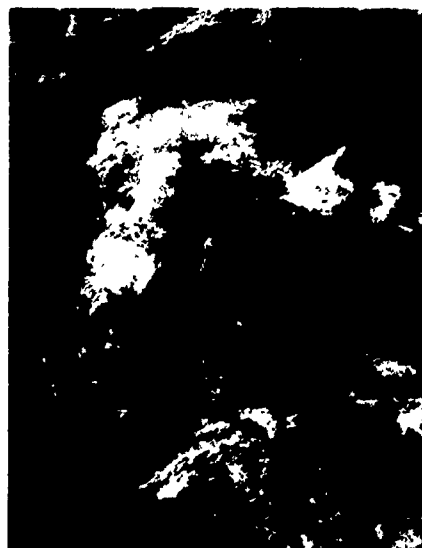
1. Convective cloud lines may form along oceanic fronts where differential heating effects induce air motion that results in a low-level convergence region along the frontal boundary.



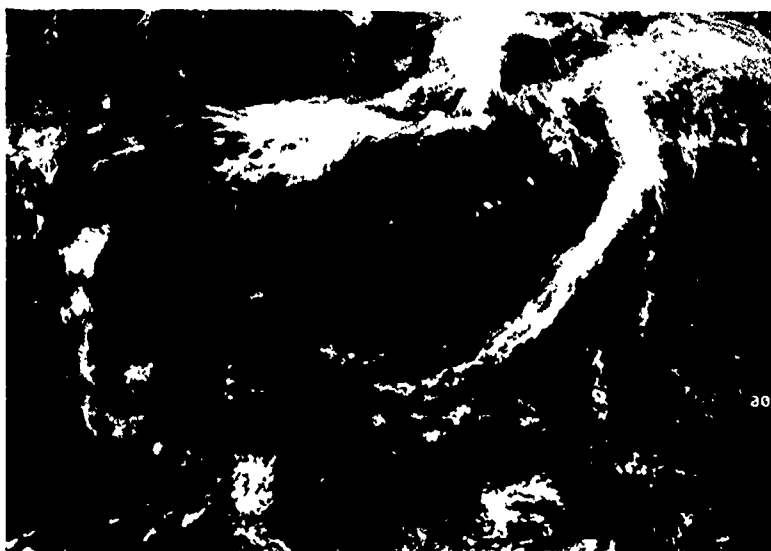
2E-12a. GOES-1. Visible Picture. Convective



2E-12b. GOES-1. Visible Picture. Convective



2E-12c. GOES-1. Visible Picture. Convective



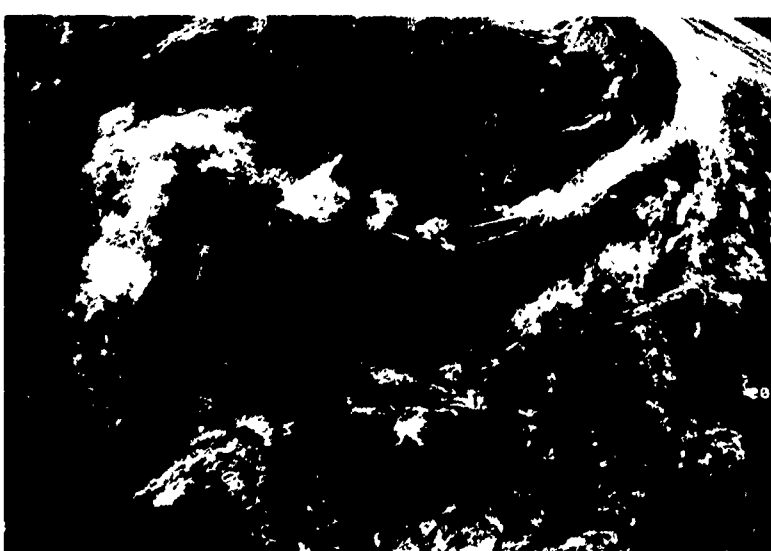
2E-12a. GOES-1. Visible Picture. Convective Cloud Line. 1700 GMT 28 April 1977.



2E-12d. GOES-1. Infrared Picture. Convective Cloud Line Along the Gulf Stream. 1700 GMT 28 April 1977.



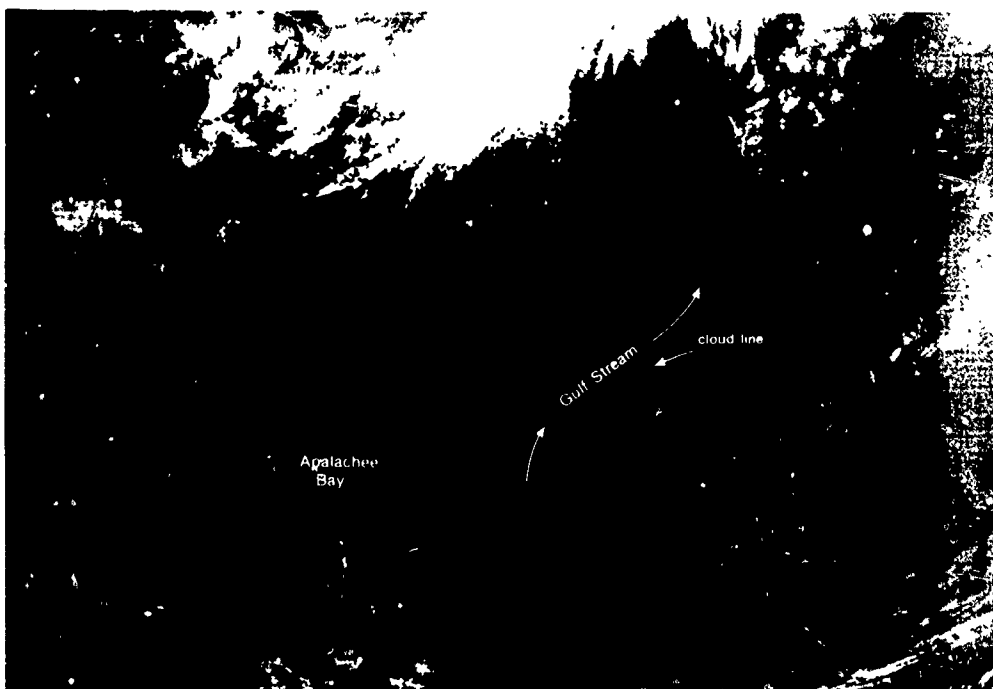
2E-12b. GOES-1. Visible Picture. Convective Cloud Line. 1700 GMT 29 April 1977.



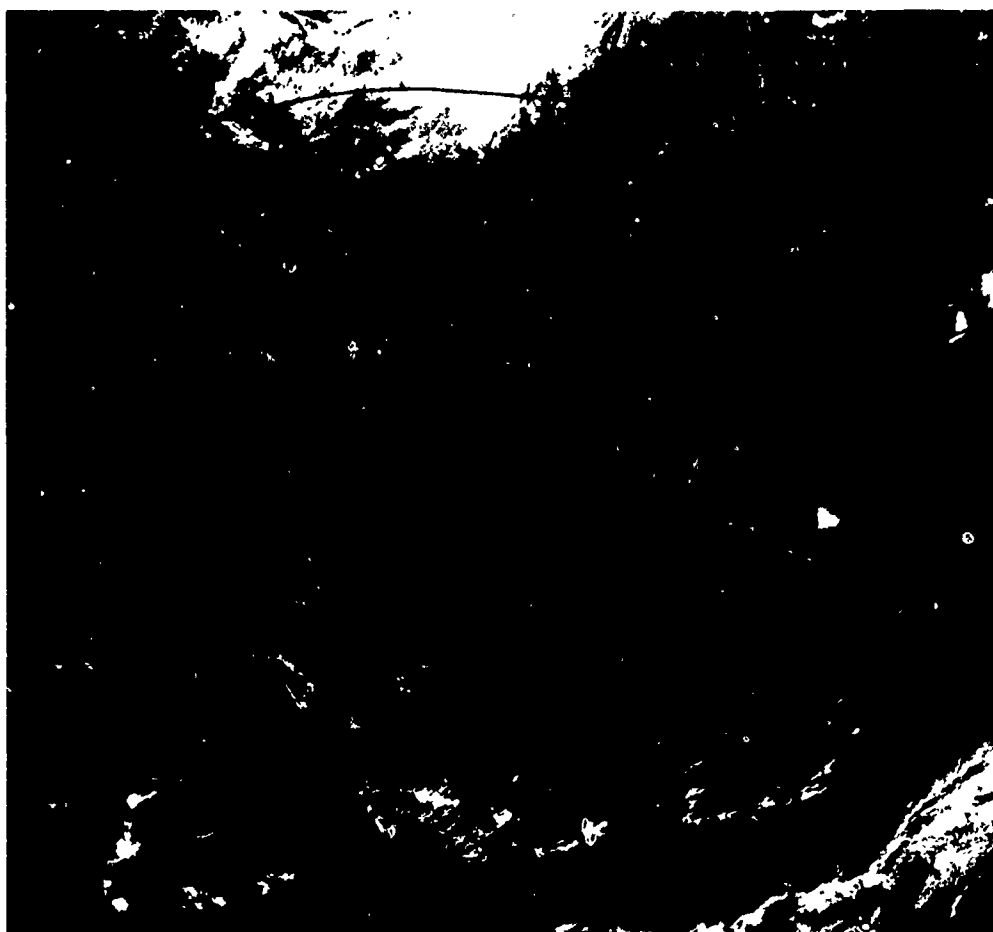
2E-12c. GOES-1. Visible Picture. Convective Cloud Line. 1700 GMT 30 April 1977.



2E-13a. FTV-35, DMSP I.F Low Enhancement, Convective Cloud Line.
1639 GMT 28 April 1977



2E-13b. FTV-35. DMSP TS T-Normal Enhancement. Convective Cloud Line Along the Gulf Stream.
1639 GMT 28 April 1977.



2E-13c. FTV-35. DMSP LF Low Enhancement. Convective Cloud Line, 1639 GMT 28 April 1977
Surface Wind Reports and Streamline Analysis. 1800 GMT 28 April 1977.

Case 6 Air-Sea Interaction

Detection of shallow water cooling areas—Bahama Banks

The shallow waters of the Bahama Banks, and shallow water areas surrounding the islands of the Caribbean, have been detected as anomalous gray shades, in the visible data mode of meteorological satellite systems, beginning with TIROS-1 (see NTAG, Vol. 1, Sec. 2B, Case 8). These shallow water areas can also be identified in satellite infrared data during the winter months.

Fig. 2E-14a is a Nimbus-5 infrared image of the Bahama Banks region taken on 24 December 1972 by the Surface Composition Mapping Radiometer (SCMR), which senses radiation in the 10.2 to 11.2 μm range. In this spectral interval, the absorption of radiation by water vapor and other atmospheric constituents is minimal. The sensor has a spatial resolution at the satellite subpoint of about 926 m (0.5 n mi), so contamination by small cloud elements is also minimized. Thus, gray shade variations in open water areas can be attributed to variations of sea surface temperature. The light-tone gray shades identify the area of

2E-14a. Nimbus-5.
SCMR Infrared Picture.
Detection of Shallow
Water Areas.
24 December 1972.



shallow water over the Bahama Banks and over the shelf area between Cuba and the Isle of Pines. Shallow water (light-tones) can also be seen over the continental shelf region of the Florida Keys, although it is not as pronounced.

The bathymetry of the Bahama Banks area averages between one and three fathoms (1.8 to 5.5 m) out to the shelf break, where it rapidly drops to 750 fathoms (1372 m) or more. There is a close correspondence between the area bounded by the five fathom contour delineating the shallow bottom topography (foldout) and the region of the cold water mass.

Infrared imagery from other satellite systems during the winter show the same relatively cool water pattern over the Bahama Banks. For example, Fig. 2E-15a shows a view of this area from the DMSP WHR sensor. Since the light-tone gray shade pattern in this DMSP picture is almost identical to that in the Nimbus-5 picture, this is additional verification that the observed surface temperature effect is a shallow water phenomenon. Note also, in this picture, that convective cloud line formation is generally restricted to the warmer water areas.



2E-15a. FTV-31.
DMSP WHR
T-Normal Enhancement.
Detection of Shallow
Water Areas.
1215 GMT
13 February 1976.

The shallow water cooling is caused by evaporational cooling and sensible heat loss to colder air masses that move over the area during the winter months. Cooling to progressively greater depths occurs continuously, and it is intensified during nighttime as the colder surface water sinks and is replaced by warmer subsurface water. In shallow water, such as over the Bahama Banks, the heat loss per unit volume must be distributed over the depth of the convective mixing layer which is only a few fathoms deep. In the surrounding deeper water, however, the convective mixing layer is determined by the location of the permanent thermocline, which is at a greater depth, so that a greater mass of water is involved in the mixing process and, as a result, the total heat loss per unit volume is much less than in the shallow water areas. Thus the surface temperature of the shallow water areas appears colder in the infrared imagery.

Ship surveys in these areas have also found colder surface temperatures in the shallow water areas over the Bahama Banks during the winter months. For example, Smith (1940) using conventional sea surface temperature data, found that the shallow water was up to 2°C colder; and that the maximum air-sea temperature difference over the Banks occurred during the month of December.

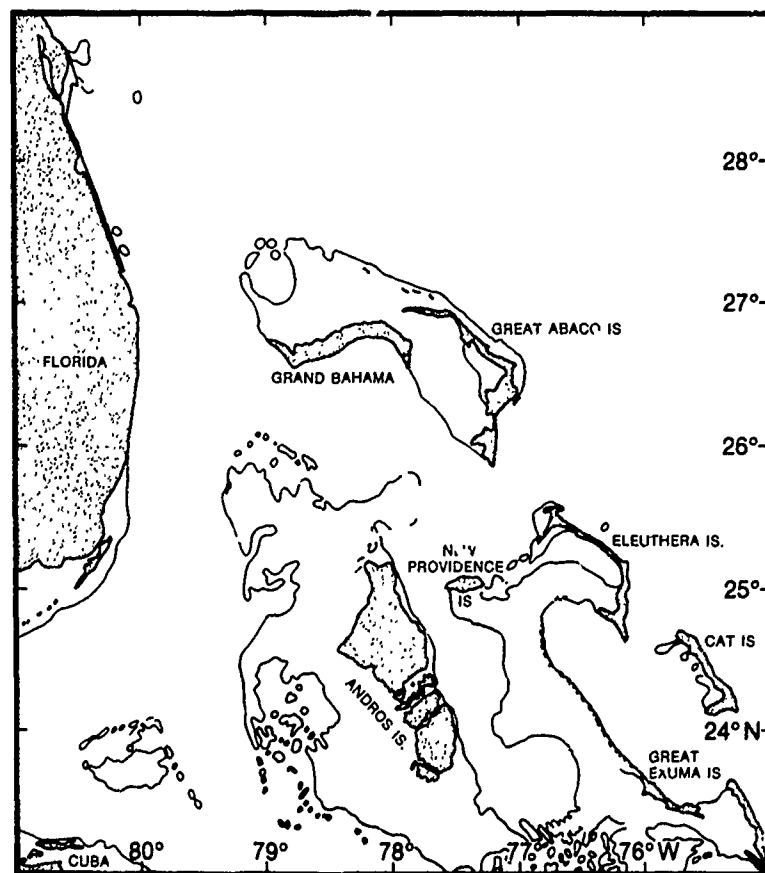
Important Conclusion

1. During the winter months, waters over shallow bank areas, such as the Bahama Banks, appear colder than the surrounding deeper water areas. These colder, shallow waters can be readily identified in satellite infrared imagery.

Reference

Smith, C.I., 1940: The Great Bahama Bank; I. General hydrographical and chemical features. *J. Marine Res.*, 3, 147-189.

2E-15a. FTV-31.
DMSP WHR
T-Normal Enhancement.
Detection of Shallow
Water Areas.
1215 GMT
13 February 1976.



Map of the
Bahama Islands
With Five
Fathom Contour.

3

Section 3

Oceanographic Phenomena and Effects

3A Oceanic Frontal Systems

Characteristics of Oceanic Fronts 3A-1

Case Studies

- 1 Oceanic fronts in a major ocean current—
The Gulf Stream 3A-4
- 2 Shallow oceanic fronts—
seas adjacent to the Korean Peninsula 3A-6
- 3 Subtropical oceanic frontal systems—
Cape San Lucas, Baja California 3A-8
- 4 Oceanic fronts in a broad surface current—
The California Current 3A-10
- 5 Intense oceanic front—
Gulf of Mexico Loop Current 3A-14

3B Oceanic Eddies

Characteristics of Oceanic Eddies 3B-1

Case Studies

- 1 Eddies formed by meanders of a strong oceanic current—
The Gulf Stream 3B-2
- 2 Eddy patterns in the western Mediterranean—
Alboran Sea Eddies 3B-4
- 3 Eddy formation due to the deflection of an ocean current
by coastal features—The California Current 3B-6
- 4 Eddy patterns in the confluence zone between two oceanic
frontal systems—The Kuroshio and Oyashio 3B-8

3C Upwelling

Characteristics of Upwelling 3C-1
Causes of Coastal Upwelling 3C-2
Other Forms of Upwelling 3C-3

Case Studies

- 1 Interaction of intense coastal upwelled waters
with a broad ocean current—The California Current 3C-4
- 2 Detection of upwelling in cold continental air outbreaks
over coastal waters—Gulf of Mexico 3C-6

3D Internal Waves

Internal Waves in the Ocean	3D-1
Satellite Observations of Internal Waves	3D-3

Case Studies

1 Internal Waves in the Sulu Sea.....	3D-4
2 Refraction of internal waves around Pratas Island and the Pratas Reef—South China Sea	3D-8

3E Other Phenomena

Other Phenomena	3E-1
-----------------------	------

Case Studies

1 Detection of Sea Ice	3E-2
2 Detection of river discharge plumes into coastal waters—The Columbia River	3E-4
3 Detection of river outflow sediments in coastal areas—The Andaman Sea	3E-5

3A Oceanic Frontal Systems

Characteristics of Oceanic Fronts

Oceanic fronts are features of the upper layers of the oceans and are located at the boundaries between water masses of different density (Cromwell, 1956; Uda, 1959; Laevastu and LaFond, 1970). Since the density of sea water is a function of both temperature and salinity, oceanic fronts are identified according to these physical properties, and are called temperature (thermal) fronts or salinity (haline) fronts. Oceanic fronts appear on the sea surface as zones of pronounced horizontal temperature and/or salinity gradients. In addition to differences in temperature and salinity there may be differences in water color, wave height, and current velocity. Across frontal boundaries beneath the sea surface there may be changes in light transmission, biological population, dissolved chemicals, and sound velocity propagation. The entire extent of the boundary between the two kinds of water, and the interactions along it are referred to as an oceanic frontal system. Knowledge of oceanic frontal systems is important to the naval environmental forecaster, not only for applications relating to underwater sound propagation, but also as a basis for tactical weather forecasts, which must take into account air-sea interactions.

References

- Cromwell, T., and J.L. Reid, Jr., 1956: A study of oceanic fronts. *Tellus*, 8, 94-101.
Laevastu, T., and E.C. LaFond, 1970: *Research Reviews* (November), Office of Naval Research, Washington D.C., 9-13.
Uda, M., 1959: Oceanographic seminars. Manuscript Report Series (Oceanographic and Limnological) No. 51, Fisheries Research Board of Canada, 1-110.

Mean Positions of Major Surface Oceanic Currents

1. Florida Current
2. Gulf Stream
3. Labrador Current
4. West Greenland Current
5. East Greenland Current
6. North Atlantic Current
7. North Equatorial Current
8. Equatorial Counter Current
9. South Equatorial Current
10. Brazil Current
11. Falkland Current
12. Antarctic Circumpolar Current
13. Benguela Current
14. Agulhas Current
15. North Equatorial Current
16. Equatorial Counter Current
17. South Equatorial Current
18. Kuroshio
19. Oyashio
20. North Pacific Current
21. Alaska Current
22. California Current
23. North Equatorial Current
24. North Equatorial Counter Current
25. Equatorial Current
26. South Equatorial Counter Current
27. South Equatorial Current
28. Humboldt Current

**Mean Positions of Major Oceanic Fronts
(After Cheney and Winfrey, 1976)**

Atlantic Ocean Fronts

1. Loop Current (Gulf of Mexico)
2. Gulf Stream
3. North Atlantic Current (North Polar Front)
4. Slope Front
5. Sargasso Sea Front
6. Subtropical Convergence
7. Iceland-Faeroe Islands Front
8. Denmark Strait Front
9. East Greenland Polar Front
10. Greenland-Norwegian Sea Front
11. Bear Island Front
12. Northwest African Upwelling
13. Gulf of Guinea Front
14. Guiana Current
15. Benguela Upwelling
16. Subtropical Convergence
17. Antarctic Convergence (South Polar Front)
18. Antarctic Divergence

Mediterranean Sea Fronts

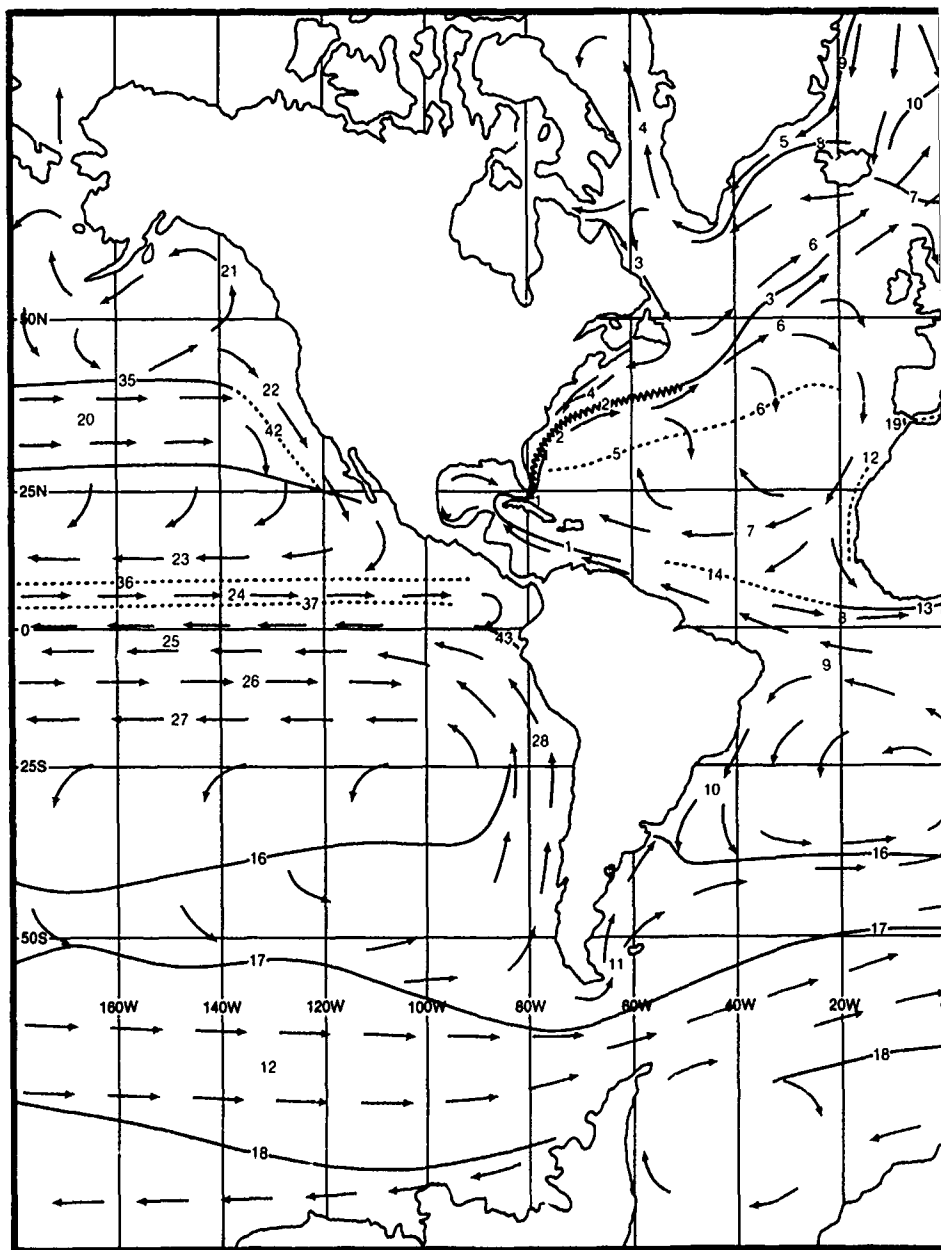
19. Huelva Front
20. Alboran Sea Front
21. Maltese Front
22. Ionian Sea Front
23. Levantine Basin Front

Indian Ocean Fronts

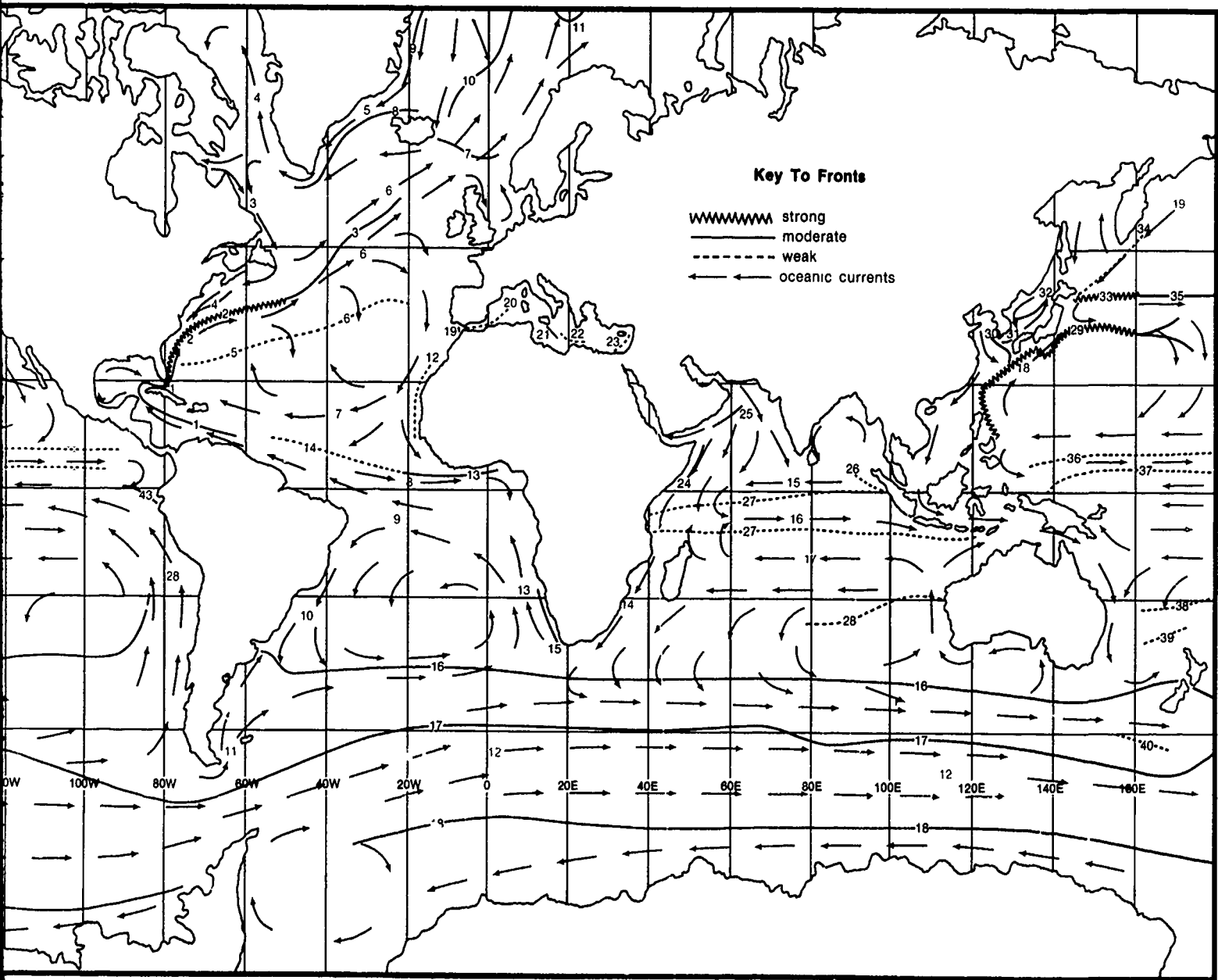
24. Somali Upwelling
25. Arabian Upwelling
26. Indian Ocean Salinity Front
27. Equatorial Countercurrent Fronts
28. West Australian Front

Pacific Ocean Fronts

29. Kuroshio Front
30. Yellow Sea Warm Current
31. Korean Coastal Front
32. Tsushima Current
33. Oyashio Front
34. Kuril Front
35. Subarctic Front
36. North Doldrum Salinity Front
37. South Doldrum Salinity Front
38. Tropical Convergence
39. Mid Tasman Convergence
40. Australian Subarctic Front
41. Subtropical Front
42. California Front
43. East Pacific Equatorial Front



Mean Surface Positions of the Major Oceanic Fronts and Currents of the World



Flow phenomena in the oceans may be considered analogous to flow phenomena observed in the atmosphere. In the oceans, however, flow phenomena are much slower and occur in a more compact form (Robinson, 1976). For example, narrow currents such as the Gulf Stream and the Kuroshio have speeds on the order of 150–260 cm s⁻¹ (3–5 kt) concentrated in zones of less than 75 km (40 n mi) wide, compared to atmospheric polar jet streams which exhibit speeds of 26 m s⁻¹ (50 kt) or more in zones exceeding 300 km (162 n mi) wide. Variability in the flow may consist of meandering of a major ocean current, eddies separated from a major current, eddies formed due to horizontal shear between two currents, and horizontal intrusions of one water mass into another. The large-scale ocean surface currents are mainly wind driven circulation systems. These currents comprise the subtropical and subpolar gyres which occur in the major ocean basins of the Atlantic and the Pacific.

The mean surface positions of the major oceanic frontal systems of the world are depicted on page 3A-2. Note that most of the frontal systems are located along the boundaries of surface oceanic currents. Oceanic frontal systems such as those found with the Gulf Stream and the Kuroshio are called permanent frontal systems, since the currents with which the fronts are associated are observed during all seasons in the same general geographic location and do not move significantly from their mean position. Transient oceanic fronts are comparatively short-lived phenomena. They may exist from a few days to several months and show considerable variation in location. They are produced primarily as a result of seasonal water changes, regional upwelling, open-sea convergences and divergences, pronounced surface heating or cooling, or river runoff. Fronts formed in the vicinity of coasts or continental shelves as a result of local circulations or ocean basin boundary zone effects are called coastal fronts.

The vertical extent of oceanic fronts below the sea surface is closely linked to how the front has formed, or to the vertical structure of the currents with which they are associated. For example, fronts found with major currents often extend to considerable depths (Gulf Stream, 1000 m; Kuroshio, 700 m), while fronts formed by surface heating or cooling or river runoff are quite shallow (50 m, or less). Frontal location and movement reflect current structure and fluctuations, seasonal change, and air-sea interactions.

The surface thermal features of oceanic fronts and currents can be monitored in infrared satellite data. Temperature differences across frontal zones produce distinct gray shade patterns which reveal oceanic frontal systems—including meanders, eddies, and intrusions. Regions of upwelling, river runoff, and current boundaries are similarly disclosed by gray shade differences. Some of the oceanic frontal features can also be observed in satellite visible imagery, in sunglint areas, where differences in sea state produce light and dark shade reflective patterns corresponding to the oceanic frontal features.

It is important to recognize that the oceanic frontal features observed in satellite data are only the surface manifestation of the subsurface frontal structure. An astute observer, however, having a thorough knowledge of a region's marine climatology, can use a combination of satellite data and marine climatology to make reasonable estimates of the relationship of subsurface conditions to surface frontal features.

References

- Cheney, R.E., and D.E. Winfrey, 1976: Distribution and classification of ocean fronts. NAVOCEANO Tech Note 3700-56-76, U.S. Naval Oceanographic Office, Washington, D.C., 23 pp.
- Robinson, A.R., 1976: Eddies and ocean circulation. *Oceanus*, 19, 2-17.

Case 1 Oceanic Frontal Systems

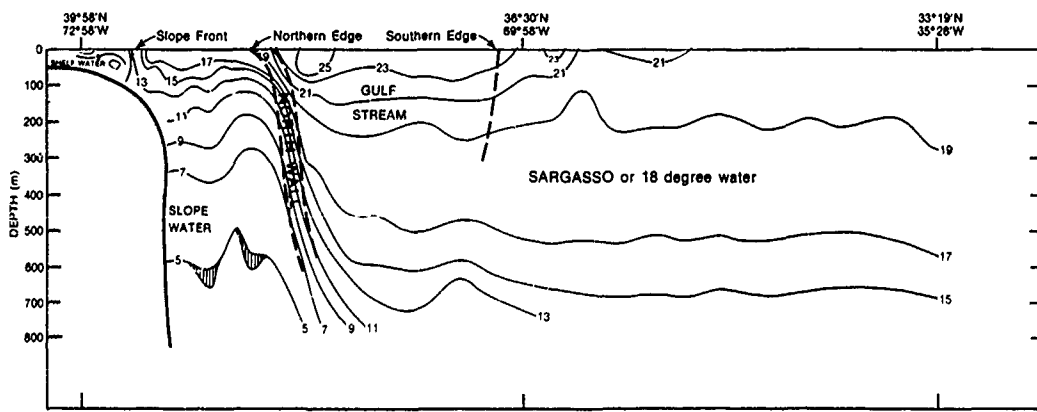
Oceanic fronts in a major ocean current—The Gulf Stream

One of the most distinct oceanic frontal systems observed in satellite imagery is associated with the Gulf Stream off the east coast of the United States. The Gulf Stream forms a sinuous and meandering boundary between the cold, low salinity coastal waters and the warm, more saline waters of the Sargasso Sea (Stommel, 1958). It is one of the fastest oceanic currents, reaching speeds of up to 250 cm s^{-1} (5 kt).

The surface thermal features of the Gulf Stream are clearly revealed in the infrared imagery shown in Fig. 3A-4a. The Gulf Stream (dark gray shade) is the meandering zone between the cold coastal waters (light gray shade) and the warm waters of the Sargasso Sea (medium gray shade). Other features are the warm anticyclonic eddy, the mixing boundary between shelf water and slope water, and cold slope water intrusions into the Gulf Stream.

The Gulf Stream Front is located in the region of the sharply-defined thermal gradient between the Gulf Stream and the coastal waters. A typical vertical cross section of temperature across the Gulf Stream during spring is shown below. Note the sharp vertical temperature gradient on the coastal side of the Gulf Stream. The persistence of this sharp vertical gradient has given rise to the term 'north wall' to describe this portion of the Gulf Stream. The north wall, as revealed by the thermal contrasts in satellite imagery, delineates the surface synoptic location of the Gulf Stream frontal system.

Features of the Gulf Stream are sometimes observed in visible imagery. Changes in sea state within a sunglint area cause reflective differences which can be used to locate oceanographic thermal features observed in infrared data. Fig. 3A-5a is the visible counterpart to Fig. 3A-4a. Note that many of the features delineated by the infrared data are also apparent in the visible imagery. The western edge of the Gulf Stream and the warm anticyclonic eddy are notable examples. On this day, northeasterly winds of $5-8 \text{ m s}^{-1}$ (10-15 kt) prevailed off the East Coast. The Gulf Stream, flowing northeastward, is subjected to surface stress by the wind flow from the northeast and, as a result, the Gulf Stream waters become rough. The roughened sea surface disperses the sunglint in this area causing the Gulf Stream to appear dark in the imagery. The shelf waters show bright sunglint and, therefore, indicate areas of relatively calm seas. Calm seas are similarly indicated by the bright, narrow band surrounding the warm anticyclonic eddy.

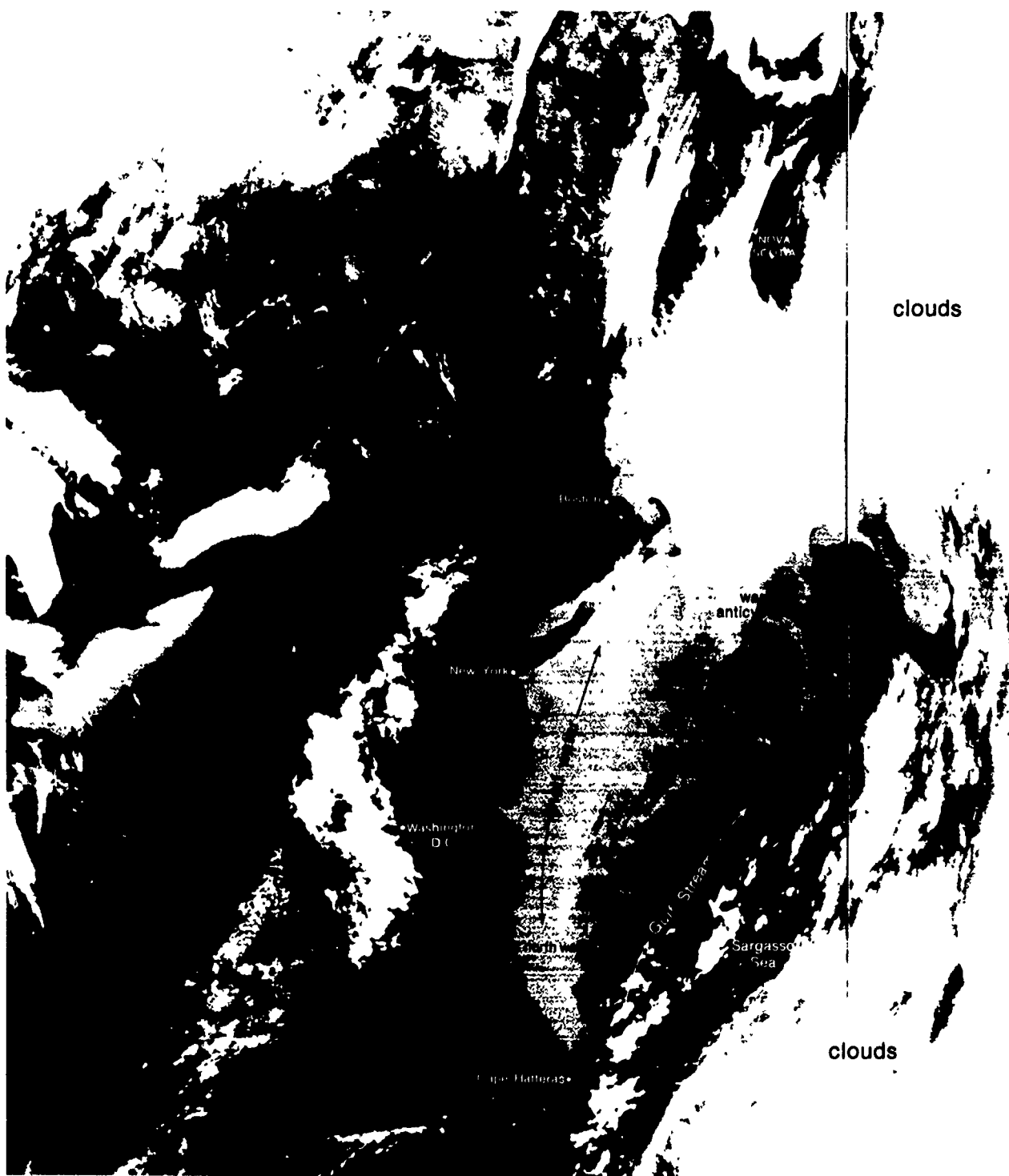


Temperature Profile Across the Gulf Stream. Time Series. 10-11 May 1974 (Gulfstream, 1974).



3A-4a. NOAA-4. Enlarged View. In

The mean monthly sea surface temperature analysis (Fig. 3A-5b) shows the distinct thermal gradient associated with the Gulf Stream frontal system. Selected bathythermographs (Fig. 3A-5c) for the month of May 1975, show the vertical temperature structure in the first 500 m (1640 ft) through the slope water, Gulf Stream, and Sargasso Sea. In this area, the seasonal thermocline (i.e., the subsurface layer of maximum vertical temperature gradient) is found between 50 and 200 m (164 and 656 ft). Strong thermocline gradients (e.g., trace 'T' near 200 m) are regions where anomalous sound propagation can be expected.



3A-4a. NOAA-4. Enlarged View. Infrared Picture. Gulf Stream Frontal System. 1430 GMT 11 May 1975.

References

- National Oceanic and Atmospheric Administration, 1974: *Gulfstream*, 9, No. 12,
U.S. Dept. of Commerce, Washington, D.C., 16 pp.
National Oceanic and Atmospheric Administration, 1975: *Gulfstream*, 1, No. 5,
U.S. Dept. of Commerce, Washington, D.C., 8 pp.
Stommel, M., 1958: *The Gulf Stream*. Univ. of California Press, Berkeley and Los Angeles,
202 pp.

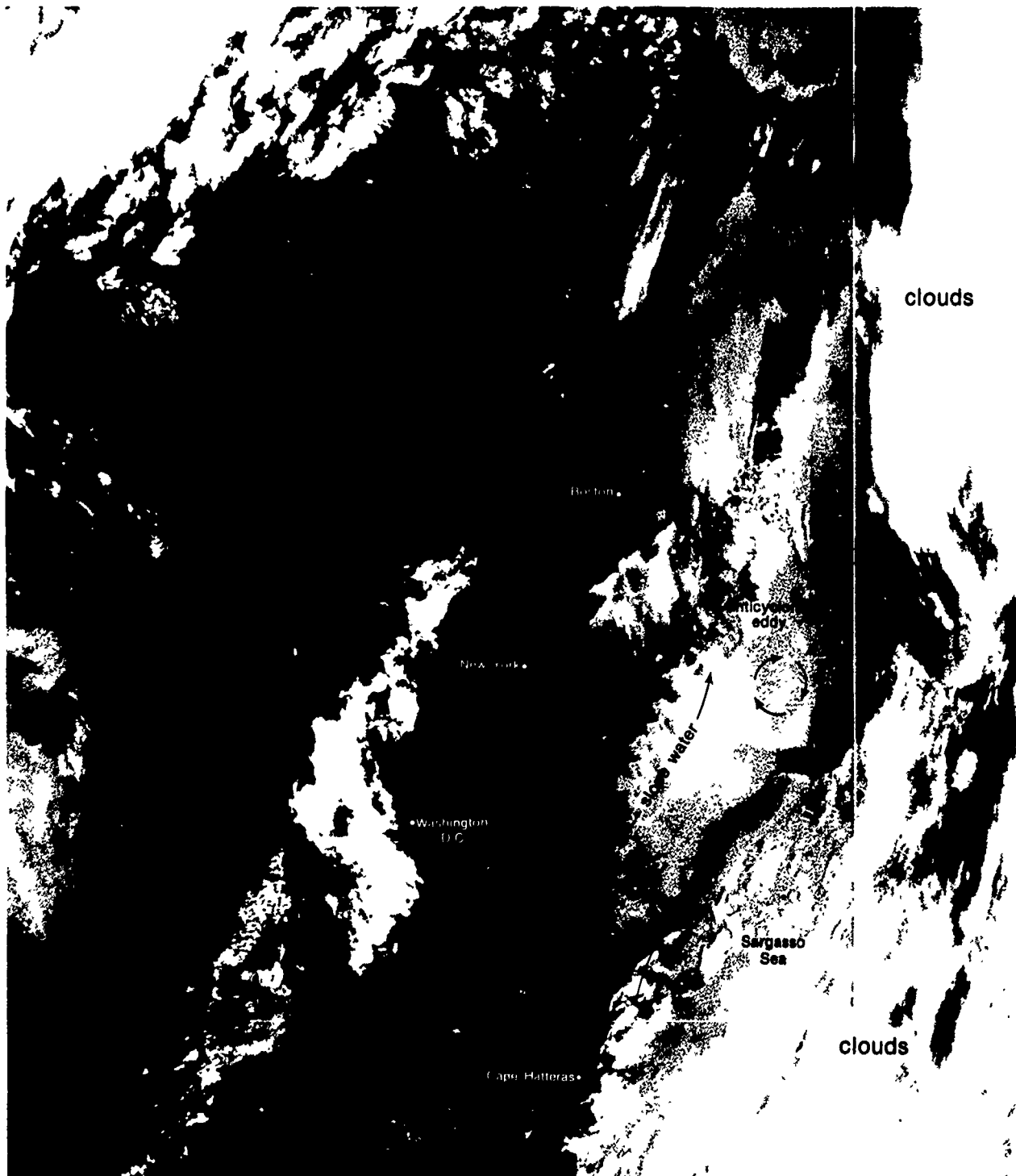
Impor
1. It
sy:
fea
2. M
de
3. At
ob
4. Th
the
su
Fr

Washing

3A-5b.
May 19



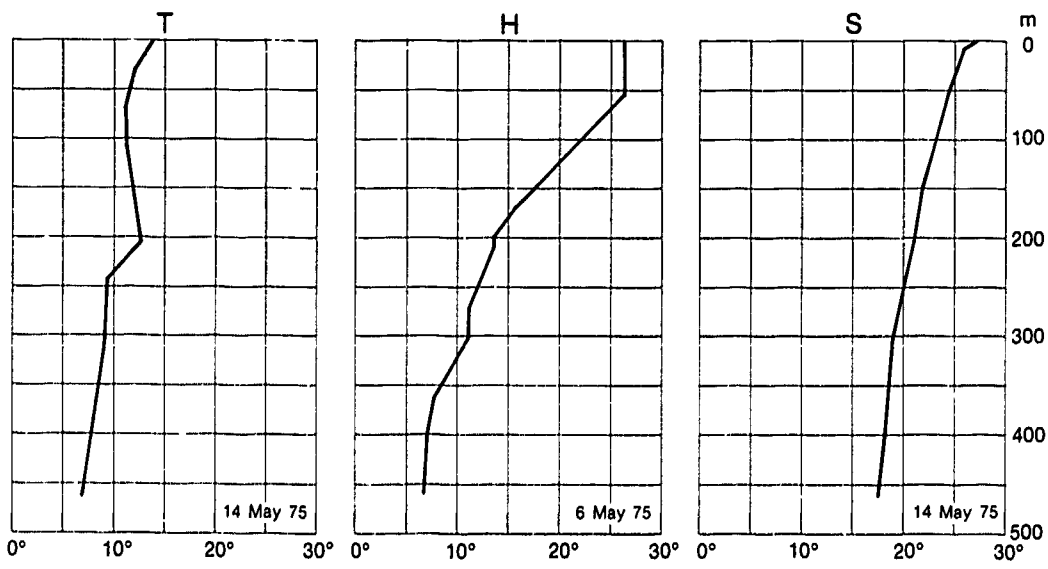
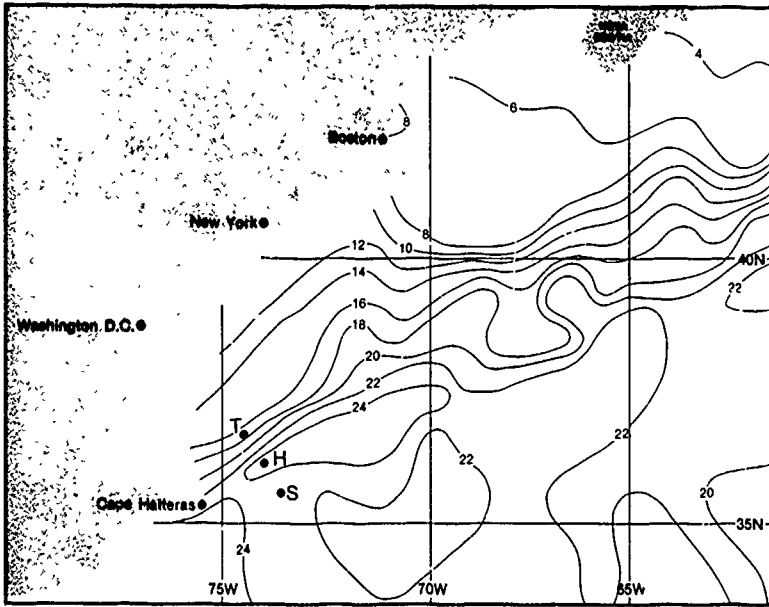
0°



3A-5a. NOAA-4. Enlarged View. Visible Picture. Gulf Stream Frontal System. 1430 GMT 11 May 1975.

Important Conclusions

1. It is possible to identify the Gulf Stream, the Gulf Stream frontal system, slope water, and shelf water from characteristic thermal features in satellite infrared imagery.
2. Mesoscale features of oceanic frontal systems such as eddies, meanders, and intrusions can also be observed in satellite infrared imagery.
3. At times, oceanic frontal systems and mesoscale features can be observed in the sunglint patterns of satellite visible imagery.
4. The sharp thermal contrasts which identify the surface location of the Gulf Stream Front also indicate the region where sharp, vertical subsurface thermal contrasts are present, since the Gulf Stream Front extends essentially vertically below the sea surface.



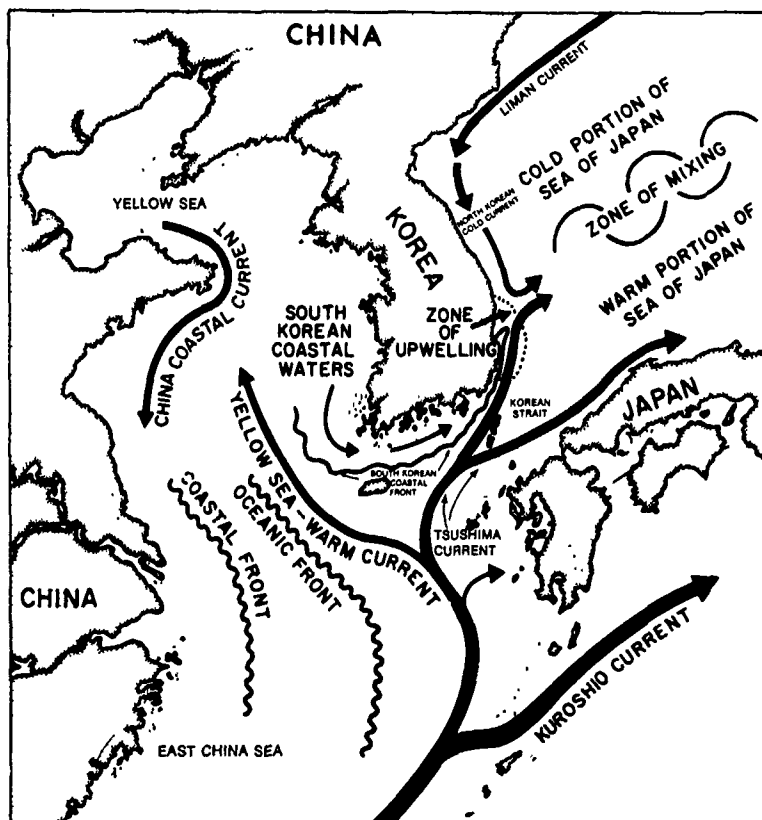
Case 2 Oceanic Frontal Systems

Shallow oceanic fronts—seas adjacent to the Korean Peninsula

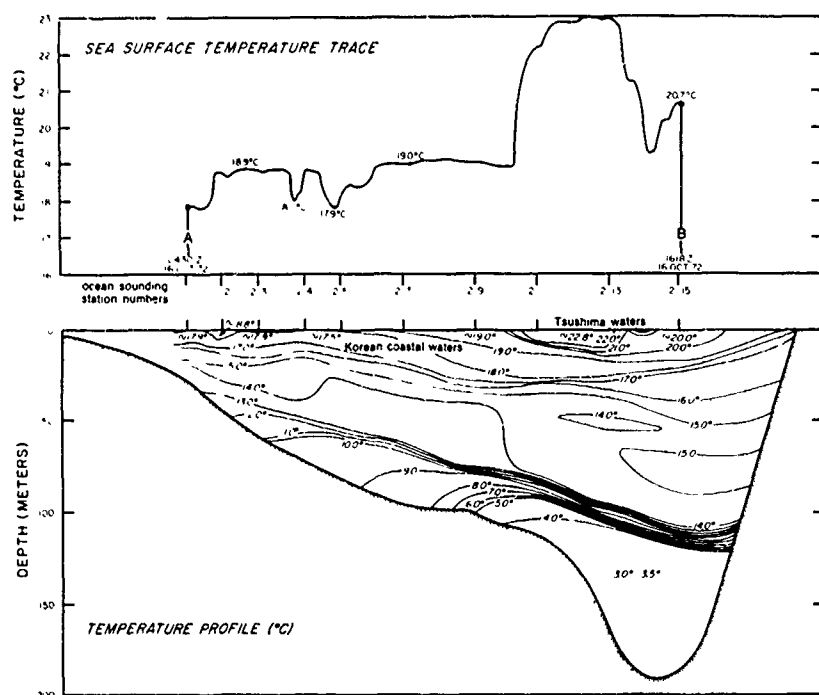
Southwest of Japan, the Tsushima Current branches off from the Kuroshio, passes through the Korean Strait, and enters the Sea of Japan (Fig. 3A-6a). The Tsushima Current, a warm water current, splits into two branches in the Korean Strait. One branch flows northeastward along the coast of Japan; the other branch flows northward along the coast of Korea, then turns to the east as it meets the colder waters of the northern half of the Sea of Japan. A zone of mixing occurs where these contrasting waters meet near 40°N. The waters of the cold portion of the Sea of Japan are fed by the Liman Current and the North Korean Cold Current.

The Yellow Sea and the western half of the East China Sea are shallow basins (maximum depth 100 m) in which seasonal changes are quickly transmitted vertically through the water column and large amounts of river runoff can spread rapidly over the upper water layers, masking the surface and subsurface features. In addition, intrusive waters such as the warm Tsushima Current may flow into and cover large areas of the Yellow Sea. The Sea of Japan, on the other hand, is a deep basin (3,000 m) whose surface and middle waters are controlled by the currents which flow into it.

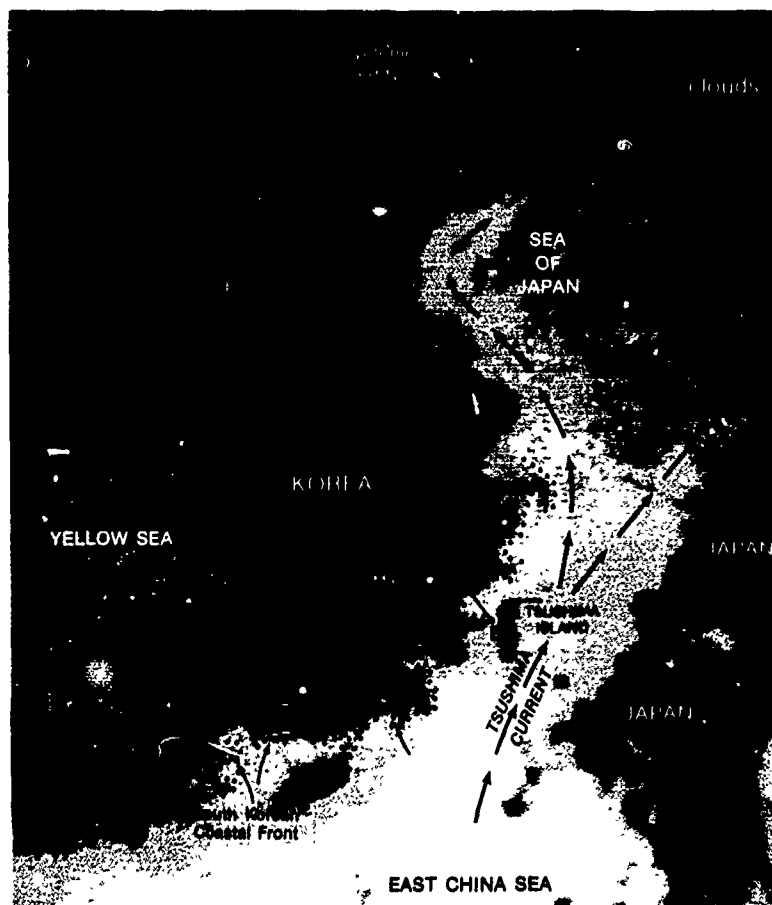
3A-6a. Currents of the Upper Water Column in the Seas Adjacent to the Korean Peninsula (after Huh, 1973).



The DMSP infrared nighttime pass over Korea (Fig. 3A-7b), taken during the period of the ocean sounding data (Fig. 3A-7a), reveals many gray shades in the waters adjacent to the Korean Peninsula. In this picture the infrared data are displayed with a reversal of tone so that warm temperatures appear as light gray shades and cold temperatures as dark gray shades (cloudy areas appear black, as do land areas on this



3A-7a. Temperature profile and cross section taken when Huh (1973) surveyed the waters across the west channel of the Korean Strait between Masan, Korea and the island of Tsushima during October–November 1972 (see Fig. 3A-7b for corresponding DMSP location). He found that surface water temperatures ranged from 17°–19°C in the Korean coastal waters, to 20°–24°C in the Tsushima Current waters. Note that the Tsushima Current is very shallow in this region. This indicates that the Korean Coastal Front, which is the boundary between the Korean coastal waters and the Tsushima Current, will also be characteristically shallow.



3A-7b. FTV-26.
Enlarged View. DMSP IR
Negative T-Expand Enhancement.
Temperature Range 270–295 K.
Seas Adjacent to Korean Peninsula.
1235 GMT 27 October 1972
(after Huh, 1973).

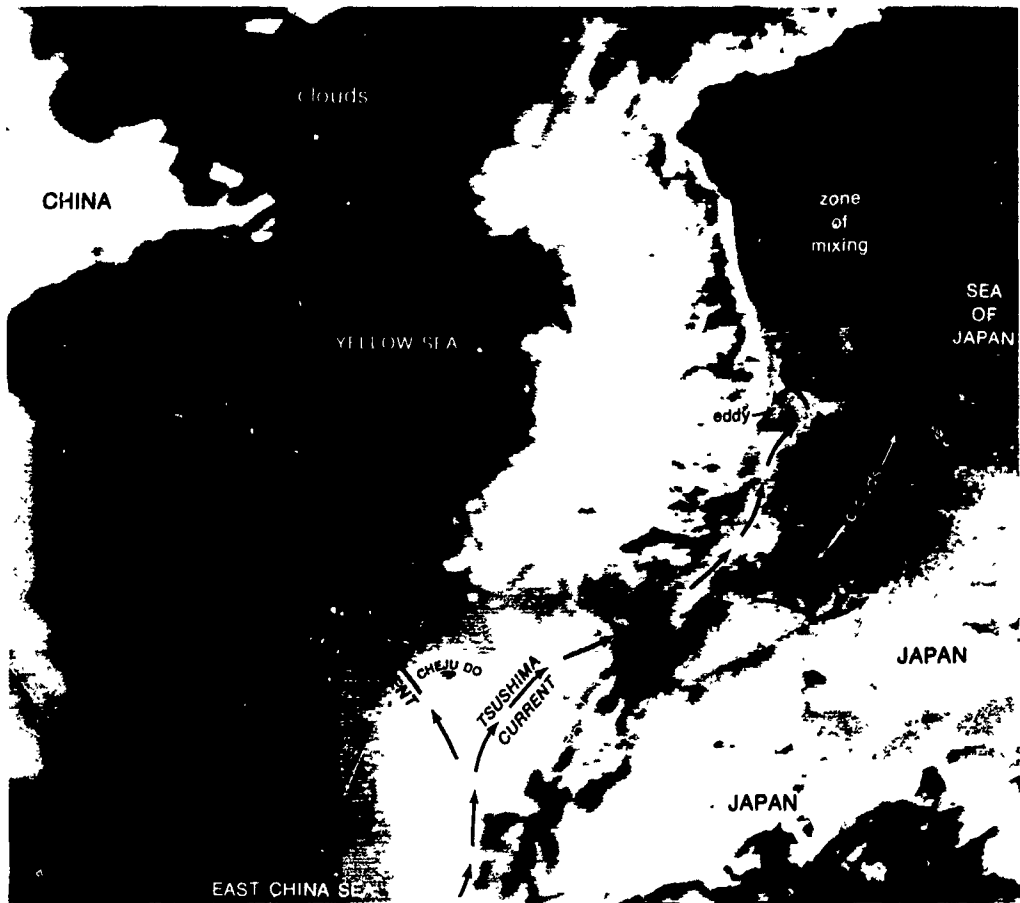
nighttime pass). The gray shade changes correspond to thermal gradients which can be used to identify and locate the position of the Korean Coastal Front. To the east of Tsushima Island, the light-tone gray shades show the splitting of the Tsushima Current into two branches as it enters the Sea of Japan. The north branch continues up the Korean Coast, and a cold cyclonic eddy is developing along the zone of mixing near 40°N.

temperature profile section taken when Huh surveyed the waters across the channel of the Korean Strait (Masan, Korea and the island of Cheju Do) during October–November (Fig. 3A-7b for corresponding location). He found that surface temperatures ranged from 15°C in the Korean coastal waters, 18°C in the Tsushima Current. Note that the Tsushima Current is shallow in this region. This means that the Korean Coastal Front, the boundary between the coastal waters and the Tsushima Current will also be characteristically

A daytime DMSP view of this same area in April (Fig. 3A-7c) shows the variability of the waters in these marine basins. The middle-tone gray shades extending west from Cheju Do indicate that a branch of the warm Tsushima Current (the Yellow Sea Current) is intruding into the Yellow Sea. The dark gray shades in the western half of the Yellow Sea are associated with cold river runoff waters which form the China Coastal Current. Light-tone gray shades show a branching of the Tsushima Current as it enters the Sea of Japan. The effects of upwelling are visible along the east Korean coast in the form of an eddying of the north branch of the Tsushima Current (light-tone gray shade) around a pool of cooler water (middle-tone gray shade). Also, a number of intrusions and eddies can be observed in the Sea of Japan along the zone of mixing where large thermal contrasts exist.

Important Conclusions

1. T-Expand enhanced infrared DMSP data can be used to identify large-scale intrusions of one water mass into another (Tsushima Current flowing into the Yellow Sea; river runoff forming the China Coastal Current).
2. T-Expand enhanced infrared DMSP data can be used to identify the regions where major oceanic currents split into branches.



3A-7c. FTV-27. Enlarged View. DMSP IR Negative T-Expand Enhancement. Temperature Range 266-291 K. Seas Adjacent to Korean Peninsula. 0223 GMT 10 April 1972 (after Huh, 1973).

Reference

Huh, O.K., 1973: Coastal oceanographic use of Data Acquisition and Processing Program (DAPP). Provisional Technical Report TR 241, U.S. Naval Oceanographic Office, Washington, D.C., 31 pp.

Case 3 Oceanic Frontal Systems

Subtropical oceanic frontal system—Cape San Lucas, Baja California

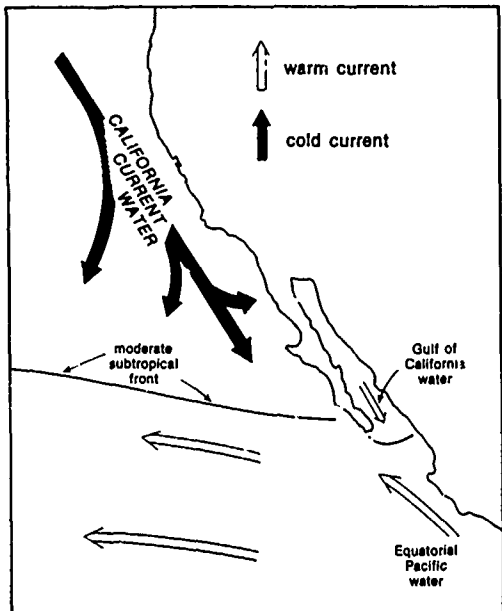
A well-defined subtropical oceanic frontal system is located off Cape San Lucas, Baja California. It occurs in the convergence zone between three distinct surface water masses (Roden and Groves, 1959) (Fig. 3A-8a) which include: (1) a branch of the California Current water from the north, flowing to the southeast off the west coast of Baja—cool and of low salinity, (2) Equatorial Pacific water from the south, flowing northwest towards Baja—warmest and of intermediate salinity, and (3) Gulf of California water, flowing out of the Gulf along the east coast of Baja—cooler and more saline than the Equatorial Pacific water. The largest thermal contrasts and, therefore, the strongest frontal system are found off Cape San Lucas in spring and summer when the maximum upwelling occurs along the California coast and the California Current carries these colder waters to the vicinity of Cape San Lucas. In the fall the strength of the California Current diminishes, as does the coastal upwelling. The warm, more saline Equatorial Pacific water begins replacing the California Current water in this area, and the frontal zone becomes weaker and less distinct from fall through winter (Griffiths, 1965).

A DMSP infrared view of this subtropical oceanic front during the winter is shown in Fig. 3A-9a. At this time, the frontal system is the boundary primarily between the California Current and the Equatorial Pacific Current, and can be observed extending westward into the Pacific from the southern tip of Baja. The gray shade pattern which delineates the front shows several loops and meanders indicative of mixing of water masses along the front. This is shown by abrupt changes in gray shade level in some areas, and more gradual changes in other areas. These changes reflect the thermal gradients and indicate that the temperature contrast across the front is moderate in some areas and weak in other areas. Ship reports on either side of the frontal zone, on this date, show that the sea surface temperature north of the front is 19.4°C (67°F), while south of the front the sea surface temperature is 23.9°C (75°F). Winds are light and from the north-north-west. The small white (cold) area at the tip of Baja is produced by cirrus cloudiness.

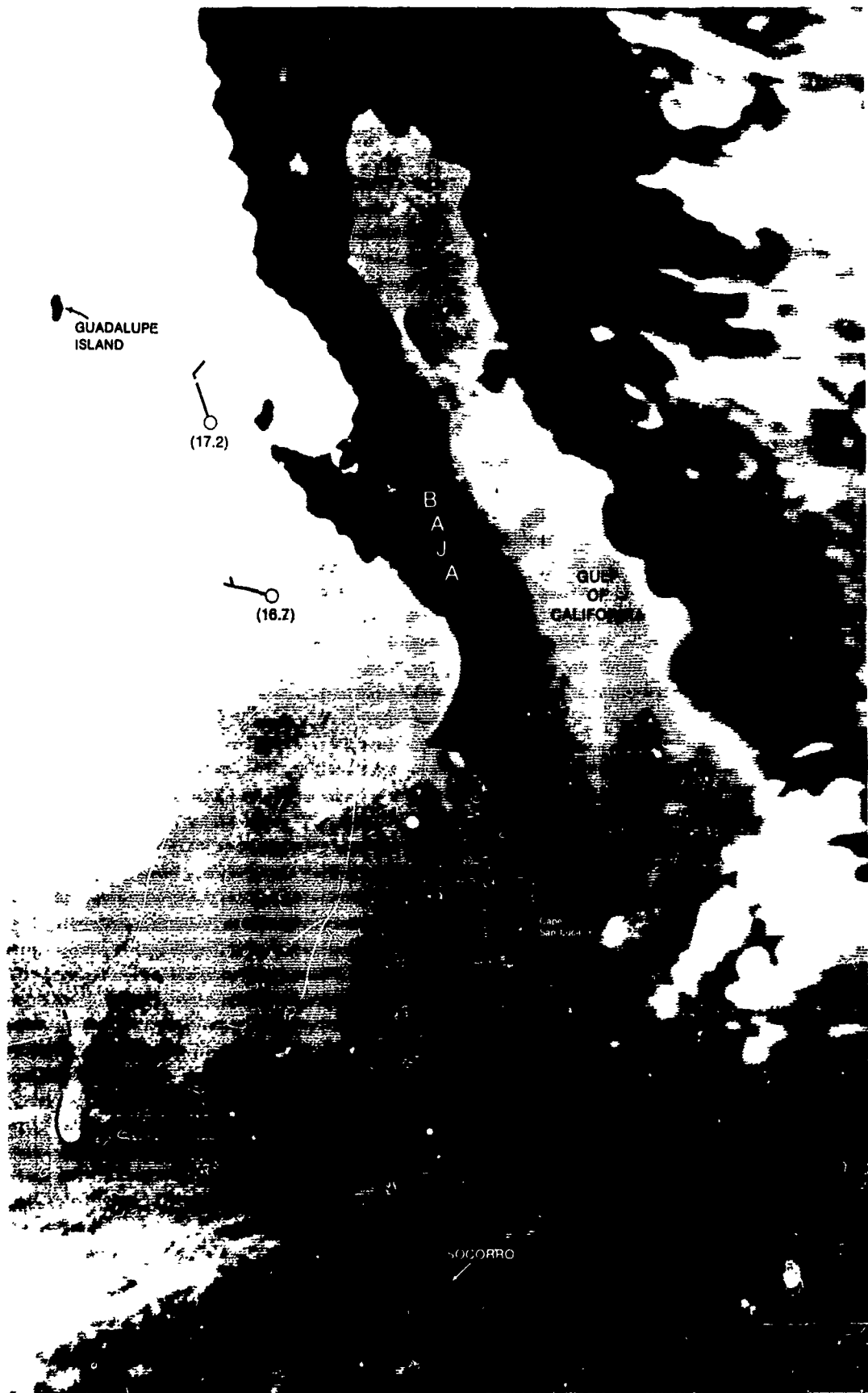
The corresponding visible picture (Fig. 3A-9b) shows that the frontal area is largely cloud-free. The cirrus cloudiness, at the tip of Baja, so prominent in the infrared imagery, appears faintly in the visible imagery as an anomalous gray shade. The lighter-tone gray shade appearing along the west coast of Baja, and extending southeastward across the waters to Mexico, is due to reflective differences caused by varying concentrations of marine haze (NTAG, Vol. 1, Sec. 2B, Case 6).

References

- Griffiths, R.C., 1965: A Study of Fronts Off Cape San Lucas, Lower California. Special Scientific Report - Fisheries No. 499. U.S. Fish and Wildlife Service, Washington, D.C. 54 pp.
Roden, G.I., and G.W. Groves, 1959: Recent oceanographic investigations of the Gulf of California. *J. of Marine Res.*, 18, 10-35.
Roden, G.I., 1975: On North Pacific Temperature, Salinity, Sound Velocity and Density Fronts and their relation to the wind and energy flux fields. *J. of Phys. Oceanogr.*, 5, 557-571.



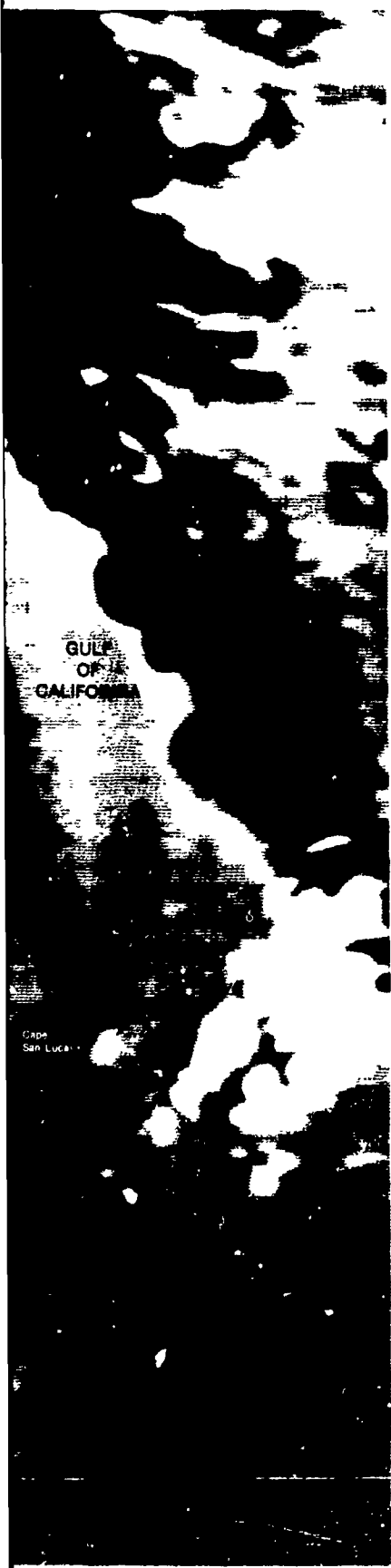
3A-8a. Subtropical Oceanic Frontal System—Baja California (after Roden, 1975).



3A-9a. FTV-29. Enlarged View. DMSP IR T-Expand Enhancement. Cape San Lucas Subtropical Oceanic Frontal System. 1855 GMT 8 December 1973. Ship Observations. 8 December 1973.

3A-9

3A-9b. FTV-
Oceanic Frot



Cape San Lucas Subtropical
Fronts. 8 December 1973.



3A-9b. FTV-29. Enlarged View. DMSP VHR Low Enhancement. Cape San Lucas Subtropical
Oceanic Frontal System. 1855 GMT 8 December 1973.

Case 4 Oceanic Frontal Systems

Oceanic fronts in a broad surface current—The California Current

As the North Pacific Current approaches the North American Continent it divides—one branch swings north to form the Alaskan Gyre and a second branch turns south as the California Current (see page 3A-3). The California Current flows parallel to the North American coast from British Columbia to California, and eventually feeds into the North Equatorial Current. In contrast to the strong, warm, concentrated Kuroshio on the west side of the Pacific, the California Current is weaker, colder and spread across a larger area.



3A-10a. FTV-33. Enlarged View. DMSP WHR T-Normal Enhancement (Table Unknown). Oceanic Fronts in California Current. 1500 GMT 13 March 1976 (after Blackstone and Whritner, 1976).

During the spring and summer, persistent northwesterly winds blow parallel to the California coast resulting in large-scale upwelling of very cold water along the coast. This cold upwelled water is patchy, instead of being in a uniform band, and the California Current system shows continuously developing meanders and eddies (Jones, 1971; Bernstein and Whritner, 1977). At the end of summer, the atmospheric circulation pattern changes, and the large-scale upwelling ceases. During the winter months the California Current gradually withdraws from the coast. Local areas of upwelling occur under strong, persistent offshore winds (for example, Santa Ana flow regimes).

Oceanic fronts which develop in the California Current are transient in nature—they vary considerably in space, time, and intensity. This is in contrast to permanent frontal systems such as are found with the Kuroshio and Gulf Stream. These frontal systems are well-defined and persistent ocean features, though the fronts may vary in intensity and meander, and portions of the frontal systems may separate to form eddies.

In the California Current, fronts are often found between upwelled water and non-upwelled water in the current. In addition, meanders of warm, low salinity offshore water intrude into the current off the southern California coast and form eddies, which may persist for long time periods. Changes in the prevailing wind direction and speed act to alter the orientation, structure, and location of the fronts formed in the current.

A DMSP WHR pass off the West Coast (Fig. 3A-10a) shows an example of a warm offshore water intrusion into the California Current. This image has been enhanced by modifying the normal linear gray shade scale to produce an output which gives three gray shade steps (light, medium, and dark), between white and black, over the small range of sea surface temperatures (4.7°C) found in this area, on this day (Blackstone and Whritner, 1976).

Light gray shade tones, indicating colder California Current waters, extend to the south and southwest from the Channel Islands. The area to the south of the Channel Islands, showing a mixture of light and medium tones, is a region of weak temperature differences ($0.5^{\circ}-1.0^{\circ}\text{C}$). To the west, tonal changes become more distinct and it is possible to locate a thermal front along the boundary of a prominent warm water intrusion (uniform, dark gray shade) stretching towards the Channel Islands. Along the western boundary of the warm water intrusion, the portions showing a distinct shift from dark to medium tones are where there are moderate sea surface temperature differences ($1.0^{\circ}-2.0^{\circ}\text{C}$) across the front. Note the areas of upwelling (light gray shades) off Point Conception and near Point Mugu—these are produced by a Santa Ana offshore wind flow during this period. Other upwelling zones are observed along the Pacific coast of Baja.

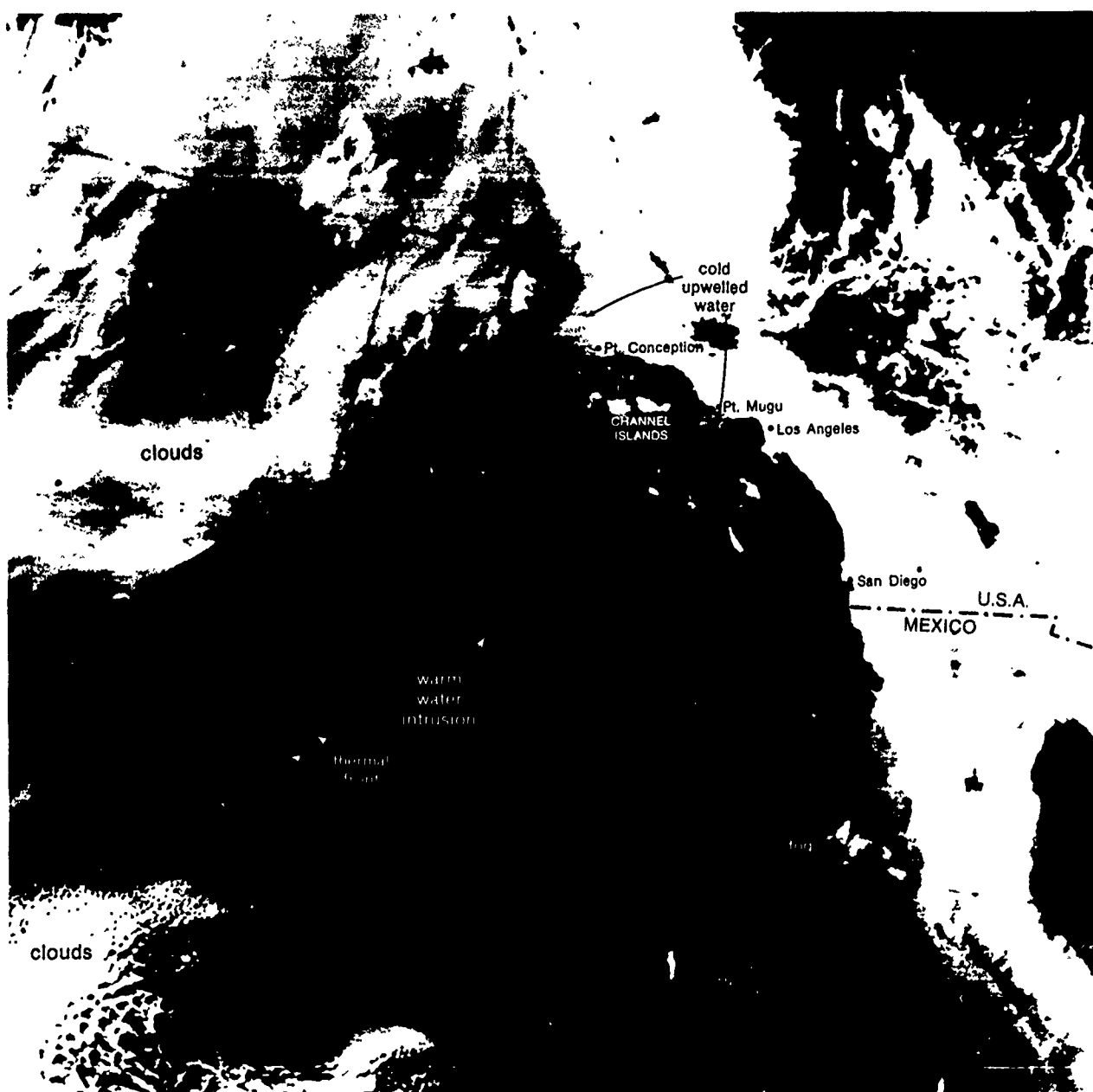
continued on following page

References

- Bernstein, R.L., L Breaker, and R. Whritner, 1977: California Current eddy formation: air, sea, and satellite results. *Science*, **195**, 353-359.
Blackstone, F.A., and R. Whritner, 1976: Applications of DMSP imagery to sea surface temperature gradient analysis. Naval Weather Service Facility, San Diego, Calif., 21 pp.
Jones, J.M., 1971: General circulation and water characteristics in the Southern California Bight. Southern California Coastal Water Research Project Report, Los Angeles, Calif.

A best estimate of the location of the thermal fronts, inferred solely from the enhanced DMSP imagery, is shown in Fig. 3A-12a. The line segments represent points along which sea surface temperature gradients were interpreted as indicating temperature differences varying from 0.75° - 2.5° C, from the warm side to the cold side of the front. This analysis is compared to a sea surface temperature analysis based on expendable bathythermographs (AXBT's), airborne radiation thermometer (ART), and continuity considerations using the enhanced DMSP infrared imagery (Fig. 3A-13a). The analysis suggests that the temperature differences along the frontal boundary derived from the satellite data are representative of the actual temperature differences observed along the frontal boundary.

To examine the relationship between the surface and subsurface thermal features, the AXBT data were used to construct isotherm

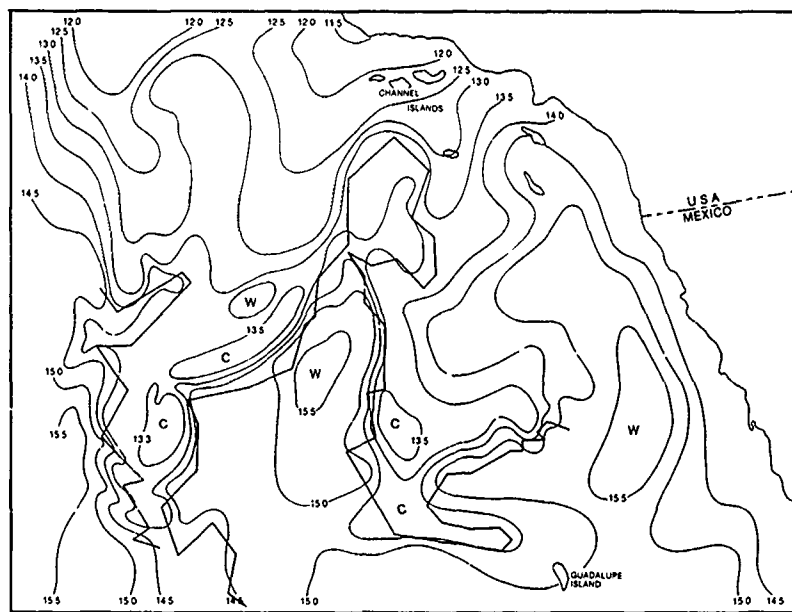


3A-12a. FTV-33. Enlarged View. DMSP WHR T-Normal Enhancement (Table Unknown). Sea Surface Temperature Gradient Analysis Derived from DMSP Gray Shade Patterns. 1500 GMT 13 March 1976 (after Blackstone and Whritner, 1976).

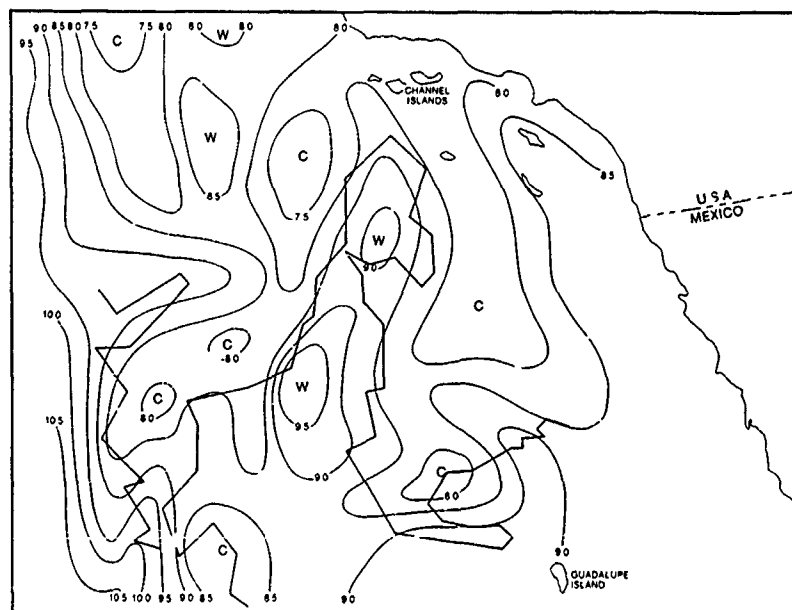
analysis for various levels below the sea surface. The strongest temperature gradients appeared at the 200 and 400 ft depths. However, in some areas the strong upper ocean temperature gradients were reflected as deep as the 1000 ft level. The 700 ft depth temperature analysis, with the DMSP imagery surface frontal boundaries superimposed, is shown in Fig. 3A-13b.

Important Conclusions

1. Temperature differences across frontal boundaries can be estimated using specially enhanced DMSP WHR imagery.
2. Although transient fronts are primarily upper ocean phenomena, areas of strong temperature gradients can, at times, be reflected to considerable depths.



3A-13a. Observed Sea Surface Temperature Analysis (13-14 March) and Sea Surface Temperature Gradient Analysis from DMSP Imagery (13 March) (after Blackstone and Whritner, 1976).



3A-13b. Temperature Analysis for 700 ft (13-14 March) and Sea Surface Temperature Gradient Analysis from DMSP Imagery (13 March) (after Blackstone and Whritner, 1976).

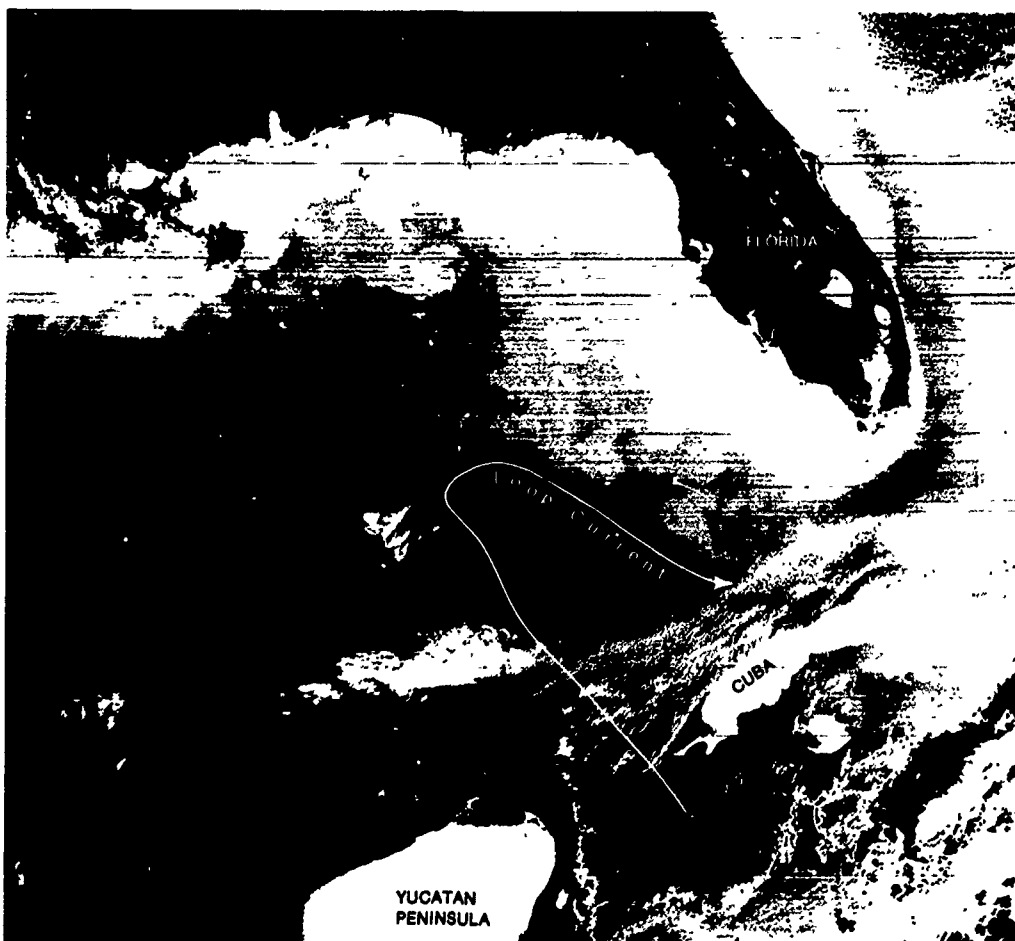
Case 5 Oceanic Frontal Systems

An intense oceanic front—Gulf of Mexico Loop Current

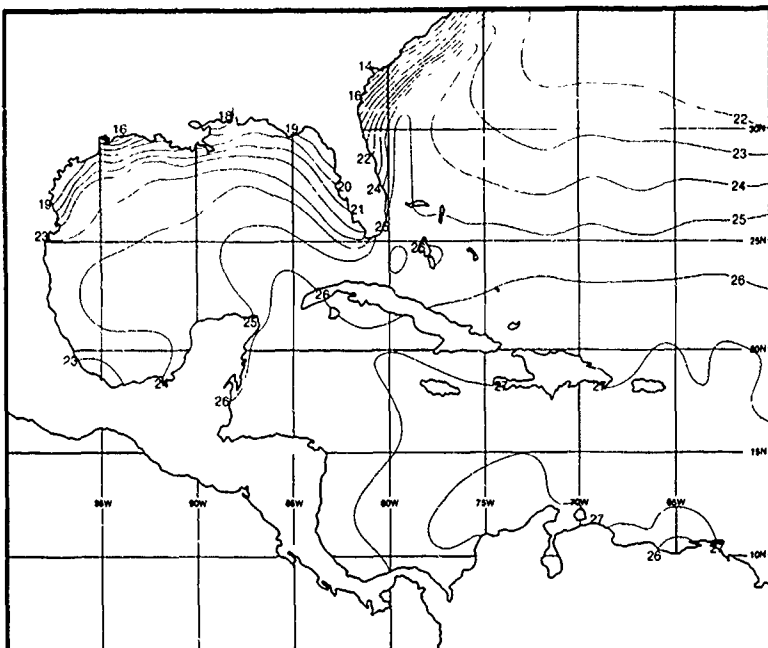
The Loop Current is a major feature of the circulation in the eastern Gulf of Mexico (Behringer, Molinari, and Festa, 1977). The current enters the eastern Gulf between Cuba and the Yucatan Peninsula (Yucatan Channel) and exits through the Florida Straits where it joins the Gulf Stream current system. The path of the Loop Current in the Gulf forms an anticyclonic loop. When the current penetrates far to the north in the Gulf, the northern portion may break off and form a large eddy which drifts slowly westward. The basic Loop Current then is reestablished as a reduced amplitude meander in the southeastern Gulf (Duernberger, 1978).

In an enhanced DMSP TF view of the Gulf of Mexico on 19 December 1977 (Fig. 3A-14a), the warmer waters (dark gray) of the Loop Current stand out in marked contrast with the cooler waters (light gray) of the Gulf. The Loop Current Front, the inshore boundary of the dark gray area, is very sharp, indicating the presence of an intense thermal frontal zone. A cold water intrusion is observed along the western periphery of the current. Sometimes these intrusions are amplified and form eddies which break off from the basic current.

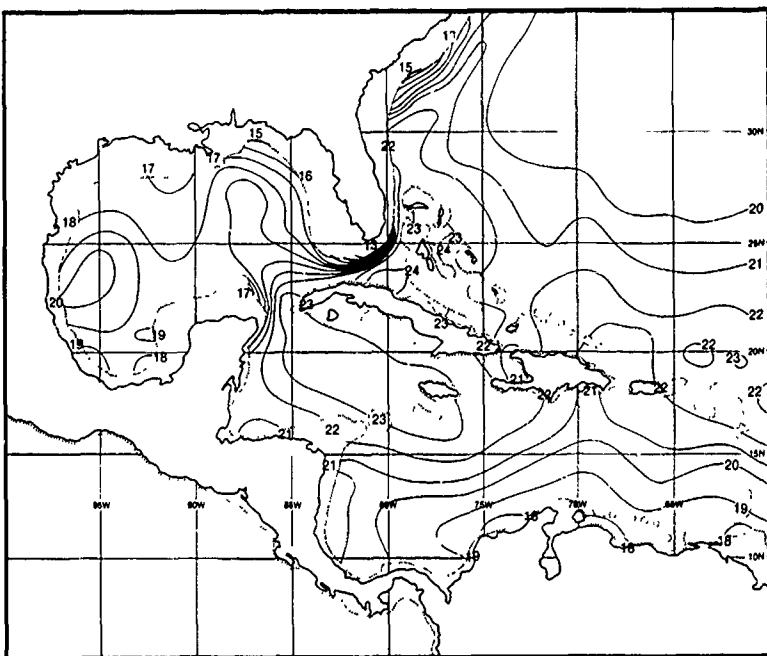
Based on the gray shade temperature enhancement scale (Table No. 17), the temperature of the Loop Current is estimated to be 22.2°C



3A-14a. FTV-35 DMSP TF T-Normal Enhancement (Table No. 17). Gulf of Mexico Loop Current.
0605 GMT 19 December 1977.



3A-15a. Mean Monthly Sea Surface Temperatures ($^{\circ}$ C). December (after Robinson, 1973).



3A-15b. Mean Monthly 150 m Temperatures ($^{\circ}$ C). December (after Robinson, 1973).

or higher (uncorrected for atmospheric attenuation due to water vapor absorption). Since there was a cold, dry, polar air mass over the Gulf, infrared radiation attenuation, due to water vapor absorption, would be minimized over the Loop Current area. This Loop Current temperature is in good agreement with the mean surface temperatures in the southeastern Gulf (Fig. 3A-15a) during the month of December (Robinson, 1973). Below the surface (Fig. 3A-15b), the bulge of the isotherms north of the Yucatan Channel reveals that the Loop Current is not a shallow phenomenon. The 20°C isotherm at 150 m is generally used to identify the position of the Loop Current Front in the southeastern Gulf region.

References

- Behringer, D.W., R.L. Molinari, and J.F. Festa, 1977: The variability of anticyclonic current patterns in the Gulf of Mexico, *J. Geophys. Res.*, **82**, 5469-5476.
- Duernberger, LCDR P., 1978: The Gulf of Mexico Loop Current, *Gulfstream*, **4**, 6-7.
- Robinson, M.K., 1973: Atlas of mean monthly sea surface and subsurface temperature and depth of the top of the thermocline, Gulf of Mexico and Caribbean Sea. Scripps Institute of Oceanography, SIO Reference 73-8.

3B Oceanic Eddies

Characteristics of Oceanic Eddies

Oceanic eddies are distinct, closed cyclonic or anticyclonic circulations in the seas. Cyclonic eddies are generally cold core, while anticyclonic eddies are generally warm core. Oceanic eddies can be produced in several different ways. They can be formed when a meander of a major ocean current becomes very large. The narrow base of the current then closes off forming a separate circulation distinct from the major current. These circulations have diameters of tens to hundreds of kilometers and, like the currents themselves, are strongest near the surface. Eddies produced in this way are the oceanic analog to high and low pressure systems in the atmosphere. Eddies are also produced by the deflection and/or channeling of an ocean current by the shape of the coastline and the ocean bottom topography. These features are especially important in the production of eddies in coastal areas and in the smaller oceanic basins. Small-scale eddies (tens of kilometers in diameter) have been observed to form from intrusions of one water into another. In this case, the intrusion closes upon itself to produce a small but rapidly rotating eddy. The surface currents of oceanic eddies influence sea surface temperatures, and thus oceanic eddies play an important role in air-sea interactions (Voorhis and Schroeder, 1976).

The surface temperature patterns of oceanic eddies have been observed directly and indirectly in satellite imagery. Temperature differences across eddies produce gray shade differences in infrared imagery which directly reveal the oceanic eddies. Indirectly, air-sea interaction processes can be attributed to an underlying warm or cold oceanic eddy. For example, a cold eddy is often partially encircled by a convective cloud line at the edge of the eddy, while a warm eddy may generate a convective cloud pattern. In addition, cold water stabilizes the lapse rate in the lower atmosphere by cooling the air near the surface, which impedes the vertical transport of stronger winds downward from aloft. Thus there is a tendency for colder water, and cold eddies, to be less rough than the surrounding warmer waters—an effect that can be observed in sunglint areas.

Reference

Voorhis, A., and E. Schroeder, 1976: Sea surface temperature during MODE-I. In "Ocean Eddies", *Oceanus*, 19, 3, 82-86.

Case 1 Oceanic Eddies

*Eddies formed by meanders of a strong oceanic current—
The Gulf Stream*

Eddies are observed north or south of the Gulf Stream when a meander in the Stream becomes a very large loop and the narrow portion of the loop closes off, producing a separate circulation which moves away from the main stream. The eddies have closed loop currents that decay slowly with time. Northward meanders of the Stream generate anticyclonic eddies of warm Sargasso Sea water, surrounded by a ring of Gulf Stream water; and southward meanders of the Stream result in cyclonic circulations of cold slope water, enclosed by a ring of Gulf Stream water (Saunders, 1971).

3B-2a. NOAA-5.
Enlarged View.
VHRR Infrared Picture.
Anticyclonic Eddies
Formed from Shoreward
Meanders of the
Gulf Stream.
1428 GMT 1 May 1977.



3B-2

Fig. 3B-2a is a NOAA-5 VHRR infrared image of the Gulf Stream. Several large anticyclonic eddies (labeled A to D) are observed to the northwest of the Stream. Cloudiness obscures the ocean circulation features to the south of the Stream. Meander "C" is in an early stage of development, since the closing off process has not been completed. In time, the meander will draw in more Stream water and complete the circulation, resulting in an eddy similar in appearance and temperature to eddy "B". The warm intrusion "E" consists of a couplet of one cyclonic and one anticyclonic circulation on either side of the axis of intrusion. These are shallow, mesoscale phenomena which form along the continental shelf waters, and are short-lived in comparison to the larger anticyclonic eddies.



3B-3a. NOAA-5.
Enlarged View.
VHRR Visible Picture.
Oceanic Eddies in a
Sunglint Pattern.
1428 GMT 1 May 1977.

3B-3a. NOAA-5.
Enlarged View.
VHRR Visible Picture.
Oceanic Eddies in a
Sunglint Pattern.
1428 GMT 1 May 1977.

The corresponding NOAA-5 VHRR visible image (Fig. 3B-3a) shows sunglint patterns over the Gulf Stream. Abrupt changes in surface roughness along the north wall of the Stream and along the eddy boundaries reveal these features in the sunglint. In particular note the sharp demarcation of the western and northern boundaries of eddy "B". Differences in surface roughness, observed in eddies and along their boundaries, are produced by differences in wind stress patterns over these areas (Strong and DeRycke, 1973). On this date, light north-easterly winds were observed over the cloudy area, veering to easterly and southeasterly along the coastal region. An aerial photograph of the Gulf Stream, across which the wind stress pattern varies, is shown in Fig. 3B-3b. Note the whitecaps over the Stream water and the distinct boundary separating this water from the calmer waters of the continental slope area.

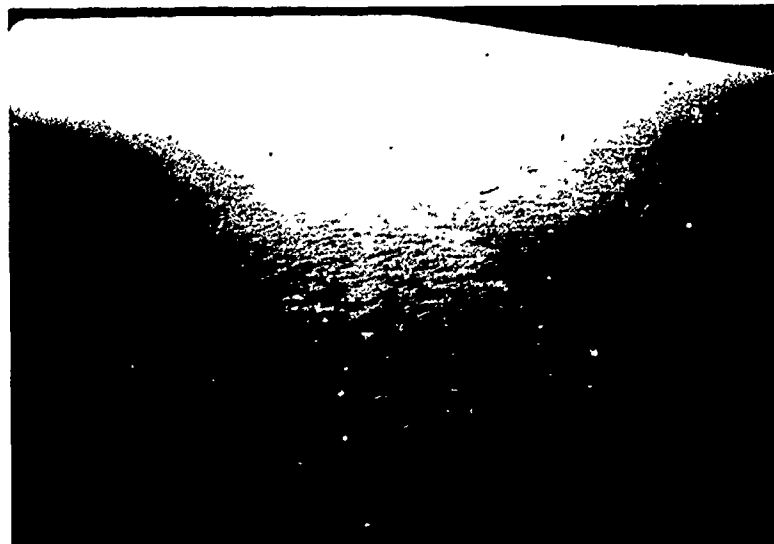
Differences in surface roughness, which produce distinctive sunglint patterns, may also be produced by air-sea interactions. Cold water stabilizes the lapse rate in the lower atmosphere by cooling the air near the surface. Vertical transport of higher wind speeds downward from aloft is therefore impeded. This results in a tendency for colder water, and thus cold eddies, to be less rough than the surrounding warmer water.

Important Conclusions

1. Northward meanders of the Gulf Stream generate anticyclonic eddies of warm Sargasso Sea water, surrounded by a ring of Gulf Stream water; and southward meanders of the Gulf Stream generate cyclonic eddies of cold slope water, surrounded by a ring of Gulf Stream water.
2. These eddies are revealed by thermal patterns in satellite infrared imagery and in sunglint patterns in satellite visible imagery.

References

- Saunders, P.M., 1971: Anticyclonic eddies formed from shoreward meanders of the Gulf Stream. *Deep-Sea Res.*, **18**, 1207-1219.
Strong, A.E., and DeRycke, R.J., 1973: Ocean current monitoring employing a new satellite sensing technique. *Science*, **182**, 482-484.



3B-3b. Aircraft Reconnaissance Photograph. Appearance of the Gulf Stream under a Northeast Wind Stress (Gulf Stream is on the left side). Anonymous.

Case 2 Oceanic Eddies

Eddy patterns in the western Mediterranean—Alboran Sea Eddies

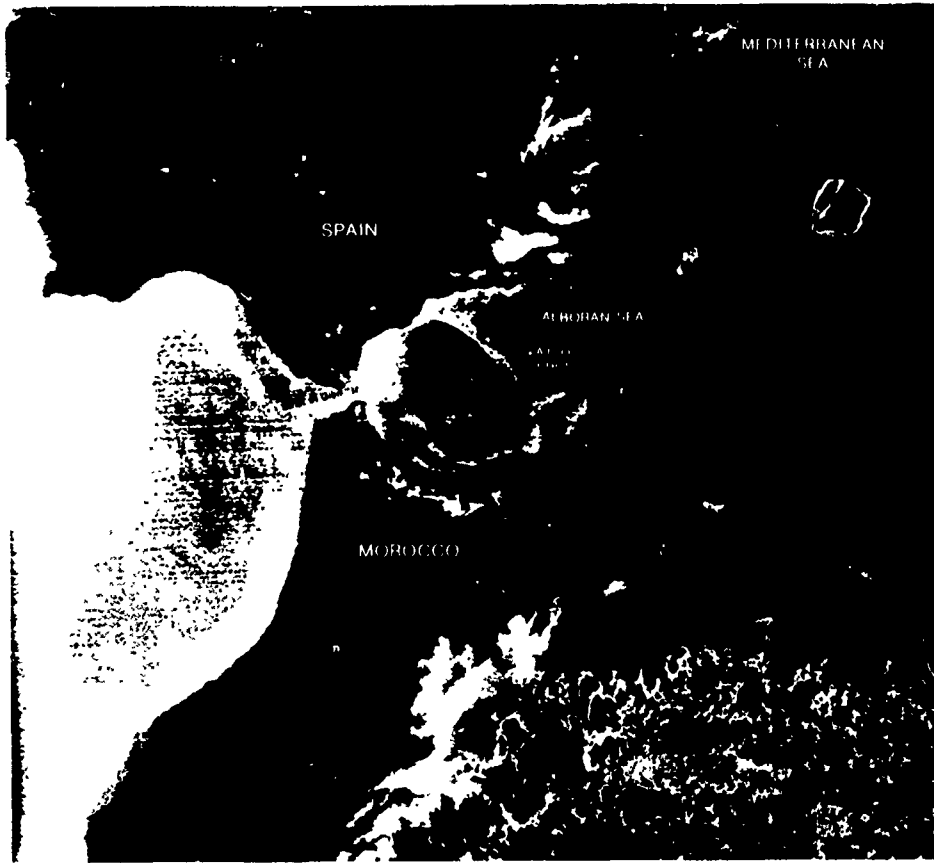
The Mediterranean Sea is an evaporative sea; that is, there is a large excess of evaporation over precipitation so that water in this region is characterized by high salinities. The Mediterranean is divided essentially into a western and an eastern basin by a sill extending from Sicily to the North African coast. At intermediate levels (400 to 600 m), higher salinity (density) waters occur in the eastern basin than at the corresponding levels in the western basin—this creates a density gradient from east to west. As a result, high salinity intermediate water from the eastern basin flows west over the sill, along the North African coast, and out below the surface through the Strait of Gibraltar into the Atlantic. This outflow below the surface is replaced by surface inflow from the Atlantic, through the Strait, into the Alboran Sea. In the mean, the surface inflow is characterized by a strong, westerly surface current.

This strong surface current in the Alboran Sea generally splits into two branches, one generating a large anticyclonic eddy to the west of Alboran Island; and the other branch generating a smaller and weaker cyclonic eddy to the east of Alboran Island. According to Mommesen (1978), alternating periods of persistent winds from the west (or east) over the Alboran Sea appear to be an important factor in increasing (or decreasing) cold water upwelling along the Spanish coast. The cold upwelled water formed along the Spanish coast is an important feature, since it becomes entrained in the circulation and appears on the rim of the primary anticyclonic eddy in the western Alboran Sea and also spreads into the eddy patterns to the east of Alboran Island.

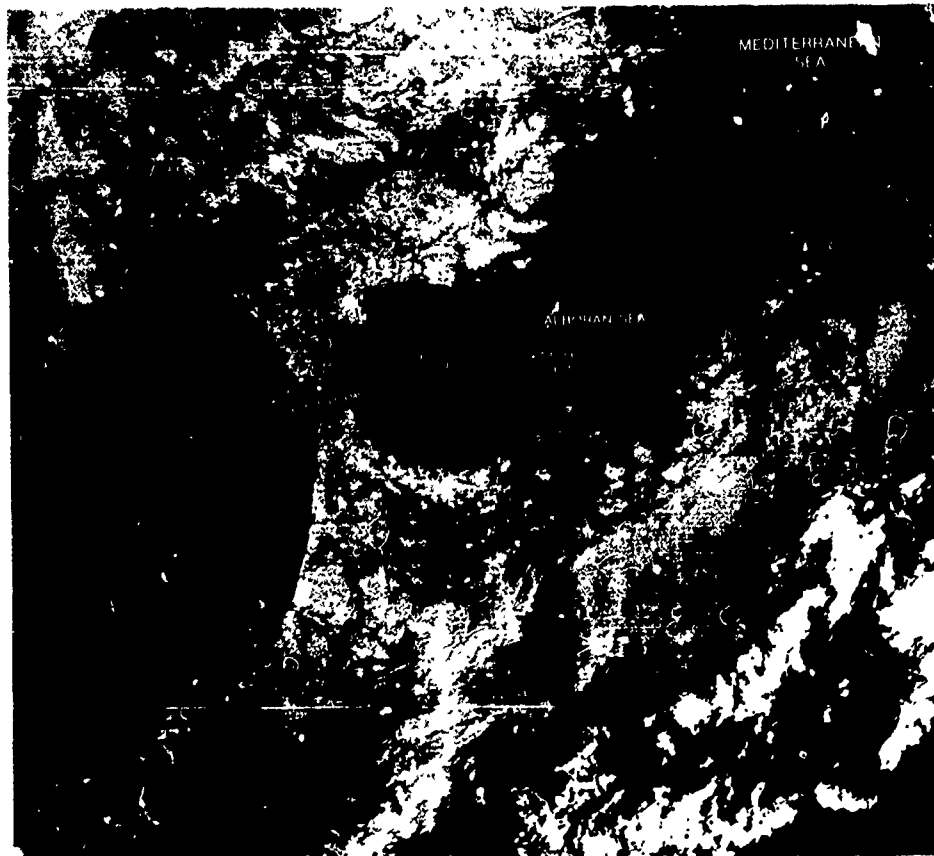
Fig. 3B-5a is a DMSP WHR enhanced picture of a typical Alboran Sea eddy pattern under persistent surface westerly flow. The large anticyclonic eddy over the western Alboran Sea shows a band of cold water extending around the circumference of this circulation. Cold surface water also extends into the eastern Alboran Sea where a complex oceanic circulation pattern is observed. In another example (Fig. 3B-5b), two large eddies are observed in the western Alboran Sea. The cold water band has moved away from the Spanish coast and does not completely encircle the primary anticyclonic eddy, which is considerably reduced in size. The presence of the second eddy in the western Alboran Sea is a departure from normal conditions observed under westerly flow, where one large anticyclonic eddy occupies the same area.

Reference

Mommesen, Jr., D.B., 1978: The effect of wind on sea surface temperature gradients in the Strait of Gibraltar and Alboran Sea. Unpublished Report. U.S. Navy Fleet Weather Central, Rota, Spain, 18 pp.



3B-5a. FTV-33.
Enlarged View.
DMSP WHR
T-Normal Enhancement
(Table Unknown).
Alboran Sea Eddies
1908 GMT 20 July 1975.



3B-5b. FTV-35.
Enlarged View.
DMSP TF
T-Normal Enhancement.
Alboran Sea Eddies.
0013 GMT 7 August 1978.

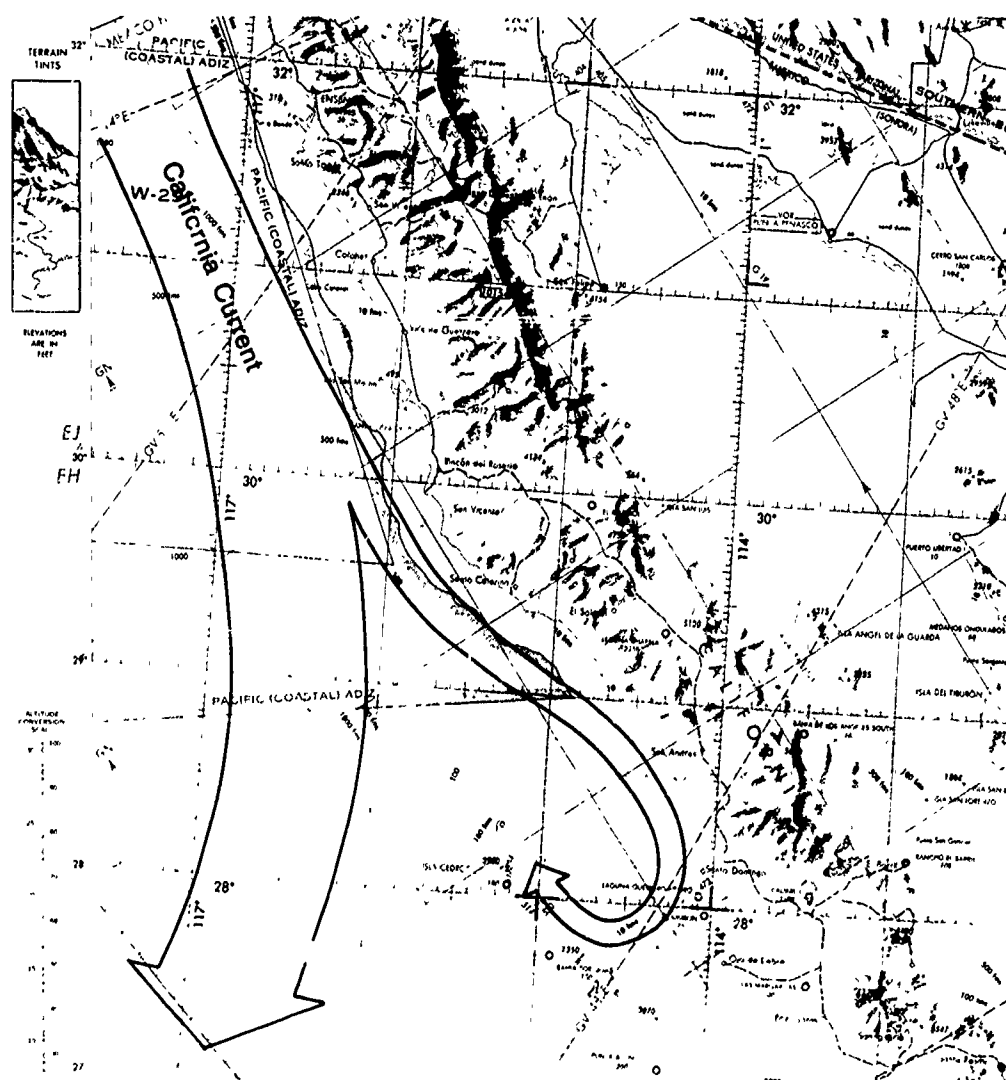
Case 3 Oceanic Eddies

Eddy formation due to the deflection of an ocean current by coastal features—The California Current

The shape of the coastline and the contour of the bottom offshore have a strong influence on the near shore flow of ocean currents. For example, during the summer months, the broad California Current flows southward along the California coastline. When a branch of this current flows in the vicinity of the Bay of Sebastian-Vizcaino off Baja, it is channeled clockwise around the curving coastline and forms a persistent anticyclonic eddy in the bay. A map of this area (Fig. 3B-6a) shows the symmetrically curved coastline around the bay, and the shallow depths (continental shelf) providing an ideal basin for channeling the flow. The superimposed streamlines depict the suggested current flow in the area when such an eddy is present.

Fig. 3B-7a is a DMSP TF enhanced picture showing an eddy which has been generated in the Bay of Sebastian-Vizcaino by a branch of the California Current. Note the strong upwelling to the north along the California coast. This water is drawn into the anticyclonic circulation in the bay and forms a ring of cold water around a very symmetric warm core.

3B-6a. Map of Coastal Features in Bay of Sebastian-Vizcaino, Baja California, with Suggested Surface Current Streamlines.

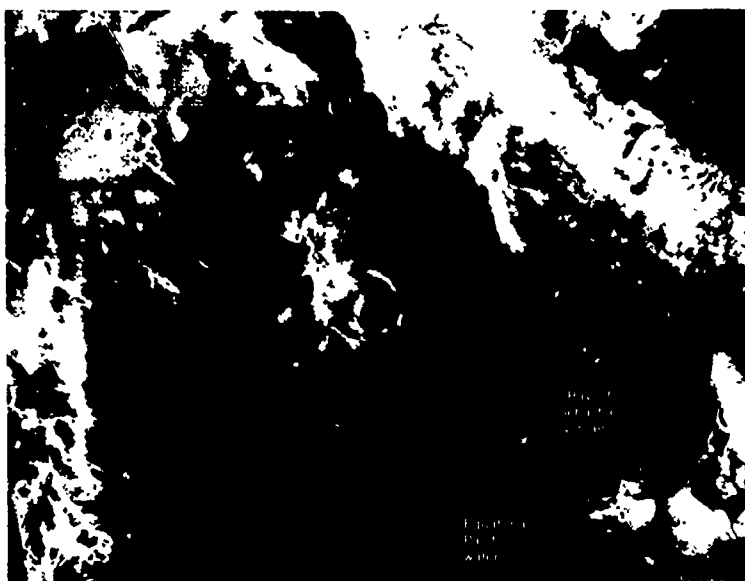


During the winter months, the California Current withdraws from the coast and the surface circulation and temperature field in the eddy are influenced by the low-level wind flow and the advection of surface water into the area. For example, in Fig. 3B-7b, note the intrusion of warm Equatorial Pacific water into the eddy. The advection of warm surface water into the area has almost completely masked the surface indications of the eddy.

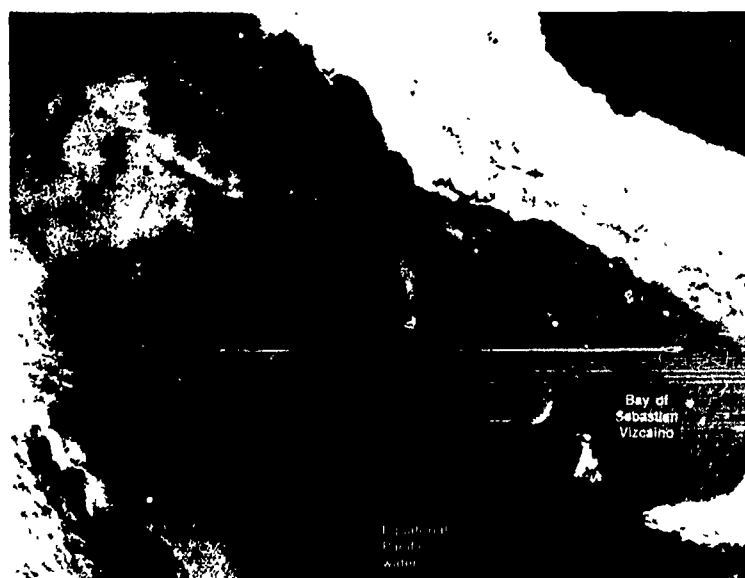
On the following day (Fig. 3B-7c), the effects of the warm water intrusion have disappeared and cold water temperatures predominate at the surface in the eddy. However, a filament of warm water outlines the position of the northern rim of the eddy—revealing its circular shape. The last day in this sequence (Fig. 3B-7d) shows the warm Equatorial Pacific water dominating the surface temperature pattern in the eddy, and the cold water confined to a narrow band along the Baja coastline.



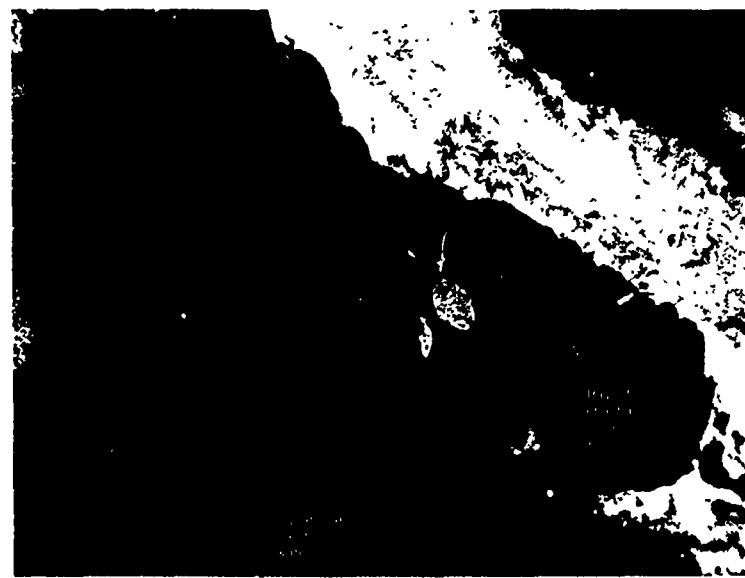
3B-7a. FTV-35.
Enlarged View.
DMSP TF
T-Normal Enhancement.
Oceanic eddy in Bay of
Sebastian-Vizcaino.
0726 GMT
19 September 1977.



3B-7b. FTV-35.
Enlarged View
DMSP TF
T-Normal Enhancement
(Table No. 15).
Surface Eddy Pattern
Masked by Intrusion of
Equatorial Pacific Water
0245 GMT
2 December 1977.



3B-7c. FTV-35.
Enlarged View.
DMSP TF
T-Normal Enhancement
(Table No. 15).
Cold Water
Predominating in
Surface Eddy Pattern
0410 GMT
3 December 1977.



3B-7d. FTV-35.
Enlarged View.
DMSP TF
T-Normal Enhancement
(Table No. 15).
Warm Water
Predominating in
Surface Eddy Pattern.
0352 GMT
4 December 1977.

Case 4 Oceanic Eddies

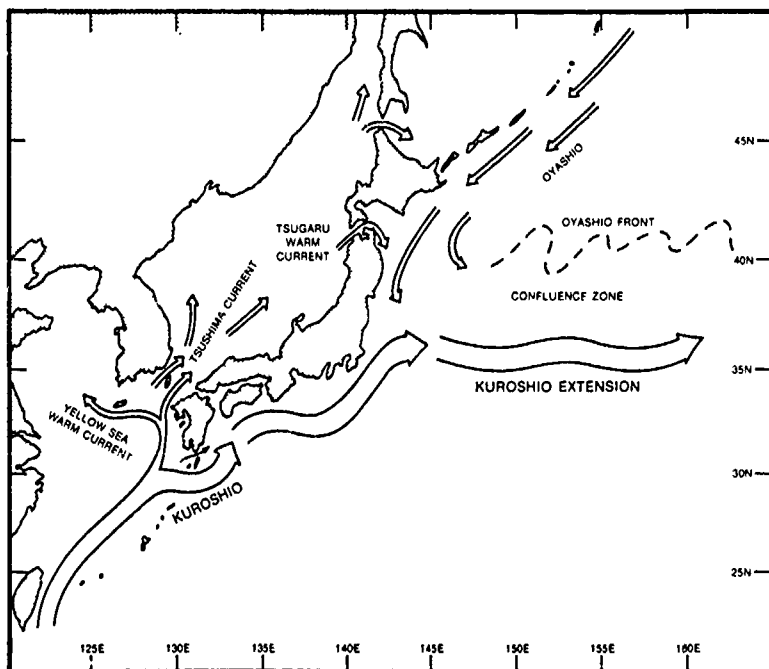
Eddy patterns in the confluence zone between two oceanic frontal systems—The Kuroshio and Oyashio

The dominant currents of the western North Pacific are the warm northward flowing Kuroshio and the cold southward flowing Oyashio (Fig. 3B-8a). The Kuroshio extends to great depths, whereas the Oyashio is a shallower current which weakens rapidly with depth. These currents meet east of Japan and interact along an extended confluence zone. The frontal zones are quite complex due to the presence of warm and cold core eddies generated by these currents, and by the introduction of water from the Sea of Japan through the Tsugaru Strait. Like Gulf Stream eddies, cyclonic (cold core) and anticyclonic (warm core) eddies are formed along the Kuroshio Front when a southerly or northerly meander becomes very large. The narrow base of the current closes off to form cyclonic or anticyclonic circulations, which are separated from the basic current. Cyclonic and anticyclonic eddies are also generated by meanders along the Oyashio Front. Subsurface data (Cheney, 1977) reveals that the Oyashio eddies extend to a much shallower depth and do not show quite the same thermal structure, in their cores, as the Kuroshio eddies.

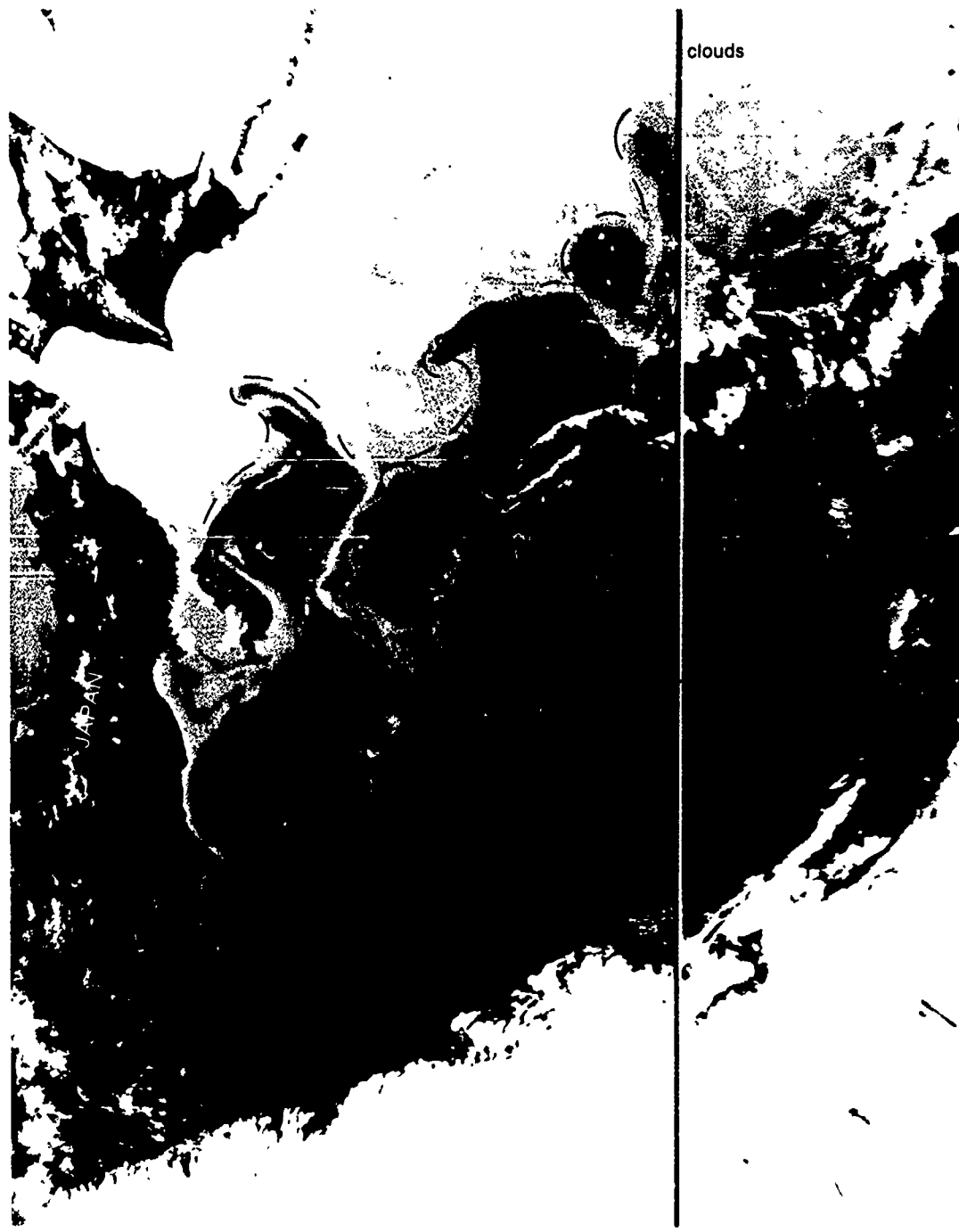
In a NOAA-5 infrared picture of the western North Pacific (Fig. 3B-9a), the complex nature of the Kuroshio and Oyashio frontal systems can be seen off the east coast of Japan. A southward meander of the Kuroshio has produced a cyclonic eddy a short distance offshore. Further offshore, a large amplitude northward meander of the Kuroshio suggests that an anticyclonic eddy may be starting to develop. Note the similarity in the shape of this northward meander and a similar meander that appears along the Oyashio Front to the northwest.

The NOAA-5 visible picture (Fig. 3B-9b) shows sunglint effects extending over the area. Areas of locally calm seas are indicated by the bright areas in the center of the sunglint pattern, and by the dark areas on either side of the sunglint pattern. In addition, note the similarity

3B-8a. Oceanic Circulation Around Japan (after Cheney, 1977).



between some of the very distinct light and dark tone patterns observed in the central area of the sunglint and the corresponding thermal features in the infrared picture. It is particularly noteworthy that cold water areas (light gray shades in the infrared) are generally calmer than warm water areas (dark gray shades in the infrared). The tendency for the sea to be calmer in cold water areas than in warm water areas is especially well revealed around features "A" and "B", which, despite their fine structure, appear equally well delineated in both the infrared and visible images. (For further information on interpretation of sunglint patterns, see NTAG, Vol. 1, Sec. 2A.)



3B-9a. NOAA-5. Infrared Picture. Oceanic Frontal Systems East of Japan. 0021 GMT 10 May 1977.

Reference

Cheney, R.E., 1977: Synoptic observations of the oceanic frontal system east of Japan,
J. Geophys. Res., 82, 34, 5459-5463.



3B-9b. NOAA-5. Visible Picture. Oceanic Features Revealed in Sunglint. 0021 GMT 10 May 1977

3C Upwelling

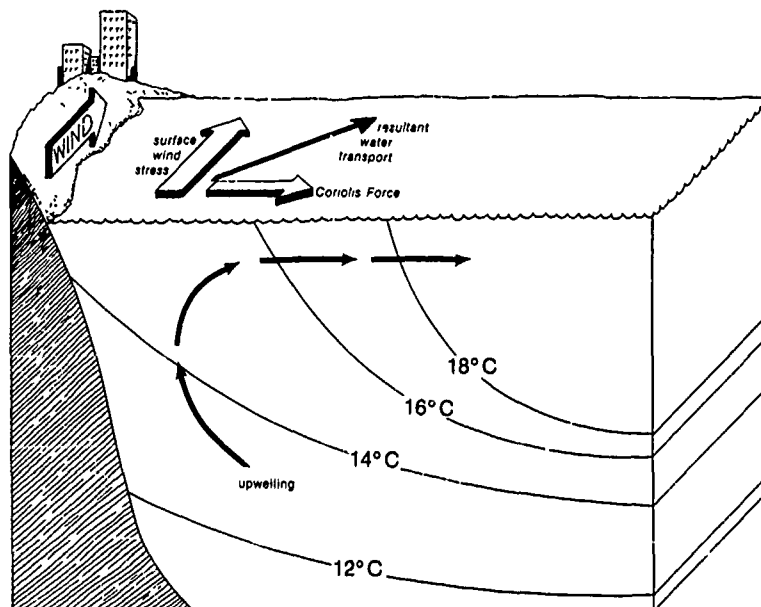
Characteristics of Upwelling

Upwelling in a body of water is a process by which subsurface water rises toward the surface. The geographic location where the vertical water motion occurs is called an upwelling area. Since water temperature generally decreases with depth, the upwelled water is colder than the surface water it replaces. Thus a characteristic region of lower temperature surface water develops in an upwelling area. Infrared satellite data can provide information on the position and strength of the surface thermal gradients associated with upwelled waters. These areas often appear as bands of lighter gray shades (colder temperatures) extending along coastlines. The gray shade pattern may also reveal plumes of cold water or cold water eddies intruding into the warmer waters further offshore. Oceanic thermal fronts may often be observed between upwelled and non-upwelled waters. Upwelled water can also exert a significant influence on meteorological conditions. For example, if the upwelled water is cooler than the air, it may cool the air sufficiently for fog or stratus to develop. The most prominent areas of coastal and oceanic upwelling are shown on page 3C-3.

Causes of Coastal Upwelling

Coastal upwelling is caused by a wind stress acting along the boundary of an ocean, in combination with the effect of the earth's rotation (Coriolis Effect), to produce a net mass transport of water offshore in the surface layer (Fig. 3C-2a). The divergence of surface waters away from the coast results in cold water being upwelled from subsurface layers to replace the offshore flowing water. The structure of the coastal bathymetry strongly influences the strength of the upwelling. Steeply sloping bathymetry produces more upwelling than gently sloping bathymetry, under the same wind stress. It is important to note that the upwelled water comes to the surface from depths which range from 50–300 m (164–984 ft), and the corresponding vertical velocities are quite small (i.e., about 20 m/month off California). The water columns are often isothermal in the upper layers due to the vertical mixing induced by the upwelling.

3C-2a. Schematic Representation of Water Circulation in Coastal Upwelling in Response to Equatorward Wind Stress (Northern Hemisphere).



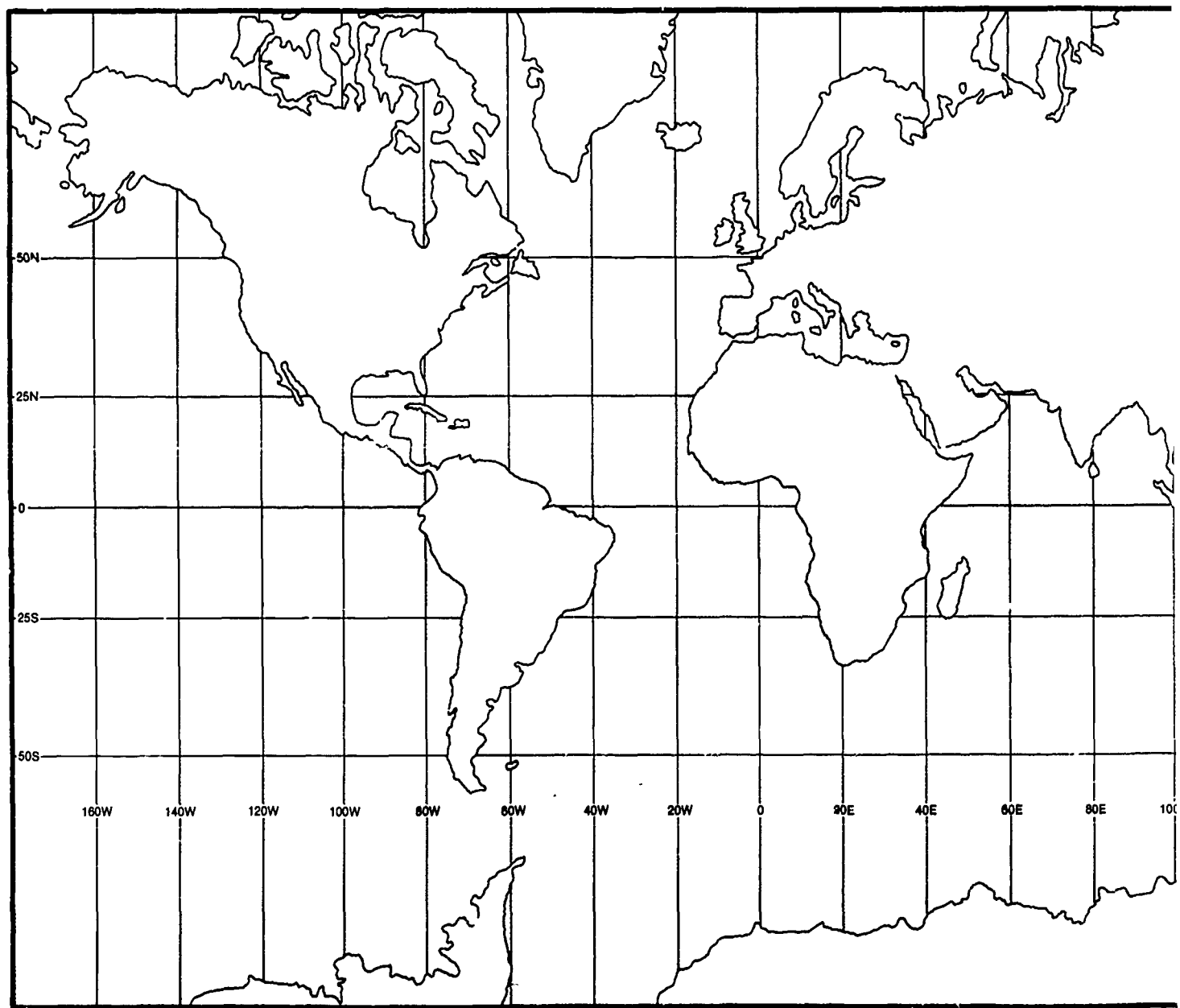
The strength of the wind induced upwelling depends on the characteristics of the wind (i.e., speed, duration, fetch, and direction) and, consequently, it varies with the seasons. Coastal upwelling is most pronounced off the Western U.S. and North African coasts from April through August, and off the Peru and Chilean coasts from March through May. Although the upwelling season lasts several months, winds do not blow steadily along the coast to produce upwelling during the whole period. Instead, short-term "upwelling events" occur on a time scale of days or weeks. The upwelling events are characterized by an increase in the longshore component of the wind and, since the sea surface temperature field responds rapidly to changes in the wind-forcing, a rapid drop in the sea surface temperature occurs near the coast (Holladay and O'Brien, 1975). The thermal gradients accompanying upwelling events are revealed by gray shade patterns in infrared satellite imagery.

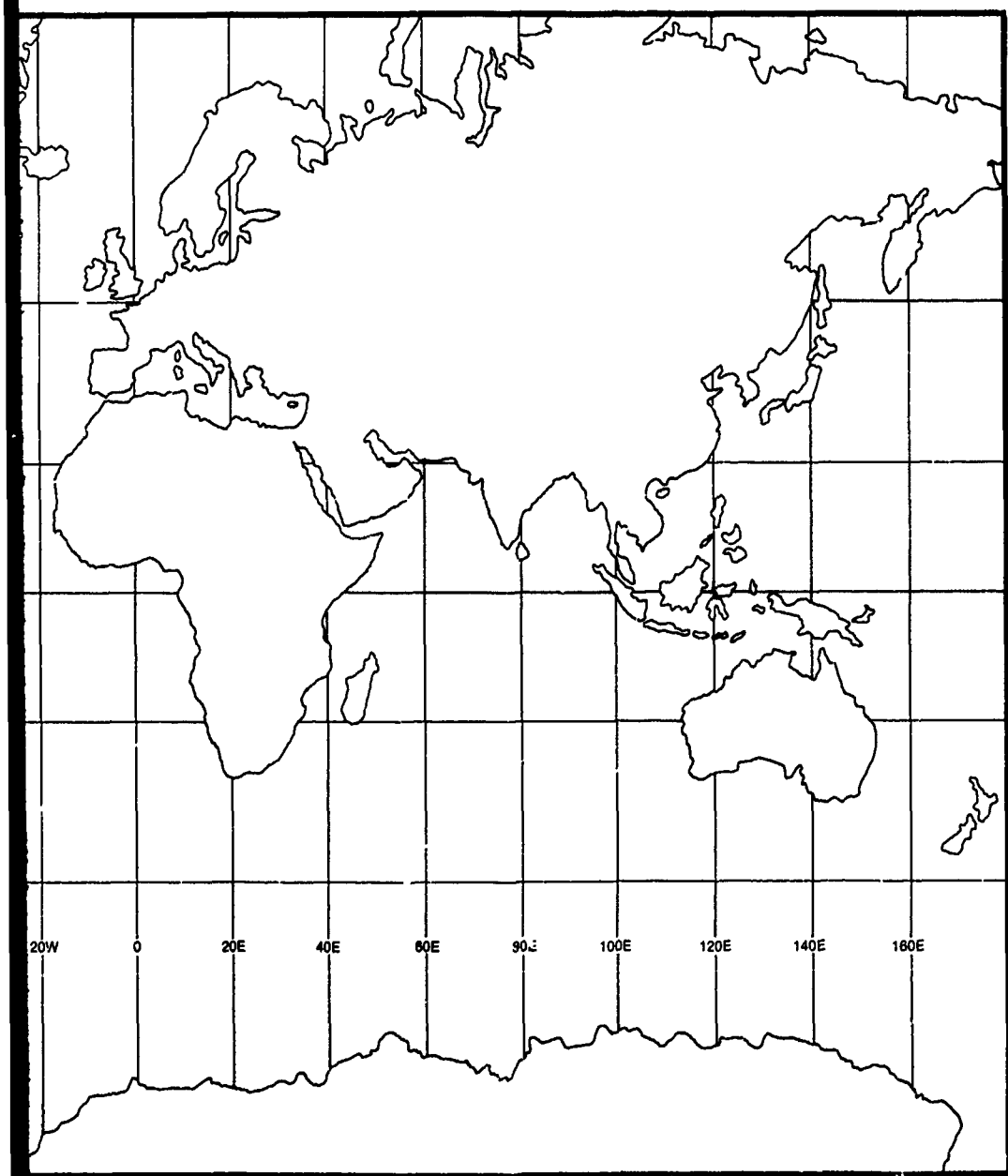
Reference

Holladay, C.G., and J.J. O'Brien, 1975: Mesoscale variability of sea surface temperatures. *Journal of Physical Oceanography*, 5, 761–772.

Other Forms of Upwelling

Dynamic upwelling results when the flow of oceanic currents causes divergence of the surface waters in the open oceans. Where the adjacent surface waters flow away from each other, the deeper water must rise to replace it. Mid-ocean upwelling has been found associated with the Equatorial Current and the northern boundary of the Equatorial Counter Current. Dynamic upwelling may also result when a strong offshore wind pushes the surface waters away from a coast. Topographically induced upwelling occurs when a current impinges on a bottom projection, which forces the current to rise and transport subsurface waters to the surface. Localized upwelling has also been found in: (1) the lee of islands; (2) the lees of large land promontories projecting into a current; and (3) counter-clockwise eddies.



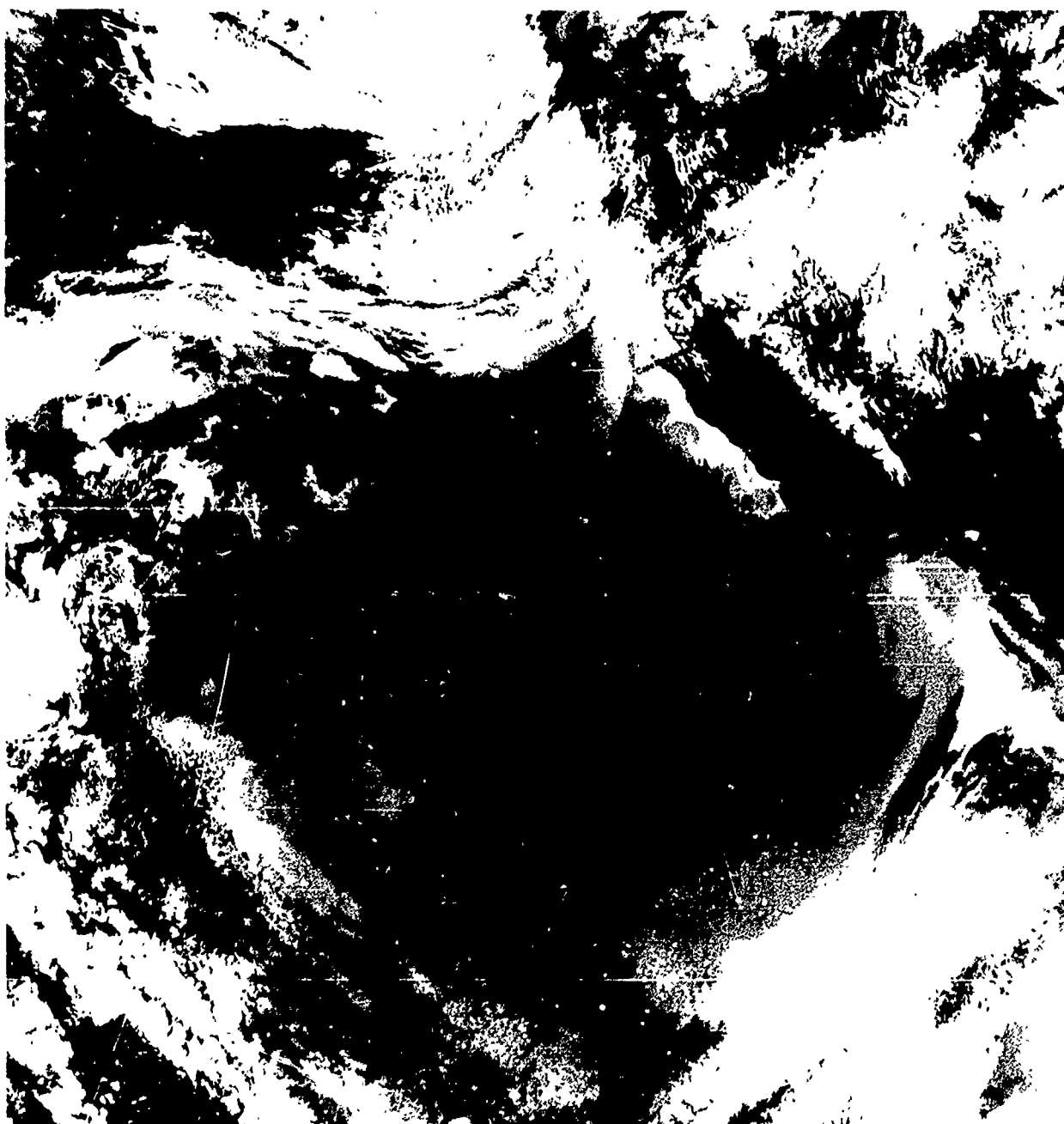


**General
World Areas
of Upwelling**

Case 1 Upwelling

Interaction of intense coastal upwelled waters with a broad ocean current—The California Current

Coastal upwelling along the California Coast is favored during the spring and summer as the semi-permanent subtropical anticyclone over the North Pacific produces steady northerly wind stress over the area. An asymptote of divergence is normally found in the southeastern section of such an anticyclone, conducive for subsidence which produces the clear skies and dry atmosphere that provides optimum conditions for observation of sea surface temperature patterns in satellite infrared data.



3C-4a. FTV-36. DMSP TF T-Normal Enhancement (Table Unknown). Oceanic Thermal Features in the California Current. 0409 GMT 30 August 1977.

In an enhanced nighttime infrared picture of the U.S. West Coast (Fig. 3C-4a), cold upwelled water (light tones) is evident in the cloud-free region from Cape Mendocino to Point Arguello, California. Interaction of the cold upwelled water with the broad, slowly moving California Current has produced several eddies and intrusions. The surface wind reports and streamline analysis are shown in Fig. 3C-5a. An enlarged view of this area (Fig. 3C-5b), reveals the striking details of the eddies and in particular two prominent cold water intrusions "A" and "B". Note that intrusion "A" is located just south of the Mendocino Ridge, which extends westward from Cape Mendocino. Cold water bands have often been noted in this area, suggesting that they may be produced, in part, by upward deflection of the cold subsurface waters in the California Current as it flows over the ridge.

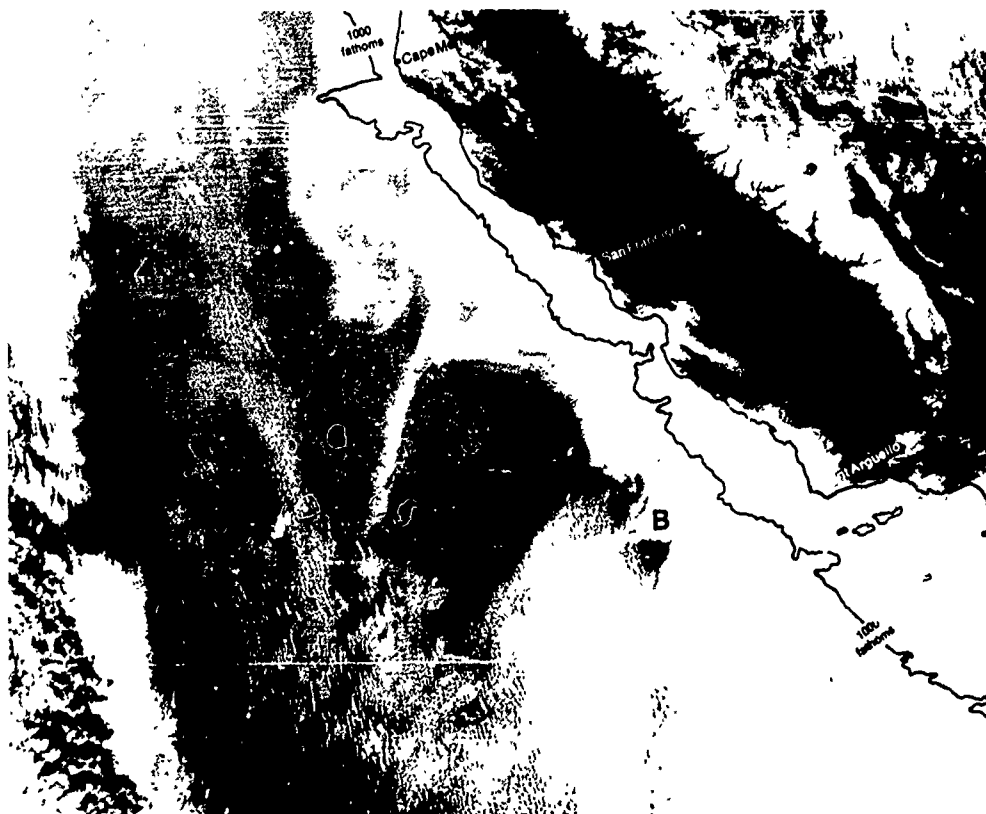
Cloud-free conditions occurred along the coast on the following night (Fig. 3C-5c), permitting a second view of the oceanic thermal features. The cold water intrusion "A" occurs roughly in the same location. The cold water intrusion "B" is partially obscured by cloudiness, although the gray shades suggest that the intrusion remains in the same area.



3C-5a. FTV-36. DMSP TF T-Normal Enhancement (Table Unknown). Oceanic Thermal Features in the California Current. 0409 GMT 30 August 1977. Surface Wind Reports and Streamline Analysis. 0600 GMT 30 August 1977.



3C-5b, FTV-36, Enlarged View, DMSP TF T-Normal Enhancement (Table Unknown). Details of Oceanic Thermal Features in the California Current (With 1000 Fathom Isobath). 0409 GMT 30 August 1977.



3C-5c, FTV-36, Enlarged View, DMSP TF T-Normal Enhancement (Table Unknown). Persistence of Oceanic Thermal Features in the California Current (With 1000 Fathom Isobath). 0352 GMT 31 August 1977.

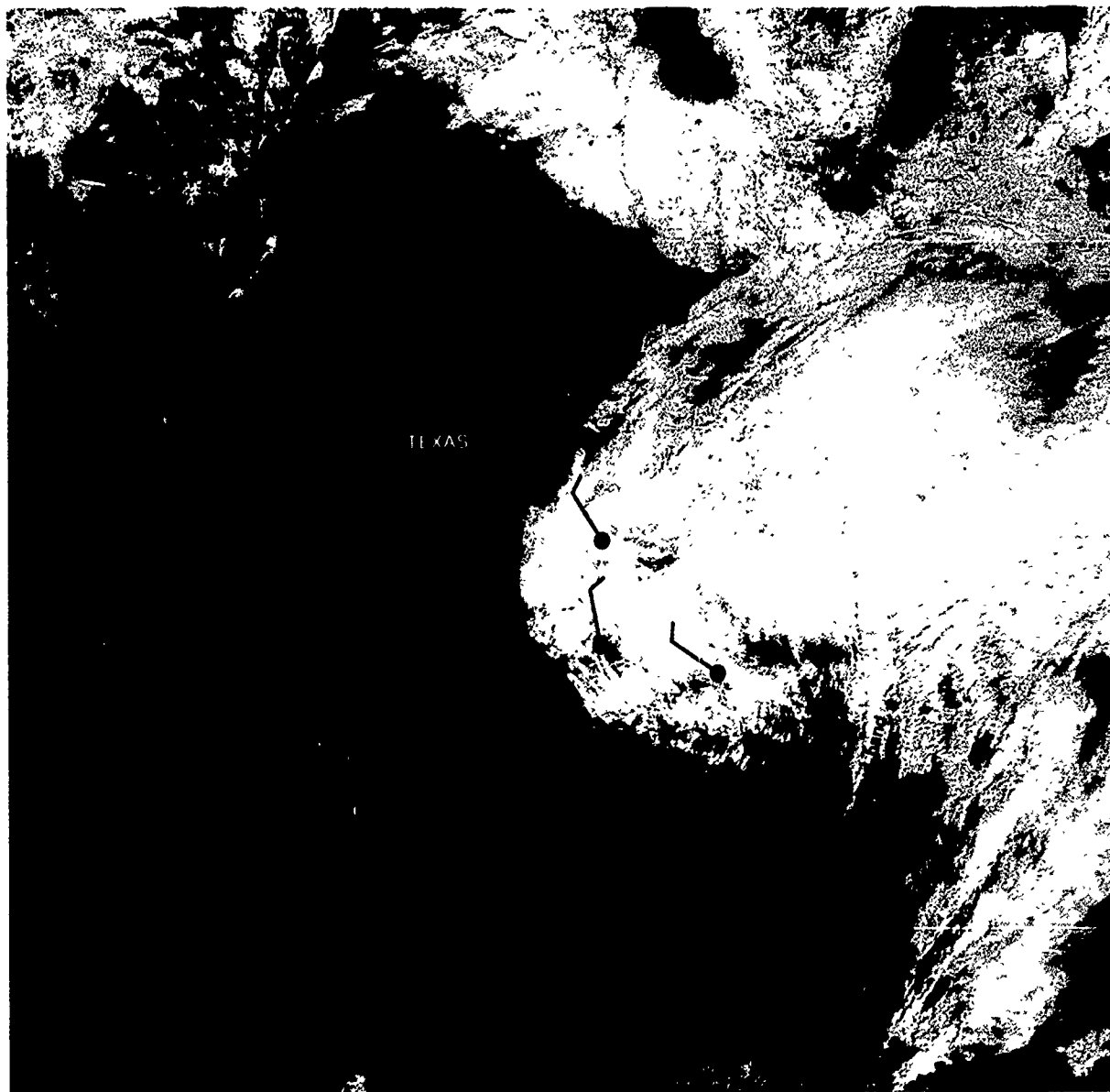
the California Current.
1977.



Case 2 Upwelling

Detection of upwelling in cold continental air outbreaks over coastal waters—Gulf of Mexico

Fig. 3C-6a is a DMSP LF view of the eastern Gulf Coast States showing a frontal vortex with a cold frontal cloud band trailing southwest to the Yucatan Peninsula. Surface reports indicate northwesterly, cold continental air offshore flow along the Texas Gulf Coast. The corresponding DMSP TS picture (Fig. 3C-7a), which has not been enhanced to display sea surface temperatures, reveals a narrow, very light-tone band of cold water along the coast. This cold water band occurs as a result of a combination of dynamic upwelling, produced by offshore wind flow which pushes the surface water away from the coast and brings up colder subsurface water; and by rapid cooling of the shallow coastal waters as the cold, dry continental air is advected over the warmer waters of the gulf.



3C-6a. FTV-35, DMSP LF Low Enhancement. Strong Offshore Flow along the Texas Gulf Coast. 1715 GMT 9 March 1978.
Surface Wind Reports. 1800 GMT 9 March 1978.

For a more detailed view of the oceanic thermal features, a special enhancement of DMSP TF imagery in the area of interest is necessary. Fig. 3C-7b shows such an enhancement of nighttime TF data, approximately 12 hours later. This picture clearly reveals a large area of cold water along the Gulf Coast and, in addition, several cold water intrusions extending offshore into the gulf. The area of coldest water closely parallels the 200 m isobath along the coast. Note that the cold water intrusions form small cyclonic eddies. A detached cyclonic eddy with a central cold core is observed off Corpus Christi.



3C-7a. FTV-35. DMSP TS T-Normal Enhancement. Cold Water Areas along the Texas Gulf Coast.
1715 GMT 9 March 1978.



3C-7b. FTV-35. Enlarged View. DMSP TF T-Normal Enhancement (Table No. 13). Cold Water Areas along the Texas Gulf Coast Showing Intrusions and Eddies (With 200 m Isobath). 0557 GMT 10 March 1978.

oast.

3D Internal Waves

Internal Waves in the Ocean

Internal waves are a wave phenomena in the ocean that form between subsurface water layers of varying density—the density differences may be due to either temperature or salinity, or both. In the open ocean, internal waves are frequently found along the main thermocline (i.e., in the layer of strong vertical temperature gradient below the surface mixed layer). Recently, surface wave manifestations of internal waves have been observed in satellite imagery, notably in sunglint areas under calm wind and sea conditions (Apel and Charnell, 1974; Fett and Rabe, 1977). Internal waves can have a disruptive influence on underwater sound propagation and, as a result, they are an oceanic phenomena which must be identified, located, and interpreted for effects on naval underseas operations.

Internal waves in the ocean may be generated in a number of ways. The generating mechanisms include: (1) tidal action, which creates a semidiurnal or diurnal vertical oscillation of the internal wave, (2) flow impinging on a continental shelf, (3) flow over irregular topography (sill) or around a topographic obstacle (island), (4) along water mass boundaries between two adjacent flows (less dense water over denser water), (5) variations in atmospheric pressure and strong winds, such as found in areas of severe tropical cyclones, and (6) seismic disturbances. Although the amplitudes of internal waves may exceed those of surface waves, internal waves usually propagate at slower speeds.

References

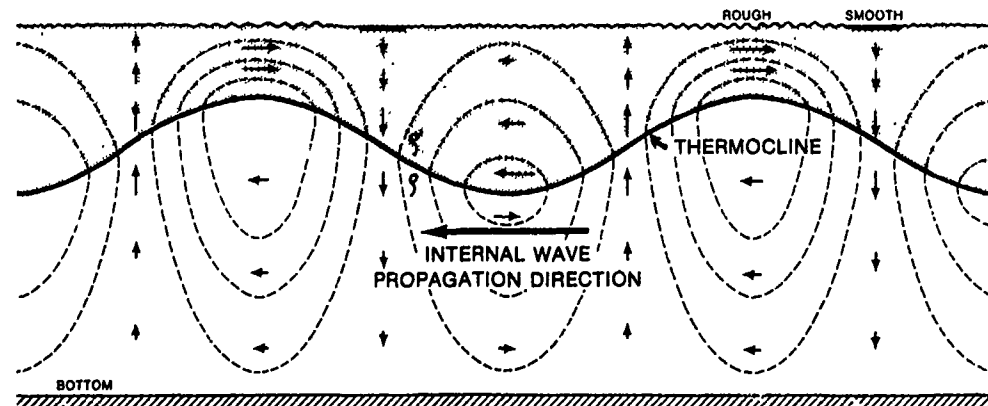
- Apel, J.R., and R.L. Charnell, 1974: Ocean internal waves off the North American and African Coast from ERTS-1. NASA Report SP-351, NASA, Washington, D.C., 1309-1316.
Fett, R., and K. Rabe, 1977: Satellite observation of internal wave refraction in the South China Sea. *Geophysical Research Letters*, **4**, 189-191.

Internal waves on a thermocline in the ocean are progressive waves, and water particles move in alternate clockwise and counterclockwise vertical orbital planes in response to the amplitude, period, and direction of propagation of the waves (Fig. 3D-2a). In this idealized case, described by LaFond and Cox (1962), the waves are sinusoidal (i.e., with a regular alternate ridge and trough pattern), and the amplitude of the waves vanishes at the sea surface. Note that the vertical motion produced between the thermocline and the surface is: (1) downward ahead of the trough due to convergence of the flow between adjacent circulation cells, and (2) upward behind the trough due to divergence of the flow between adjacent circulation cells.

The surface features in this idealized schematic are based primarily on visual observations from ships and aircraft. The rough zone at the surface is assumed to be caused by an increase in the speed of the flow just below the surface as a ridge replaces a trough and the water is forced to pass through the constricted region between the surface and the raised thermocline. (The speed of the flow in the horizontal direction is inversely proportional to the thickness of the layer between the thermocline for orbital oscillations limited to the vertical plane, as in this idealized schematic.) The smooth area, or surface slick, occurs in the convergence zone above the downward flow between adjacent cells.

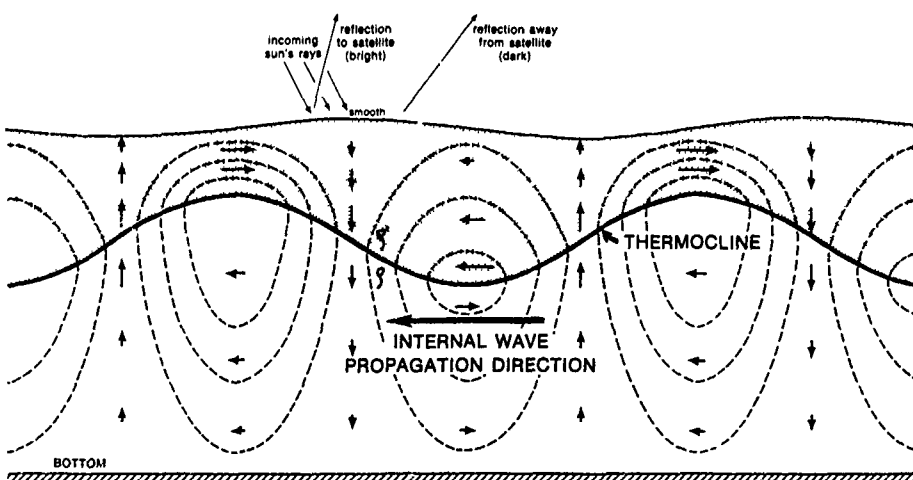
The occurrence of internal waves along the thermocline has a direct influence on underwater sound transmission (Katz, 1967). This is due to refractive effects which depend on the temperature gradient within the thermocline and the angle of intersection of the sound waves with the thermocline. When the thermocline undulates, the sound waves intersect at varying angles resulting in a disruption of acoustical wave propagation. Thus, the use of sonar may be adversely affected within and through an area of internal waves. In addition, sound rarefaction and condensation effects can suggest false targets, while permitting actual targets to pass undetected.

Internal waves have also been suspected as being dangerous to submarine operations. For example, a submarine passing through the upward current portion of the cellular circulation of an internal wave (Fig. 3D-2a) and diving to maintain a constant depth, could suddenly find itself on the opposite side of the cell—in the downward current portion—and diving at an increased rate. When the large amplitude and strength of the internal wave circulation are considered along with the initial depth of operation, it is possible that structural limitations could be exceeded or contact made with bottom topography. This situation has been considered as a possible explanation for the loss of USS THRESHER (Larson, Dale, and Laevastu, 1971).



3D-2a. Schematic of the Structure of Progressive Internal Wave Motion Along a Sharp Thermocline.
The Small Arrows Represent Streamlines of Particle Flow (after LaFond and Cox, 1962).

3D-3a. FTV-28. Enlarged View. DMSP VHR Low Enhancement. Internal Waves in the Sulu Sea. 0419 GMT 2 April 1973.



3D-3b. Revised Schematic of the Structure of Progressive Internal Wave Motion Along a Sharp Thermocline. The Small Arrows Represent Streamlines of Particle Flow.



3D-3c. Apollo 9 Photograph. Internal Wave Refraction Around the Cape Verde Islands. 9 March 1969.

3D-3a. FTV-28. Enlarged View. DMSP VHR Low Enhancement. Internal Waves in the Sulu Sea. 0419 GMT 2 April 1973.

Satellite Observations of Internal Waves

Internal waves in the ocean cannot be directly observed from satellite platforms. However, surface manifestations of internal waves can be detected in polar-orbiting satellite visible data when they occur in areas of nearly calm winds and sea conditions, and where sunglint patterns are also present. The surface manifestations create distinctive alternate bright and dark bands in the sunglint area that reveal the internal wave front patterns below the ocean surface.

There are several concepts proposed to describe the characteristic appearance of the alternate bright and dark bands observed on the surface in areas of internal waves. LaFond and Cox (op. cit.) suggest that the orbital motions induced by internal waves sweep together surface oil and debris to form a slick in the regions of surface water convergence (see Fig. 3D-2a). According to this concept, brilliant reflection would be observed in a sequence of bands at or near the Primary Specular Point (PSP)—with each of the bright bands (slicks) separated by a darker band of slightly rougher seas. The effect would be reversed at large distances to the north or south of the PSP. Apel *et. al.* (1976) suggest that “small waves are concentrated in the convergence regions due to wave-current stresses”, with intervening smoother regions. In this case, dark bands separated by brighter bands would be observed near the PSP.

If it is assumed that the internal waves are non-vanishing at the sea surface, as is indicated in Fig. 3D-2a, and that small, sea-surface oscillations are caused by internal waves (seismograms recorded on the Arctic ice show oscillations with periods characteristic of internal waves; Monin, Kamenkovich, and Kort, 1974), the reflective pattern from these surface waves (swell) would produce the alternate banded structure observed. At the crest of each surface wave, contiguous bright and dark bands would be produced, with intervening bright areas between the bands, as shown in the DMSP data of Fig. 3D-3a and schematically in Fig. 3D-3b. It is important to note that although many cases of internal waves have been documented showing areas of rough water alternating with surface slicks, these features have not been noted in all cases and are not necessary to produce the reflective effects often observed in visible satellite imagery.

An Apollo 9 photograph (Fig. 3D-3c) shows similar contiguous light and dark bands, within a sunglint area, refracting around the lee of the Cape Verde Islands. This effect is not caused by clouds because all the clouds in this view produce shadows on the sea surface. These waves have wavelengths on the order of 1.5–2.5 km (0.8–1.3 n mi) which are not characteristic of surface gravity waves, since the phase speed associated with such wavelengths would be very large. The appearance and wavelength of the bands suggests that they are probably topographically-induced internal waves, creating surface waves of slight amplitude.

3D-3b. Revised Schematic of the Structure of Progressive Internal Wave Motion Along a Sharp Thermocline. The Small Arrows Represent Streamlines of Particle Flow.

3D-3c. Apollo 9 Photograph. Internal Wave Refraction Around the Cape Verde Islands. 9 March 1969.

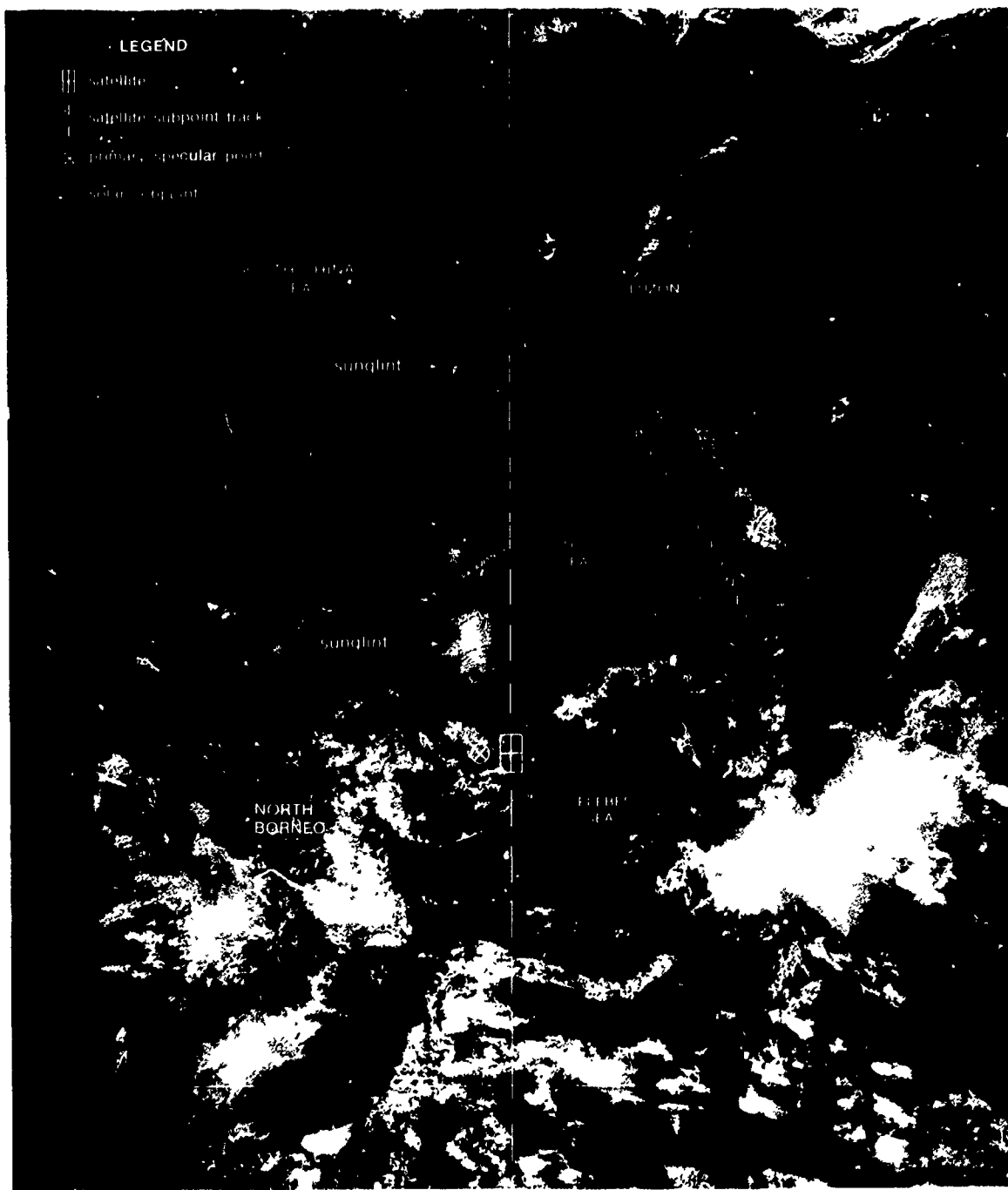
References

- Apel, J.R., H.M. Byrne, J.R. Proni, and R. Sellers, 1976: A Study of Oceanic Internal Waves Using Satellite Imagery and Ship Data. *Remote Sensing of the Environment*, 5, 125–135.
Katz, E.J., 1967: Effect of the propagation of internal waves in underwater sound transmission. *J. Acoustic Soc. Amer.*, 42, 83–87.
LaFond, E.C., and C.S. Cox, 1962: Internal Waves, *The Sea*. Vol. I, M.N. Hill (Ed.), Interscience Publishers, New York, 731–763.
Larson, S., D. Dale, and T. Laevastu, 1971: Large-scale “Turnover” in the oceans. ENVPREDRSCHFAC Tech. Paper No. 1-71, Naval Environ. Pred. Res. Fac., Monterey, Calif., 28 pp.
Monin, A.S., V.M. Kamenkovich, and V.G. Kort, 1974: *Variability of the Oceans*. Translated by J.J. Lumley, John Wiley and Sons, New York, 1977, 241 pp.

Case i Internal Waves

Internal Waves in the Sulu Sea

A long, narrow, north-south sunglint pattern is observed in this DMSP VHR view of the Philippines (Fig. 3D-4a). On this pass, the solar subpoint is located over North Borneo and the Primary Specular Point (FSP) just west of the satellite subpoint track. The brighter sunglint to the west of Luzon is produced by relatively calm seas in the shallow waters of the Scarborough Shoal (see NTAG, Vol. 1, Sec. 2A, Case 6; and Sec. 2C, Case 9). The brilliant sunglint to the south indicates calm winds and seas over the central area of the Sulu Sea.



3D-4a. FTV-28, DMSP VHR Low Enhancement. Internal Waves in the Sulu Sea. 0419 GMT 2 April 1973.

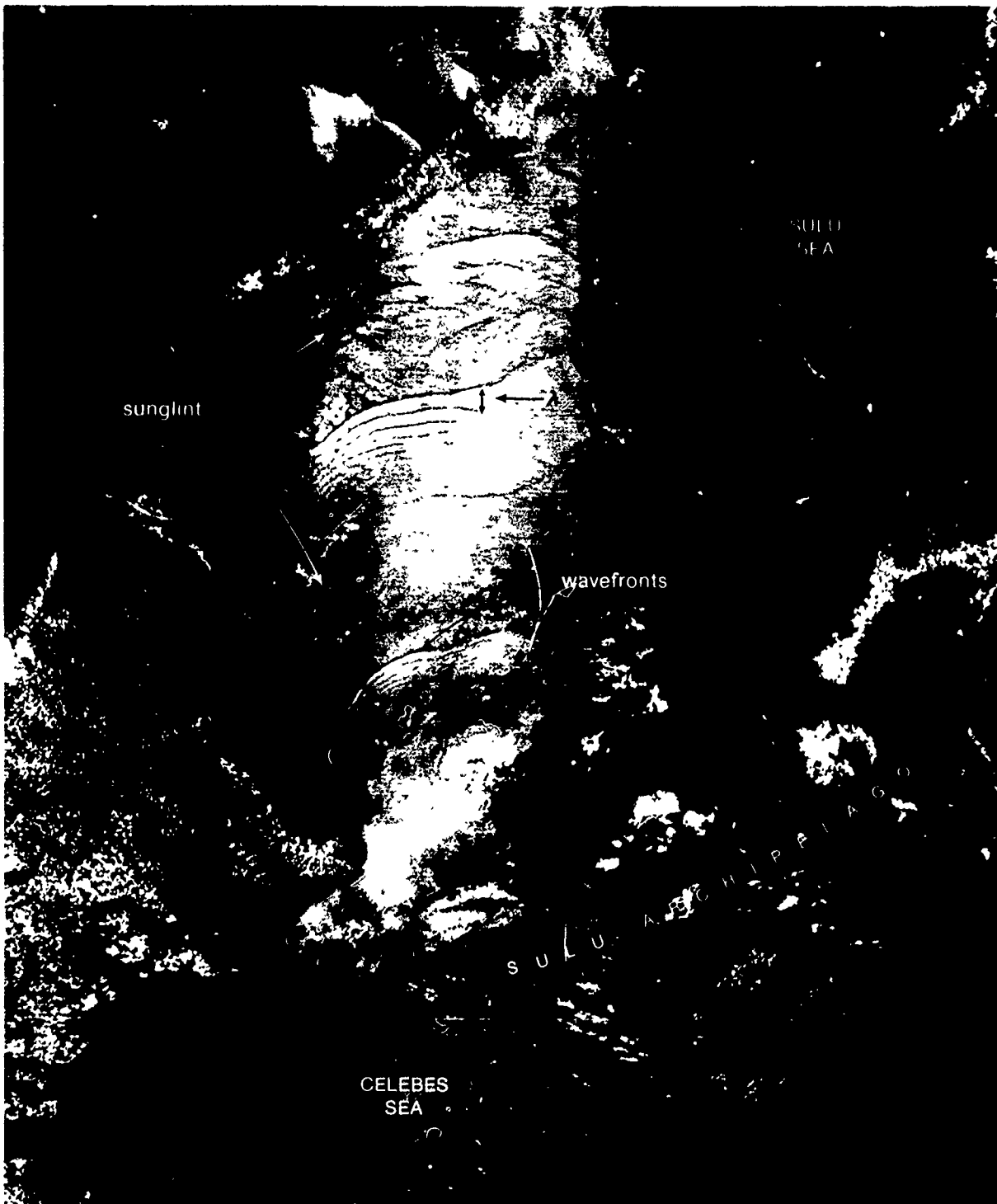
In an enlarged view of the Sulu Sea (Fig. 3D-5a), note the presence of wave-like patterns within the sunglint. This characteristic pattern suggests internal waves emanating from the vicinity of the Sibutu Passage in the Sulu Archipelago. At least 5 separate packets can be distinguished. Assuming the packets are produced by semidiurnal tidal oscillations on the thermocline, giving a speed of translation of about 3 ms^{-1} (6 kt), a life-cycle for the waves in transiting the Sulu Sea is estimated at about 60 hours. In packet 3, the longest wavelength is about 7 km (4 n mi), and the wavelength decreases from the front to the rear of the packet. A close examination of the wave pattern reveals bright bands contiguous with dark bands. This is the effect that would be expected with the solar subpoint located over North Borneo. Brilliant reflection is received by the satellite sensor from the southern slopes of the surface waves and a minimum reflection from the northern slopes.

continued on following page



3D-5a. FTV-28. Enlarged View. DMSP VHR Low Enhancement. Internal Waves in the Sulu Sea. 0419 GMT 2 April 1973.

Internal wave patterns were observed in this area on a pass one week later (Fig. 3D-6a). Two curved wavefronts appear to be radiating from openings between islands in the Sulu Archipelago. As in the previous example, the internal waves probably have been generated by tidal action causing water to move in and out of the Sulu Sea, over the sills between the islands. Note that the wavelength of the internal waves increases downstream from the generating area. In the northern half of the Sulu Sea, refraction patterns appear, which may be related to shallower water in that area (see map, Fig. 3D-7a).



3D-6a. FTV-28. Enlarged View. DMSP VHR Low Enhancement. Internal Waves in the Sulu Sea. 0419 GMT 9 April 1973.



3D-7a. Map of the Sulu Sea.

Case 2 Internal Waves

Refraction of internal waves around Pratas Island and the Pratas Reef—South China Sea

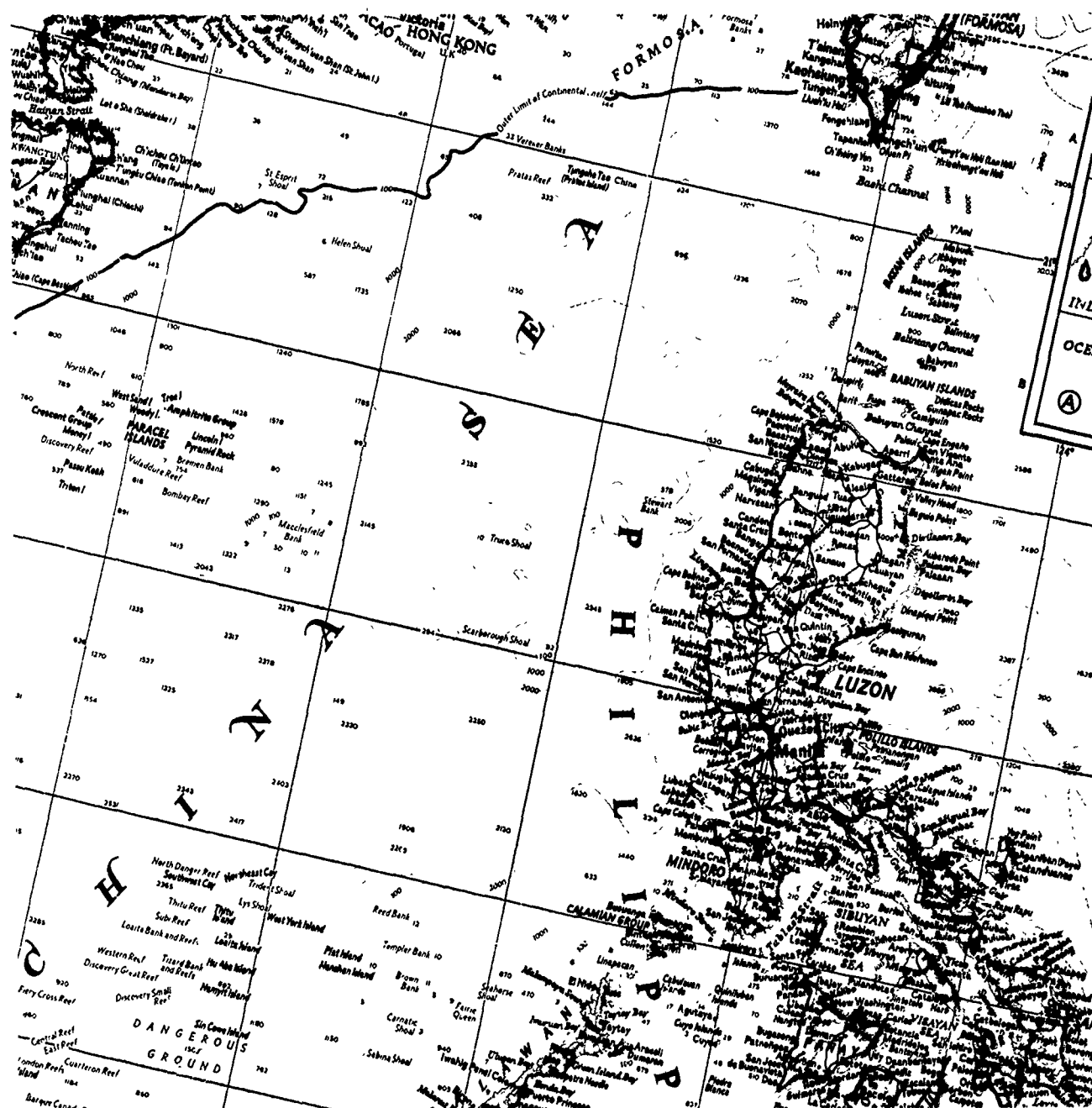
This DMSP VHR picture over the South China Sea (Fig. 3D-8a) shows the characteristic light-dark bands, within a sunglint region, that indicate the presence of internal waves. An enlarged view (Fig. 3D-9b) allows a more detailed examination of the internal wave pattern. The adjacent large brilliant and dark areas across Pratas Reef signify calm winds and sea state. A map of the region (Fig. 3D-9a) shows that the island is located on a bank close to the outer limit of the continental shelf.



3D-8a. FTV-28. DMSP VHR Low Enhancement. Refraction of Internal Waves Around Pratas Island. 0418 GMT 21 May 1973.

According to LaFond (1966), waters of high salinity enter the South China Sea during the winter regime which leads to a salinity maximum at a depth of 100–200 m (328–656 ft) in the northern sector. The salinity gradient persists into the summer regime, although with diminished intensity. The internal waves observed in this case have probably formed on the salinity interface separating waters of different density.

The convex shape of the waves to the east of the island and the refractive pattern in the lee, indicate that the internal waves are approaching from the east. This suggests that the waves may be of tidal origin, since the lunar tidal waves are known to enter the South China Sea regularly through the Bashi Channel between Taiwan (Formosa) and the Philippines (Thuy, 1969).



3D-9a. Map of the South China Sea.

3D-9b. FTV
Island. 0418

Note that the internal wave packets are refracted as they cross the continental shelf to the northwest of Pratas Island. This accounts for the change in the propagation angle of the wavefronts between the island and the continental shelf area.

References

- LaFond, E.C., 1966: The South China Sea, *Encyclopedia of Oceanography*, R.W. Fairbridge (Ed.), Van Nostrand Reinhold Company, New York, 829-837.
Thuy, N.N., 1969: Some features of the formation of tidal phenomena in the South China Sea, *Oceanology*, 9, 189-202.



3D-9b. FTV-28. Enlarged View. DMSP VHR Low Enhancement. Refraction of Internal Waves Around Pratas Island. 0418 GMT 21 May 1973.

3E Other Phenomena

Other Phenomena

This section contains important oceanographic phenomena observed in DMSP visible and infrared imagery, such as coastal sediments, sea ice detection, etc., which do not fit into any broad category.

Case 1 Other Phenomena

Detection of Sea Ice

The detection and monitoring of sea ice conditions is of vital importance to the Navy forecaster for operating at higher latitudes. Icebergs, calved off ice shelves, and floes can pose a danger to ship operations, while the growth and extent of pack ice can have an impact on fleet and support functions. In addition, anomalous acoustical propagation occurs at and under the edge of an ice field.

In order to map areas of sea ice from satellite visible imagery, it is necessary to distinguish sea ice from clouds or snow covered terrain of similar brightness. One method of resolving this problem is to notice that ice and clouds frequently have characteristically different patterns, shapes, or textures; and that clouds cross coastlines, cast shadows, or possess partial transparency. Sea ice often has a granular structure, and leads of open water are frequently observed within an ice field. Another method useful for distinguishing between sea ice and clouds is continuity of observations. Fields of sea ice are relatively conservative, not changing much in appearance from day to day. Clouds, on the other hand, seldom retain the same shape or remain in the same location for more than a few hours. Knowledge of the geography and climatology of a region is also helpful for identifying areas of sea ice.

A large area of sea ice is visible in an April DMSP VHR view of the Sea of Okhotsk, east of the U.S.S.R. (Fig. 3E-3a). Pack ice is displaced sea ice; deriving either from landfast ice (ice attached to the shore), part of which always comes adrift in the spring, or from the margins of the Arctic pack ice. The pack ice in this example has a granular appearance and shows some fracturing due to thawing of the ice. The gray shade variations within the ice field are caused by variations in ice coverage concentrations; the concentration of ice being greater to the north and less to the south. Drift ice (areas of ice which have broken off the main region of pack ice) is apparent farther south. Shore polynyas (open water areas between the ice and the shore) and the occurrence of ice strings along the eastern ice edge are an indication of the influence of the northwesterly flow of the Siberian high pressure system on movement and structure of the ice field. Other features of the ice field are the areas of landfast ice and the isolated ice floes in the open water east of Sakhalin.

The ice-water boundary of the ice field can also be located. Notice that the western margin of the ice field is more clearly defined than the eastern margin. For sonar operations it has been observed that a compact ice edge is more disruptive to underwater sound propagation than a diffuse edge (Diachok, 1976). Thus, satellite imagery can be used to locate those areas in ice fields which may have potentially greater disruptive effect on sonar operations.

Important Conclusions

1. Important sea ice features, such as pack ice, drift ice, and ice floes, can be located and identified in DMSP VHR imagery.
2. Diffuse and compact ice-water boundaries can also be located and identified in DMSP VHR imagery. Such identification is important for use in ASW applications.

Material for this study was provided by Dr. Oscar Huh, Coastal Studies Institute, Louisiana State University.

Reference

Diachok, O.I., 1976: Recent advances in arctic hydroacoustics. *Naval Research Review*, 29, 48-63.



3E-3a. FTV-28. Enlarged View. DMSP VHR Low Enhancement. Sea Ice in the Sea of Okhotsk. 0417 GMT 13 April 1972.

Case 2 Other Phenomena

Detection of river discharge plumes into coastal waters— The Columbia River

Along the U.S. West Coast, waters discharged by rivers into the ocean during the summer tend to be warmer than the coastal waters. The detection of river discharge plumes in satellite imagery is determined, in part, by the amount of the river discharge, the degree of mixing with coastal waters, and magnitude of the temperature difference between the river water and the coastal waters.

Fig. 3E-4a is a DMSP TF view of the U.S. Pacific Northwest coast showing the discharge of the Columbia River into the Pacific Ocean. The river outflow is clearly delineated as a plume of warm water (darker gray shade) extending out from the mouth of the river. The colder offshore waters provide a distinct contrast with the warmer waters of the plume.



Detail of
Columbia River
Outflow into the
Pacific Ocean.



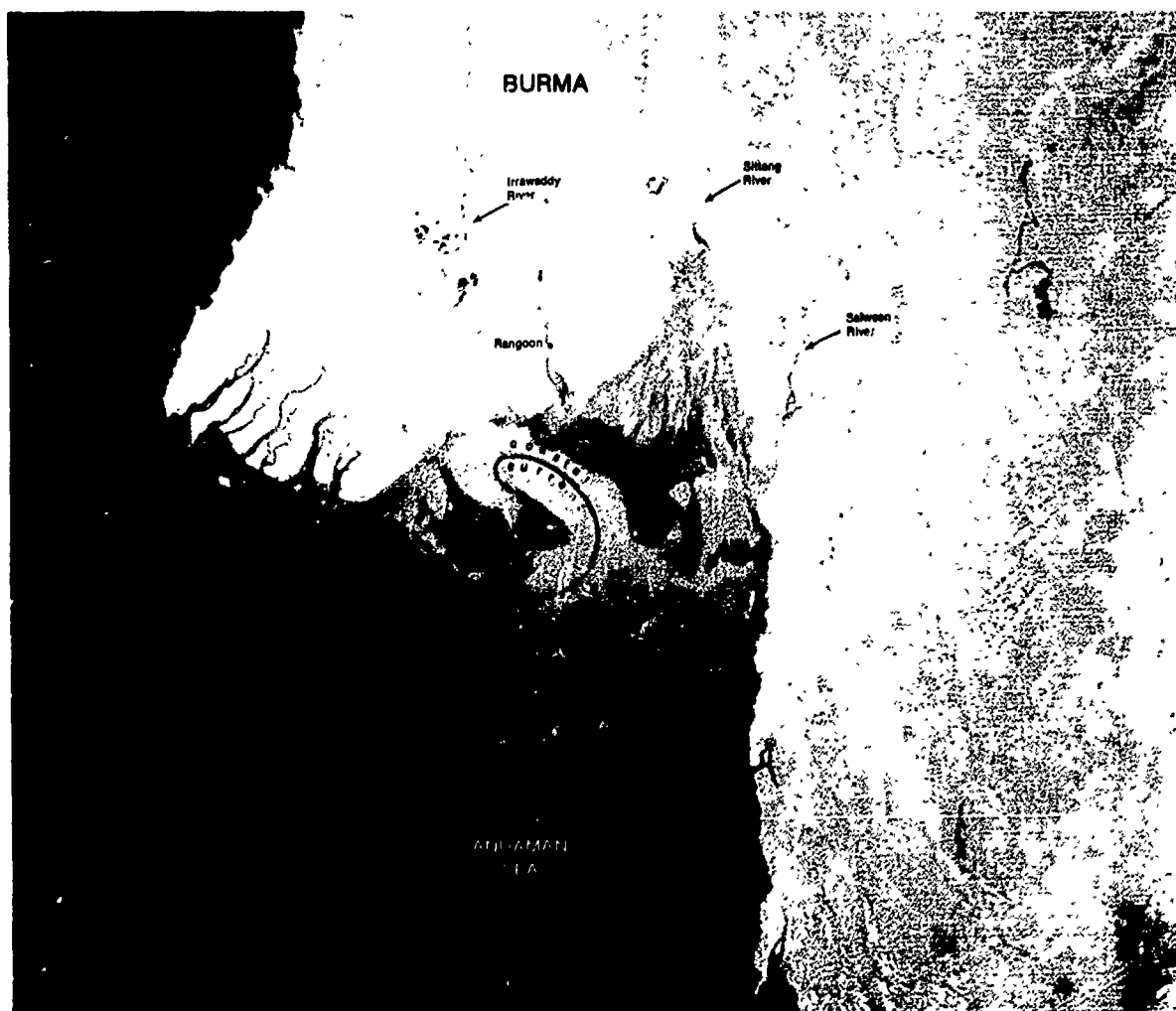
3E-4a. FTV-35, Enlarged View, DMSP TF T-Normal Enhancement, Columbia River Outflow into the Pacific Ocean, 0735 GMT 6 September 1977.

Case 3 Other Phenomena

Detection of river outflow sediments in coastal areas— The Andaman Sea

During the northeast monsoon, heavy rainfall along the southern coast of Burma greatly increases the flow in the Irrawaddy, Sittang, and Salween Rivers. These rivers are heavily-ladened with silt which is transported to the Irrawaddy-Salween River Deltas bordering on the Gulf of Martaban. The Irrawaddy River alone discharges up to 250 million tons of sediment in a year. In addition, up to 250 m of river sediment covers the bottom of the Gulf of Martaban and portions of the Andaman Sea.

Fig. 3E-5a is a DMSP LF picture showing striking anomalous gray shade patterns in the Gulf of Martaban. The anomalous gray shades are produced by reflection from suspended river sediments and/or reflection from the bottom in shallow water areas. Currents in the coastal waters distort the outflow. In particular, note the large, curved anomalous gray shade which suggests the presence of a cyclonic circulation in the gulf.



3E-5a. FTV-35. Enlarged View. DMSP LF Log Enhancement. River Outflow Sediments in the Gulf of Martaban.
0331 GMT 14 January 1978.

Appendix

Sea Surface Temperature Gradient Analysis Using Enhanced Infrared Imagery

The primary need for special enhancements when analyzing sea surface temperature (SST) gradients in DMSP imagery is to display a small change in the normal gray shade presentation in a manner that is readily apparent to the data analyst. The technique used is made possible by modifying the gray shade scales to produce distinctive contrasts in output for small changes in input. Enhancement of high resolution infrared imagery by gray shade manipulation is the key to SST gradient analysis.

There are presently three methods which can be used to display the infrared portion of DMSP data:

Temperature Normal

64 gray shades (black to white) are distributed linearly over a 100° temperature range (210-310 degrees Kelvin (K)), producing a thermal interval of approximately 1.5625 degrees per gray shade.

Temperature Thresholding

Any three preselected temperatures give four visual gray shades, e.g., 215, 220, and 225 K preselected temperatures give the following outputs:

- a. Colder than 215 K appears white.
- b. 215 to 220 K appears light gray.
- c. 220 to 225 K appears medium gray.
- d. Warmer than 225 K appears black.

Temperature Expand

Output consists of a limited number of gray shades (black to

white) spread evenly between two preselected temperatures. For example, selected temperatures of 240 K and 290 K give the entire spectrum (displayed as 32 gray shades from black to white) spread evenly between those temperatures.

It is possible to display SST gradients using either Temperature Expand or Thresholding, but this would require numerous processing runs to determine the optimal input temperature range.

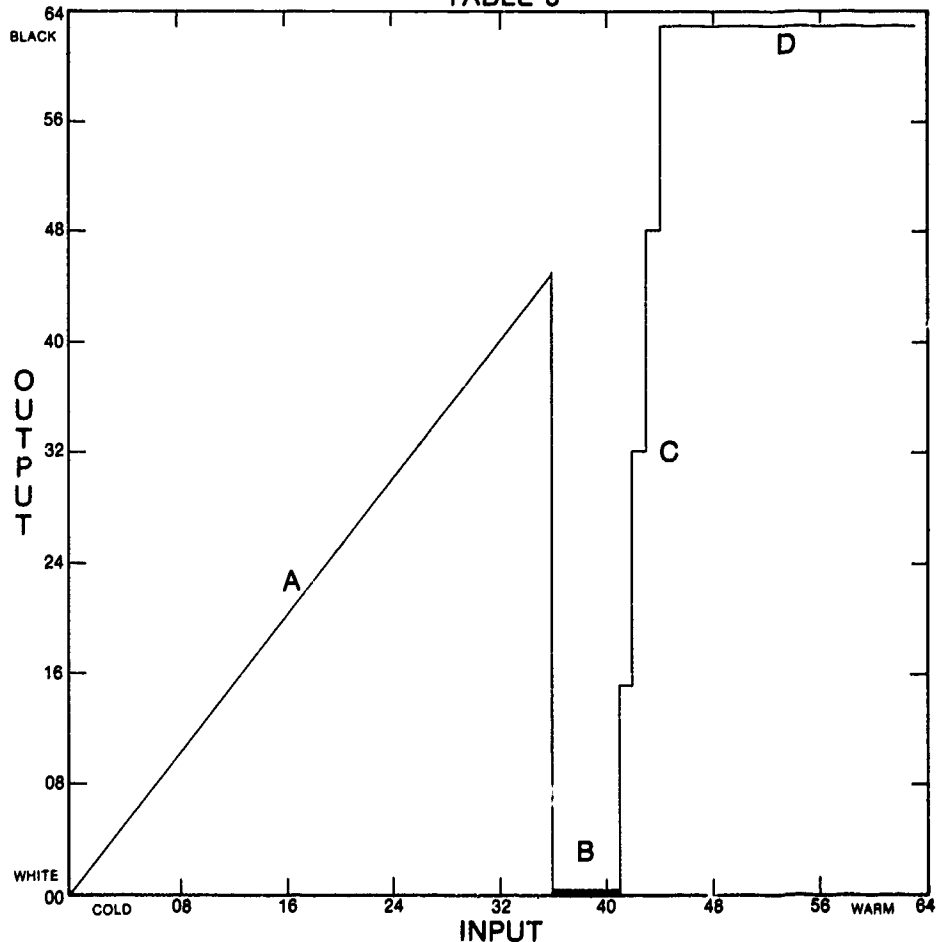
The true temperature sensed by the spacecraft for any point is an aggregate of temperatures emitted by a point on earth and all contamination between that point and the spacecraft. The DMSP spacecraft is a sun-synchronous polar orbital vehicle which rotates slowly around the earth from pass to pass and does not cross the same geographic surface points daily. Thus, the instruments sense through different amounts of atmosphere (from day to day or pass to pass) when viewing a particular geographic point. This means that the desired temperature range must be selected each time a SST gradient analysis is desired.

To provide necessary contrasts for data analysis, the temperature range must be selected so that only five or six output gray shades are displayed. This provides sufficient contrast to distinguish between different output gray shades. The Temperature Normal method permits selection of input/output gray shades by modifying computer software (Blackstone and Whritner, 1976).

Reference

Blackstone, F.A., and R. Whritner, 1976: Applications of DMSP imagery to sea surface temperature gradient analysis. Naval Weather Service Facility, San Diego, Calif., 21 pp.

TABLE 8



DMSP INFRARED ENHANCEMENT TABLES

Table 1				Table 2				Table 3				Table 4			
00	36	63	63	48	63	00	01	00	63	63	00	00	32	00	45
37	40	00	00	00	47	63	02					33	37	00	00
41	44	15	15									38	38	15	15
45	48	27	27									39	39	32	32
49	52	39	39									40	40	48	48
53	56	51	51									41	63	63	63
57	63	63	63									(37-40)			
Table 5				Table 6				Table 7				Table 8			
00	33	00	45	00	34	00	45	00	35	00	45	00	36	00	45
34	38	00	00	35	39	00	00	36	40	00	00	37	41	00	00
39	39	15	15	40	40	15	15	41	41	15	15	42	42	15	15
40	40	32	32	41	41	32	32	42	42	32	32	43	43	32	32
41	41	48	48	42	42	48	48	43	43	48	48	44	44	48	48
42	63	63	63	43	63	63	63	44	63	63	63	45	63	63	63
	(38-41)			(39-42)			(40-43)			(41-44)					
Table 9				Table 10				Table 11				Table 12			
00	37	00	45	00	38	00	45	00	39	00	45	00	40	00	45
38	42	00	00	39	43	00	00	40	44	00	00	41	45	00	00
43	43	15	15	44	44	15	15	45	45	15	15	46	46	15	15
44	44	32	32	45	45	32	32	46	46	32	32	47	47	32	32
45	45	48	48	46	46	48	48	47	47	48	48	48	48	48	48
46	63	63	63	47	63	63	63	48	63	63	63	49	63	63	63
	(42-45)			(43-46)			(44-47)			(45-48)					
Table 13				Table 14				Table 15				Table 16			
00	41	00	45	00	42	00	45	00	43	00	45	00	44	00	45
42	46	00	00	43	47	00	00	44	48	00	00	45	49	00	00
47	47	15	15	48	48	15	15	49	49	15	15	50	50	15	15
48	48	32	32	49	49	32	32	50	50	32	32	51	51	32	32
49	49	48	48	50	50	48	48	51	51	48	48	52	52	48	48
50	63	63	63	51	63	63	63	52	63	63	63	53	63	63	63
	(46-49)			(47-50)			(48-51)			(49-52)					
Table 17				Table 18				Table 19				Table 20			
00	45	00	45	00	46	00	45	00	47	00	45	00	48	00	45
46	50	00	00	47	51	00	00	48	52	00	00	49	53	00	00
51	51	15	15	52	52	15	15	53	53	15	15	54	54	15	15
52	52	32	32	53	53	32	32	54	54	32	32	55	55	32	32
53	53	48	48	54	54	48	48	55	55	48	48	56	56	48	48
54	63	63	63	55	63	63	63	56	63	63	63	57	63	63	63
	(50-53)			(51-54)			(52-55)			(53-56)					

By using table 1 (the search table) only two computer runs are required for correct data display for any area. Table 1 presents six gray shades (spread evenly from white to black), covering any sea surface temperature gradient in the majority of the world ocean areas. The first two columns of each table represent inputs directly related to the temperature sensed by the spacecraft. The next two columns represent outputs designed for contrasting scales, thus the analyst can select the best enhancement table for the sea surface temperature gradient in the area of interest. Table 2 is a special enhancement which displays albedos in the near-infrared portion of the visible mode data inverted from the normal (low albedos appear as light gray shades, middle albedos appear as middle and dark gray shades, and high albedos appear white). Table 3 is simply the T-Normal input-output.

These enhancement tables were devised by the personnel of the Navy Satellite Van Facility, San Diego, Calif.

GRAY SHADE TO STANDARD TEMPERATURE CONVERSION

shade	kelvin	centigrade	fahrenheit	shade	kelvin	centigrade	fahrenheit
0	210.8	-62.2	-80.0	32	260.8	-12.2	10.0
1	212.3	-60.7	-77.2	33	262.3	-10.7	12.8
2	213.9	-59.1	-74.4	34	263.9	-9.1	15.6
3	215.5	-57.5	-71.6	35	265.5	-7.5	18.4
4	217.0	-56.0	-68.7	36	267.0	-6.0	21.3
5	218.6	-54.4	-65.9	37	268.6	-4.4	24.1
6	220.2	-52.8	-63.1	38	270.2	-2.8	26.9
7	221.7	-51.3	-60.3	39	271.7	-1.3	29.7
8	223.3	-49.7	-57.5	40	273.3	0.3	32.5
9	224.8	-48.2	-54.7	41	274.8	1.8	35.3
10	226.4	-46.6	-51.9	42	276.4	3.4	38.1
11	228.0	-45.0	-49.1	43	278.0	5.0	40.9
12	229.5	-43.5	-46.2	44	279.5	6.5	43.8
13	231.1	-41.9	-43.4	45	281.1	8.1	46.6
14	232.7	-40.3	-40.6	46	282.7	9.7	49.4
15	234.2	-38.8	-37.8	47	284.2	11.2	52.2
16	235.8	-37.2	-35.0	48	285.8	12.8	55.0
17	237.3	-35.7	-32.2	49	287.3	14.3	57.8
18	238.9	-34.1	-29.4	50	288.9	15.9	60.6
19	240.5	-32.5	-26.6	51	290.5	17.5	63.4
20	242.0	-31.0	-23.7	52	292.0	19.0	66.3
21	243.6	-29.4	-20.9	53	293.6	20.6	69.1
22	245.2	-27.8	-18.1	54	295.2	22.2	71.9
23	246.7	-26.3	-15.3	55	296.7	23.7	74.7
24	248.3	-24.7	-12.5	56	298.3	25.3	77.5
25	249.8	-23.2	-9.7	57	299.8	26.8	80.3
26	251.4	-21.6	-6.9	58	301.4	28.4	83.1
27	253.0	-20.0	-4.1	59	303.0	30.0	85.9
28	255.5	-18.5	-1.2	60	304.5	31.5	88.8
29	256.1	-16.9	1.6	61	306.1	33.1	91.6
30	257.7	-15.3	4.4	62	307.7	34.7	94.4
31	259.2	-13.8	7.2	63	309.2	36.2	97.2

Each gray shade covers a temperature interval
of 1.5625 K (2.8125°F).
Temperature shown is midpoint of this interval.